Politecnico di Milano
Dipartimento di Ingegneria Civile e Ambientale
Doctoral Programme in Environmental and
Infrastructure Engineering

Large-Eddy Simulation: A tool to study land-atmosphere interactions

Doctoral Dissertation of:
Giulia Ercolani

Supervisor:
Prof. Marco Mancini

Co-supervisor:
Dr. Chiara Corbari

Tutor:
Prof. Giuseppe Passoni

The Chair of the Doctoral Program:
Prof. Alberto Guadagnini

2014 – XXVII Cycle

Giulia Ercolani
Politecnico di Milano
Dipartimento di Ingegneria Civile e Ambientale
giulia.ercolani@gmail.com

Abstract

Large-Eddy Simulations (LES) of the Atmospheric Boundary Layer (ABL), if coupled with a Land Surface Model (LSM), can reproduce the feedback that exists between the ground and the overlying air. This is of great importance in terms of land-atmosphere interactions, but the resulting modelling framework is complex and also challenging to verify and to setup. Hence, a profound awareness of the model capabilities is fundamental in order to produce valuable results that can be used in studies concerning land-atmosphere interactions.

In this thesis the capabilities of the open source mesoscale model RAMS (Regional Atmospheric Modeling System) in performing LES of the ABL are assessed in both idealized and realistic conditions. Then, a coupled LES-LSM is used to quantify the impact that the spatial distribution of meteorological forcings has on the water and energy balance at the surface.

In particular, RAMS-LES performances are extensively investigated under idealized free convection and neutral regimes. The impact of grid resolution is determined, providing guidelines for grid design in both the examined conditions. Cell aspect ratio (horizontal over vertical resolution) has resulted to be a key parameter for grid design in RAMS. In fact, to obtain a correct reconstruction of ABL turbulence, it requires not only a sufficiently fine horizontal resolution, but also an adequate corresponding vertical grid spacing. Different values of the optimal aspect ratio and minimum horizontal resolution are identified for free convection and neutral regimes. The analysis of RAMS-

LES capabilities in convective conditions is enriched by the comparison with the results obtained with the Weather Research and Forecasting (WRF) model, for which a minor role of grid aspect ratio is revealed. RAMS-LES is also evaluated in simulating ABL evolution and land-atmosphere interactions when coupled with a land-surface model and used in real conditions. The coupled model predictions are compared against field measurements and a good agreement is found for both temporal and spatial patterns. The impact that surface heterogeneity level of description has on the coupled model results is examined, and a different role in ABL turbulence and surface quantities reproduction is evidenced. Finally, the error that is introduced in surface water and energy balance by the spatial interpolation of meteorological forcings is assessed thanks to a coupled LES-LSM. The impact of meteorological forcings spatial distribution on turbulent heat fluxes has resulted to be regulated by soil water content. Moreover, an alternative interpolation method that improves microscale meteorological fields reconstruction is proposed and tested.

Contents

1 Introduction

Large-Eddy Simulation (LES) has been recognized to be a valuable tool for reproducing Atmospheric Boundary Layer (ABL) turbulence since the works of Deardorff (1970, 1972, 1974). The initial applications of LES to ABL modelling considered almost exclusively idealized regimes, namely homogeneous surfaces properties, prescribed fluxes at the ground and periodicity as lateral boundary condition. In addition, these initial applications were confined into purely atmospheric or fluid dynamics research. But the continuous increase in computational capabilities has led to LES of more complex ABL flows, that overcome the above-said idealized constraints. Grid nesting techniques are used to relate microscale turbulence with the larger-scale flow, and the coupling of LES with a Land-Surface Model (LSM) allows to dynamically compute surface fluxes during the simulation, and therefore to reproduce the feedback existing between the land surface and the atmosphere. In this context Numerical Weather Prediction-Limited Area Models (NWP-LAMs) appear to be particularly attractive tools to perform LES of the ABL, because natively supplied with the capability of nesting and with the equations of motion coupled with a LSM. Moreover, in recent years computational capabilities have reached the level that makes the cost of LES of the ABL affordable even with standard resources at disposal. Consequently, LES of the ABL is becoming a widespread tool of investigation in several fields not traditionally linked to Large-Eddy Simulation, such as hydrology, renewable energy production, agrometeorology and others.

In particular, in the hydrological context the interest in LES of the

ABL is mainly oriented to land-atmosphere interactions, and therefore LES is mainly used coupled with a LSM. In fact surface fluxes of sensible and latent heat, that are the expression of land-atmosphere interaction, are two fundamental terms of the hydrological balance. Consequently their accurate estimation is of great importance in water resources management at both the regional or basin scale and the field scale. For instance, coupled LES-LSM can be employed to assess surface heterogeneity impact on ABL structure and evolution and in turn on surface turbulent fluxes, to quantify the importance of the land-atmosphere feedback on the estimation of the fluxes themselves, and also to support the interpretation of turbulent fluxes field measurements.

In this thesis we explore the capabilities of the mesoscale model RAMS in performing LES of the ABL and then we employ it to quantify the impact of meteorological forcings spatial distribution on a water and energy balance model. In fact RAMS may be considered a suitable instrument for hydrologically-oriented applications, since its equations of motion are natively coupled with a LSM. But RAMS is originally designed to simulate mesoscale flows, and therefore an evaluation of its performances in reproducing microscale turbulence is needed to obtain valuable results (Gibbs and Fedorovich, 2014a; Paiva et al., 2009). Moreover, the complexity of the coupled modelling system, combined with its diffusion to fields not traditionally linked to LES, reinforces the importance of an extensive investigation of the code capabilities under various conditions and with different setups. The conditions analyzed in the thesis are idealized free convection, idealized neutral regime and a real diurnal cycle over a heterogeneous surface. The impact of grid resolution is deeply investigated in order to provide guidelines for grid design in future applications. For the coupled LES-LSM the role of the scale at which surface heterogeneity is described is examined. The performed evaluation validates the use of the coupled model for practical applications. In particular in this thesis the results of a coupled LES-LSM are used to assess the impact that the spatial distribution of meteorological forcings has on a water and energy balance model.

The thesis is organized as follows. Chapter 2 provides a brief presentation of the atmospheric boundary layer structure, temporal evolution and turbulence, with the aim to be of support for the thesis and not an exhaustive dissertation.

Chapter 3 gives an overview about applications of LES of the ABL,

with a specific focus on studies performed with the two NWP-LAMs used in the thesis, namely RAMS and WRF (Weather Research and Forecasting model). Moreover, in the first part of the chapter the rationale of the LES technique and the typical set of equations for ABL modelling are described.

Chapter 4 illustrates RAMS equations, numerics, and its land surface model LEAF-3 (Land Ecosystem-Atmospheric Feedback version 3).

In Chapter 5 an extensive investigation of RAMS capabilities in performing LES of the ABL in convective conditions is presented, with a detailed analysis of grid spacing impact on the results. Nine simulations are performed combining three different horizontal and vertical resolutions but maintaining an identical idealized free convection setup. Moreover the verification of RAMS-LES is enriched by the comparison with WRF model performances under the same conditions. The analysis aims to fill the lack of studies that evaluate RAMS-LES capabilities and also to define guidelines about grid design for both codes.

Chapter 6 completes the verification of RAMS-LES capabilities by performing an analysis analogous to that of the previous chapter but under neutral conditions. Again, the aim is also to identify grid resolutions and aspect ratios (horizontal over vertical grid spacing) that provide the optimal results. Turbulent structures in neutral regime are smaller and more elongated that in convective conditions, and therefore a different behaviour of the code is expected.

In Chapter 7 it is presented an evaluation of RAMS-LES performances in simulating ABL evolution and land-atmosphere interactions when coupled with a land-surface model and used in real conditions. The coupled model results are compared with field observations of surface fluxes and micrometeorological states. The case study is an agricultural area in Spain, that was the site of the experimental field campaign REFLEX 2012: its flatness and the hydrological disconnection between the groundwater and the surface are appealing characteristics for a coupled LES-LSM evaluation. This additional evaluation of the model is crucial if the final goal is to use it in realistic conditions. In fact the coupling with a land-surface model increases the complexity of the modelling framework and time-varying forcings and surface heterogeneity are to be faced.

Chapter 8 investigates the impact of the scale of surface heterogeneity on a coupled LES-LSM, in terms of both ABL characteristics and surface quantities. Besides its intrinsic relevance, the analysis has also

a practical purpose. In fact confidence with the coupled modelling framework can be increased by the assessment of the influence that a surface characterization coarser than that required by LES needs has on the model results. For this analysis five simulations with an increasingly coarser spatial resolution of the surface parameters are performed. The remaining setup of the simulations is identical to that used in the previous chapter.

Chapter 9 presents an analysis based on the results of the coupled LES-LSM performed in Chapter 7. The role that the spatial pattern of meteorological forcings has on a distributed surface energy and water balance is assessed by using meteorological fields obtained from the coupled simulation results. Typically, the maps of forcings such as air temperature, air humidity and wind speed are obtained through spatial interpolation of punctual measurements, but the error introduced in the water and energy balance by the interpolation could be rigorously assessed only if distributed meteorological data were available at a very high spatial resolution in a sufficiently wide area. Therefore, we use LES-LSM fields as proxy of real atmospheric data in order to evaluate this error. Energy and water balance results from simulations forced with the physically based fields are compared with those obtained with interpolated fields. Moreover, an alternative interpolation method that overcomes the limitations that standard methods based over physical distance between points have in reproducing microscale variations is proposed and tested.

Finally in Chapter 10 the importance of aerodynamic resistance in the estimation of surface heat fluxes is briefly discussed, and some literature formulas performances are evaluated against experimental data. In fact the key role that aerodynamic resistance has in the estimation of surface fluxes, and therefore in the reproduction of the land surface-atmosphere feedback, may be considered a significant weakness of the sophisticated coupled LES-LSM system analyzed in the present thesis.

Part I

Theory and model

2 The Atmospheric Boundary Layer

In this chapter a brief presentation of the Atmospheric Boundary Layer (ABL) is provided, with the only aim to be functional to the present thesis an not to be an exhaustive dissertation. The description will follow mainly Stull (1988) and Garratt (1994), the two most widespread and complete handbooks about ABL. Other useful texts about this topic are *i*) Kaimal and Finnigan (1994), more circumscribed than the above-said handbooks but still a comprehensive presentation of the ABL with a particular focus on measurements techniques; *ii*) Wyngaard (2010), where a valuable dissertation of atmospheric turbulence is provided; *iii*) Fedorovich et al. (2010), a collection of recent developments in atmospheric turbulence and mesoscale meteorology.

General characteristics and concepts about ABL are described in Section 2.1, a typical diurnal cycle over land is illustrated in Section 2.2 and some thermodynamics concepts are reported in Section 2.3. Finally, few considerations about ABL turbulence are presented in Section 2.4.

2.1 Generalities

The Atmospheric Boundary Layer (ABL) is the part of the troposphere that is directly influenced by the presence of the earth's surface and that responds to surface forcings with a timescale of an hour or less (Stull, 1988). Surface forcings are frictional drag, heat transfer, evapotranspiration, pollutant emissions and terrain induced flow modi-

fication. Garratt (1994) provides a very similar definition for the ABL, namely the layer of air directly above the earth's surface in which the effects of the surface (friction, heating and cooling) are felt directly on timescales less than a day, and in which significant fluxes of momentum, heat or matter are carried by turbulent motions on a scale of the order of the depth of the boundary layer or less. The two definitions differ for the timescale indicated for the ABL response to surface forcings (one hour for Stull (1988) and one day for Garratt (1994)), but they both limit the ABL on the basis of the strict relation existing with the earth's surface. The troposphere is the lower part of the atmosphere, ranging from the ground up to about 15 km. ABL height vary significantly in both time and space, but typical values are $100 - 3000$ m. The remaining part of the troposphere, above the ABL, is called free atmosphere, meaning "free from the earth's surface influence" in opposition to the definition of the ABL. ABL and free atmosphere differ in several aspects:

- ABL is almost continuously turbulent throughout its depth, while free atmosphere is mostly laminar.
- ABL is subjected to strong shear because of the presence of the earth's surface, and therefore a large energy dissipation is present, while in free atmosphere energy dissipation is small and due to viscosity.
- ABL turbulent nature implies rapid mixing in both horizontal and vertical directions. In the free atmosphere only small molecular diffusion is present in accordance to its laminar status. Mean wind can generate a horizontal rapid transport.
- ABL thickness is significantly smaller than that of the free atmosphere, i.e. $100 - 3000$ m against $8 - 18$ km. In addition ABL height varies in space and experiences diurnal oscillations, while free atmosphere depth changes slowly in time.

ABL importance and the interest of studying it are motivated by the fact that humans live in it and consequently many aspects of their lives are directly connected to the ABL. For instance its turbulence affects the design of structures, its characteristics and processes determine crops growth and air pollution destiny, and what it is called for brevity "wind energy" is actually energy from the atmospheric boundary layer. Therefore the ABL is of interest for many areas of study,

such as hydrology, mesoscale and agricultural meteorology, renewable energy, urban planning, building design and fluid mechanics. But the ABL can be studied only facing relevant difficulties that characterize both measurements and mathematical description of it, whose primary and common cause is the turbulent nature of the ABL, that implies unpredictable and chaotic motions (Kaimal and Finnigan, 1994).

2.2 ABL temporal evolution

As already anticipated, ABL height changes in time and space, since it is determined by surface forcings. It grows with the cumulative input of surface sensible heat flux (Driedonks, 1982), and, in particular, it follows a diurnal cycle over land, while over oceans variations are slower because of the large thermal inertia of the oceans themselves. Instead the ground warms and cools with a daily timescale in response to solar radiation, and through transport processes it adds or subtracts energy to the overlaying air, forcing changes in the ABL. Figure 2.1 illustrates the ABL diurnal cycle over land. It can be seen that ABL structure changes dramatically between night and day, but the lower 10% of the ABL is always called *surface layer*, regardless the above conditions. The surface layer is characterized by the fact that within it vertical turbulent fluxes are nearly constant with height and therefore almost equal to their surface values. The lowest few centimeters of it are in turn called *roughness* or *interfacial* layer, and they correspond to where molecular transport dominates over the turbulent one. The daytime ABL is characterized by the presence of the *mixed layer*, that is a layer where turbulence tends to mix uniformly all the ABL quantities, as heat, moisture and momentum. Mixed layer turbulence is usually of convective nature, generated by an upward buoyancy flux at the surface due to the higher temperature of the ground in respect to that of the overlaying air and by radiative cooling from the top of the cloud layer. Consequently, when clouds are not present, mixed layer starts to develop about a half hour after the sunrise because of solar heating of the surface. Thermals of warm air rise from the ground, increasing turbulence and causing entrainment of less turbulent air from above. The rise of the thermals is limited by a statically stable layer at the top of the mixed layer that is called *entrainment layer*, since the entrainment process occurs there. The mixed layer reaches the maximum depth in the late afternoon. The characteristic virtual

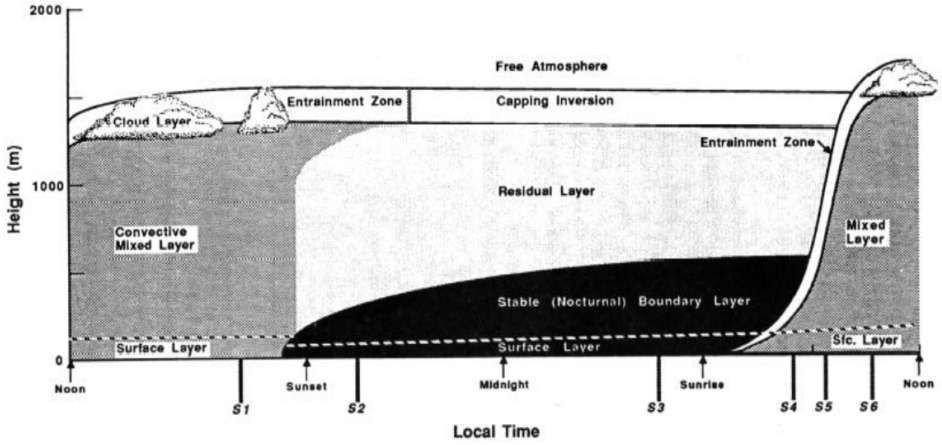

Figure 2.1: Temporal evolution of the atmospheric boundary layer over land. From Stull (1988)

temperature profile is adiabatic in the middle of the mixing layer and superadiabatic in the surface layer. It is important to specify that also strong winds can generate a well mixed layer. When before the sunset the ground temperature equal the air temperature thermals are no more generated, and turbulence in the mixed layer starts to decay transforming the mixed layer into the *residual layer*, that is neutrally stratified. But as the night progresses an increasingly part of the residual layer is transformed into a *nocturnal stable layer* because of the cooling caused by the contact with the ground. Turbulence is weak and sporadic, since its static stability acts in suppressing it. The next day the mixed layer will develop overcoming the nocturnal stability and it will rise quickly to the height of the previous day as it will reach the residual layer.

2.3 Basic air thermodynamics

Air temperature profiles in the atmosphere are usually expressed in terms of *potential temperature* and *virtual potential temperature*. The potential temperature θ is the temperature that a parcel of air would have if it was brought adiabatically to a reference pressure P_0 (Garratt, 1994). The reference pressure is usually posed equal to 1000 hPa but

it is often replaced by surface pressure in ABL context.

$$\theta = T \left(\frac{P}{P_0} \right)^{\frac{R_d}{c_p}} \tag{2.1}$$

where $R_d = 287$ J kg^{-1} K^{-1} is the gas constant for dry air, $c_p = 1004.67$ J kg^{-1} K^{-1} is the specific heat for dry air at constant pressure, T is air temperature (K) and P is air pressure (hPa). Therefore potential temperature removes the influence of altitude on air temperature. The virtual temperature T_v is the temperature that a parcel of dry air must have to equal the density of moist air at the same pressure

$$T_v = T\,(1 + 0.61q) \tag{2.2}$$

where q is the air specific humidity, defined as the mass of water vapour per unit mass of moist air. Virtual temperature (for unsaturated air) is higher than standard temperature since the density of moist unsaturated air is lower than that of dry air. Hence, if adopting virtual temperature, air density variations due to moisture content are taken into account as variations of temperature. Finally the virtual potential temperature θ_v is defined as

$$\theta_v = \theta\,(1 + 0.61q) \tag{2.3}$$

Another common way, in addition to specific humidity, to express air moisture content is the water vapour mixing ratio r, i.e. the mass of water vapour per unit mass of dry air. Specific humidity is related to it by

$$q = \frac{r}{r+1} \tag{2.4}$$

Consequently the approximation $q \approx r$ is usually adopted.

A flow is said to be stable if it is becoming or it remains laminar. On the opposite a flow that is becoming or it remains turbulent is said unstable. The condition depends on the balance between stabilizing and destabilizing factors, i.e. when these latter predominate turbulence will occur. Atmospheric temperature profiles determine the static stability of the ABL, that is the measure of the capability for buoyant convection. It does not depend on wind, since it is an evaluation of air stability in static conditions. Air is statically unstable if layers with a higher density are above less dense layers, namely warmer or moister layers. In this case convective motions develop and lighter air rises to the top of the unstable layer in order to stabilize the fluid.

Both local and non-local definitions are available for static stability. The local criterion determines it on the basis of the air local lapse rate. In particular, the atmosphere is statically stable (unstable) if the local lapse rate is smaller (greater) than the adiabatic lapse rate (i.e. about 9.8 K km^{-1}). If the adiabatic rate is perfectly matched the atmosphere is said to be neutral. This local definition frequently fails in the convective mixed layer, where the local lapse rate is almost adiabatic, but convection dominates with thermals rising from the surface because of their excess of buoyancy. Therefore, in order to define ABL as neutral, both the conditions of an adiabatic lapse rate and of the absence of convection must be satisfied. This rationale led Stull (1988) to conclude that measurements of the local lapse rate alone are not sufficient to determine the static stability. Instead, the whole profile of virtual potential temperature must be known, or in alternative turbulent buoyancy flux must be measured. In non-local definition the static stability of a certain layer of air is determined on the basis of the virtual potential temperature profile of the whole ABL or thanks to measurements of buoyancy flux. If at the surface the buoyancy flux is upward (downward) or displaced air parcels rise (return to the starting point), the ABL is unstable (stable). If the buoyancy flux is almost zero or much smaller than the mechanical production of turbulent kinetic energy, the ABL is neutral. Dynamical stability, in contrast to the static one, depends even on wind. In fact wind shear can generate turbulence even in statically stable conditions and if it succeeds in doing it, the ABL is dynamical unstable. A dimensionless number that expresses dynamic stability is the *Richardson flux number* Ri_f

$$Ri_f = \frac{\frac{g}{\overline{\theta_v}}\overline{w'\theta'_v}}{\overline{u'w'}\frac{\partial \overline{U}}{\partial z} + \overline{v'w'}\frac{\partial \overline{V}}{\partial z}} \tag{2.5}$$

where g is the gravitational acceleration and, following Reynolds decomposition, $\overline{U}$ and $\overline{V}$ are the temporal mean of wind velocity along $x-$ and $y-$direction respectively, u', v', w' are the oscillations around the mean of horizontal (u, v) and vertical (w) wind components and $\overline{(.)}$ indicates temporal average. The numerator of equation (2.5) represent the production of turbulent kinetic energy by buoyancy, while the denominator is the mechanical (i.e. by wind shear) production. In case of static stability buoyancy acts against turbulence development, and both the numerator and denominator are negative, resulting in a positive Ri_f. When the absolute value of the buoyancy flux is greater than

the mechanical production, i.e. $Ri_f > 1$, the static stability is strong enough to suppress the turbulence, meaning that a turbulent flow is going to become laminar and it can be defined dynamically stable. On the opposite, if the absolute value of the buoyancy flux is smaller than the mechanical production ($Ri_f < 1$), the static stability is insufficient to suppress the mechanical turbulence and the flow is turbulent, namely dynamically unstable. Finally, in statically unstable conditions also the buoyancy term, in this case positive, contributes to turbulence generation and the flow is dynamically unstable. It is important to underline that Richardson number is only an indication about the presence or absence of turbulence, but it does not say anything about its intensity. The flux Richardson number has the peculiarity to be defined only for turbulent flows, since it is based on turbulent oscillations. In order to overcome this issue the *gradient Richardson number* Ri is defined following the flux version, but substituting turbulent covariances with the corresponding mean quantity gradients

$$Ri = \frac{\frac{g}{\overline{\theta_v}}\frac{\partial \overline{\theta_v}}{\partial z}}{\left(\frac{\partial \overline{U}}{\partial z}\right)^2 + \left(\frac{\partial \overline{V}}{\partial z}\right)^2} \tag{2.6}$$

But local gradients are rarely known and therefore the *bulk Richardson number* Ri_B is used in practice, where gradients are approximated by finite differences

$$Ri_B = \frac{g\Delta\overline{\theta_v}\Delta z}{\overline{\theta_v}\left[(\Delta\overline{U})^2 + (\Delta\overline{V})^2\right]} \tag{2.7}$$

2.4 ABL turbulence

ABL turbulence is generated by forcings from the ground, namely by wind shear and by solar heating, this latter traducing into surface warming and finally into big turbulent eddies that are called thermals. In the extreme case of zero mean wind the ABL is said to be in *free convection* regime, while when both thermal and mechanical factors are active the regime is of *forced convection*. The presence of turbulence in the ABL enhances transport processes, making them several orders of magnitude more effective than in laminar conditions, in which they are driven only by viscous diffusion. It is this high transfer capability that makes the ground able to influence the overlaying air, since with only viscous diffusion surface fluxes would be almost negligible (Stull,

1988). Therefore an important feedback between the ground and the ABL is present, being turbulence both the source and the consequence of surface-air exchanges.

Reynolds number Re is a dimensionless quantity defined as the ratio between inertial and viscous forces in a flow, that hence expresses their relative importance (Kundu and Cohen, 2000). The more inertial forces dominate the more the flow is turbulent. Re is defined as

$$Re = \frac{UL}{\nu} \tag{2.8}$$

where U is the characteristic velocity of the flow, L is the characteristic length and ν is the kinematic viscosity of the fluid. Considering typical values for the ABL, for instance a geostrophic wind of 10 ms^{-1}, a depth of 1000 m and the air kinematic viscosity equal to 1.46 $\mathrm{m}^2\mathrm{s}^{-1}$, Re results to be of order 10^8. In a turbulent flow many spatial scales coexist, and the separation between the largest and the smallest ones widens with increasing Re (Tennekes and Lumley, 1972). Therefore in the ABL a large range of scales is present, with the largest eddies characterized by a representative spatial scale that is comparable to the ABL depth, typically within $100 - 3000$ m.

The main turbulent scaling quantities used in ABL context are listed in the following. In the description the Cartesian coordinate system and Reynolds decomposition for turbulent quantities are used. The $z-$axis corresponds to the vertical direction, while x and y are the horizontal ones. $\overline{(\cdot)}$ indicates the temporal average while $(\cdot)'$ is the instantaneous deviation from it.

- The surface friction velocity u_* is defined as

$$u_* = \left[(\overline{u'w'})_0^2 + (\overline{v'w'})_0^2\right]^{1/4} \tag{2.9}$$

  where u, v, w are the velocity components along $x-$, $y-$ and $z-$direction respectively. The subscript $(\cdot)_0$ means that the quantity is evaluated at the surface.

- The Obukhov length L is defined as

$$L = \frac{-\overline{\theta_v} u_*^3}{kg\left(\overline{w'\theta_v'}\right)} \tag{2.10}$$

  where k is the Von Karman constant and g is the gravitational acceleration. The absolute value of the Obukhov length is proportional to the height above the surface at which turbulence is first

generated more by buoyancy than by wind shear. In convective conditions $L < 0$, while in stable conditions $L > 0$ and $L \to \infty$ in near neutral conditions. For instance $L = -5$ m indicates very unstable conditions, while $L = -100$ m corresponds to a slight instability.

- The convective velocity w_* is used as a velocity scale in the mixed layer and it is defined as

$$w_* = \left[\frac{g(\overline{\theta_v' w'})_0 z_i}{\overline{\theta_v}} \right]^{1/3} \tag{2.11}$$

where z_i the convective boundary layer height.

The mean flow and turbulence characteristics in the surface layer can be recovered following Monin-Obukhov similarity (MOS) theory (Monin and Obukhov, 1954). It states that in the surface layer profiles of wind velocity, temperature and humidity depend only on the surface friction velocity u_*, the surface kinematic heat flux $(\overline{w'\theta_v'})_0$, the height above the surface z and the buoyancy variable g/θ_v. On the basis of dimensional analysis it was found that profiles can be retrieved through similarity functions that depend on the dimensionless length $\xi = z/L$, where L is the Obukhov length. For instance, in the simplest case of neutral conditions, wind profile in the surface layer follows the well-known logarithmic law. MOS is valid only when the flow is horizontally homogeneous and quasi-stationary, the turbulent fluxes are constant with height, viscous diffusion is negligible in respect to turbulent dispersion and rotational effects can be ignored in the surface layer. For details about the similarity functions and the corresponding profiles we refer to texts such as Garratt (1994), Stull (1988) or Arya (2001), since here the only aim was to introduce the theory and the assumptions needed for its validity.

3

The Large-Eddy Simulation technique for ABL modelling

This chapter presents the basis of the Large-Eddy Simulation (LES) technique and an overview about its application in modelling the Atmospheric Boundary Layer (ABL). In particular, in Section 3.1 various turbulence modelling techniques are illustrated and discussed; the typical set of equations for Large-Eddy Simulation of the ABL and details about the SGS model used in the thesis are reported in Section 3.2; Section 3.3 is dedicated to a discussion about the evolution and the various applications of LES of the ABL; finally, Section 3.4 illustrates issues related to the usage of Numerical Weather Prediction-Limited Area Models for LES of the ABL.

3.1 Numerical simulation of turbulence

In order to obtain a complete numerical reproduction of the dynamics of fluids in flow, the governing equations of fluid motion, i.e. the Navier-Stokes equations, must be solved for all the space and time scales involved in the process. This means that both the time and space discretization must be sufficiently fine, namely they must be smaller than the time and space scales representative of the smallest dynamically active structures present in the flow (Sagaut, 2002). In terms of Computational Fluid Dynamics (CFD) techniques, the fulfillment of such condition on time and space discretization corresponds to a Direct Numerical Simulation (DNS) of the flow, that is, as above-said, an explicit reproduction of all the temporal and spatial scales of

motion.

In case of turbulent flows the restrictions on both spatial and temporal discretization become highly constrictive, since turbulence is characterized by a wide range of scales, with the separation between the largest and the smallest eddies widening as the Reynolds number of the flow increases (Tennekes and Lumley, 1972). For example, in case of an isotropic and statistically homogeneous turbulence, Kolmogorov stated that the ratios between the characteristic scales of the largest and smallest structures are (Pope, 2000):

$$\frac{L}{\eta} = O(Re^{3/4}) \tag{3.1}$$

$$\frac{T}{t_\eta} = O(Re^{1/2}) \tag{3.2}$$

where L (η) and T (t_η) are respectively the spatial and temporal scales of the largest (smallest) eddies, and $Re = UL/\nu$ is the Reynolds number of the flow (the ratio between inertial and viscous forces), with U the representative velocity of the flow and ν the kinematic viscosity of the fluid. Therefore, assuming a cubic domain with a size comparable to the characteristic length of the largest structures ($LxLxL$), a spatial discretization of $O(Re^{9/4})$ elements would be required to fully simulate the motion. Then, if an explicit time integration is used, an accurate solution requires that the fluid particles move only a fraction of the grid spacing Δx in a single time step Δt, i.e. the Courant number $Cr = \Delta t U/\Delta x$ must be lower than one (Press et al., 1996). Therefore, on the basis of the linear dependence between Δt and Δx, and considering a duration of the simulation equal to the temporal scale of the largest turbulent structures T, the number of the required time steps is $O(Re^{3/4})$. This turns into numerically solving the governing equations $O(Re^3)$ times in the cubic domain of $LxLxL$ (Sagaut, 2002).

The evident conclusion from the previous example is that the currently available computational resources limit the applicability of DNS to Reynolds numbers that are significantly lower than those typical of the Atmospheric Boundary Layer turbulence, i.e. around $10^8 - 10^9$ (see Section 2.4). Consequently a Computational Fluid Dynamic technique that brings down the computational cost is needed when the aim is to simulate ABL turbulence. Reducing the computational cost of a simulation means executing a lower number of operations during the simulation itself, that in CFD implies to solve the dynamics of only

part of the scales of motions. But the non-linearity of the Navier-Stokes equations corresponds to a coupling between the dynamics of different scales in the flow, and therefore the selected turbulent scales can be simulated correctly only if additional terms, that mimic the average effect of the interaction between the unresolved and resolved structures, are included in the equations (Sagaut, 2002).

Two of the most common approaches in reducing the computational cost of a numerical simulation of a turbulent flow are the RANS (Reynolds Average Navier-Stokes) and LES (Large-Eddy Simulation) techniques.

- In RANS simulations only the statistical average of the exact solution is explicitly computed, while the turbulent fluctuations are included through a turbulence model, that should mimic their average effect on the mean flow. Equation (3.3) represents the decomposition of the exact velocity field $\boldsymbol{u}$ into the sum of a statistical average $\langle \boldsymbol{u} \rangle$ and a fluctuation $\boldsymbol{u'}$.

$$\boldsymbol{u}(\boldsymbol{x}, t) = \langle \boldsymbol{u}(\boldsymbol{x}, t) \rangle + \boldsymbol{u'}(\boldsymbol{x}, t) \tag{3.3}$$

  In practice the statistical average is commonly computed as a temporal average (Equation (3.4)), and therefore steady Navier-Stokes equations are simulated, excluding the possibility of reproducing *rare* events (Sagaut, 2002).

$$\langle \boldsymbol{u}(\boldsymbol{x}, t) \rangle \approx \bar{\boldsymbol{u}}(\boldsymbol{x}) = \lim_{T \to \infty} \frac{1}{T} \int_0^T \boldsymbol{u}(\boldsymbol{x}, t) dt \tag{3.4}$$

  Such decomposition leads to the appearance of covariances of velocity fluctuations in the Reynolds average equations. These terms are unknowns called Reynolds stresses that represent the interaction between the mean flows and the fluctuating components, and therefore must be determined adopting models that mimic the average effect they have on the mean quantities. Several different turbulence models are available in literature, based on turbulent viscosity hypothesis or from modelled Reynolds-stress transport equations. A close examination of the various turbulence models goes beyond the goal of the thesis, and we refer to specific books (e.g. Pope, 2000) for further details about the Reynolds-stress closure problem.

  The important observation in relation to this thesis is that, when RANS technique is adopted, turbulence fluctuations and structures are not reconstructed at all, but only their average effect

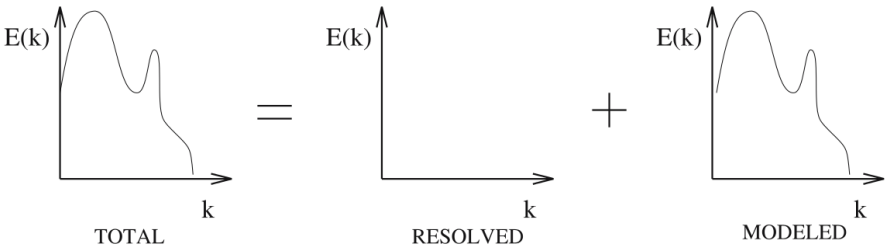

Figure 3.1: Symbolic representation of the energy spectrum decomposition in RANS simulations. Spectral energy density in function of the wavenumber. From Sagaut (2002).

on the mean flow is captured. Figure 3.1 elucidate this concept, showing that the turbulence model in RANS simulations is responsible for the whole energy spectrum.

- In Large-Eddy Simulations the larger-scale turbulent structures are explicitly reconstructed, while the role of the smaller-scale eddies is modelled through specific terms in the governing equations. Therefore LES lies between RANS and DNS in terms of both the level of turbulence description and the computational cost. LES is particularly suited for those flows where most of the turbulent energy and anisotropy are related to larger eddies and small structures are mainly responsible for dissipation and have, to some extent, a universal character (Pope, 2000). The energy spectrum in Figure 3.2 clarifies the LES approach, highlighting that only the smaller-scale turbulence is delegated to a model and that the bulk of the energy is explicitly solved in the simulation. The following Section is dedicated to a more specific description of this CFD technique.

3.1.1 Large-Eddy Simulation rationale

As already stated, the Large-Eddy Simulation is a CFD technique where only the more energetic turbulent structures are solved, while the smaller-scale eddies are modelled. Therefore, a separation between resolved and modelled turbulence is needed, and it is obtained by applying a low-pass spatial filter to the velocity field. The result is the decomposition of the generic state variable x into resolved $\tilde{x}$ and

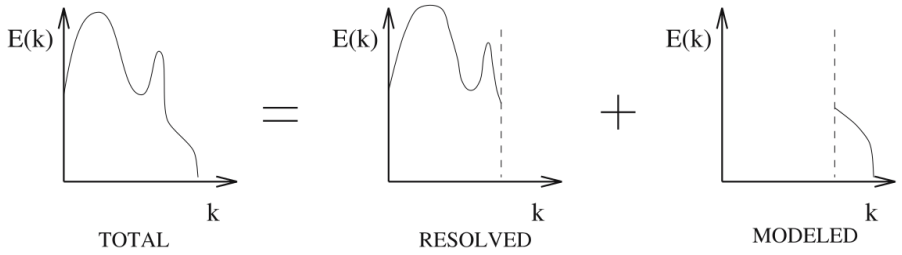

Figure 3.2: Symbolic representation of the energy spectrum decomposition in LES. Spectral energy density in function of the wavenumber. From Sagaut (2002).

subgrid-scale (SGS) x' components:

$$x = \tilde{x} + x' \tag{3.5}$$

Equation (3.5) appears to be quite similar to the Reynolds averaging operation described in Equation (3.3), but the fundamental differences are that the filtered variable has a random nature and that in general the filtered residual is non-zero (Pope, 2000):

$$\tilde{x'} \neq 0 \tag{3.6}$$

Figure 3.3 shows an example of the filtering operation on a turbulent signal of velocity. The filtered velocity is the bold line in the upper part of the plot, while the original signal is the thin line; the filter size is also indicated in the figure. It can be noticed that the filtered component is a smoothed version of the full velocity, namely it maintain the larger-scale fluctuations but those with a length-scale smaller than the filter size have been removed. In addition the lower part of the plot shows the just mentioned fact that the filtered residual (bold line) is non-zero.

In LES the evolution of the filtered velocity is described by the filtered Navier-Stokes equations, whose non-linearity leads to the appearance of a residual unknown term after the filtering operation. This term, called SGS stress tensor, is responsible for the effect that the subfilter structures have on the larger-scale ones. Therefore it must be modelled in order to obtain the closure of the set of equations and to make it numerically resolvable. In turbulent flows smaller-scales eddies are mainly responsible for the dissipation of larger-scales energy, although backscatter, i.e. energy transfer from smaller- to larger-scales turbulent structures, is potentially a relevant phenomena (Piomelli

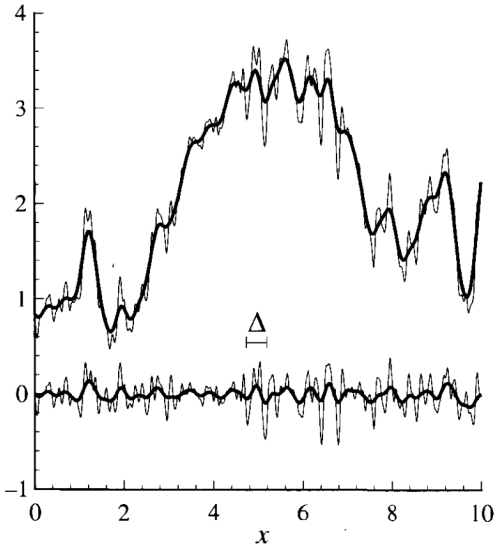

Figure 3.3: Turbulent velocity signal and the corresponding filtered component in bold line (upper part of the Figure). Residual from the filtering operation and the corresponding filtered component in bold line (lower part of the figure). From Pope (2000).

et al., 1991). Some SGS models take it into account (e.g. Mason and Thomson, 1992), even though the most common SGS models mimic only the dissipative effect of the smaller-scale eddies. Among these, the simplest and most diffused SGS model is that proposed by Smagorinsky (1963). It is based on the eddy-viscosity approach, namely the SGS stress τ_{ij}^{SGS} is related to the filtered rate of strain tensor $\tilde{S}_{ij}$ by eddy viscosity, meaning that the additional stress introduced by the turbulence is taken into account by increasing the molecular viscosity of the fluid.

$$\tau_{ij}^{SGS} = -2\nu_t \tilde{S}_{ij} \tag{3.7}$$

The eddy viscosity ν_t is estimated by recalling Prandtl's mixing-length theory:

$$\nu_t = l_s^2 (2\tilde{S}_{ij}\tilde{S}_{ij})^{1/2} \tag{3.8}$$

$$l_s = C_s \Delta \tag{3.9}$$

where l_s is a lengthscale analogous to the mixing-length scale, which is proportional to the filter width Δ through the Smagorinsky coefficient C_s. Lilly (1967) derived a constant value of about 0.17 for C_s on the basis of theoretical considerations, while subsequently procedures

to compute it dynamically at each simulation time step have been derived (Lilly, 1992; Germano et al., 1991). Several other SGS models are available in the literature (e.g. Kosovic, 1997; Porté-Agel et al., 2000; Zhou et al., 2001; Chow et al., 2005), but their description goes beyond the aim of this chapter, whose objective is to introduce the LES technique and its potential in describing ABL turbulence.

3.2 LES equations for Atmospheric Boundary Layer modelling

Typically, in order to model ABL turbulence, the incompressible form of the equations of motion with the Boussinesq approximation is used (Stull, 1988). In fact in the ABL the variations of the air density are small in respect to its mean value, and therefore the impact of these differences on inertial terms is negligible, while it becomes relevant when density variations are multiplied by the gravity. Consequently, the Boussinesq approximation, that neglects density differences in the equations of motion except that in buoyancy (gravity) terms can be applied. The main advantage of using the incompressible Navier-Stokes equations with the Boussinesq approximation in respect to the application of their compressible form is that sounds waves can not generate in the flow, since they are related to density variations. In addition a simpler set of equations is used and the numerical treatment gains advantage from this.

The basic set of equations for LES of ABL includes the filtered continuity equation in incompressible form (3.10), the filtered transport equation for momentum with Boussinesq approximation (3.11) and filtered equations for virtual potential temperature (3.12) and moisture (3.13).

$$\frac{\partial \tilde{u}_i}{\partial x_i} = 0 \tag{3.10}$$

$$\frac{\partial \tilde{u}_i}{\partial t} + \tilde{u}_j \frac{\partial \tilde{u}_i}{\partial x_j} = -\frac{1}{\rho}\frac{\partial \tilde{p}}{\partial x_j} - f(U_{gi} - u_j)\epsilon_{ij3} - g\frac{\tilde{\vartheta}}{\vartheta_0}\delta_{i3} - \frac{\partial \tau_{ij}}{\partial x_j} \tag{3.11}$$

$$\frac{\partial \tilde{\vartheta}}{\partial t} + u_i \frac{\partial \tilde{\vartheta}}{\partial x_i} = -\frac{\partial \tau_{\vartheta i}}{x_i} + S_\vartheta \tag{3.12}$$

$$\frac{\partial \tilde{q}}{\partial t} + u_i \frac{\partial \tilde{q}}{\partial x_i} = -\frac{\partial \tau_{qi}}{x_i} + S_q \tag{3.13}$$

where $\tilde{u}_i$ are the resolved velocity components along the horizontal ($i = 1, 2$) and vertical ($i = 3$) directions, ρ is the reference air density, $\tilde{p}$ is the resolved pressure, f is the Coriolis parameter, U_{gi} are the geostrophic wind components, ϵ_{ij3} is the alternating unit tensor, g is the gravity, $\tilde{\vartheta}$ is the resolved virtual potential temperature, ϑ_0 is the reference potential temperature, $\tilde{q}$ is the resolved air moisture, S_ϑ and S_q are the source/sink terms of virtual potential temperature and moisture respectively. Besides, the filtering operation gives rise to SGS fluxes of momentum τ_{ij}, potential temperature $\tau_{\vartheta i}$ and air moisture τ_{qi}.

$$\tau_{ij} = (\widetilde{u_i u_j} - \tilde{u}_i \tilde{u}_j) \tag{3.14}$$

$$\tau_{\vartheta i} = (\widetilde{u_i \vartheta} - \tilde{u}_i \tilde{\vartheta}) \tag{3.15}$$

$$\tau_{qi} = (\widetilde{u_i q} - \tilde{u}_i \tilde{q}) \tag{3.16}$$

Since the SGS fluxes depend on unresolved quantities, they need to be modelled in order to close the set of equations and make it resolvable.

3.2.1 Deardorff subgrid-scale model

As described in Section 3.1.1, one of the most common SGS model is that by Smagorinsky (1963). As other similar models, it is based on the assumption that a local equilibrium balance between shear production and dissipation of SGS turbulent kinetic energy (TKE) exists. But this condition is frequently violated also in simple flows, as, for example, in turbulence dominated by buoyancy (Sullivan et al., 1994). Since strong buoyancy is recurrent in the ABL, it is common to prefer SGS models that overcome this limitation. A possibility are kinetic energy models, that estimate the eddy viscosity by explicitly solving a prognostic equation for the TKE, and that therefore do not need the assumption of local equilibrium between shear production and dissipation of TKE. The most diffused kinetic energy model is that developed by Deardorff (1980). This 1.5-order-of-closure SGS model has been used in several LES of the ABL (e.g. Moeng, 1984; Nieuwstadt and Brost, 1986; Avissar et al., 1998; Kim et al., 2004; Patton et al., 2005; Moeng et al., 2007; Brunsell et al., 2011; Sullivan and Patton, 2011; Talbot et al., 2012), and it is employed also in the present thesis.

The Deardorff scheme is an eddy viscosity model as the Smagorinsky one, meaning that the SGS stress is computed following equation (3.7) and that a SGS scalar flux is estimated from the gradient of the resolved

component of the scalar itself through an eddy diffusion coefficient. For example for the buoyancy flux $\tau_{\vartheta i}$ we have:

$$\tau_{\vartheta i} = -\nu_\vartheta \frac{\partial \tilde{\vartheta}}{\partial x_i} \tag{3.17}$$

where ν_ϑ is the eddy diffusivity for heat. The eddy viscosity and eddy diffusivity for heat, and also for other scalars, are computed in function of the subgrid-scale turbulent kinetic energy e

$$\nu_t = C_k l \sqrt{e} \tag{3.18}$$

$$\nu_\vartheta = (1 + 2\frac{l}{\Delta})\nu_t \tag{3.19}$$

where C_k is a constant, Δ is an average grid spacing and l is a mixing length. Usually in finite differences codes the average grid spacing is computed as

$$\Delta = \sqrt[3]{\Delta x \Delta y \Delta z} \tag{3.20}$$

where Δx, Δy and Δz are grid spacings along the three cartesian directions. The mixing length l coincides with the average grid spacing Δ in unstable conditions, while it is reduced in presence of a local stable stratification

$$0.76 \frac{\sqrt{e}}{\sqrt{\frac{g}{\vartheta_0}\frac{\partial \vartheta}{\partial z}}} \tag{3.21}$$

This reduction has been found to be fundamental to model an ABL with a strong capping inversion (Sullivan et al., 1994). The prognostic equation for the SGS turbulent kinetic energy e is

$$\frac{\partial e}{\partial t} + u_i \frac{\partial e}{\partial x_i} = P + B - \epsilon + D \tag{3.22}$$

where P represents the shear production, B is the buoyancy, ϵ is the dissipation and D the diffusion. These latter terms can be modelled as

$$P = -\tau_{ij} \tilde{S}_{ij} \tag{3.23}$$

$$B = \frac{g}{\vartheta_0} \tau_{\vartheta 3} \tag{3.24}$$

$$\epsilon = C_\epsilon \frac{e^{3/2}}{l} \tag{3.25}$$

$$D = \frac{\partial}{\partial x_i}(2\nu_t \frac{e}{x_i}) \tag{3.26}$$

The SGS model requires the definition of two constants, C_k and C_ϵ. Using spectral analysis in convective conditions, Moeng and Wyngaard (1988) estimated for them values of 0.1 and 0.93. If the shear production and the dissipation terms are supposed to balance in the prognostic equation for TKE (3.22), the standard Smagorinsky model is obtained.

3.3 An overview of LES applications to the Atmospheric Boundary Layer

Large-Eddy Simulation has been extensively used to reproduce atmospheric turbulence in the Atmospheric Boundary Layer since the pioneering works of Deardorff (Deardorff, 1970, 1972, 1974). In fact, as discussed in the previous sections of this chapter, it is the only CFD technique that allows turbulence reconstruction at its typical Reynolds numbers ($Re \approx 10^8 - 10^9$).

Most LES applications to ABL modelling deal with idealized regimes, i.e. homogeneous surface properties, prescribed fluxes at the surface and periodic lateral boundary conditions. Such regimes are particularly suited for the verification of simulation results, since some theoretical expectations about turbulence statistics and flow structures are available for idealized conditions. Therefore, Large-Eddy Simulations in idealized regimes are frequently used to test numerical codes, subgrid turbulence schemes and others modelling features. For instance, in Nieuwstadt et al. (1993) the performances of four different large-eddy models are compared in simulating a Convective Boundary Layer (CBL) forced by a constant in time and homogeneous in space surface heat flux, i.e. in an idealized convective regime. The same four numerical codes have been compared also in case of a neutrally stratified Ekman layer in Andren et al. (1994), again adopting idealized conditions. In Moeng (1984) an idealized CBL is simulated in order to evaluate the capabilities of the presented LES model. A further investigation on the quality of the simulated turbulence is described in Moeng and Wyngaard (1988), where the same idealized setup is adopted. Idealized conditions has been used also to evaluate specific aspect of LES, as SGS models (Mirocha et al., 2010; Kirkil et al., 2012) and mesh resolution (Sullivan and Patton, 2011). In both Mirocha et al. (2010) and Kirkil et al. (2012), a neutral, horizontally homogeneous and infinite ABL is simulated to compare and test different SGS models. In fact, in idealized neutral conditions, the expected profiles near the

surface (i.e. the law of the wall or logarithmic velocity profile) are usually poorly reconstructed by LES (Mason and Thomson, 1992). This is mostly due to SGS models deficiencies (Sullivan et al., 1994), and therefore a neutral idealized ABL is an appropriate test case when the aim is to evaluate different SGS schemes. An analogous ABL is used by Brasseur and Wei (2010) in order to deeply investigate the just mentioned mismatch of LES results with the law of the wall. A solution to this issue, based on restrictions on the combination of grid resolution, aspect ratio and SGS parametrization, is proposed. Instead Sullivan and Patton (2011) employed an idealized setup in order to assess the role of mesh resolution in LES reproduction of the CBL turbulence. In Khanna and Brasseur (1997) LESs forced with a constant and homogeneous surface heat flux are employed to evaluate LES capability in reproducing Monin-Obukhov similarity theory (Monin and Obukhov, 1954) under various levels of atmospheric instability and in function of grid spacing and SGS parametrization. In fact being aware about LES ability in reproducing Monin-Obukhov similarity becomes fundamental as LES is diffusing as a tool to study ABL structure and is increasingly substituting field measurements or at least accompanying them.

Overturning the just described approach, i.e. LES models and various specific modelling features are tested against theoretical expectations about turbulence under specific settings of the simulations, LES in idealized conditions has been used as a means to verify and enhance theories about turbulence. For instance, in Cai and Steyn (1996) LESs of a neutral, stationary and horizontal homogeneous ABL are performed in order to improve the knowledge about the value of the Von Karman Constant, since numerical simulations are totally controllable and high Reynolds numbers ($Re \approx 10^9$) can be reached. In fact field observations suffer the inherent uncontrollability of the real world (i.e. the real ABL rarely meets the requirements of neutrality, stationarity and horizontal homogeneity that are required to evaluate the Von Karman constant). Moreover they are affected by measurements errors more than in controlled conditions, with the result of scattered values for the Von Karman constant. Therefore, the authors attempt to give a contribution in this issue using numerical simulations, judging the approximations of a LES, as the SGS model, preferable to the uncertainties related with field observations.

But when the purpose of the studies is about the investigation of the ABL behaviour in real conditions, idealized regimes are substituted

by semi-idealized or realistic setup. With semi-idealized conditions we refer to the adoption of heterogeneous surface properties and surface heat fluxes, but with these latter externally prescribed. Instead realistic conditions take into account the crucial feedback that exist between the land surface and the ABL (Garratt, 1994; Stull, 1988). This is done by dynamically computing the surface heat fluxes that force the ABL evolution during the simulation on the basis of the ABL turbulence itself.

A large number of LESs that aim at assessing the impact of the surface heterogeneity on the ABL structure and characteristics are performed in semi-idealized conditions (e.g. Hechtel et al., 1990; Hadfield et al., 1991, 1992; Shen and Leclerc, 1995; Avissar and Schmidt, 1998; Albertson and Parlange, 1999b; Raasch and Harbusch, 2001; Kim et al., 2004; Huang and Margulis, 2009; Sühring and Raasch, 2013; Sühring et al., 2014). Both Huang and Margulis (2009) and Hechtel et al. (1990) adopt realistic heterogeneity for the prescribed surface heat fluxes, namely they derived it from field measurements, and simulated a diurnal time evolution of the CBL. But the conclusions they obtain are different. Huang and Margulis (2009) identified an impact of surface heterogeneity on potential temperature profiles and velocity fields. Instead Hechtel et al. (1990) showed a negligible impact of the quasi-random realistic surface heterogeneity on both area-averaged statistics and thermals structures. They have identified a possible reason for the slight impact of the surface patchiness on the CBL in the combination of the small length-scale of the patchiness and the relatively strong mean wind. LES with an idealized surface heterogeneity, i.e. strip-like or chessboard-like patchiness, allow to assess the role of the inhomogeneities length-scale. Shen and Leclerc (1995) found that the effect of surface heterogeneity appears only when the patchiness has a characteristic length-scale larger than the ABL height. In Avissar and Schmidt (1998) it is found that the impact is maximum for scales of $5 - 10$ km. The wind attenuation of the impact of surface heterogeneity on the ABL structure has been assessed in several studies. The common conclusion is that the impact of surface heat flux patchiness significantly diminishes with a background wind stronger than 5 m s $^{-1}$ (Hadfield et al., 1992, 1991; Avissar and Schmidt, 1998). Moreover, the importance of the wind direction in respect to the heat flux inhomogeneities orientation has been identified (Raasch and Harbusch, 2001; Kim et al., 2004). In particular, Kim et al. (2004) evidenced a relevant effect of the surface heat flux patchiness on potential

temperature also under a strong wind, on the condition that it is perpendicular to the orientation of the heterogeneities. In Sühring and Raasch (2013) semi-idealized LESs have been used, not only to evaluate the impact of surface heterogeneity on the ABL, but also as a support in field measurements interpretation. This proves that, even if they neglect the feedback between the land-surface and the atmosphere, semi-idealized LESs are a suitable tool to reconstruct realistic ABL turbulence. The same LES model, again with surface variability prescribed in terms of imposed sensible heat fluxes, has been used to investigate the impact of a $1 - D$ strip-like heterogeneity on the mixed layer entrainment. This latter has been found to decrease in presence of small amplitudes of the patchiness and to increase for larger amplitudes in respect to the homogeneous case. In particular, the increase was maximum with the length-scale of the patches of the order of the CBL height, while for significantly smaller and larger sizes the entrainment tended to be similar to that of the homogeneous case. Lastly, semi-idealized conditions are also used to test specific modelling issues. For instance in Huang et al. (2008a) the negligible role of sub-grid models, when large eddies dominate (i.e. in CBL), is proved through a set of LES with prescribed non-homogeneous surface heat flux.

But, although semi-idealized simulations are accepted as a valuable tool to study ABL characteristics, when a more realistic reconstruction of the ABL evolution and of the interaction with the land surface must to be simulated, the fundamental mechanism that must be added into the model is the feedback that exists between the surface and the ABL. This can be done by coupling the LES with a Land-Surface Model (LSM), i.e. a scheme that computes the turbulent fluxes (sensible and latent heat fluxes and momentum flux) at the soil-atmosphere interface on the basis of the simulated turbulence itself. These fluxes are the lower boundary condition for the LES. Huang and Margulis (2010) demonstrated that ignoring these feedbacks causes an error in the estimation of the sensible heat flux up to 18% and of the near-surface soil moisture up to 10%. For the case they examined, the impact on latent heat flux and on surface temperature resulted to be minor. The importance of the land surface-air feedbacks was demonstrated also in Timmermans et al. (2008), where they stated that the feedbacks tend to limit the spatial variability of surface fluxes and that neglecting them will cause errors in fluxes estimations, especially in extreme conditions. Therefore, for a detailed analysis of the surface heterogeneity impact on ABL structure, on micro-meteorological states and

on turbulent exchanges themselves, a coupled model should provide results that are more representative of the reality in respect to semi-idealized simulations. But, at the same time, when a coupled model is adopted, additional uncertainty associated with the land processes scheme is introduced in the simulation (Avissar et al., 1998). In addition the requirements that the Land-Surface Model should satisfy in order to be adequately coupled with LES still need to be better defined (Shao et al., 2013; Liu and Shao, 2013). Consequently, a careful choice between coupled and uncoupled LES should be made in function of the specific objective of the study. Brunsell et al. (2011) studied the effect of a realistic surface heterogeneity in terms of vegetation and soil moisture on surface-atmosphere exchanges of mass and energy, and therefore they had to use a coupled LES-LSM to do it. Different length-scales of the heterogeneities implied a pronounced change in the partitioning of the surface energy between latent and sensible heat flux, with the latter being dominant for intermediate length scales. On the contrary the latent heat flux was more important in more homogeneous configurations, i.e. with smaller or larger scales of heterogeneity. In conclusion, the Bowen ratio was found to decrease while passing from heterogeneous to homogeneous conditions. Their analysis extend also to the impact on micro-meteorological states (air temperature and humidity). The first published work that used a fully coupled LES-LSM in order to investigate the heterogeneity impact on the ABL is Patton et al. (2005), that enhanced the partially-coupled approach of those studies where prescribed soil temperature and moisture are used (e.g. Albertson and Parlange, 1999a; Albertson et al., 2001; Kustas and Albertson, 2003). Their aim was to explore the influence of an idealized $1-D$ strip-like soil moisture heterogeneity on the convective boundary layer in stationary conditions. They could conclude that the strip-like heterogeneity dramatically alters the structure of the CBL by inducing significant organized circulations. Their findings partially differ from the impact shown in other studies that used prescribed surface fluxes. In particular, they discovered that the strongest stationary local circulation generated by wet and dry strips is generated when their length-scale is from 4 to 9 times the height of the CBL. Huang and Margulis (2012) performed a similar analysis, but they evaluated the impact of an idealized two-dimensional soil moisture heterogeneity, namely adopting a chessboard-like patchiness and not a strip-like one. They focused on the effect on surface fluxes, ABL characteristics, micro-meteorological states and also clouds development. They found

that the examined soil moisture patchiness significantly influences the water vapour transfer within the ABL, and consequently the cloud distribution, that in turn has a feedback on both the ABL and the surface energy budget. The impact of soil moisture gradient resulted to be stronger than that of the heterogeneity length-scale when this latter is large enough to organize thermal circulations inside the ABL, revealing that both forms of heterogeneity are important. But the first coupled LES-LSM considering not only strip-like patchiness, but also chessboard-like variability, is Courault et al. (2007), where heterogeneity in terms of both soil moisture and surface roughness length was investigated. Their conclusion is that more isotropic chessboard-like configurations of wet and dry patches generate a weaker local thermal circulation than an equivalent strip-like variability. This circulation weakens as the patch size decreases, with a length-scale of 2.5 km maximizing their impact. Huang et al. (2009) extended the use of a coupled LES-LSM to the investigation of the impact of the surface heterogeneity on carbon dioxide fluxes from vegetation. They analyzed the effect of strip-like patchiness of soil moisture in comparison with wet and dry spatially homogeneous cases and also with the results obtained from an uncoupled LSM usage. First of all they found that the carbon dioxide turbulent organized structures behave more similarly to those of water vapour than to those of potential temperature. Then they observed a large spatial variation of all the surface turbulent fluxes when the LSM is coupled with the above air motions even in presence of surface homogeneity and spatially constant solar radiation. This proves that the turbulent organized structures of the CBL have an important role in the exchange between the land surface and the overlaying air. In addition the importance of the feedbacks was demonstrated by the fact that the LSM alone underestimates the sensible heat fluxes and overestimates those of latent heat and carbon dioxide.

Besides to investigate the surface heterogeneity impact on multiple aspect of the ABL and land-atmosphere interactions, LES of the ABL is used also as a support in field measurements understandings and refinement of specific techniques. For instance several studies that try to identify the physical processes causing the recurrent energy imbalance of eddy covariance measurements use LES of the ABL (e.g. Kanda et al., 2004; Inagaki et al., 2006; Steinfeld et al., 2007; Huang et al., 2008b). In fact, in field experiments it is often observed that single tower eddy covariance measurements of surface fluxes (i.e. a

time-based eddy covariance method) underestimate the available energy. Therefore the energy balance is not satisfied for single towers (e.g. Lee and Black, 1993; Panin et al., 1998; Twine et al., 2000; Beyrich et al., 2002). Using LES, it has been proved that the spatial eddy covariance method (i.e. based on the horizontal averaging of the spatial covariances of the vertical velocity and the transported scalar) does not cause any bias on the fluxes estimation if in presence of horizontally homogeneity (Schröter et al., 2000). Several reasons for the single tower energy imbalance have been identified (Mahrt, 1998), some related to uncertainties about site and instruments and others directly connected to the ABL turbulence (Kanda et al., 2004). The advantage of employing LES to investigate the imbalance problem is that in numerical simulations the first category of uncertainties is eliminated. Moreover simulations can help in better defining the second class of problems, since LES can reproduce larger-scale turbulent structures of the ABL. Stationary simulations with prescribed homogeneous surface sensible heat flux have shown that turbulent organized structures, namely a cluster of thermals moving together with a larger time scale that of single plumes, are mainly responsible for the underestimation of the surface fluxes (Kanda et al., 2004; Steinfeld et al., 2007). In fact, these organized structures generate local advection that alters the eddy covariance measurements. These results have been confirmed in Huang et al. (2008b), that realized a similar study with a different LES model, definitely proving that the obtained results are not a model artifact. In Inagaki et al. (2006), again using LES of the ABL, it was found that larger amplitudes in an idealized 1-D sinusoidal variation of the surface sensible heat flux reduce the energy imbalance by weakening the organized turbulence structures that are responsible for it. They also showed that the imbalance decreases with stronger geostrophic winds by repeating the simulations in different regimes. In Bertoldi et al. (2013) a fully coupled LES-LSM was used to improve aircraft flux measurements understanding. The analysis led to the conclusion that it would be important for footprint models to consider different source areas between sensible and latent heat flux under strongly advective conditions. LES is employed also for footprint evaluation, starting from the work of Leclerc et al. (1997) and passing through more recent studies (e.g. Mao et al., 2008; Prabha et al., 2008; Markkanen et al., 2009; Cai et al., 2010). This demonstrates again that LES is nowadays the most valuable tool to study ABL turbulence and issues related to it.

3.4 NWP-LAM for LES of the ABL

As already discussed in Section 3.3, a large number of LES applications to ABL modelling consider idealized regimes, i.e. they use homogeneous surface properties, prescribed fluxes at the surface, and periodic lateral boundary conditions. But the continuous increase in computational capabilities has resulted in increased interest in the use of LES as a tool to study more complex meteorological ABL flows at the microscale, and applications that go beyond idealized conditions are targeted. In Section 3.3 it has been presented that most of the recent works that explore the impact of surface heterogeneity on the micro-meteorological conditions have substituted the prescribed heat flux boundary condition at the surface with the coupling with a Land-Surface Model. In fact the coupled system provides a more realistic description of the ABL dynamics, because it captures the local-scale feedbacks between land states, surface turbulent fluxes and surface properties (Huang and Margulis, 2010). Instead, in order to overcome the adoption of lateral boundary conditions and to relate the microscale turbulence with the larger-scale flow, a possibility has been identified in grid nesting technique. An investigation of the capabilities of the technique has been realized in Moeng et al. (2007), where various nested large-eddy simulations have been performed in idealized conditions with the aim of assessing the quality of the results. Then the technique has been applied in practice, among others, by Talbot et al. (2012). They simulated a realistic ABL flow, starting at the mesoscale (horizontal resolution 10 km) and moving down to LES (horizontal resolution 50 m). Also Liu et al. (2012) applied grid nesting to LES. In particular, they coupled a mesoscale model with a LES code in order to use real boundary conditions for simulations of a realistic urban environment in China. Liu et al. (2011) exploited data assimilation to perform a nested mesoscale-LES over real terrain for wind power applications.

Given these premises, Numerical Weather Prediction Limited Area Models (NWP-LAMs) appear to be particularly suitable to perform LES of the ABL in realistic conditions because of *i)* their capability of nesting, which enables the progressive increase in resolution from the reanalysis data used at the lateral boundaries to the microscale, and hence it overcomes the need of periodic lateral boundary conditions for the LES *ii)* the presence of one or more land surface models coupled with the equations of motion. However, to successfully em-

ploy such category of codes for large-eddy simulation of the ABL, it is fundamental to careful verify if models that are primarily developed with the aim of simulating mesoscale flows can correctly reconstruct turbulence in the lower part of the atmosphere (Gibbs and Fedorovich, 2014a; Paiva et al., 2009).

The Regional Atmospheric Modelling System (RAMS) (Pielke et al., 1992) and the Weather Research and Forecasting model (WRF) (Skamarock et al., 2008) are two of the most popular NWP-LAMs, and their performances in LES of a PBL in realistic conditions (i.e. with heterogeneous surface properties, time-varying surface heat fluxes and for WRF also lateral boundary conditions from large scale flows) have been evaluated by Avissar et al. (1998) and Talbot et al. (2012) respectively. Simulations results have been compared with field measurements, showing a good agreement. However, in such realistic simulations, the uncertainty on initial conditions, turbulence forcings, surface parameters and measurements themselves, does not allow to clearly assess the model capability in reproducing microscale turbulence. In order to evaluate codes performances, steady state idealized simulations (i.e. homogeneous and flat surface, periodic lateral boundary conditions, constant turbulence forcing) should be performed, because in these conditions previous LES and theoretical expectations about turbulence statistics and flow structures are available for comparison. Gibbs and Fedorovich (2014a) recently contributed in answering weather WRF is a suitable tool for LES of the PBL. They realized Large-Eddy Simulations of a turbulent flow in a dry atmospheric convective boundary layer using a conventional LES code and WRF. Their most relevant conclusion is that WRF tends to over-dissipate smaller-scale turbulence structures and to generate too less variable velocity fields in respect to the conventional LES code. They attributed these characteristics to WRF numerics and filters, suggesting that further investigation is required. Some other conclusions about WRF capabilities in performing LES of the PBL, in both neutral and convective conditions, can be deducted from studies whose primary objective is not to perform this evaluation, but where the presented results provides evidences for it (e.g. Moeng et al., 2007; Mirocha et al., 2010; Kirkil et al., 2012). In our knowledge no studies with the aim of assessing and deeply investigating RAMS capabilities in LES of the PBL are present in literature. Some indications can be obtained from Cai et al. (1995) and Cai and Steyn (1996), where the neutral atmospheric boundary layer is simulated and some comparison with theoretical pro-

files are shown. Other applications of RAMS-LES have been published during years, but without a preliminary verification in idealized conditions. In Hadfield et al. (1991, 1992) RAMS-LES was employed to study the impact of 1-D strip-like heterogeneity of the surface heat flux on the CBL; instead in Walko et al. (1992) it was used to assess the influence of moderate hills on the CBL, while in Cai (1999) the goal was to investigate the impact of different surface patchiness on thermal plumes in the CBL; more recently it has been used to simulate the flow in a urban street canyon and results have been compared with wind tunnel measurements (Cui et al., 2004; Cai, 2012). The previous works demonstrates that valuable results can be obtained with RAMS when employed to perform LES, but they are not exhaustive in characterizing its capabilities to reproduce atmospheric turbulence at the microscale, especially in convective conditions.

4

The Regional Atmospheric Modeling System: RAMS

This chapter describes the main features of the limited area model RAMS (Regional Atmospheric Modeling System). In particular, only basic characteristics and those relevant in the present study are accounted for, while for a complete description of the model we refer to Walko and Tremback (2001), that is the main source of the present chapter, and to some milestone papers about it (Tremback et al., 1986; Pielke et al., 1992; Cotton et al., 2003). RAMS is primarily designed for mesoscale simulations (domain from tens to hundreds of kilometers) of meteorological phenomena but there is no lower limit to the simulated domain and to grid cell size. Several versions of RAMS have been developed by several groups over the years, mainly by scientists at Colorado State University, the ASTeR division of Mission Research Corporation and the company ATMET (ATmospheric, Meteorological and Environmental Technologies). The present thesis employs RAMS 6.0 (Tremback and Walko, 2006), that is the last release of the code. RAMS is an open source code running primarily under UNIX and Linux operative systems, mainly written in FORTRAN with some input/output procedures written in C. It is recognized to be a highly flexible model, especially in comparison with other weather prediction models such as the Mesoscale Model 5 (MM5) and the Weather Research and Forecasting model (WRF) (Paiva et al., 2009). For instance in RAMS the numerical grid and the boundary conditions can be changed without recompiling the code. In addition some customizations, such as the employment of user defined surface characterization,

are already arranged in the code. Therefore it is an appealing and suitable tool to perform simulations in a research framework, where code and input customizations are often required.

The chapter id organized as follows. Section 4.1 describes the governing equations of RAMS, and Section 4.2 illustrates the numerics used to solve them. Section 4.3 is dedicated to the land-surface model present in RAMS, i.e. LEAF-3.

4.1 General equations

The core of RAMS solves the non-hydrostatic compressible momentum equations (4.1), (4.2), (4.3), the continuity equation (4.4), a thermodynamic equation (4.5) and transport equations for moisture and generic scalars (4.6). Table 4.1 describes the meaning of the employed symbols.

$$\begin{aligned}\frac{\partial u}{\partial t} = &-u\frac{\partial u}{\partial x} - v\frac{\partial u}{\partial y} - w\frac{\partial u}{\partial z} - \theta\frac{\partial \pi'}{\partial x} + fv + \\ &+ \frac{\partial}{\partial x}\left(K_m\frac{\partial u}{\partial x}\right) + \frac{\partial}{\partial y}\left(K_m\frac{\partial u}{\partial y}\right) + \frac{\partial}{\partial z}\left(K_m\frac{\partial u}{\partial z}\right)\end{aligned} \tag{4.1}$$

$$\begin{aligned}\frac{\partial v}{\partial t} = &-u\frac{\partial v}{\partial x} - v\frac{\partial v}{\partial y} - w\frac{\partial v}{\partial z} - \theta\frac{\partial \pi'}{\partial y} - fu + \\ &+ \frac{\partial}{\partial x}\left(K_m\frac{\partial v}{\partial x}\right) + \frac{\partial}{\partial y}\left(K_m\frac{\partial v}{\partial y}\right) + \frac{\partial}{\partial z}\left(K_m\frac{\partial v}{\partial z}\right)\end{aligned} \tag{4.2}$$

$$\begin{aligned}\frac{\partial w}{\partial t} = &-u\frac{\partial w}{\partial x} - v\frac{\partial w}{\partial y} - w\frac{\partial w}{\partial z} - \theta\frac{\partial \pi'}{\partial z} - \frac{g\theta'_v}{\theta_0} + \\ &+ \frac{\partial}{\partial x}\left(K_m\frac{\partial w}{\partial x}\right) + \frac{\partial}{\partial y}\left(K_m\frac{\partial w}{\partial y}\right) + \frac{\partial}{\partial z}\left(K_m\frac{\partial w}{\partial z}\right)\end{aligned} \tag{4.3}$$

$$\frac{\partial \pi'}{\partial t} = -\frac{R\pi_0}{c_v\rho_0\theta_0}\left(\frac{\partial \rho_0\theta_0 u}{\partial x} + \frac{\partial \rho_0\theta_0 v}{\partial y} + \frac{\partial \rho_0\theta_0 w}{\partial z}\right) \tag{4.4}$$

$$\begin{aligned}\frac{\partial \theta_{il}}{\partial t} = &-u\frac{\partial \theta_{il}}{\partial x} - v\frac{\partial \theta_{il}}{\partial y} - w\frac{\partial \theta_{il}}{\partial z} + \left(\frac{\partial \theta_{il}}{\partial t}\right)_{rad} + \\ &+ \frac{\partial}{\partial x}\left(K_h\frac{\partial \theta_{il}}{\partial x}\right) + \frac{\partial}{\partial y}\left(K_h\frac{\partial \theta_{il}}{\partial y}\right) + \frac{\partial}{\partial z}\left(K_h\frac{\partial \theta_{il}}{\partial z}\right)\end{aligned} \tag{4.5}$$

Symbol	Definition
u	east-west wind component
v	north-south wind component
w	vertical wind component
f	Coriolis parameter
K_m	eddy viscosity for momentum
K_h	eddy viscosity for scalars
θ_{il}	ice-liquid water potential temperature
r_n	water mixing ratio species of total water, rain, snow
ρ	density
g	gravity
θ_v	virtual potential temperature
T	temperature
π	Exner function
π'	perturbation Exner function
p	pressure
p_0	reference pressure equal to 1000 hPa
c_v	specific heat at constant volume
c_p	specific heat at constant pressure
R	gas constant
rad	subscript for tendency from radiation parameterization

Table 4.1: Symbols used in the governing equations of RAMS.

$$\frac{\partial r_n}{\partial t} = -u\frac{\partial r_n}{\partial x} - v\frac{\partial r_n}{\partial y} - w\frac{\partial r_n}{\partial z} + \\ + \frac{\partial}{\partial x}\left(K_h\frac{\partial r_n}{\partial x}\right) + \frac{\partial}{\partial y}\left(K_h\frac{\partial r_n}{\partial y}\right) + \frac{\partial}{\partial z}\left(K_h\frac{\partial r_n}{\partial z}\right) \tag{4.6}$$

where the Exner function is

$$\pi = \left(\frac{p}{p_0}\right)^{R/c_p} = \frac{T}{\theta} \tag{4.7}$$

4.2 Numerical solution

RAMS numerically solves the above-described equations on a Cartesian Arakawa-C (Mesinger and Arakawa, 1976) staggered grid. All the thermodynamic and moisture variables are defined at cell centers, while velocity components u, v and w are staggered of $1/2\Delta x$, $1/2\Delta x$ and $1/2\Delta x$ respectively. Δx, Δy and Δz are the grid spacings along the

horizontal and vertical directions. The horizontal spacings are constant throughout the domain, while Δz can change, typically refining while approaching the surface. Along the vertical direction the σ_z terrain-following coordinate system from Gal-Chen and Somerville (1975) and revised in Clark (1977) is used. It is a system where the top of the domain is exactly flat and the bottom follows the topography of the area. In particular the coordinates are defined as

$$\begin{aligned} x^* &= x \\ y^* &= y \\ z^* &= H\left(\frac{z - z_g}{H - z}\right) \end{aligned} \tag{4.8}$$

where H is the height of the domain top and z_g is the local topography. RAMS permits grid nesting to enhance spatial resolution in domain parts that are of particular interest. Nesting is both horizontal and vertical, and the vertical extension of the nested grid can be smaller than that of the parent domain. The employed technique is the two-ways nesting described in Clark and Farley (1984) and Clark and Hall (1991), and finally revised in Walko et al. (1995). Details about the technique are not described, since grid nesting is not used in the present thesis.

The governing equations are integrated in time using the leapfrog method stabilized with a Robert-Asselin filter (Asselin, 1972; Robert, 1966) and formulated with a time-split scheme (Tripoli and Cotton, 1982) that is similar to the procedure described in Klemp and Wilhelmson (1978a) and Klemp and Wilhelmson (1978b) and to the explicit scheme of Gadd (1978). The time-split technique is required for the propagation of the fast modes in the momentum equations (i.e. acoustic and gravity waves), and basically it consists in using smaller time step for the integration of these terms.

The spatial discretization expresses advective terms in the flux form in order to conserve mass and momentum. Second-order centered finite differences are used.

As implicit in the equations listed in Section 4.1, RAMS parametrizes the unresolved transport with the eddy viscosity approach, in which turbulent fluxes are computed as the product of an eddy coefficient (K_m for momentum and K_h for scalars) and the mean gradient of the transported quantity. RAMS offers four possibilities for turbulent mixing parameterization, i.e. to compute the coefficients K_m and K_h. Two are purely local schemes, with mixing coefficients depending only

on local and current flow properties. They are based on Smagorinsky (1963) scheme, in which eddy viscosity and diffusion are computed on the basis of the deformation rate. Atmospheric stability is taken into account through the Brunt-Vaisala frequency (Hill, 1974) and the Richardson number (Lilly, 1962). The other two schemes estimates eddy coefficients on the basis of local values of subgrid-scale turbulent kinetic energy, for which a prognostic equation is solved. These methods are considered non-local, since the local value of the turbulent kinetic energy can be generated in other areas of the domain and than transported in new parts of it. For both the local and non-local approach, one scheme is to be used in case of horizontal grid spacing comparable with the vertical one, namely when convective motions are resolved, and the other one in case of a horizontal grid spacing significantly larger than the vertical one. In the first case eddy viscosity is the same along both horizontal and vertical directions and symmetry of the Reynolds stress tensor is assured. In the second situation a larger mixing coefficient along the horizontal directions than along the vertical one is required. In the present thesis the non-local method for comparable horizontal and vertical spacings is used. It is the Deardorff (1980) scheme and it is described in detail in Section 3.2.1. For a detailed description of the other options we refer to Tremback and Walko (2006).

For lateral boundary conditions three possibilities are available. The first one is periodicity for all the variables, that is the condition used in all the simulations performed in the present thesis. Another option is to use observational data through a form of the nudging scheme by Davies (1976). Finally, a radiative condition can be applied to normal velocity components

$$\frac{\partial u}{\partial t} = -(u + c)\frac{\partial u}{\partial x} \tag{4.9}$$

where u is the wind component normal to the boundary and c is the phase velocity whose form has to be specified. RAMS offers three schemes to determine c, the Orlanski (1976) scheme, the modified Klemp and Lilly (1978) scheme (Durran and Klemp, 1982) and the Klemp and Wilhelmson (1978a) scheme. For the other variables zero gradient, or constant outflow/inflow or radiative outflow conditions can be imposed. At the domain top a rigid lid, meaning zero vertical fluxes and vertical velocity component, or the Klemp and Durran (1983) gravity wave radiative condition can be employed. The latter

should be avoided in presence of a non-steady flow, such as in deep convective conditions. In the thesis the rigid lid option is used. An absorbing layer can be added to both the conditions as a Rayleigh friction layer. The lower boundary condition is given to the model in the flux form, i.e. surface turbulent fluxes of momentum, heat and moisture are computed and provided to the model. They can be estimated on the basis of a prescribed constant temperature and moisture difference between the surface and the first air layer using Monin Obukhov Similarity theory (Monin and Obukhov, 1954), or through the coupling with a surface model. The role of the surface model is to simulate the evolution of the land surface temperature and humidity on the basis of which turbulent exchange fluxes can be computed. The surface model of RAMS is called LEAF-3 and is described in the next section.

4.3 LEAF-3

LEAF-3 (Land Ecosystem-Atmosphere Feedback version 3) is the land surface model of RAMS 6.0. Its role is to compute surface turbulent fluxes of momentum, heat and moisture required by the atmospheric grid as lower boundary condition. It includes prognostic equations for soil temperature and moisture in multiple layers, vegetation temperature, surface water, snow cover in multiple layers, and temperature and humidity of the air layer directly influenced by the surface. In fact LEAF-3 is mainly designed to be used in mesoscale simulations, where the first atmospheric layer is usually placed at some tens of meters above the ground (a typical value is 50 m). Hence a conceptual layer of air more linked to the surface is introduced in the model. Only processes relevant for the present thesis are described in the following, while for a more comprehensive description we refer to Campo (2006), that is also the main source of the summary here reported.

4.3.1 Generalities

LEAF-3 discretizes the surface in rectangular pixels, whose Δx and Δy are the same used in the atmospheric grid, and each pixel is completely independent from the others. Pixels can be divided into multiple patches in order to take into account subgrid variations of the surface (e.g. vegetation type, soil type etc). This feature is particularly valuable in mesoscale applications, where pixels dimensions are hundreds of meters, but it is not used in the microscale simulations

Soil class	ψ_s	η_s	b	K_s	K_{s0}	η_{fc}
01-sand	-0.121	0.395	4.05	$0.18e-3$	$0.50e-3$	0.135
02-loamy sand	-0.090	0.410	4.38	$0.16e-3$	$0.60e-3$	0.150
03-sandy loam	-0.218	0.435	4.90	$0.34e-4$	$0.77e-3$	0.195
04-silt loam	-0.786	0.485	5.30	$0.72e-5$	$0.11e-4$	0.255
05-loam	-0.478	0.451	5.39	$0.69e-5$	$0.22e-2$	0.240
06-sandy clay loam	-0.299	0.420	7.12	$0.63e-5$	$0.15e-2$	0.255
07-silty clay loam	-0.356	0.477	7.75	$0.17e-5$	$0.11e-3$	0.322
08-clay loam	-0.630	0.476	8.52	$0.24e-5$	$0.22e-2$	0.325
09-sandy clay	-0.153	0.426	10.4	$0.22e-5$	$0.22e-5$	0.310
10-silty loam	-0.490	0.492	10.4	$0.10e-5$	$0.10e-5$	0.370
11-clay	-0.405	0.482	11.4	$0.13e-5$	$0.13e-5$	0.367

Table 4.2: Soil parameters for USDA soil classes used in LEAF-3. Part I.

performed in the present thesis. Vertically the soil is discretized into multiple layers, usually covering $0.5 - 1.0$ m of thickness. The typical setup uses around 10 layers whose thickness increases with the depth, starting from a value of about 0.01 m and reaching about 0.50 m.

The surface is characterized through standard parameters, such as vegetation fraction, albedo, emissivity, vegetation and soil roughness length, vegetation height, LAI (Leaf Area Index), minimum stomatal resistance and vegetation roots depth. Each pixel is treated as bare soil or vegetated land on the basis of its vegetation fraction f_v. Vegetated land requires $f_v > 0.1$. LEAF-3 is furnished of a dataset that provides monthly values of the above parameters defined over the globe at 1/120 degree spacing of latitude and longitude. But these data are not used in the present thesis and therefore details about them are not reported. Soil parametrization requires data of saturation moisture potential ψ_s, saturation volumetric moisture content η_s, an exponent b to correct parameters value for unsaturated conditions, saturation soil hydraulic conductivity K_s, saturation soil hydraulic conductivity at the surface K_{s0}, dry soil volumetric heat capacity c_p, dry soil density ρ, volumetric water content at field capacity η_{fc} and percentage content of sand $xsand$, clay $xclay$ and organic matter $xorgan$. LEAF-3 provides values of all the above-said parameters for USDA soil classes, as shown in Table 4.2 and 4.3.

Soil class	c_p	ρ	$xsand$	$xclay$	$xorg$
01-sand	$1465e3$	1600	0.97	0.03	0.00
02-loamy sand	$1407e3$	1600	0.92	0.07	0.01
03-sandy loam	$1344e3$	1600	0.80	0.18	0.02
04-silt loam	$1273e3$	1600	0.57	0.40	0.03
05-loam	$1214e3$	1600	0.60	0.35	0.05
06-sandy clay loam	$1177e3$	1600	0.65	0.31	0.04
07-silty clay loam	$1319e3$	1600	0.35	0.59	0.06
08-clay loam	$1227e3$	1600	0.48	0.45	0.07
09-sandy clay	$1177e3$	1600	0.50	0.42	0.08
10-silty clay	$1151e3$	1600	0.30	0.61	0.09
11-clay	$1088e3$	1600	0.25	0.65	0.10

Table 4.3: Soil parameters for USDA soil classes used in LEAF-3. Part II.

4.3.2 Radiative forcing

The main forcing of surface-atmosphere interaction is radiation. RAMS provides to LEAF-3 incoming shortwave R_s (solar) and longwave R_l (emitted from the atmosphere) radiation. The radiative balance is computed as follows.

- shortwave radiation reflected from soil:

$$R_{s-g} = R_s(1 - f_v)A_g \tag{4.10}$$

- shortwave radiation towards vegetation:

$$R_{s-v} = R_s f_v[1 - A_v + (1 - f_v)A_g] \tag{4.11}$$

- longwave radiation emitted by soil (or snow):

$$R_l^g = \epsilon_g \sigma T_g^4 \tag{4.12}$$

- longwave radiation emitted by vegetation:

$$R_l^v = \epsilon_v \sigma T_v^4 \tag{4.13}$$

- longwave radiation emitted by atmosphere absorbed by vegetation

$$R_{l-v}^a = R_l f_v[\epsilon_v + (1 - f_v)(1 - \epsilon_g)] \tag{4.14}$$

- longwave radiation emitted by atmosphere absorbed by ground (or snow)

$$R_{l-g}^a = R_l(1 - f_v)\epsilon_g \tag{4.15}$$

- longwave radiation emitted by vegetation absorbed by ground (or snow)

$$R^v_{l-g} = R^v_l f_v \epsilon_g \tag{4.16}$$

- longwave radiation emitted by vegetation going towards the atmosphere

$$R^v_{l-a} = R^v_l f_v (2 - \epsilon_g - f_v + \epsilon_g f_v) \tag{4.17}$$

- longwave radiation emitted by ground absorbed by vegetation

$$R^g_{l-v} = R^g_l f_v \epsilon_v \tag{4.18}$$

- longwave radiation emitted by ground going towards the atmosphere

$$R^g_{l-a} = R^g_l (1 - f_v) \tag{4.19}$$

- longwave radiation from the atmosphere reflected by ground (or snow) and vegetation

$$R^a_{l-a} = R_l[f_v(1 - \epsilon_v) + (1 - f_v)(1 - f_v)(1 - \epsilon_g)] \tag{4.20}$$

where σ is the Stefan-Boltzmann constant, A_g, A_v are the ground and vegetation albedo and ϵ_g, ϵ_v are the ground and vegetation emissivities.

4.3.3 Fluxes toward the atmosphere

Surface turbulent fluxes of momentum M, heat H and moisture E are computed using Louis (1979) scheme. These fluxes represent the lower boundary condition for the atmospheric grid and are computed as follows.

$$M_x = -\rho u_*^2 \frac{u}{U} \tag{4.21}$$

$$M_y = -\rho u_*^2 \frac{v}{U} \tag{4.22}$$

$$M_z = -\rho u_*^2 K(z, \theta, t_*, u_*) \tag{4.23}$$

$$H = -\rho t_* u_* \tag{4.24}$$

$$E = -\rho r_* u_* \tag{4.25}$$

where M_x, M_y, M_z are the momentum fluxes along x, y and z, ρ is the air density in the first layer of the atmospheric grid, u and v are the velocity components along x and y in the firs layer of the atmospheric grid, U is their module and K is an empirical factor for the computation

of the momentum flux along the vertical. The shear velocity u_* and the terms t_* and r_* are estimated with

$$u_* = max\left[0.1, \frac{k}{ln(z/z_0)} U\sqrt{f_m}\right] \tag{4.26}$$

$$r_* = \frac{k^2}{ln^2(z/z_0)} \frac{U}{u_*}(r_a - r_{sa}) f_h \tag{4.27}$$

$$t_* = \frac{k^2}{ln^2(z/z_0)} \frac{U}{u_*}(\theta_a - \theta_{sa}) f_h \tag{4.28}$$

where z_0 is the patch roughness length, k is the Von Karman constant, z is the height of the first atmospheric layer, r_a, r_{sa}, θ_a, θ_{sa} are the water vapour mixing ratio and the potential temperature of the first atmospheric layer and of the air directly influenced by the surface. The factors f_m and f_h for stability corrections are computed in stable conditions as

$$\begin{aligned} f_m =& \frac{1}{1 + \frac{10 Ri_B}{\sqrt{1+5Ri_B}}} \\ f_h =& \frac{1}{1 + \frac{15 Ri_B}{\sqrt{1+5Ri_B}}} \end{aligned} \tag{4.29}$$

in unstable conditions as

$$\begin{aligned} f_m =& 1 - \frac{10 Ri_B}{1 + 75 \frac{k^2}{ln^2(z/z_0)} \sqrt{\frac{z}{z_0}|Ri_B|}} \\ f_h =& 1 - \frac{15 Ri_B}{1 + 75 \frac{k^2}{ln^2(z/z_0)} \sqrt{\frac{z}{z_0}|Ri_B|}} \end{aligned} \tag{4.30}$$

The bulk Richardson number is computed as $Ri_B = \frac{gz(\theta_a - \theta_s a)}{U^2(\theta_a + \theta_{sa})/2}$.

4.3.4 Internal fluxes

As already introduced, LEAF-3 employs an intermediate conceptual air layer between the land surface and the first level in the atmospheric grid. This is in order to deal with the fact that in its standard use the first atmospheric level height is at tens of meters above the ground. Hence, internal fluxes between the land surface and the conceptual air layer must be estimated. In absence of snow and precipitation they are computed accordingly to the following procedure.

The heat H_i and evaporation E_i fluxes from the ground to the air are estimated with

$$H_i = \rho c_p \frac{T_s - T_{sa}}{R_d} \tag{4.31}$$

$$E_i = min\left[\rho \frac{r_s - r_{sa}}{R_d}, \frac{W_s}{\Delta t}\right] \tag{4.32}$$

where T_s and T_{sa} are the temperatures of the ground surface and of the air layer, r_s and r_{sa} are the corresponding water vapour mixing ratios and W_s is the volume of available water in the top layer of the soil, that is used to estimate the upper bound of the evaporation flux. R_d is the soil resistance, that is computed differently in case of bare (4.33) or vegetated (4.34) soil.

$$R_d = 5/u_* \tag{4.33}$$

$$\begin{aligned} R_d = \frac{5}{u_*}(1-c) + \frac{ln(z/z_0)}{k^2 U} 1.0811 \cdot \\ \cdot c \cdot exp\left\{2.5 - exp\left[1.575\left(\frac{1 - h_v + z_0}{h_v}\right)\right]\right\} \end{aligned} \tag{4.34}$$

where $c = min(1, 0.51 \cdot TAI)$, h_v is the vegetation height and TAI is the Total Area Index, defined as the sum of LAI and additional contributions to the plant mass as stems biomass. In a vegetated patch also fluxes from the vegetation component are taken into account. The heat flux H_v is computed as

$$H_v = 2 \cdot TAI \rho c_p \frac{T_v - T_{sa}}{R_b} \tag{4.35}$$

where T_v is the vegetation temperature and the resistance R_b is estimated as

$$R_b = \frac{1 + 0.5 \cdot TAI}{0.01\sqrt{116.55 u_*}} \tag{4.36}$$

The humidity flux is split into evaporation from water over the leaves surface E_v (4.37) and transpiration Tr (4.38).

$$E_v = min\left[2 \cdot TAI \rho \frac{r_{satv} - r_{sa}}{R_b}\left(\frac{W_v}{0.2 \cdot TAI}\right)^{2/3}, \frac{W_v}{\Delta t}\right] \tag{4.37}$$

$$Tr = \rho \frac{r_{satv} - r_{sa}}{R_b + R_c} LAI \left[1 - \left(\frac{W_v}{0.2 \cdot LAI}\right)^{2/3}\right] \tag{4.38}$$

where r_{satv} is the vegetation mixing ratio taken as the saturation value, W_v is the available water for evaporation over plants leaves, that is provided by precipitation, and R_c is the stomatal resistance, that is estimated from its minimum value (provided as an input parameter for surface characterization) and corrected in function of several quantities, among which humidity and temperature. Finally, temperatures and water contents of both vegetation and the air layer are updated on the basis of the previous fluxes. In particular for the air layer values at the instant $n+1$ are computed as

$$T_{sa}^{n+1} = T_{sa}^{n} + \frac{\Delta t}{h_C}\left(H_i + H_v - H\right) \tag{4.39}$$

$$r_{sa}^{n+1} = r_{sa}^{n} + \frac{\Delta t}{w_C}\left(E_i + E_v + Tr - E\right) \tag{4.40}$$

where h_C and w_C are respectively thermal and water capacity of the air layer. Vegetation fluxes H_v, E_v are absent in a bare soil patch.

4.3.5 Soil temperature and moisture

LEAF-3 uses the multi-layer soil model presented in Tremback (1985). The number of layers is customizable, but usually comprised between 7 and 12, covering a depth of about 0.5 meters in a standard simulation. Each layer is characterized by an internal energy e per thickness unit (Jm^{-1}), that in the generic layer k is updated between time step n and $n+1$ with

$$e_k^{n+1} = e_k^{n} + \frac{\Delta t}{\Delta z_k}(Hg_k - Hg_{k+1}) \tag{4.41}$$

where Δz_k is the thickness of the layer k, Δt is the time step and Hg_k is the heat flux between layers k and $k-1$, that is compute as

$$Hg_k = -\frac{2(T_k - T_{k-1})}{\Delta z_k / Cg_k + \Delta z_{k-1}/Cg_{k-1}} \tag{4.42}$$

where Cg_k is the thermal conductivity of the layer k and T_k is its temperature. The heat flux for the top layer is instead computed as

$$Hg_{top} = H_i + LE_i - R_{l-g}^{a} - R_{l-g}^{v} + R_{l-a}^{g} + R_{l-v}^{g} \tag{4.43}$$

and its internal energy is updated with

$$e_{top}^{n+1} = e_{top}^{n} + \frac{\Delta t}{\Delta z_{top}} - R_{s-g} \tag{4.44}$$

Soil moisture is expressed as volumetric water content η and is updated in the soil column accordingly to the following procedure. The total water potential Φ_k in the layer k is obtained with

$$\Phi_k = z_k + \psi_s \left(\frac{\eta_s}{\eta_k} \right)^b \tag{4.45}$$

where z_k is the layer depth, ψ_s is saturation potential, η_s is the water content at saturation and b is a parameter depending on the soil type as shown in Table 4.2. Available water W_k in the layer k is found as

$$W_k = \Delta z_k (\eta_k - \eta_{wp}) \tag{4.46}$$

where η_{wp} is the water content corresponding to the wilting point. The water flux WF_k between layers k and $k-1$ is computed accordingly to the gradient of the water potential, and then bounded by actual water availability

$$\begin{aligned} WF_k =& \frac{\Delta t}{\Delta z_k} K_s \left(\frac{\eta_k + \eta_{k-1}}{2\eta_s} \right)^{(2b+3)} (\Phi_{k-1} - \Phi_k) \\ WF_k =& min \left(WF_k, W_k, \frac{(\eta_s - \eta_k)\Delta z_k}{2} \right) \end{aligned} \tag{4.47}$$

where K_s is the saturation hydraulic conductivity. Finally, water content in a generic layer (excluded the surface one) is updated as

$$\eta_k^{n+1} = max \left[\eta_{wp}, \eta_k^n - \frac{WF_{k+1} - WF_k}{\Delta z_k} \right] \tag{4.48}$$

While for the top layer

$$\eta_{top}^{n+1} = \eta_{top}^n - \frac{E_i}{\rho_w} \frac{\Delta t}{\Delta z_{top}} \tag{4.49}$$

where ρ_w is water density. The procedure is concluded by subtracting the transpiration flux of vegetation Tr from the moistest soil layer of the root zone, i.e. within the root depth. The subtraction is limited by water availability.

$$\eta_{kmoist} = \eta_{kmoist} - min \left[\frac{Tr}{\rho_w} \frac{\Delta t}{\Delta z_{kmoist}}, \eta_{kmoist} - \eta_{wp} \right] \tag{4.50}$$

Part II

RAMS-LES verification for ABL modelling

Introduction to RAMS-LES verification for ABL modelling

In Section 3.4 the advantages of using a NWP-LAM to perform LES of the ABL have been presented. But also the need to careful verify the capabilities of a code mainly designed to work at the mesoscale to explicitly simulate the turbulence in the ABL has been highlighted (Gibbs and Fedorovich, 2014a; Paiva et al., 2009). In addition a lack of studies focusing on this issue for RAMS-LES has been recognized in the literature (see Section 3.4). Hence, the first part of the present thesis aims at giving a contribution in RAMS-LES verification for ABL turbulence reconstruction, producing a solid basis for its usage in LES of more complex atmospheric flows. As discussed in Section 3.3, simulations of an idealized regime (i.e. over homogeneous and flat surface and with periodic lateral boundary conditions and constant turbulence forcing) are particularly suited and often used to test numerical codes (e.g. Nieuwstadt et al., 1993; Andren et al., 1994; Moeng, 1984), subgrid turbulence schemes and other modelling features (Mirocha et al., 2010; Kirkil et al., 2012; Sullivan and Patton, 2011), because the flow and turbulence properties are well understood.

For RAM-LES verification we simulate the two ideal conditions per excellence, namely the free-convection (turbulence generated by surface heating and absence of mean wind) and neutral (turbulence forced by a geostrophic wind in adiabatic conditions) regimes. Convective conditions are those of major interest when dealing with ABL modelling

with the final aim of simulating and studying turbulent fluxes that are of interest for hydrological purposes (i.e. sensible and latent heat fluxes). But the neutral case is more challenging in terms of LES (turbulent structures in neutral conditions have smaller characteristic size than eddies in convective regime), and therefore examining also RAMS-LES performances in neutral conditions adds further information in the code verification. Since the general aim is to produce solid basis for RAMS-LES usage in LES of real atmospheric flows, it is investigated also the impact that the computational grid has on the results in both regimes, in order to draw up a guideline about grid design for RAMS-LES when applied to ABL modelling.

5

RAMS and WRF performances in free convection regime and the role of grid spacing

In this chapter an extensive investigation of RAMS capabilities in performing LES of the ABL in convective conditions is presented. To this aim an idealized (i.e. over a homogeneous, flat and infinite surface and with a constant turbulence forcing) free-convection regime is simulated because of its well known turbulent statistics and flow structures and the various LES performed in the past for it (e.g. Deardorff, 1972; Lenschow et al., 1980; Nieuwstadt et al., 1993; Moeng et al., 2007; Lenschow et al., 2012) facilitate the models performance evaluation. The verification of RAMS-LES is enriched by the comparison with another NWP-LAM, the Weather Research and Forecasting model (WRF) (Skamarock et al., 2008), for which some information about its capabilities in performing LES of the ABL are available in the literature (Gibbs and Fedorovich, 2014a; Kirkil et al., 2012; Mirocha et al., 2010; Moeng et al., 2007). On the contrary an exhaustive evaluation of RAMS in terms of LES of the ABL is missing. In addition no comparative studies between the two NWP-LAMs, when used for LES of the ABL, are at disposal in the literature.

The analysis presented in this chapter focus not only on the overall evaluation and comparison of the performances of the two codes, but also on a detailed investigation of the influence that the grid spacing has on the results. The final aim of the activity is to define the role of the horizontal and vertical spatial resolution in RAMS and WRF, and therefore to provide guidelines on suitable grid spacing for both codes

when performing LES of the convective boundary layer (CBL).

The investigation is carried out by performing 9 simulations on a fixed computational domain of $6 \times 6 \times 2$ km using different computational grids in order to evaluate the impact of the grid spacing on the quality of the results. The nine computational grids are obtained combining three different horizontal (120, 60, 30 m) and vertical (20, 10, 5 m) spatial resolutions. The considered resolutions are within the typical range adopted in studies where LES is used to better understand phenomena in a real ABL and at soil-atmosphere interface (e.g. Albertson and Parlange, 1999a; Pedersen et al., 2012; Timmermans et al., 2008; Huang and Margulis, 2012; Shao et al., 2013; Courault et al., 2007; Bou-Zeid et al., 2007; Huang and Margulis, 2010; Brunsell et al., 2011), and whose computational costs is reasonable for practical applications. The results are post-processed in terms of mean profiles of potential temperature, heat flux, turbulence kinetic energy and velocity variances, spectra and flow visualizations. The analysis focuses on comparing model outcomes to the expected results for the considered idealized conditions, on analyzing the effect of changing the grid spacing, and on identifying the differences, and potential reasons for these differences, between the results obtained using both codes.

The chapter is organized as follows. In Section 5.1 a brief description of the LES module in both RAMS and WRF is presented. Details about the simulation setup are given in Section 5.2, while results are extensively analyzed in Section 5.3, and finally conclusions are presented in Section 5.4.

5.1 LES equations

Although RAMS and WRF models solve compressible equations, the flow that is examined in this analysis is a low-Mach-number flow (less than 0.01); therefore, for the sake of clarity, it is possible to refer to the incompressible equations with Boussinesq approximation reported in Section 3.2. A brief description of the specific equations and numerics used by the LES option of the two codes employed in this analysis is provided in the following.

5.1.1 RAMS-LES

RAMS-LES solves the non-hydrostatic compressible momentum equations, a thermodynamic equation, transport equations for moisture

and generic scalars, and a set of microphysical equations (for radiation, land parametrization and other physical processes that are not used in this study). A complete description of these equations can be found in Pielke et al. (1992), while here only the main characteristics are summarized. The time integration uses a leapfrog method stabilized with a Robert-Asselin filter (Asselin, 1972; Robert, 1966) and formulated with a time-split scheme (Tripoli and Cotton, 1982). The time-split technique is required for the propagation of the fast modes in the momentum equations (i.e. acoustic and gravity waves). The advective terms are expressed in flux form and discretized with a second-order centered finite differences scheme applied on an Arakawa-C staggered grid. Along the vertical direction the σ_z terrain-following coordinate system from Gal-Chen and Somerville (1975) and revised in Clark (1977) is used. The subgrid stress tensor is modeled with the eddy viscosity approach, and the turbulent viscosity is computed using the 1.5-order-of-closure scheme of Deardorff (1980) (see Section 3.2.1). The scheme determines the eddy coefficient on the basis of the turbulent kinetic energy, for which a prognostic equation is solved. Monin-Obukhov similarity theory (Monin and Obukhov, 1954) is applied to compute the momentum and heat fluxes at the surface. Periodicity is imposed at the lateral boundaries, and a vanishing vertical velocity combined with free-slip for horizontal components is used at the top of the domain. A top damping layer is not activated.

5.1.2 WRF-LES

WRF-LES solves a set of equations similar to RAMS, including the fully compressible Navier-Stokes equations in the flux form and thermodynamic, transport and microphysics equations. But differently to RAMS it employs a terrain-following hydrostatic-pressure coordinate system η (Laprise, 1992). In the present work the default numerics of WRF are selected. In terms of time integration they consist in a third-order Runge Kutta scheme applied with a time-split technique, that is required to maintain stability with a feasible time step for simulations (Klemp et al., 2007; Wicker and Skamarock, 2002). The sixth-order spatial filter and the vertical velocity damping filter are turned off, while the three-dimensional damping filter, the external-mode filter and the semi-implicit acoustic step off centering are maintained for acoustic wave damping, as suggested in Skamarock et al. (2008). The spatial discretization uses an Arakawa-C staggered grid and consists

Characteristic	RAMS	WRF	Comment
Basic equations	Fully compressible Navier-Stokes	Fully compressible Navier-Stokes	-
Time integration	Leapfrog, Asselin filter, time split	RK3, time split, three dimensional divergence damping filter, external mode filter, semi-implicit acoustic step off-centering filter	Higher accuracy in WRF; possible damping from filters for stablity in WRF
Spatial discretization	2nd order centered finite differences	3rd order finite differences for vertical advection 5th order finite differences for horizontal advection	Higher accuracy and larger numerical diffusion in WRF
Coordinate system	Terrain-following σ_z	Terrain-following hydrostatic-pressure η	Almost equivalent coordinate system with flat topography
Computational grid	Arakawa-C staggered	Arakawa-C staggered	-
SGS model	1.5-order TKE Deardorff	1.5-order TKE Deardorff	-

Table 5.1: Main characteristics of the two models

in a fifth-order finite difference advection scheme along the horizontal direction and a third-order scheme for the vertical advection. Both schemes are upwind-biased and inherently diffusive. The subgrid stress tensor is modeled using the eddy viscosity assumption and the same 1.5-order-of-closure scheme as the one selected in RAMS (Deardorff, 1980) (see Section 3.2.1) is adopted to compute the turbulent diffusion coefficient. Momentum and heat surface fluxes are computed following Monin-Obukhov similarity theory (Monin and Obukhov, 1954). Periodicity is adopted at the lateral boundaries and vanishing vertical velocity with free-slip for horizontal components are imposed at the top of the domain. Top damping is deactivated, as well as physics options like cumulus parametrization, radiation etc.

A summary of RAMS and WRF characteristics is reported in Table 5.1.

5.2 LES experiment setup

To assess the effect of the mesh resolution on CBL-LES in RAMS and WRF, simulations on a fixed domain but varying the grid spacing are performed. The selected setup is a quasi-steady free convection

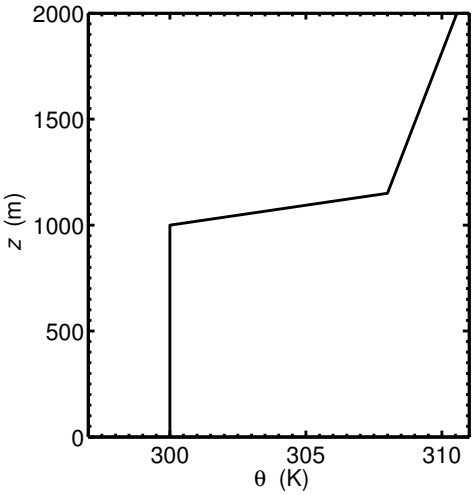

Figure 5.1: Initial vertical profile of potential temperature.

regime over a flat and homogeneous surface, because it is an idealized condition with well known statistics and flow structures (Deardorff, 1972; Lenschow et al., 1980). In addition various LES experiments of this ABL regime have been performed in previous studies (Lenschow et al., 1980; Schmidt and Schumann, 1989). Therefore it represents a suitable test case when models and their parameterizations are to be assessed. Nieuwstadt et al. (1993), Moeng et al. (2007) and Gibbs and Fedorovich (2014b,a) are examples of studies where free-convection quasi-steady simulations over homogeneous and flat surfaces have been used to evaluate numerical codes, their settings or the capabilities of specific techniques. The only turbulence forcing in free-convection conditions is the heat flux from the surface, while the mean wind is absent. The resulting flow is characterized by cellular structures near the surface and its main scaling quantities are the CBL depth z_i and the convective velocity $w_* = [(g/T_0)Q_0 z_i]^{1/3}$, where g is the gravitational acceleration, T_0 the surface reference temperature and Q_0 the kinematic surface heat flux (Jonker et al., 1999; Lothon et al., 2009; Stull, 1988).

In this study a simulation setup that requires a short simulation time has been adopted in order to limit the computational effort. Turbulence forcing is the upward heat flux generated by an initial temperature gradient of 5 K between the surface and the overlaying air. This setup has been shown to correctly reproduce a quasi-steady free con-

Run	Δx (m)	Δy (m)	Δz (m)	Grid Points	$\Delta x/\Delta z$
$A1$	120	120	20	$50 \times 50 \times 100$ (250000)	06.0
$A2$	120	120	10	$50 \times 50 \times 200$ (500000)	12.0
$A3$	120	120	5	$50 \times 50 \times 400$ (1000000)	24.0
$B1$	60	60	20	$100 \times 100 \times 100$ (1000000)	03.0
$B2$	60	60	10	$100 \times 100 \times 200$ (2000000	06.0
$B3$	60	60	5	$100 \times 100 \times 400$ (4000000)	12.0
$C1$	30	30	20	$200 \times 200 \times 100$ (4000000)	01.5
$C2$	30	30	10	$200 \times 200 \times 200$ (8000000) RAMS	03.0
				$134 \times 134 \times 200$ (3591200) WRF	
$C3$	30	30	5	$100 \times 100 \times 400$ (4000000)	06.0

Table 5.2: Characteristics of the nine computational meshes

vection regime and it has been used to test the capabilities of the LES module in WRF model (Moeng et al., 2007). The three-layer profile shown in Figure 5.1 is used to impose a homogeneous initial potential temperature sounding. The initial ABL height z_{i0} is 1000 m and a capping inversion of 8 K over 150 m is adopted to prevent significant ABL growth during the 2.5 h of simulation, limiting the size of the convective turbulent structures. Periodic lateral boundary conditions are applied, and the computational domain size is selected such that it is sufficiently large to allow the turbulent eddies to develop without the influence of periodicity. In fact an extent of $(L_x, L_y, L_z) = (6, 6, 2)$ km is used, which in terms of z_{i0}, and consequently of eddy size, satisfies the conditions specified in Schmidt and Schumann (1989). The simulation design is completed by a homogeneous surface roughness length $z_0 = 0.10$ m, a Coriolis parameter $f = 10^{-4}$ s^{-1}, zero mean wind, and dry air.

The grid spacing impact on LES capabilities of RAMS and WRF models is assessed by performing nine simulations with each code. In particular three different horizontal, $\Delta x = (120, 60, 30)$ m, and vertical resolutions, $\Delta z = (20, 10, 5)$ m, are combined in order to obtain nine computational grids. The declared vertical resolutions are averaged values for WRF grids. In fact, as specified in Section 5.1.2, WRF uses a terrain-following hydrostatic-pressure coordinates system, that implies a non-constant grid spacing along the vertical direction. Nevertheless, in all the nine cases, Δz differs from its averaged value of less than 10% at maximum. The adoption of a σ_z (RAMS) or η (WRF) coordinate system can impact simulations results in presence of significant topography, but in case of a flat surface it should not have any

influence, in particular not on first- and second-moment statistics (Moeng et al., 2007). The examined grid spacings are coarse compared to the high resolution studies where the focus is a detailed comprehension of the effect of the mesh on the CBL characteristics (e.g. Sullivan and Patton, 2011), but they are in the typical range adopted in studies where LES is used for more practical purposes (e.g. Albertson and Parlange, 1999a; Pedersen et al., 2012; Timmermans et al., 2008; Huang and Margulis, 2012; Brunsell et al., 2011; Shao et al., 2013; Courault et al., 2007; Bou-Zeid et al., 2007; Huang and Margulis, 2010).

Details about the nine computational grids are collected in Table 5.2. Simulations $C2$ for WRF and $C3$ for both RAMS and WRF are performed with a smaller domain because of computational limits of the available resources. To verify if the smaller domain extent is in conflict with periodic lateral boundary conditions, the grid resolution of simulation $B2$ is used with both the full and the smaller domain. The differences in the results were found to be negligible and an additional analysis of the auto-correlation further supported the conclusion that the reduced domain extent is sufficiently large for this specific application.

5.3 Results

The impact of mesh resolution on CBL-LES of RAMS and WRF models is evaluated by comparing mean vertical profiles, second order statistics and velocity spectra from the nine simulations described in the previous paragraph. In fact the adequacy of a computational grid for a certain LES experiment can be assessed through these quantities without any dependence on the specific characteristics of the model, such as the SGS model and the numerics (Mirocha et al., 2010). In order to approximate ensemble averages, statistics are obtained by first averaging over horizontal planes and then over time (Kirkil et al., 2012; Sullivan and Patton, 2011). Hereafter the ensemble averages are denoted by $\langle \cdot \rangle$ and fluctuations by $\cdot'$ All the reported results are for quasi-steady state conditions (the last 1 hour of simulation). This can be verified in Figure 5.2.a and 5.2.b, where the time evolution of the total turbulent kinetic energy (TKE) averaged across the ABL is plotted for RAMS and WRF. The total TKE is the sum of resolved and modelled contributions, i.e. $TKE =< 0.5u_i'u_i' + e >$, where e is the modelled kinetic energy. The nearly constant value of TKE during the

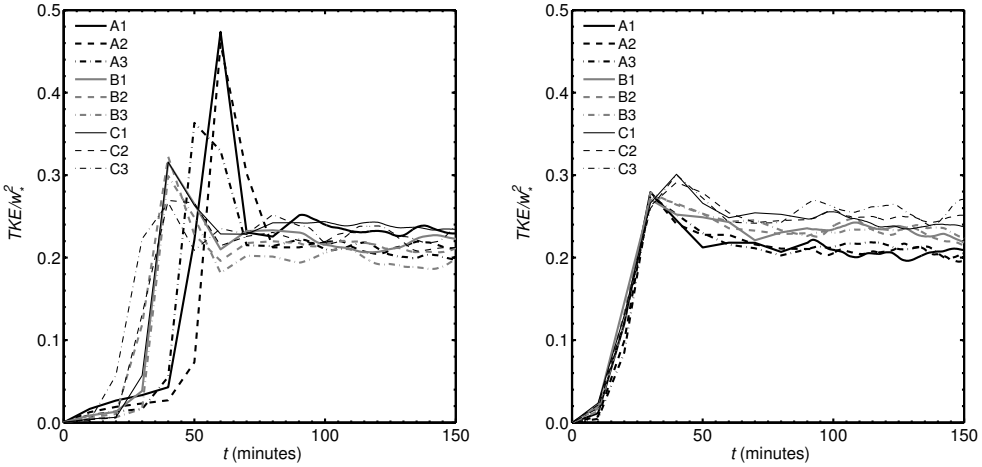

a. RAMS b. WRF

Figure 5.2: Total TKE averaged across the ABL in function of time.

Run	$A1$	$A2$	$A3$	$B1$	$B2$	$B3$	$C1$	$C2$	$C3$
RAMS	300.9	300.9	301.1	300.9	301.0	301.0	300.9	301.0	301.0
WRF	301.4	301.5	301.5	301.4	301.4	301.5	301.4	301.4	301.4

Table 5.3: Mean mixed layer potential temperature (K).

data collection interval ensures a quasi-stationary state.

5.3.1 Potential temperature and heat flux profiles

A first basic requirement for simulations of the CBL is to correctly reproduce the mean potential temperature profile, i.e. a nearly constant value in the mixed layer. Both RAMS and WRF match this condition in all the nine simulations (corresponding plots not shown here for the sake of brevity). The average value of the potential temperature across the mixed layer is reported in Table 5.3, where a negligible dependence of mean potential temperature profile on the grid resolution is revealed for both codes.

The temperature profile is strictly related to the vertical heat flux profile, which should exhibit a linear dependence on height in a quasi-stationary CBL (Nieuwstadt et al., 1993). The total vertical heat flux $\langle w\theta \rangle$ is computed as the sum of resolved and SGS contributions, where the latter is evaluated from the SGS eddy viscosity model as the product between the local vertical gradient of the potential temperature θ

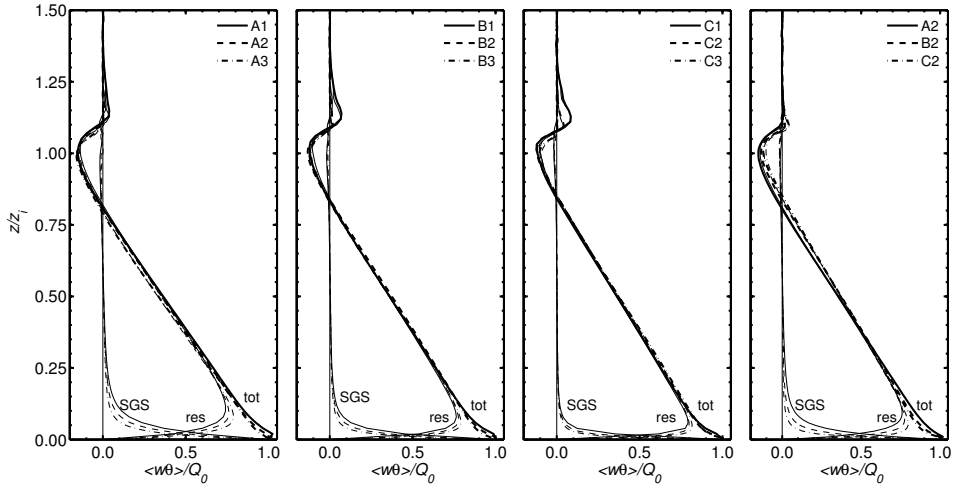

Figure 5.3: Vertical profile of total heat flux, resolved and subgrid contributions in function of dimensionless height z/z_{i0} (RAMS)

and the eddy diffusion coefficient for scalars ν_h:

$$\langle w\theta \rangle = \langle w\theta \rangle_{resolved} + \langle w\theta \rangle_{SGS} = \langle w'\theta' \rangle - \nu_h \frac{\partial \theta}{\partial z} \tag{5.1}$$

The normalized mean vertical profile is obtained by first scaling the heat fluxes with their corresponding surface value Q_0 and then averaging over time. Figures 5.3 and 5.4 show the profiles for RAMS and WRF respectively.

In the middle of the CBL both codes predict the expected linear behaviour and only limited dependency on the grid resolution is observed. In the entrainment layer and in the lower part of the surface layer, where the contribution of the SGS model to the total heat flux increases rapidly, larger discrepancies between RAMS and WRF are observed, and more pronounced grid dependency effects become apparent. Both codes show the expected behaviour in terms of grid dependency: an increased resolved contribution is obtained when increasing the grid resolution in both the horizontal and vertical directions. In the resulting total heat flux the influence of varying the grid resolution is limited, but it is different between both codes, especially in the surface and entrainment layers. The following discussion focuses on this fact.

A first important observation is that in RAMS the resolved contribution to the vertical heat flux starts to decrease at a larger distance

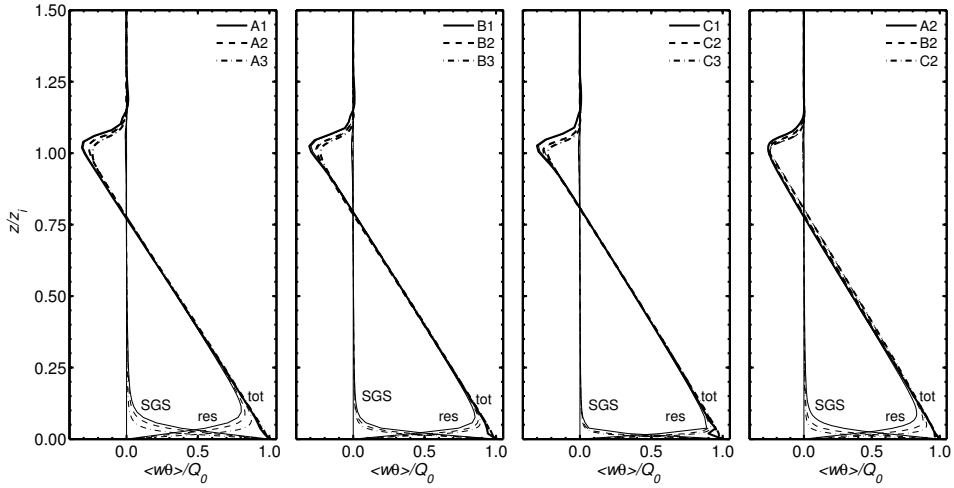

Figure 5.4: Vertical profile of total heat flux, resolved and subgrid contributions in function of dimensionless height z/z_{i0} (WRF)

from the ground ($z/z_{i0} = 0.25$) than it does in WRF ($z/z_{i0} = 0.20$). This is likely to be related to the greater accuracy of WRF numerical discretization along both horizontal and vertical directions (see Table 5.1). Coherently, on equal computational grids, the SGS contribution is larger and with a broader vertical extension in RAMS than in WRF. Another difference between the models is that RAMS produces a deviation from the expected linear behaviour of the total vertical heat flux in the lower part of the surface layer in all simulations, while it is always matched in WRF results. Exceptions are runs $B1$ and $C1$, where a sharp bend near the surface appears. This characteristic is present also in simulation $A1$, although less evident. Being the vertical resolution ($\Delta z = 20$m) the common feature between runs $A1$, $B1$ and $C1$, it can be assert that a grid vertical spacing of 20m is insufficient for WRF to assure a correct reproduction of the heat flux profile close to the surface, but refining Δz the linearity is recovered. On the contrary, as above-said, RAMS does not maintain the liner profile near to the surface in any simulation. In fact the rate of change of the resolved and SGS components does not balance when approaching the wall. Since both RAMS and WRF employs the same SGS turbulence model (see Table 5.1), it is reasonable to argue that RAMS shortcoming lies in the quality of the resolved flow close to the surface, and therefore probably in the lower numerical accuracy given by a second order scheme in respect to a third and fifth order in WRF.

In the entrainment layer further differences between both codes are observed, and here a larger influence of the mesh resolution on the total heat flux is present. RAMS shows a limited influence of the grid spacing on the entrainment flux, which is defined as the minimum value of the vertical heat fluxes (Nieuwstadt et al., 1993). Its absolute value in RAMS results is slightly lower than $|-0.2Q_0|$, that is the value observed in previous LES results (e.g. Nieuwstadt et al., 1993; Schmidt and Schumann, 1989; Sullivan and Patton, 2011). Instead, WRF shows a more negative entrainment flux than the typical value of $-0.2Q_0$ for most grids, and a more pronounced effect of the grid resolution on it. In particular it is sensitive to the vertical resolution, whose increased values result in less negative entrainment fluxes, approaching $-0.2Q_0$ with the finest adopted Δz, regardless of the horizontal resolution. Marked unwanted positive heat fluxes appear in the stable layer for RAMS runs $A1$, $B1$ and $C1$, while they are not present in $A3$, $B3$, $C3$ and slightly present in $B2$ and $C2$. These results indicate that in RAMS an adequately fine Δz is necessary but also sufficient to correctly reproduce the stable layer above the entrainment. In fact when $\Delta z = 5$m the stable layer is well simulated, while with $\Delta z = 20$m it is not, in both cases regardless of the horizontal resolution.

From this analysis it can be concluded that both models generate the expected linear profile of the vertical heat flux in all the conducted simulations within the mixed layer, with a negligible impact of computational grids. A slight modification of the profile slope is to be attributed to the horizontal resolution for both models. Instead, the entrainment and surface layers are substantially affected by the vertical resolution, and results improve when Δz is refined, quite independently from the adopted Δx. In particular WRF benefits from the enhanced Δz especially in the entrainment layer, with the best results achieved when $\Delta z = 5$m. For RAMS, that generates entrainment fluxes similar to the expected value in all the simulations, the major impact is on the stable layer above the entrainment, moving from the marked positive heat fluxes of $\Delta z = 20$m to their complete absence when $\Delta z = 5$m. But the vertical grid spacing refinement tested in this work does not succeed in making RAMS reconstruct a linear profile in the surface layer as WRF does in almost all the runs. As speculated above, this shortcoming is probably due to the lower order advective scheme of RAMS in respect to that one used in WRF.

5.3.2 Variances analysis

Comparing the resolved and SGS contributions to the total velocity variance provides an indication of the capability of the LES to resolve the energy-containing turbulence scales. In this section we present results for the total and subgrid scale values of the TKE and the velocity components variance obtained with the nine computational meshes using RAMS and WRF.

Figure 5.5 and 5.6 compare vertical profiles of the normalized total and subgrid-scale TKE. For both models the SGS contribution to the total TKE is below 37% throughout the boundary layer. The SGS contribution correctly decreases when grid resolution increases, and it is smaller in WRF than in RAMS, in accordance with the lower order numerics of the latter model. The total TKE shows a certain level of grid-dependency in all simulations. There are significant differences between both codes in terms of the effect of the resolution on the TKE profiles, but the variations remain acceptable with a maximum difference in TKE of 32% in RAMS and 26% in WRF.

Figure 5.5 shows that RAMS profiles of TKE are influenced by both the horizontal and vertical grid resolution, with the impact of Δz becoming less important as Δx refines. In fact the TKE profiles of group C, corresponding to the finest horizontal spacing, are almost identical between them, while in group A, corresponding to the coarsest Δx, a decreasing in TKE throughout the whole CBL is caused by the refinement along the vertical direction. This suggests that Δz has a minor impact on the TKE profile when Δx is finer than a certain threshold level. Spectral and flow visualization analysis (section 5.3.3 and 5.3.4 respectively) will provide a possible explanation to these observations. The influence of the horizontal grid resolution is more pronounced and it varies over the height of the CBL. In the upper part of the CBL the total TKE increases if Δx refines, indicating an improvement in turbulent structures reproduction due to the smaller Δx. In the near wall region the effect of the Δx refinement is the opposite. In fact the surface layer tail of high values that is present in all the simulations of group A is reduced when passing to group B, and it almost vanishes in group C. This could be caused by the inability of the SGS model to correctly reproduce fluxes near the rough surface in case of coarse Δx (Brasseur and Wei, 2010), combined with the fact the outer flow is grid dependent. Figure 5.6 immediately reveals that the TKE profiles of WRF are almost insensitive to the vertical resolution. In fact pro-

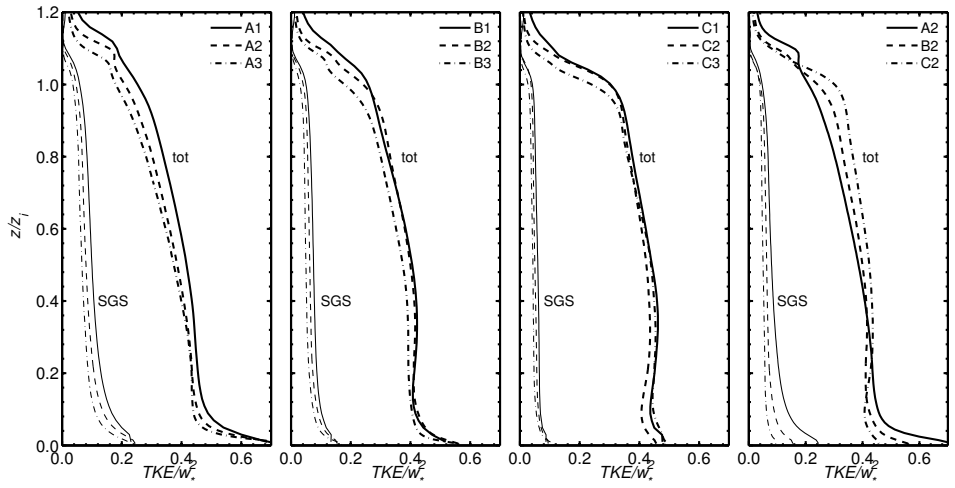

Figure 5.5: Vertical profile of normalized total TKE and subgrid contribution in function of dimensionless height z/z_{i0} (RAMS)

files corresponding to the same Δx show negligible differences when Δz changes. This observation indicates that the turbulent structures mainly contributing to the TKE are not influenced by the refinement of Δz. Instead, the TKE profiles do show a relevant dependence on the horizontal grid spacing. When Δx refines, the total TKE increases throughout the entire height of the CBL, from the entrainment layer to the near wall region. Therefore increasing the horizontal resolution enhances those turbulent structures that contribute mainly to the TKE production throughout the whole CBL. A possible explanation to this behaviour will be derived from spectral and flow visualization analysis (section 5.3.3 and 5.3.4 respectively).

Profiles of total vertical velocity variance $\langle w^2 \rangle = \langle w'^2 + 2/3e \rangle$ and its SGS contribution are shown in Figures 5.8 and 5.9 for RAMS and WRF respectively. The SGS contribution is taken to be $2/3e$, assuming isotropy of small eddies (Moeng et al., 2007). In both codes the influence of the mesh resolution on the total vertical velocity variance is small, with a maximum difference of 15% in RAMS and 18% in WRF. As for the total TKE, the effect of the computational grid on the profiles differs between the two codes. In RAMS the height at which the peak of the vertical variance occurs slightly increases with the resolution, settling down to the typical value of $0.4z_i$. When the horizontal spacing is sufficiently fine (groups B and C) RAMS peaks are in the standard range of $0.5w_*^2$, while in group C they are slightly

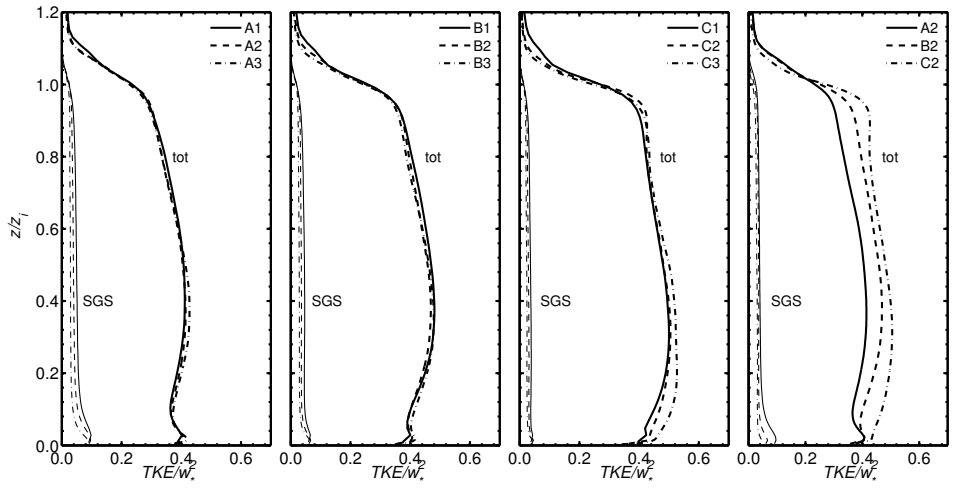

Figure 5.6: Vertical profile of normalized total TKE and subgrid contribution in function of dimensionless height z/z_{i0} (WRF)

smaller, especially for finer values of Δz (i.e. simulations $A2$ and $A3$). In fact the effect of Δz refinement is to decrease the total vertical velocity variance above the surface layer (inside the surface layer it almost has no effect) in simulations of group A and B. In group C its effect is negligible. The impact of Δx is coherent to the variations observed in the TKE profiles (Figure 5.5): as Δx refines, the values near the top of the boundary layer increase, while the near wall vertical variance decreases. These observations suggest that the vertical refinement of the computational grid, when the horizontal resolution is not fine enough, weakens the turbulence. Instead, a greater resolution along the horizontal direction seems to reinforce the turbulence in the upper part of the CBL and to decreases it in the lower part, where vertical velocity variance values are too large in cases of a too coarse Δx (simulations of group A). Again, a possible explanation for this behaviour will be obtained through spectral and flow visualization analysis (section 5.3.3 and 5.3.4 respectively). Figure 5.9 shows that the vertical variance predicted by WRF peaks at $0.4z_i$ in all the simulations, but the peak values are about $0.6w_*^2$, and therefore larger than the reference of $0.5w_*^2$. This tendency to overestimation of peak values has been already noticed in previous works (Moeng et al., 2007). Coherently to what observed for the total TKE, the total vertical variance in WRF is independent of the vertical grid resolution, while it tends to increase over the entire height of the boundary layer with increas-

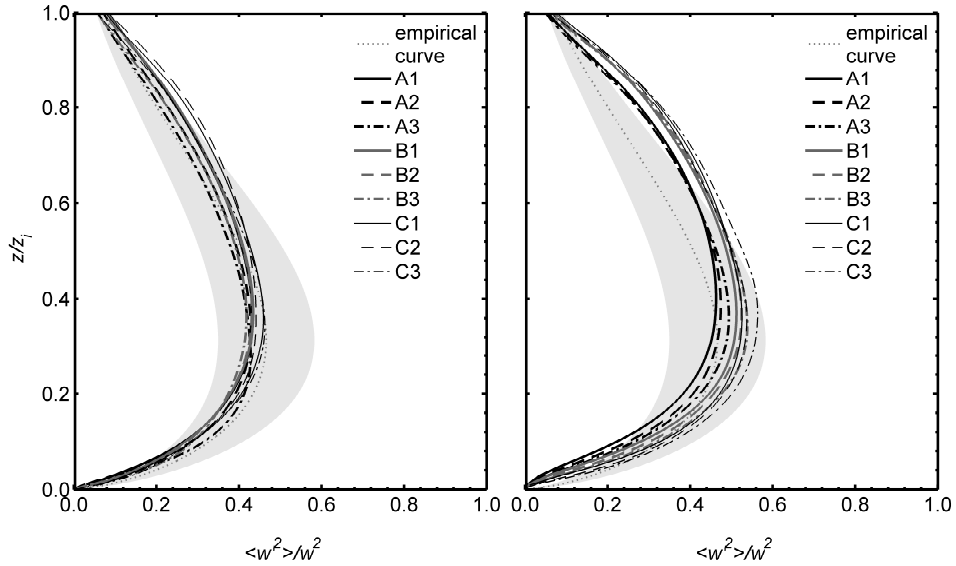

Figure 5.7: Vertical profile of normalized resolved variance of the vertical velocity in function of dimensionless height z/z_{i0} in comparison with the empirical curve. The grey area indicates the ±25% from the empirical curve. (RAMS on the right and WRF on the left)

ing horizontal resolution. In order to evaluate weather the above-said global increase of the vertical velocity variance in WRF is desirable, we present a comparison of the resolved variances with the empirical curve by Lenschow et al. (1980) (Figure 5.7):

$$\frac{\langle w'^2 \rangle}{w_*^2} = 1.8 \left(\frac{z}{z_i} \right)^{2/3} \left(1 - 0.8 \frac{z}{z_i} \right)^2 \tag{5.2}$$

It can be noticed that RAMS gives a slight underestimation in the lower part of the CBL and a weak overestimation in the upper part, but globally its variance profile is more similar to the empirical one than that by WRF for all the nine computational grids. In fact WRF variances are up to 68% higher than the empirical reference with all the tested resolutions, especially in the upper part of the CBL and for finer resolutions.

Figures 5.10 and 5.11 show the total variance of horizontal velocity $\langle u_h^2 \rangle = \langle u'^2 + v'^2 + 4/3e \rangle$ and its SGS contribution. For both models the values are largely independent of the vertical grid spacing, while the horizontal resolution has a significant effect, with a maximum difference of 35% in RAMS and 38% in WRF. This result reveals that

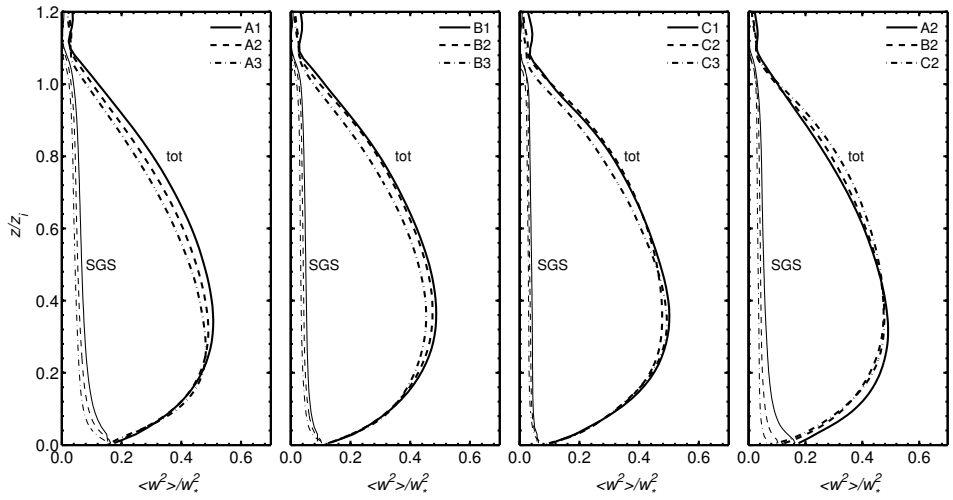

Figure 5.8: Vertical profile of normalized total variance of the vertical velocity and subgrid contribution in function of dimensionless height z/z_{i0} (RAMS)

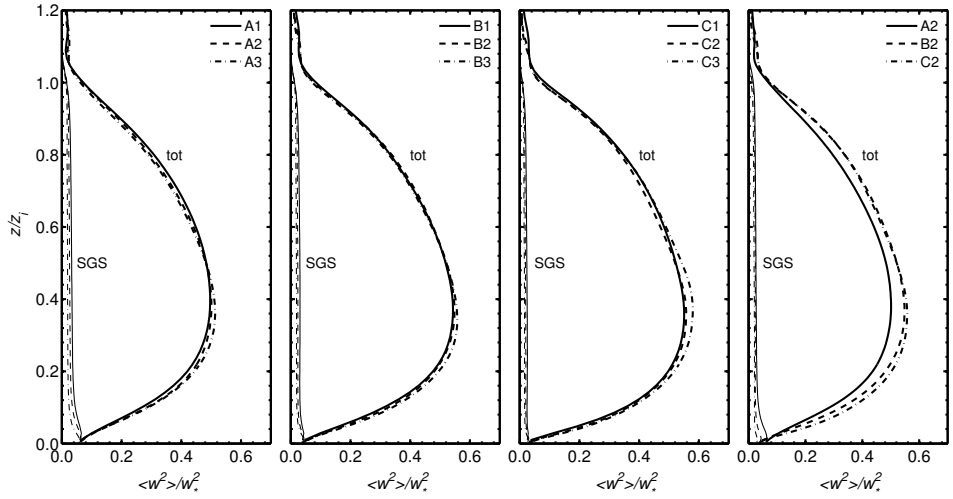

Figure 5.9: Vertical profile of normalized total variance of the vertical velocity and subgrid contribution in function of dimensionless height z/z_{i0} (WRF)

the horizontal variance is the main source of TKE mesh sensitivity for both RAMS and WRF, as already found for others models (Sullivan and Patton, 2011). The impact of the computational grid is again different for both codes, and it is in agreement with the above-mentioned observations for the total TKE. RAMS shows again the opposite effect of Δx in the inversion layer and in the near wall region. The profiles corresponding to the lower horizontal resolutions show high peaks in the horizontal velocity variance in the close to the wall region, explaining the high TKE values near the ground surface observed in Figure 5.5, and the peaks decrease when Δx refines. At the opposite in the inversion layer the variance increases with finer Δx. This combined effect results in only small impact of the horizontal grid spacing in the middle of the CBL. In fact, in this region the horizontal velocity variance is almost insensitive to the computational grid and it tends to a constant value of $0.4w_*^2$, which is in accordance with the typical value of $0.2w_*^2$ for each horizontal velocity component. Figure 5.11 shows that in WRF the influence of the horizontal resolution is more pronounced that in RAMS. In fact the refinement of Δx leads to an increase of the horizontal velocity variance over the entire height of the CBL. In particular in the middle of the CBL the values pass from less than $0.4w_*^2$ (group A) to more than $0.5w_*^2$ (group C), revealing the tendency of WRF to overestimate also the horizontal velocity variance and not only the vertical velocity one.

From this analysis we can conclude that for both models the horizontal resolution impact on TKE and velocity variance profiles is predominant in respect to the vertical one. But, as extensively discussed in this section, the nature of the effect that both Δx and Δz have on profiles differs between RAMS and WRF. In order to explain such different impact of grid spacing on the two codes further analysis are required (and they will be performed in the next sections). But from the present section it is possible to affirm that in order to reproduce TKE and velocity variance profiles with reasonable accuracy a sufficiently fine horizontal resolution is needed for both models. Coherently with the fact that WRF employs higher order numerics than RAMS (see Table 5.1), it allows the adoption of a coarser Δx than RAMS ($\Delta x \sim$ 30m in RAMS and $\Delta x \sim$ 60m in WRF). It is however important to underline that a tendency to overestimate TKE and velocity variances has been found in WRF. This issue has been already noticed in Gibbs and Fedorovich (2014a) and they have explained it showing that WRF generates less variable velocity fields but with more contrasted structural turbulent

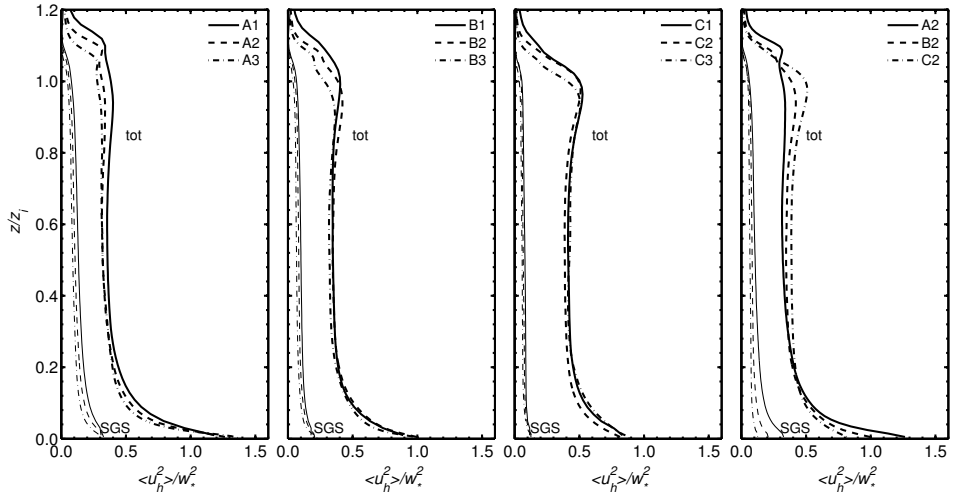

Figure 5.10: Vertical profile of normalized total variance of the horizontal velocity and subgrid contribution in function of dimensionless height z/z_{i0} (RAMS)

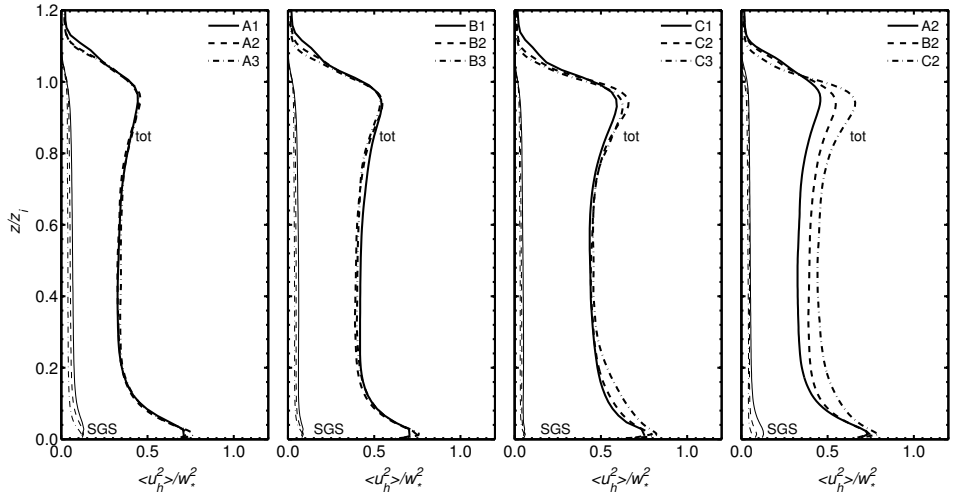

Figure 5.11: Vertical profile of normalized total variance of the horizontal velocity and subgrid contribution in function of dimensionless height z/z_{i0} (WRF)

features in respect to those obtained with more standard and tested LES code, i.e. few values that deviate strongly from the mean are the cause of WRF larger variances throughout the whole CBL. They have speculated that the reason could lie in WRF numerics more than in other differences between the two compared code (e.g. the use of incompressible or compressible Navier-Stokes equations). Our analysis seems to confirm this hypothesis. First of all we have shown that WRF tendency to overestimate TKE and velocity variances is strongly influenced by the computational grid spacing, fact that points to the numerical methods adopted in the model as the main cause for it. In addition the comparison with RAMS almost exclude the possibility that the reason of WRF tendency to generate strongly contrasting features in the flow could lie in the adoption of the fully compressible Navier-Stokes equations instead of using the Boussinesq approximation with incompressible equations. In fact RAMS does not show the same overestimation tendency of WRF although it employs the same form of the governing equations (see Table 5.1).

5.3.3 Spectral analysis

In this section we present compensated velocity spectra for the vertical and horizontal (only x-component) velocity on a log-log scale. The spectral analysis gives the possibility to further assess the adequacy of different computational grids for the CBL under consideration and, as specified in Section 5.3.2, to identify a possible explanation for the different role of Δx and Δz in RAMS and WRF. Compensated spectra relate the product of the power spectral density Φ and the wavenumber k to the wavenumber itself. The spectra should show both the range of the energy production scales, and part of the inertial range. The inertial range corresponds to a slope of $-2/3$ when plotting the compensated spectra on a loglog scale (Mirocha et al., 2010). The spectra are computed along the x-direction at each y grid point and at every time-step. Subsequently they are averaged over the xy-plane and lastly over time.

Figures 5.12 and 5.13 show spectra of the vertical velocity at the non-dimensional heights $z/z_i = 0.1$, 0.5 and 0.9 from RAMS and WRF respectively. The overall conclusion is similar for both codes. The computational grids of group A are not adequate for LES in both RAMS and WRF models, since no inertial range can be identified. The horizontal resolution of group B is sufficient to allow the presence of the

inertial range for both RAMS and WRF in the middle of the boundary layer, where the $-2/3$ slope is clearly present. The results of group C show a larger inertial range in the middle of the boundary layer, and the appearance of a small inertial range at the other heights. In the middle of the CBL the change of slope that indicates the beginning of the numerical dissipation is well defined. Both RAMS and WRF spectra of the vertical velocity present a gradual shift of the peak towards higher wavenumbers with decreasing z/z_i. This fact reveals that the eddy size correctly reduces closer to the surface. Figures 5.14 and 5.15 show the horizontal velocity (x-component) spectra, which lead to similar conclusions. The main difference is that the inertial range at $z/z_i = 0.1$ is more evident than in the vertical velocity spectra, with a clear slope change when numerical dissipation starts.

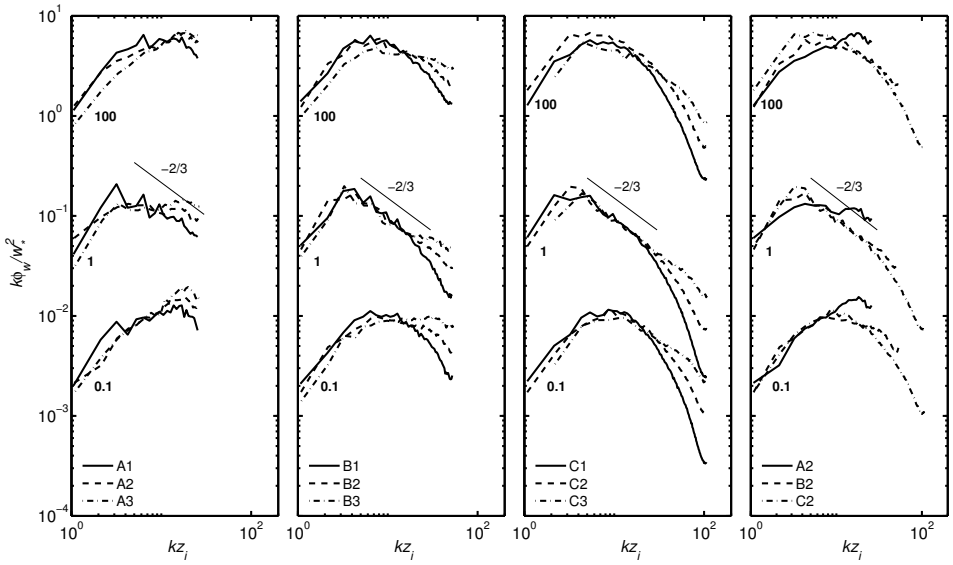

Figure 5.12: Spectra of time- and plane-averaged vertical velocity w along the x-direction. The groups of spectra in the top, middle and bottom of each plot are referred to dimensionless heights $z/z_{i0} = 0.9, 0.5, 0.1$ respectively. Spectral amplitudes in each group are multiplied by the numerical factor on the left-hand side of the plot. These results are obtained with RAMS.

Besides these general observations, there are a number of differences between both codes that should be considered. At the lowest horizontal resolutions (group A) RAMS does not seem to dissipate energy properly, but it does in both group B and C, especially when the vertical spacings is coarser, i.e. when the aspect ratio of the grid is

low. At the opposite, for larger aspect ratios the dissipation at high wave numbers is gradually substituted by an apparent extension of the inertial subrange. This behaviour reveals that refining Δz without a comparable refinement of Δx (i.e. increasing the grid aspect ratio) causes a strong and inadequate reduction of energy dissipation. The reason probably lies in the combination of RAMS SGS model and spatial discretization. When, with a certain Δx, a too small Δz is adopted, the eddy viscosity assumes a too low value, and it diminishes the diffusion in both horizontal and vertical directions because of the SGS model isotropy. In addition RAMS uses second-order centered finite differences for advection, i.e. a lower order scheme without inherent diffusion, that can not compensate the over-reduction of turbulent diffusion and that contributes to add spurious oscillations in the velocity field. The combined effect is that in case of a high aspect ratio the damping of smaller-scale structures becomes inadequate in respect to the computational grid and the inertial subrange of velocity spectra is artificially extended. Both Figure 5.12 and 5.14 show that an aspect ratio of 3 produces correct results, while a value of 6 does not. This fact provide a possible explanation for the influence that

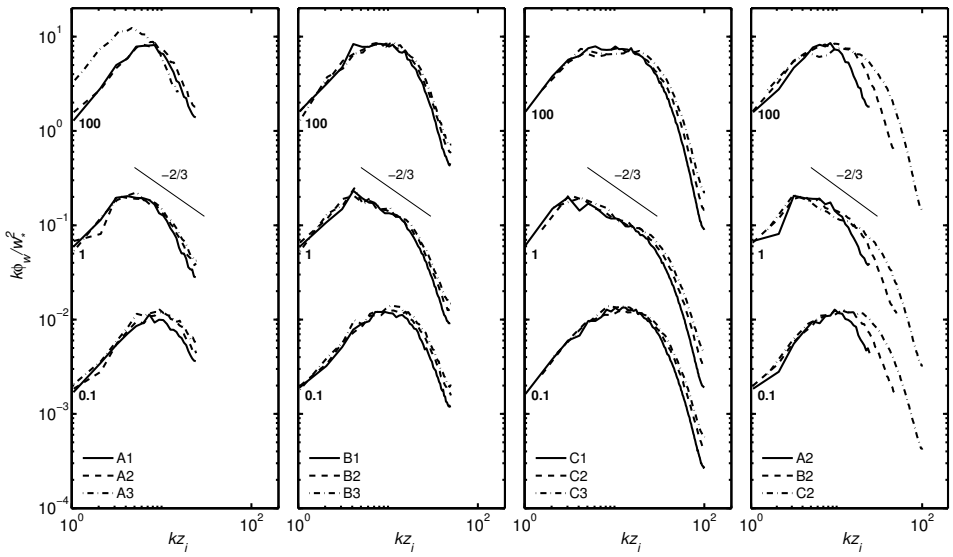

Figure 5.13: Spectra of time- and plane-averaged vertical velocity w along the x-direction. The groups of spectra in the top, middle and bottom of each plot are referred to dimensionless heights $z/z_{i0} = 0.9, 0.5, 0.1$ respectively. Spectral amplitudes in each group are multiplied by the numerical factor on the left-hand side of the plot. These results are obtained with WRF.

the vertical resolution has on TKE and velocity variances profiles in RAMS (Section 5.3.2). The smaller-scales spurious structures that are generated in the flow when the grid aspect ratio is increased (e.g. when Δz is refined with a constant Δx) break up the turbulence, weakening the larger-scales features, and consequently diminishing the TKE. This is what probably happens in simulations of group A and B (see Figure 5.5), while in group C the TKE profiles are almost unaffected by the variations of Δz in accordance with the fact that the aspect ratios are lower and therefore this mechanism does not trigger. The appearance of spurious smaller-scale structures in case of a too high aspect ratio will be confirmed by the flow visualization presented in Section 5.3.4.

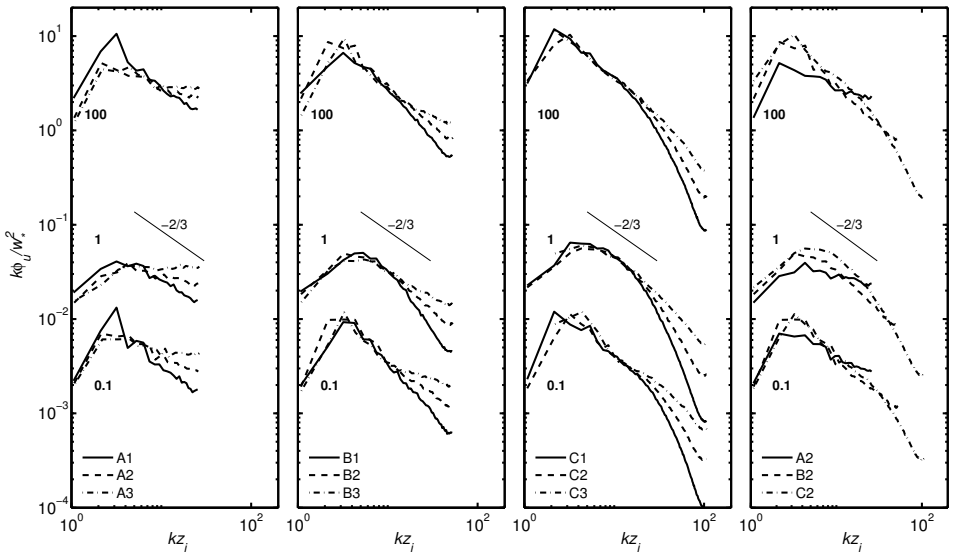

Figure 5.14: Spectra of time- and plane-averaged horizontal velocity u along x-direction. The groups of spectra in the top, middle and bottom of each plot are referred to dimensionless heights $z/z_{i0} = 0.9$, 0.5, 0.1 respectively. Spectral amplitudes in each group are multiplied by the numerical factor on the left-hand side of the plot. These results are obtained with RAMS.

Figure 5.13 and 5.15 reveal a completely opposite response of WRF to variations of the vertical resolution. In fact they demonstrate that for WRF the influence of Δz on velocity spectra is minimal. The refinement of the vertical grid spacing should have an almost identical effect on the eddy viscosity that in RAMS, given that they use the same SGS model (see Table 5.1). But WRF dicretizes advection

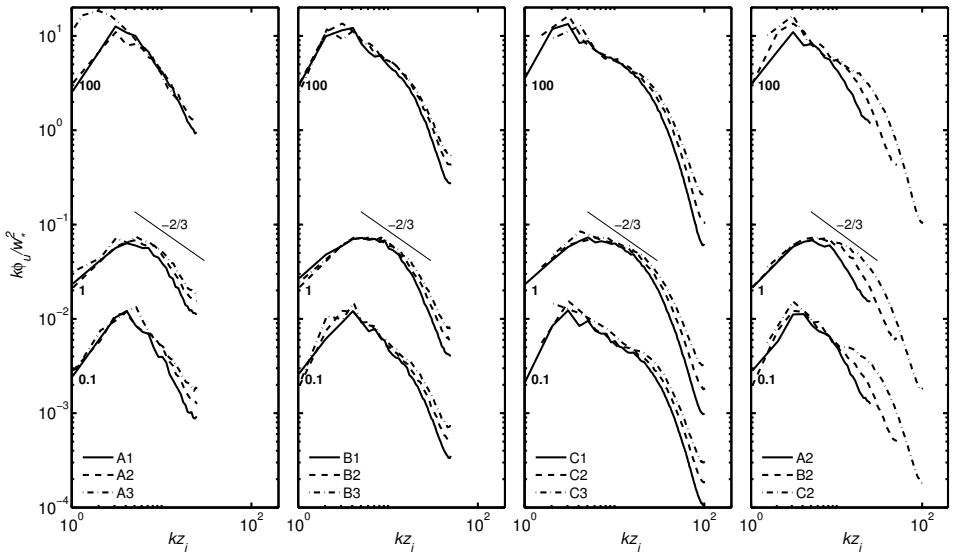

Figure 5.15: Spectra of time- and plane-averaged horizontal velocity u along x-direction. The groups of spectra in the top, middle and bottom of each plot are referred to dimensionless heights $z/z_{i0} = 0.9$, 0.5, 0.1 respectively. Spectral amplitudes in each group are multiplied by the numerical factor on the left-hand side of the plot. These results are obtained with WRF.

terms with odd finite differences (fifth-order along the horizontal direction and third-order along the vertical direction), which add numerical diffusion in the flow for their nature. In addition WRF employs filters for numerical stability (the three dimensional damping filter, the external-mode filter and the semi-implicit acoustic step off centering), that could in part influence the smallest turbulent scales (Skamarock and Klemp, 1992). Therefore a possible explanation for the negligible impact of Δz variations on velocity spectra is that here the reduction of the eddy viscosity is hidden by the numerical diffusion of WRF numerics, especially of the fifth-order finite differences. An overdamping at the higher wavenumbers has been observed also by Gibbs and Fedorovich (2014a), and they attribute it mainly to the odd finite differences schemes and only in minor part to the filters. Instead the refinement of the horizontal resolution gives the expected result of extending the inertial subrange, shifting the dissipation to higher wave numbers while correctly maintaining it. Δx variations do affect the velocity field, and consequently the spectra, because in our computational grids the horizontal spacing is the limiting factor, i.e. it is

considerably coarser than Δz, and also because its refinement should increase substantially the accuracy of the flow reproduction given that advection terms are fifth-order along the horizontal direction, while third-order along the vertical one. The fact that the flow reveals the variations of Δx, while it is almost insensitive to changes of Δz, seems to confirm what supposed by Gibbs and Fedorovich (2014a), i.e. that the main source of WRF over-damping on high wavenumbers should be the fifth-order advection scheme along the horizontal direction. The previous speculations help to interpret the impact of grid spacing on the TKE and velocity variance profiles (see Section 5.3.2). The profiles (Figures 5.6, 5.9 and 5.11) do not change in function of Δz because the velocity fields themselves are almost insensitive to the variations of the vertical resolution, as demonstrated by the velocity spectra, and probably because of the above described mechanism. Instead TKE and velocity variances increase with a refinement of Δx because, as above explained, it causes a decrease of diffusion (both numerical and turbulent) and an enhancement in accuracy, that result in more energy in the flow.

From this spectral analysis some additional recommendations about computational grid design can be provided. First of all the coarsest examined horizontal resolution ($\Delta x = 120$ m) is not sufficient for a correct CBL turbulence reconstruction in both codes. In fact the corresponding spectra show the absence of the inertial subrange (WRF) and of both the inertial and the dissipation subranges (RAMS). A horizontal spacing of 60 m produces acceptable results, but in order to achieve a good turbulence reconstruction also in the surface layer a value of 30 m is suggested. In RAMS high grid aspect ratios generates spurious smaller-scale structures that alter the results quality, and therefore, if a fine vertical spacing is desired, a comparable refinement along the horizontal direction is required. Our results indicate that an aspect ratio of 3 produces correct results, while a value of 6 already causes a considerable distortion of the velocity spectra (energy is not properly dissipated at the high wavenumbers). As above discussed in more detail, the inadequate dissipation that appears with high grid aspect ratios probably originates from the combination of RAMS SGS-model and second-order centered finite differences. At the contrary in WRF high aspect ratios are admissible, but it is important to be aware that refining the vertical resolution without a comparable refinement along the horizontal direction has a negligible effect on the flow. Instead, in our tests an enhancement in turbulence reconstruction has

been obtained when Δx has been refined, both because the horizontal fifth-order finite differences should probably be the main source of WRF over-damping of the smaller-scale structures, and because in our grids Δx is the limiting factor (i.e. it is coarser than Δz).

5.3.4 Flow visualization

In this section we present a visual inspection of velocity fields in order to consolidate the previously discussed results. Figures 5.16 and 5.17 show nine instantaneous vertical velocity fields in the xy-plane at the dimensionless height $z/z_i = 0.1$, corresponding to the nine computational grids for both models. The figures are organized with the velocity fields from run $A1$, $A2$ and $A3$ on the upper row; $B1$, $B2$ and $B3$ on the second row; and $C1$, $C2$ and $C3$ on the third row. Therefore vertical grid resolution increases from left to right and the horizontal one from top to bottom. In general, the plots show that the grid refinement leads to better defined coherent structures and to the appearance of smaller eddies. A careful inspection however reveals some differences between the codes, which match the observations from the spectra presented in section 5.3.3.

In WRF, typical hexagonal patterns are clearly visible in the velocity fields for all the resolutions, demonstrating that higher-order numerical schemes face better the adoption of coarse computational grid. Smaller-scale coherent structures appear when $\Delta x = 30m$ (group C, last line of Figure 5.17), and they are the reason for the larger inertial subrange observed in group C in respect to group B (see Figure 5.15 and 5.13). In fact in group B the flow is already well reproduced but small features are rare (second line of Figure 5.17). Velocity fields with the same horizontal grid spacing (each line of Figure 5.17) seems to be almost equivalent, apart from a slight enrichment of smaller-scale structures, in accordance with the spectra invariance to Δz. In fact, as discussed in more detail in section 5.3.3, in WRF the main source of damping is probably the numerical diffusion induced by the fifth-order finite differences scheme applied along the horizontal direction. Therefore refining the vertical grid spacing causes only a minor damping reduction in comparison with the amount related to horizontal discretization, even if Δz acts on both the eddy viscosity (a finer Δz corresponds to a lower eddy viscosity) and the numerical diffusion due to the vertical integration. The final result of this mechanism is that refining the vertical grid spacing has led to negligible differences in

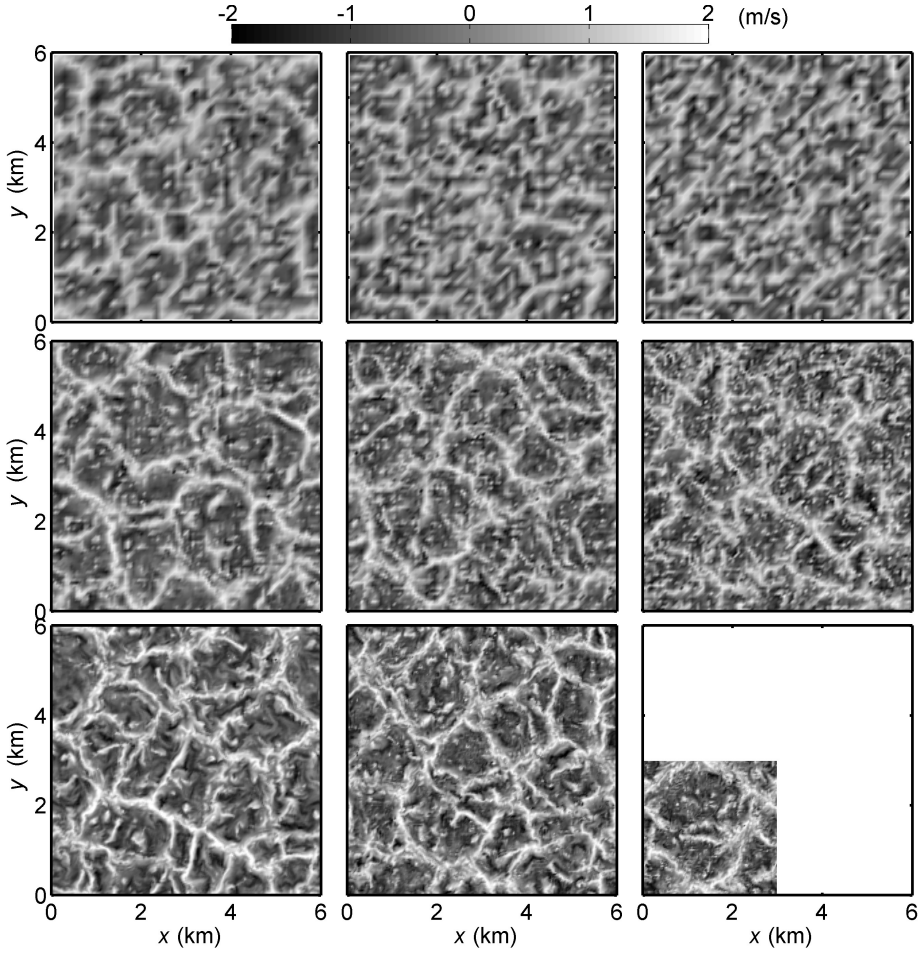

Figure 5.16: Visualization of the instantaneous vertical velocity field in the xy-plane at dimensionless height $z/z_{i0} = 0.1$. Starting from the top left plot and going toward right along rows, velocity fields belong to runs $A1$, $A2$, $A3$, $B1$, $B2$, $B3$, $C1$, $C2$, $C3$. These results are obtained with RAMS.

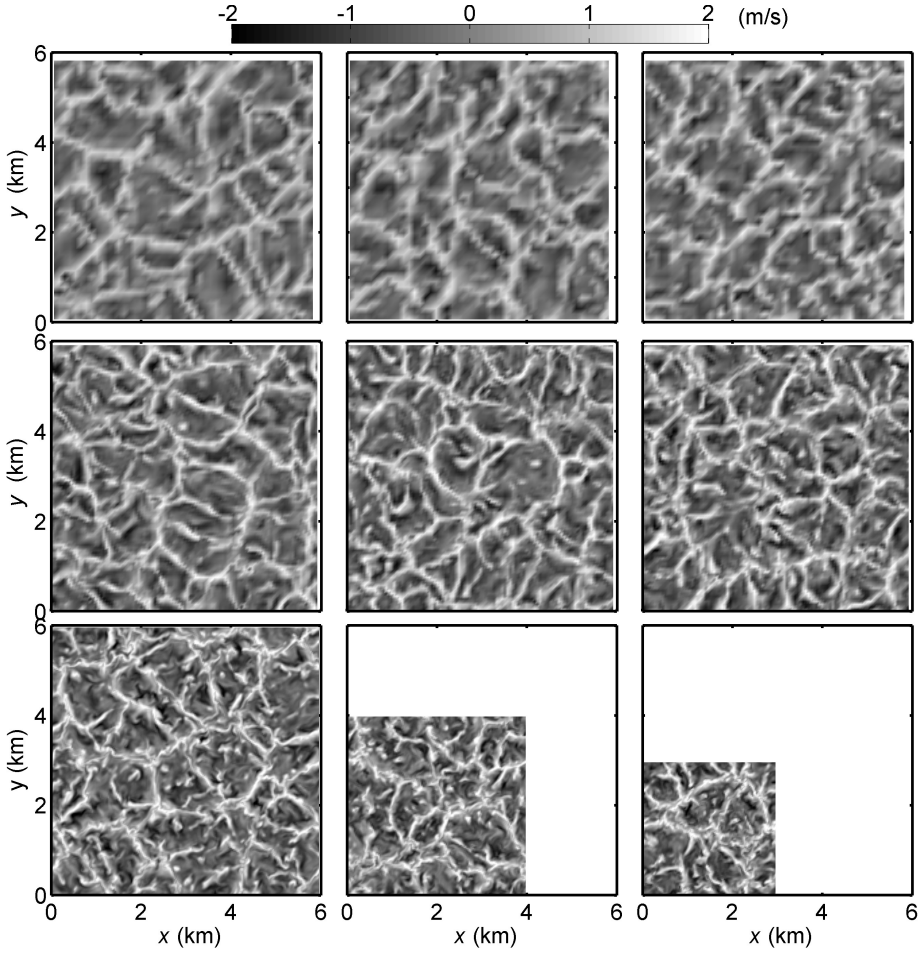

Figure 5.17: Visualization of the instantaneous vertical velocity field in the xy-plane at dimensionless height $z/z_{i0} = 0.1$. Starting from the top left plot and going toward right along rows, velocity fields belong to runs $A1$, $A2$, $A3$, $B1$, $B2$, $B3$, $C1$, $C2$, $C3$. These results are obtained with WRF.

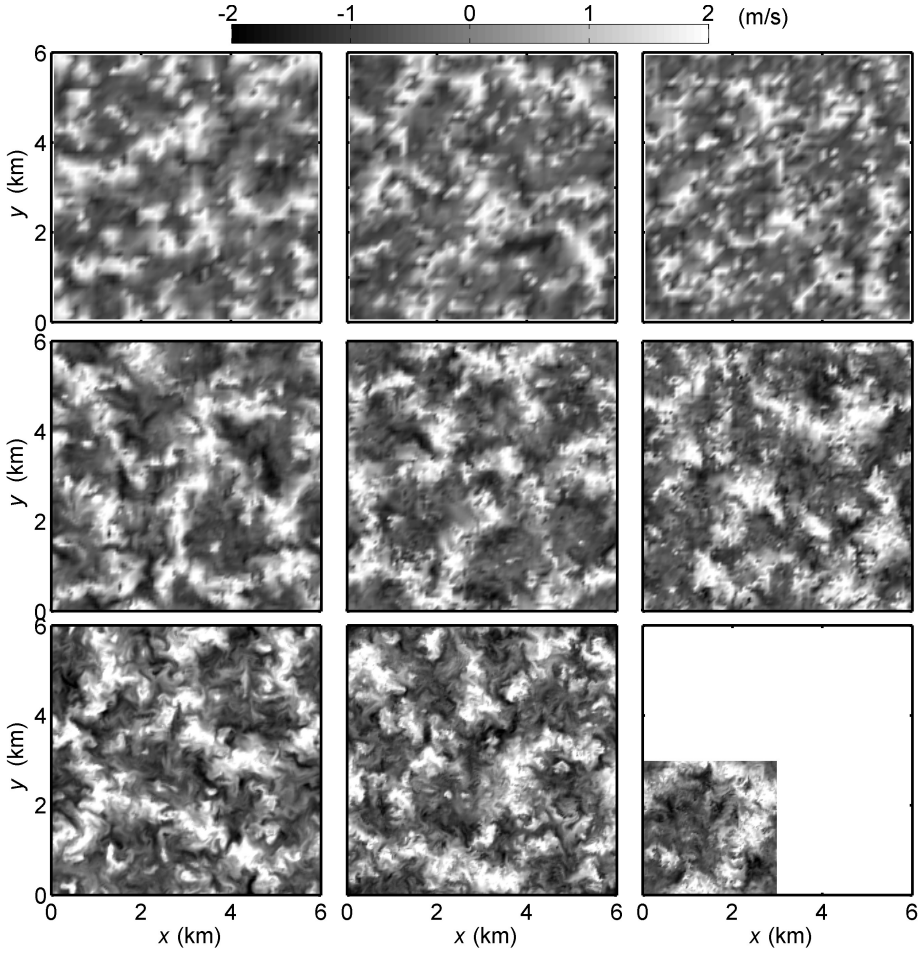

Figure 5.18: Visualization of the instantaneous vertical velocity field in the xy-plane at dimensionless height $z/z_{i0} = 0.5$. Starting from the top left plot and going toward right along rows, velocity fields belong to runs $A1$, $A2$, $A3$, $B1$, $B2$, $B3$, $C1$, $C2$, $C3$. These results are obtained with RAMS.

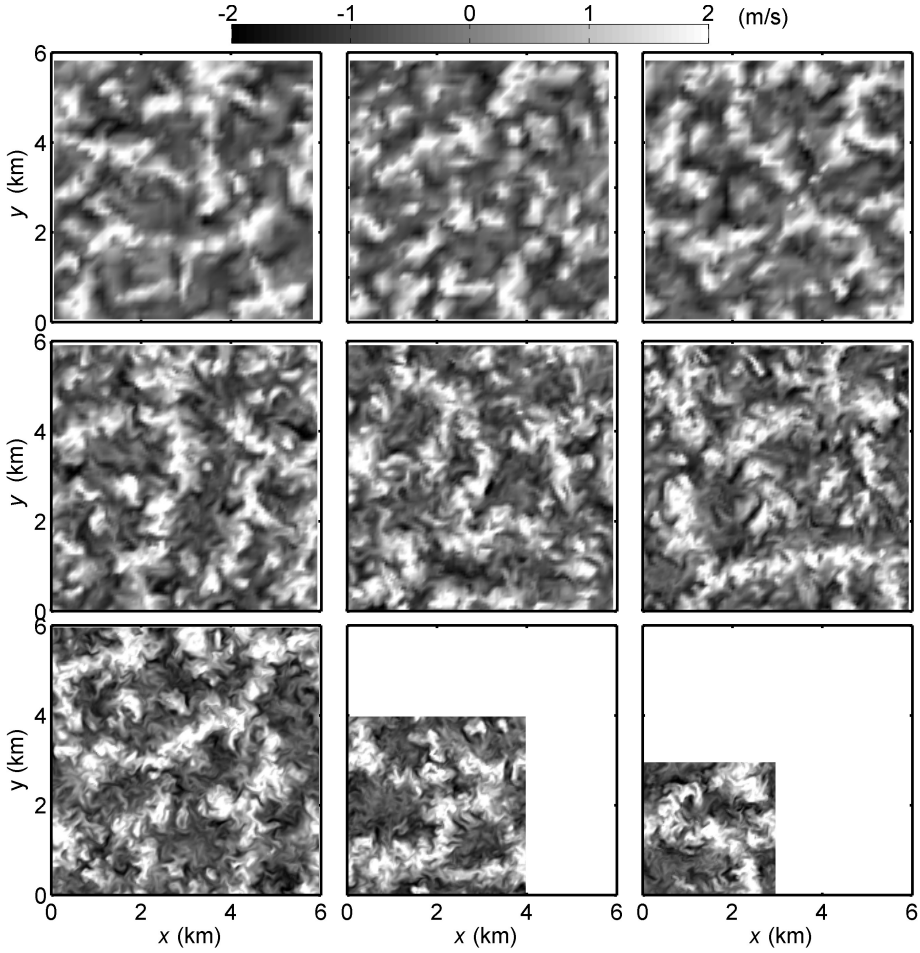

Figure 5.19: Visualization of the instantaneous vertical velocity field in the xy-plane at dimensionless height $z/z_{i0} = 0.5$. Starting from the top left plot and going toward right along rows, velocity fields belong to runs $A1$, $A2$, $A3$, $B1$, $B2$, $B3$, $C1$, $C2$, $C3$. These results are obtained with WRF.

the turbulence reconstruction, while finer Δx has improved it, because the total damping of the code considerably reduces when horizontal resolution increases.

In RAMS vertical velocity fields (Figure 5.16), one can observe very small-scale features at almost all the horizontal resolutions. Their appearance is mostly related to the vertical resolution, while the main effect of the horizontal resolution is to enhance the definition of large hexagonal patterns. Observing the flow fields in the first column of Figure 5.16 (runs $A1$, $B1$ and $C1$) it can be seen how increasing the horizontal resolution results in more, better defined larger structures. Moving along rows from left to right it can be seen that, when increasing the vertical resolution, smaller features start to appear in the flow. This corresponds to the previous observation about spectra, i.e. that refining the computational grid in the vertical direction results in an increase of the energy at high wavenumbers. The visual inspection of the velocity fields immediately hints that in runs $A2$, $A3$, $B2$, $B3$ and $C3$ this high wavenumbers energy is due to numerical oscillations that are not correctly damped by the model and it is not due to a more detailed representation of the turbulence. In facts, as explained in more detail in section 5.3.3, when the grid aspect ratio is high RAMS does not dissipate energy properly because of the combination of its isotropic SGS model and its second-order centered finite difference scheme for advection. The scheme does not add numerical diffusion and therefore the eddy viscosity, that reduces even if only Δz is refined, is not sufficient to damp spurious oscillations.

Figures 5.18 and 5.19 are equivalent to 5.16 and 5.17 but at $z/z_i = 0.1$. They show that both models correctly reproduce the evolution of the surface hexagonal structures into plumes when increasing the distance from the ground, and substantially confirm the previous observations about the impact of Δx and Δz on the flow.

This final analysis adds confidence in what speculated in the previous sections. In fact it confirms that in case of high aspect ratios the additional energy present in RAMS spectra at high wavenumbers is due to spurious oscillations and therefore it highlights the importance of adopting a computational grid with comparable horizontal and vertical resolutions. About WRF it visually shows that, for the values here adopted, a refinement of only the vertical resolution generates negligible effects on the flow, while the level of detail in turbulence reconstruction is tuned by the horizontal grid spacing. In addition, confronting RAMS and WRF vertical velocity fields, the same WRF

characteristic that has been observed by Gibbs and Fedorovich (2014a) is found, i.e. WRF fields are less variable than RAMS fields, but with more contrasted structure. Again, this is related to the over-damping nature of WRF in respect to RAMS, and to the fact that a surplus of energy on larger-scale structures can be present because of the absence of small features to be fed by the latter (Gibbs and Fedorovich, 2014a).

5.4 Conclusions

The impact of grid spacing on large-eddy simulation of the dry atmospheric convective boundary layer has been evaluated for two of the most popular Numerical Weather Prediction Limited Area Models, namely RAMS (Regional Atmospheric Modeling System) and WRF (Weather Research and Forecasting model). Nine simulations have been performed on a fixed computational domain, combining three different horizontal and vertical resolutions. An idealized, well understood, free convection regime has been selected to assess the performances of the two models. The tested grid resolutions were selected to be within the typical affordable range for practical applications, in order to understand if the LES mode of the two models can become a widespread tool for applied studies of ABL phenomena without requiring extremely high computational loads. The influence of the various adopted computational grids on results has been assessed through the analysis of various turbulent statistics and flow analysis: mean vertical profiles of potential temperature, vertical heat fluxes, turbulent kinetic energy and velocity variances, velocity spectra and flow visualization.

For both models the potential temperature profiles are almost insensitive to grid resolution and the expected uniform value in the mixed layer is always correctly modelled. The linear variation of the heat flux with height inside the mixed layer is reproduced in both WRF and RAMS for all the simulations, with a negligible impact of the computational grid. Heat fluxes in the entrainment and stable layers are mainly influenced by Δz, while Δx has a minor effect. For both models the best results (in relation to theoretical expectations and previous large-eddy simulations) are achieved with the finest tested vertical resolution, i.e. 5m. In the examined range of resolutions RAMS does not maintain the linear slope in the surface layer, while WRF does. Probably this shortcoming of RAMS is related to its lower-order numerics (see Table 5.1).

In terms of TKE and velocity variance, both models show a predominant impact of horizontal grid spacing on the profiles. But the effect of Δx and Δz is different between WRF and RAMS. In WRF the vertical grid spacing essentially does not influence the profiles, while the refinement of Δx results in an increment of the variances. Spectral analysis and flow visualization have shown that in WRF the simulated velocity fields are almost unaffected by the vertical resolution (nearly overlapping spectra and flow fields visually very similar), and therefore variance profiles remain unchanged when Δx is maintained constant, regardless the value of Δz. A possible explanation is that the main source of diffusion in WRF is the fifth-order finite differences schemes used for horizontal advection. When Δz is refined, both the eddy viscosity computed by the SGS-model and the numerical diffusion of the third-order scheme along the vertical direction diminish, but that one of the fifth-order scheme remain unchanged. If the latter is predominant, the flow does not feel the decreases of the others. Additional confidence in this hypothesis is given by the fact that, at the contrary, when Δx is refined the quality of turbulence reproduction improves, i.e. smaller-scales structures appear in the velocity field and coherently the inertial subrange in spectra extends to higher wavenumbers. Another effect of refining the horizontal resolution is that TKE increases, again because dissipation decreases and therefore more energy is present in the flow. But it is important to underline that our analysis has confirmed the tendency of WRF to overestimate velocity variances that has been already pointed out by Gibbs and Fedorovich (2014a). They have shown that WRF generates less variable velocity fields but with more contrasted structural turbulent features in respect to those obtained with more standard and tested LES code, and they attribute this fact to WRF numerics more than to other differences between the two compared codes (e.g. governing equations in compressible or incompressible form). Our results seem to confirm this explanation. We have shown that velocity variances and TKE depend on the computational grid, and this indicates that the overestimation is related to numerics. In addition we have substantially excluded the possibility that the overestimation tendency of WRF is related to the nature of governing equations, because RAMS does not present it although it employs the same compressible Navier-Stokes equations of WRF. In RAMS the role of the vertical resolution is more active. Velocity spectra and flow visualization has shown that, when Δz is refined without a comparable reduction of Δx (i.e. in case of high grid aspect ratios),

spurious smaller-scale structures appear in the flow. In this cases an evident increase of energy at high wavenumbers appears in the spectra, with an artificial extension of the inertial subrange that gradually substitutes the dissipation range. The observation of the corresponding velocity fields suggests that this energy accumulation is due to spurious numerical oscillations that are not correctly damped by the model. This is probably due to the combination of RAMS numerics and SGS model. The refinement of Δz causes a reduction of the eddy viscosity and, because of the SGS model isotropy, a decrease of diffusion in both horizontal and vertical direction. The resulting damping is probably inadequate in respect to the horizontal grid spacing, and therefore spurious oscillation in velocity, due to the lower-order non-diffusive finite difference scheme, appear in the flow. This mechanism impacts also TKE and velocity variance profiles. In fact when the grid aspect ratio is too high the spurious small features break up the turbulence, weakening the larger-scale structures and consequently diminishing the TKE and velocity variance.

From the performed analysis two main conclusions can be drawn. First of all we have verified that both RAMS and WRF can perform LES of the CBL without requiring extremely high computational loads. Assessing if a model that was originally built to simulate mesoscale atmospheric flow can adequately reproduce turbulence at the microscale is a relevant question (Paiva et al., 2009; Gibbs and Fedorovich, 2014a) and limited knowledge about this issue is at disposal in literature. In particular no studies whose focus is to evaluate RAMS performances in LES are available. In addition we can provide some recommendations about grid design when the aim is to perform a LES of the CBL with RAMS or WRF. The coarsest tested horizontal resolution of 120m appears to be insufficient to correctly reproduce atmospheric turbulence at the microscale for both models (velocity spectra clearly show it). WRF can produce adequate results in terms of both TKE profiles and velocity spectra with an horizontal grid spacing of 60m, while RAMS at this resolution still present some flaws, especially in the near-wall region, as demonstrated by horizontal velocity variance profiles and spectra. RAMS need of a higher resolution is coherent with its lower-order numerics. But, when one aims at a good turbulent reconstruction also in the surface layer, a value of 30m for Δx is suggested for both models. In RAMS high grid aspect ratios cause the appearance of spurious smaller-scale structures in the flow, and therefore when a fine vertical resolution is desired a comparable refinement

along the horizontal direction is required. Our results indicate that an aspect ratio of 3 correctly simulates turbulent structures, while a value of 6 already causes a considerable corruption of the velocity fields. At the contrary in WRF high aspect ratios are admissible, but it is important to be aware that refining the vertical resolution has a negligible impact on the flow until the limiting factor is the horizontal grid spacing. In conclusion the two models react differently to changes of grid spacings in horizontal and vertical direction, coherently with their different numerics, but if the computational grid is properly designed they can both achieve valuable results in LES of the CBL.

6

RAMS performances in neutral conditions

This chapter concludes the evaluation of RAMS capabilities in performing LES of the ABL, considering the more challenging case of neutral conditions. In fact, under this regime, turbulent structures are smaller than in convective conditions, and consequently the inertial subrange establishes at higher wavenumbers. Therefore finer grid resolutions are needed to correctly simulate the neutral ABL and reversely a greater role is attributed to the SGS model if the same spatial resolution is used. In particular, the neutral ABL here simulated is a steady state flow over a flat and homogeneous surface, because, as for the free-convection regime, theoretical expectations about its flow statistics and structures are available (Moeng and Sullivan, 1994; Lin et al., 1997) and the literature offers several LES in similar conditions (e.g. Andren et al., 1994; Chow et al., 2005; Ludwig et al., 2009; Mirocha et al., 2010; Talbot et al., 2012). Hence the evaluation of the model performances is facilitated. Coherently with the analysis performed in free-convection conditions (see Chapter 5), the focus is not only on the overall evaluation of the model capabilities in reproducing turbulence in the neutral ABL, but also on the impact that grid spacings have on the results. The final objective is to provide guidelines on suitable mesh resolution when performing LES of the neutral ABL.

To this aim nine simulations on a fixed computational domain of $4096 \times 4096 \times 1024$ m are performed using nine different computational grids. The grids are obtained combining three different horizontal (64, 32, 16 m) and vertical (16, 8, 4 m) spatial resolutions. The results are post-processed in terms of mean profiles of horizontal velocity, momen-

tum flux and velocity variances, spectra and flow visualizations. The analysis compares the model outcomes to the expected results for the considered idealized conditions and analyzes the effect of changing the grid spacing.

The chapter is organized as follows. Details about the simulation setup are given in Section 6.1, while results are extensively analyzed in Section 6.2, and finally conclusions are presented in Section 6.3.

6.1 LES experiment setup

In this analysis an atmospheric boundary layer in neutral steady conditions is simulated over a flat and homogeneous surface, since its flow statistics and structures are known (Moeng and Sullivan, 1994; Lin et al., 1997) and other LES in similar conditions are available in the literature for comparison (e.g. Andren et al., 1994; Chow et al., 2005; Ludwig et al., 2009; Mirocha et al., 2010; Talbot et al., 2012). Hence it represent another typical test case, besides the free-convection regime explored in the previous chapter, for LES models whose performances are to be evaluated. In neutral conditions the turbulent structures are smaller than in a convective regime, and consequently the inertial subrange establishes at higher wavenumbers. Therefore finer grid resolutions are needed to correctly simulate it and reversely a greater role is attributed to the SGS model if the same spatial resolution is used. Neutral conditions are characterized by the absence of a surface sensible heat flux and the only driving force of the turbulence is the surface shear generated by large-scale pressure gradients (i.e. geostrophic wind). The resulting typical turbulence structures in proximity of the surface are streaks of high-low velocity aligned with the mean wind direction. The main scaling quantities of the flow are the ABL height H and the surface friction velocity u_* (Moeng and Sullivan, 1994).

In our setup turbulence is forced by a constant geostrophic wind of $10ms^{-1}$ along the $x-$direction and the Coriolis acceleration is considered, with a Coriolis parameter $f = 10^{-4}$ s^{-1}. Periodicity is imposed at the lateral boundaries, while at the domain top a rigid lid with a damping layer of about 48 m is employed. The simulation design is completed by a homogeneous surface roughness length $z_0 = 0.10$ m, zero surface heat flux, an adiabatic initial temperature profile and dry air. As in free-convection simulations (see Section 5.1) the turbulent viscosity is computed using the 1.5-order-of-closure scheme of Deardorff

Run	Δx (m)	Δy (m)	Δz (m)	Grid Points	$\Delta x/\Delta z$
$A1$	64	64	16	$64 \times 64 \times 64$ (262164)	04.0
$A2$	64	64	8	$64 \times 64 \times 128$ (524288)	08.0
$A3$	64	64	4	$64 \times 64 \times 256$ (1048576)	16.0
$B1$	32	32	16	$128 \times 128 \times 64$ (1048576)	02.0
$B2$	32	32	8	$128 \times 128 \times 128$ (2097152	04.0
$B3$	32	32	4	$128 \times 128 \times 256$ (4194304)	08.0
$C1$	16	16	16	$256 \times 256 \times 64$ (4194304)	01.0
$C2$	16	16	8	$256 \times 256 \times 128$ (8388608)	02.0
$C3$	16	16	4	$256 \times 256 \times 256$ (16777216)	04.0

Table 6.1: Characteristics of the nine computational grids

(1980) (see Section 3.2.1). A fixed domain size of $(L_x,\, L_y,\, L_z) = (4096,\, 4096,\, 1024)$ m is used for all the simulations, and nine different computational grids are employed in order to investigate the impact of the spatial resolution. The nine computational grids are obtained by combining three different horizontal, $\Delta x = (64,\, 32,\, 16)$ m, and vertical,$\Delta z = (16,\, 8,\, 4)$ m, resolutions. The examined grid spacings are smaller than those employed for the corresponding analysis in convective conditions (see Section 5.2), coherently with the above-said fact that eddies in a neutral ABL are smaller than the large thermals that drives the turbulence under free-convection regime. Details about the nine computational grids are collected in Table 6.1.

6.2 Results

RAMS capabilities in performing LES of the neutral ABL and the effect that the grid spacing has on the quality of results are evaluated by comparing mean vertical profiles, second order statistics and velocity spectra from the nine simulations described in the previous paragraph. In fact the adequacy of a computational grid for a certain LES experiment and the overall performances of a model can be assessed through these quantities without any dependence on the specific characteristics of the model itself, such as the SGS model and the numerics (Mirocha et al., 2010). In order to approximate ensemble averages, statistics are obtained by first averaging over horizontal planes and then over time (Kirkil et al., 2012; Sullivan and Patton, 2011). Hereafter the ensemble averages are denoted by $\langle \cdot \rangle$ and fluctuations by $\cdot'$. All the reported results are for steady state conditions, namely the statistics

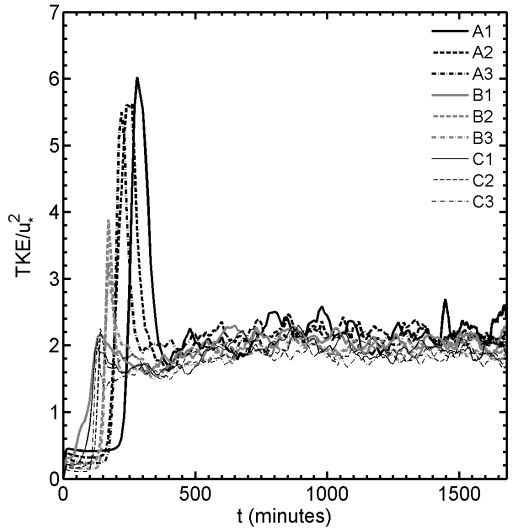

Figure 6.1: Total TKE averaged across the ABL in function of time.

are obtained by averaging results of the last 4 hours of simulation after 24 hours of turbulence spinup. This can be verified in Figure 6.1, where the time evolution of the total turbulent kinetic energy (TKE) averaged across the ABL is plotted. The total TKE is the sum of the resolved and modelled contributions, i.e. $TKE =< 0.5u_i'u_i' + e >$, where e is the modelled kinetic energy. The nearly constant value of TKE during the data collection interval ensures a stationary state. It can be noticed that both the spinup and the data collection periods are significantly longer in respect to those of the free-convection case, in which they were equal to 1.5 and 1.0 hours respectively (see Section 5.3). In fact pure shear turbulence is characterized by longer characteristic time-scales than convective eddies, and this fact implies that a longer duration of the simulation is necessary. Hence, a significant increase of the computational cost follows, even adopting a computational grid with the same number of elements. A possible strategy to shorten the spinup period and therefore to decrease the computational cost of a neutral simulation is to initially impose a constant weak surface heat flux for about 1 hour and then to turn it off and run the simulation for some few hours waiting for the establishment of neutral conditions (Moeng et al., 2007).

6.2.1 Mean velocity analysis

In presence of shear driven turbulence, the adequacy of a computational grid for a specific LES, namely for a combination of a specific setup and a specific numerical code, can be assessed through SGS and resolved stress components and their sum, i.e. the total simulated stress. Figure 6.2 shows the total vertical-streamwise stress (i.e.

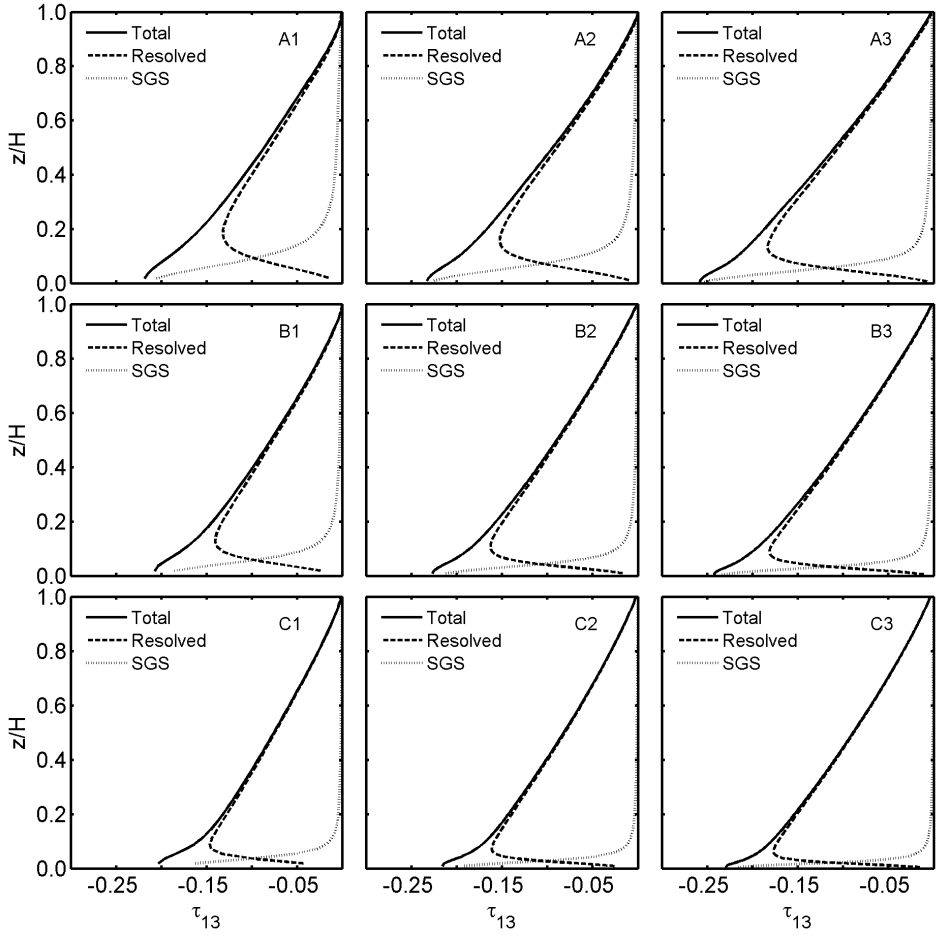

Figure 6.2: Vertical profile of time- and plane-averaged τ_{13} stress components in function of dimensionless height z/H.

$u-$momentum flux along the vertical direction) and its resolved and modelled components for the nine performed simulations. The subgrid stress component is evaluated from the SGS model as the product between the local vertical gradient of the $u-$velocity component and the

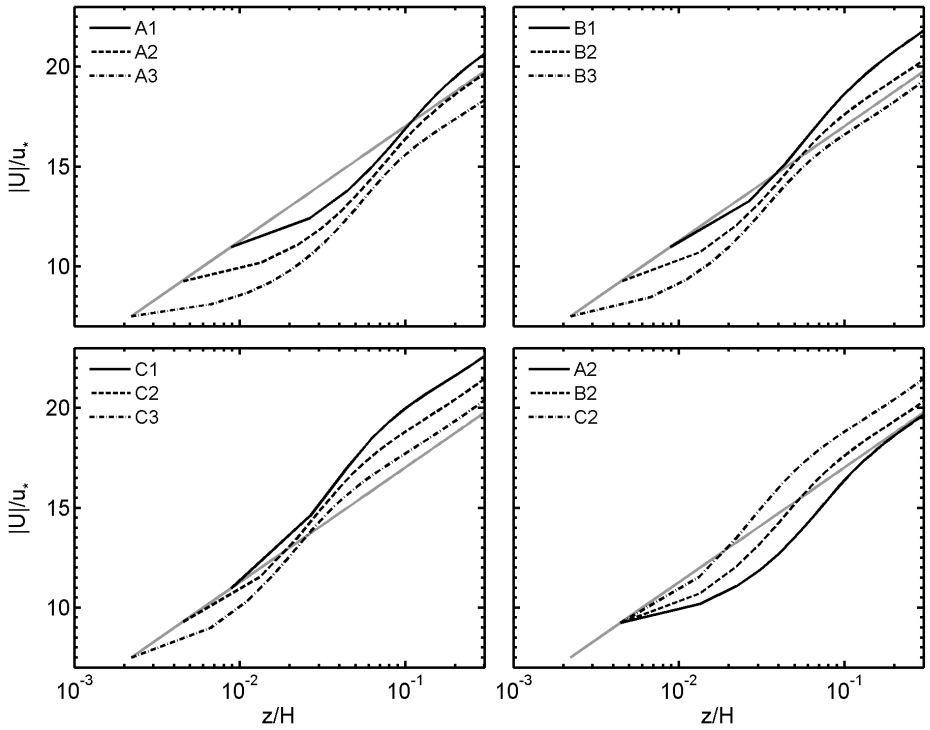

Figure 6.3: Vertical profile of time- and plane-averaged horizontal wind speed scaled by surface friction velocity u_* in function of dimensionless height z/H. The theoretical logarithmic profile is in gray.

eddy viscosity ν_t. The resolved component is the covariance between streamwise, u, and vertical, w, velocities.

$$\tau_{13} = \langle u'w' \rangle - \nu_t \frac{\partial u}{\partial z} \tag{6.1}$$

Figure 6.2 is organized as follows: profiles corresponding to run $A1$, $A2$ and $A3$ are in the first row; $B1$, $B2$ and $B3$ in the second row; and $C1$, $C2$ and $C3$ in the third row. Hence vertical grid spacing is refined moving from left to right and the horizontal one from top to bottom. It can be noticed that most of the stress is resolved in all the simulations, suggesting that all the nine computational grid could be adequate for this specific LES. The only exception is near the surface where the SGS contribution dominates. Furthermore the resolved contribution correctly increases and the SGS one correctly decreases as the grid spacing is refined. Another consequence of grid refinement is that the height at which the resolved component of the stress starts to decrease

in magnitude moves towards the surface, meaning that a more accurate reproduction of turbulence is obtained at smaller distances from the lower boundary. These improvements in the reconstruction of the near surface turbulence are obtained, not only by refining the vertical grid spacing Δz, but also increasing the horizontal resolution Δx while Δz is maintained constant (i.e. moving along columns in Figure 6.2). In fact vertical turbulent fluctuations are damped more strongly than the horizontal ones while moving towards the surface (Mirocha et al., 2010). As the horizontal grid resolution is refined the total stress deviates from the expected linear profile at the height at which the SGS contribution becomes predominant, pointing out that the SGS model overestimates the stress close to the wall. This shortcoming of the model is particularly evident for simulations that employ the finest horizontal resolution (group C), while it is almost negligible when the coarsest Δx is used (group A).

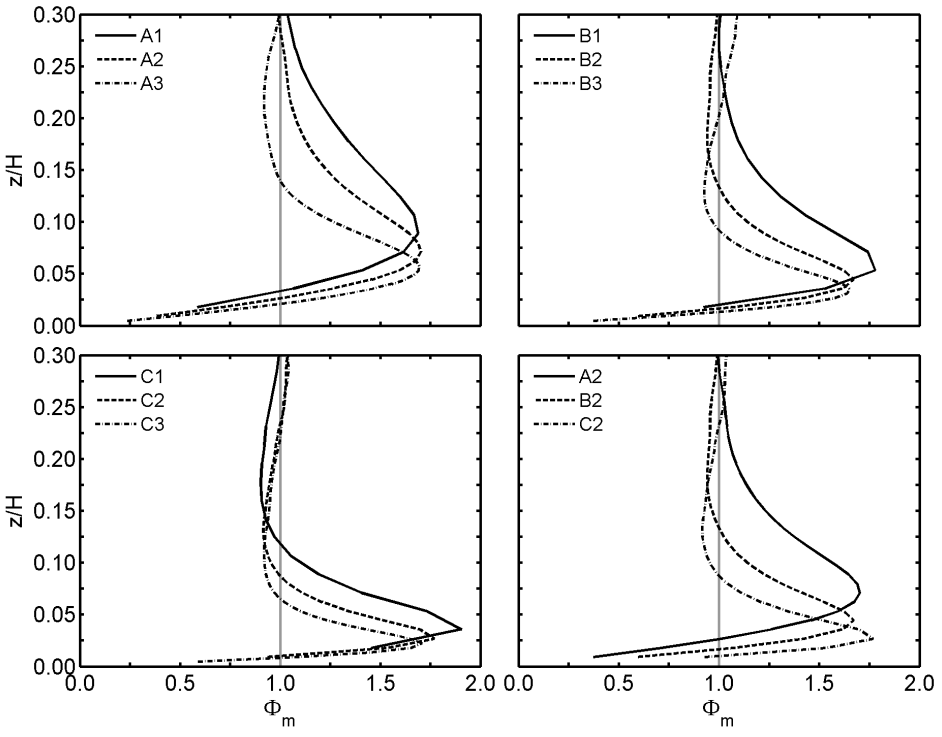

Figure 6.4: Vertical profile of time- and plane-averaged dimensionless shear $\Phi(z) = (kz/u_*)(\partial U/\partial z)$ in function of dimensionless height z/H. The expected theoretical profile $\Phi = 1$ is in gray.

Figure 6.3 shows vertical profiles of time- and plane-averaged horizontal velocity module, scaled with the surface friction velocity u_*, in function of the dimensionless height z/H. According to Monin-Obukhov similarity (Monin and Obukhov, 1954), the expected profile over a flat and rough surface in neutral conditions is the logarithmic Law Of The Wall (LOTW) but none of the simulations successfully matches it. The simulated profiles tend to underestimate the velocity immediately above the surface, recovering this deficit aloft, in some cases up to an overestimation of the velocity (runs $A1$, $B1$, $B2$, $C1$, $C2$, $C3$). This shape of the profile is maintained in all the simulation, with the grid spacing influencing only the intensity of the velocity deficit and consequently that of the aloft overestimation. Comparing the profiles it can be seen that the parameter mainly influencing the LOTW reproduction is the grid aspect ratio ($AR = \Delta x/\Delta z$). In fact its reduction, that can be due to both an increase of Δz with the same Δx or to a refinement of Δx with the same Δz, diminishes the velocity deficit immediately above the surface. Moreover the best agreement with LOWT is always achieved with an aspect ratio equal to 4 for all the three groups of simulations. The central role of the aspect ratio for LOTW reproduction has been already pointed out in several studies (Brasseur and Wei, 2010; Mirocha et al., 2010) and it has also been considered more important than the vertical resolution itself (Chow et al., 2005; Kirkil et al., 2012). The LOTW mismatch is clarified by Figure 6.4, showing the vertical profile of the dimensionless shear Φ_m, defined as

$$\Phi_m = \frac{kz}{u_*}\frac{\partial |U|}{\partial z} \tag{6.2}$$

where k is the Von Kármán constant, taken equal to 0.41 for coherence with RAMS code, and $|U|$ is the horizontal wind speed module. In accordance with LATW, Φ_m should have a constant value of 1 in the whole surface layer, but usually LES of the neutral ABL produces an overshoot close to the surface (Brasseur and Wei, 2010). All our simulations show it, confirming the over-dissipative nature of the TKE subgrid model here employed (e.g. Mason and Thomson, 1992; Porté-Agel et al., 2000). Refining the spatial resolution the peak of Φ_m moves towards the surface, as already noticed in previous LES (Brasseur and Wei, 2010). The LOTW mismatch in LES of the neutral ABL is a longstanding problem and different solutions have been proposed during years (Mason and Thomson, 1992; Sullivan et al., 1994; Porté-Agel et al., 2000). The majority of them consists in diminishing the vertical

shear near to the surface.

6.2.2 Variances analysis

Vertical profiles of dimensionless velocity variance are shown in Figures 6.5, 6.6 and 6.7, referring respectively to $u-$, $v-$ and $w-$velocity components. The Figures are subdivided into four panels. In each of the first three panels results from the three simulations that use the same horizontal resolution and differ only for the vertical grid spacing are reported. Hence the three panels correspond to runs of group A, B and C going from left to right. In order to show the impact of Δx more clearly, the fourth panel compares results of simulations that use an equal vertical grid spacing (the intermediate one, i.e. 8m) but different horizontal resolutions.

Resolved velocity variances are another index of the quality of turbulence reconstruction (Kirkil et al., 2012) and assume a fundamental role when the focus is on particle transport in the ABL (e.g. Michioka and Chow, 2008). The general effect of refining the computational grid resolutions, both horizontal and vertical, is the same for all the three velocity components and consists in an increase of the variance peak and its displacement towards the surface. The variances are more influenced by the refinement of the horizontal grid spacing than by that of the vertical one. In addition the impact of Δz decreases and acts on increasingly limited heights as Δx diminishes. For instance, referring to the $w-$component variance and hence to Figure 6.7, variations in Δz change the profile in the whole depth of the ABL in runs of group A but influence only layers below $0.2z/H$ in runs of group C. This fact indicates that the limiting factor for the turbulence reconstruction, in terms of computational grid, is the horizontal resolution. Also some differences can be detected between the impacts on the three velocity components variances. The $v-$component variance changes in function of Δx and Δy only in the surface layer and just above it (at maximum below $z/H = 0.3$), while the $w-$component variance is affected by variations in grid resolution throughout the whole boundary layer. This sort of grid invariance of the $v-$component variance in the upper part of the ABL should indicate that all the nine computational grids are adequate for the reproduction of $v-$velocity fields, while for $u-$ and $w-$components only the horizontal resolution of 16m is sufficiently fine. In terms of profiles peaks all the nine simulations are within the range suggested by previous studies (e.g. Grant, 1992, and

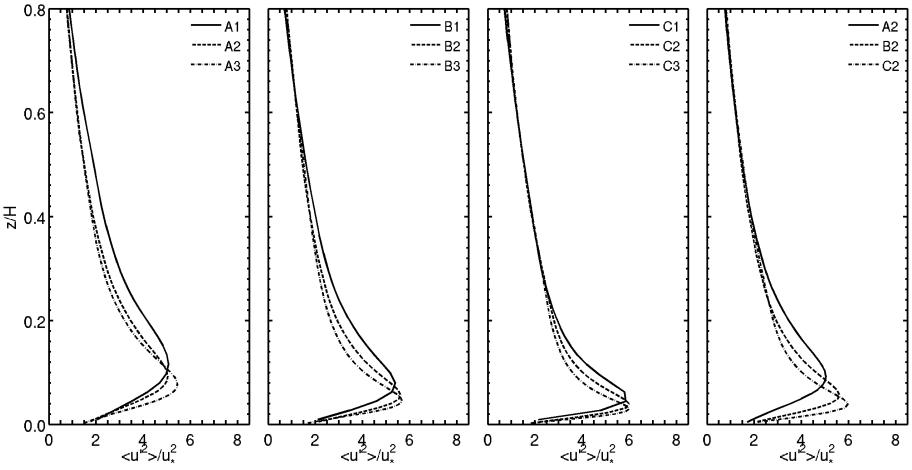

Figure 6.5: Vertical profile of time- and plane-averaged resolved variance of $u-$velocity component normalized by the surface friction velocity u_* in function of dimensionless height z/H.

references therein) for the $u-$component, i.e. $5-7$. The minimum value of the peak is nearly 5.5 in $A1$ and the maximum peak is about 6 in $B2$, $B3$, $C1$, $C2$. Instead, the peaks of the dimensionless variance of the $v-$component are sensibly lower than the reference range of $3-4$, with the maximum peak of $C3$ equal to 1.5. Also the dimensionless variance peak of the $w-$component tends to be lower than the expected range of $1-2$, with only $B3$, $C2$ and $C3$ reaching the value of 1.

The general impact of the grid refinement on the vertical profiles of velocity variances here observed is similar to that reported in Kirkil et al. (2012) for the adoption of less dissipative and more complex SGS models than the standard Smagorinsky (1963) and Deardorff (1980) schemes. This fact suggests that the shortcomings of the Deardorff (1980) SGS model here used, in particular its over-dissipative nature, can be mitigated by adopting finer computational grids.

6.2.3 Spectral analysis

Velocity spectra can be considered the most significant instruments for LES evaluation, giving indications about the consistency of a certain turbulence reproduction, obtained with a specific code and setup, with the state-of-the-art understanding of turbulence dynamics (Gibbs and Fedorovich, 2014a). In fact velocity spectra should show both the

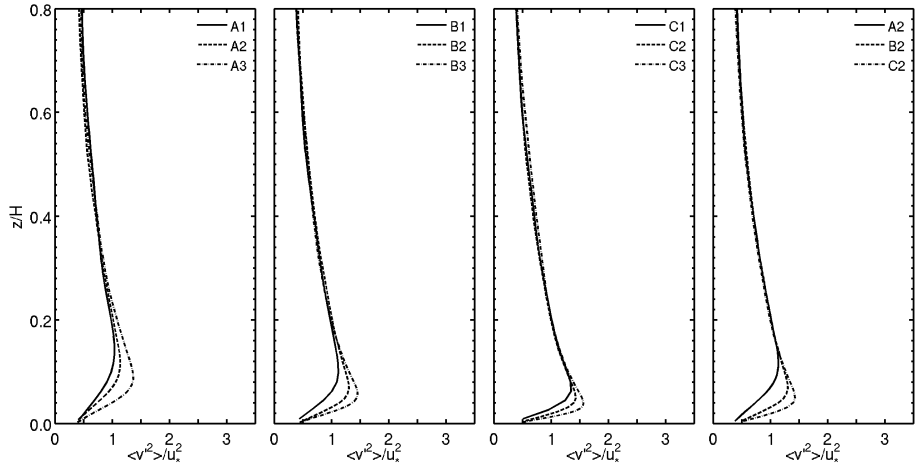

Figure 6.6: Vertical profile of time- and plane-averaged resolved variance of $v-$component normalized by the surface friction velocity u_* in function of dimensionless height z/H.

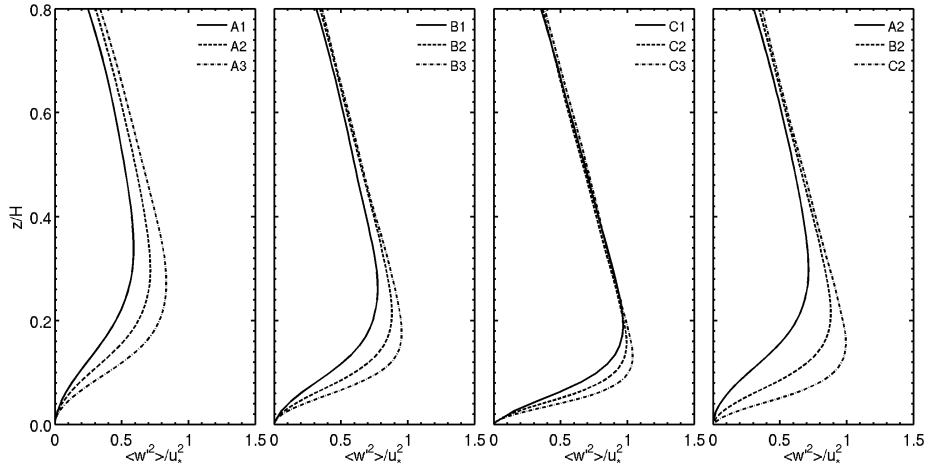

Figure 6.7: Vertical profile of time- and plane-averaged resolved variance of $w-$component normalized by the surface friction velocity u_* in function of dimensionless height z/H.

range of the energy production scales, i.e. a peak of the spectral energy at low wavenumbers, and part of the inertial range. The inertial range corresponds to a slope of $-2/3$ when plotting the compensated spectra on a log-log scale (Mirocha et al., 2010). Compensated spectra relate the product of the power spectral density Φ and the wavenumber k to the wavenumber itself. In this Section we show compensated velocity spectra for the vertical and horizontal (only u-component) velocity plotted on a log-log scale. The aim id to further investigate the ability of the code in performing LES of the neutral ABL and also to assess the adequacy of each single computational grid. The spectra are computed along the x-direction at each y grid point and at every time-step. Subsequently they are averaged over the xy-plane and lastly over time. They are computed at the dimensionless heights $z/H = 0.04$ and $z/H = 0.12$, with the latter being more interesting, because at this height the turbulence is still influenced by the presence of the surface but it is sufficiently above it to have a significant part of the stress resolved (see Figure 6.2).

Figure 6.8 shows compensated spectra of the $u-$velocity component along the $x-$direction. It can be seen that the coarsest horizontal grid spacing ($\Delta x = 64$ m, corresponding to simulations of group A) produces spectra that totally lack the inertial subrange at both the examined heights. Therefore there is a direct passage from production to dissipation, with the extreme case of simulation $A1$ (coarsest horizontal and vertical grid spacings; $\Delta x = 64$ m and $\Delta z = 16$ m) where also a peak at low wavenumbers that should indicate energy production is not present. In general the production peak in the $u-$component spectra computed along the $x-$direction is not clearly visible, and this is to be attributed to the fact that many SGS models, including the 1.5-order-of-closure here used (Deardorff, 1980), tend to generate elongated correlations in the streamwise direction (here the $x-$direction) near the surface (Mirocha et al., 2010). The grid refinement mainly causes an extension of the inertial subrange, with the dissipation starting at higher wavenumbers, and an increase of the reproduced turbulent kinetic energy. The inertial subrange is clearly marked only in simulations of group C (the finest horizontal grid spacing, $\Delta x = 16$ m). Greater impact is obtained by refining the horizontal grid spacing, indicating that in the examined meshes it is the limiting factor, as it has been already noticed in Section 6.2.2. Both Δx and Δz reduction is more effective closer to the surface (spectra at $z/H = 0.04$), namely where the turbulence scale is smaller and therefore a greater

resolution is required in order to explicitly reproduce it. Another important effect of grid refinement is the kinetic energy redistribution from larger- to smaller-scales, meaning that the unrealistic highly correlated structures in the streamwise direction, that will be discussed in Section 6.2.4, are correctly weakened. Figure 6.9 shows compensated spectra of the $w-$velocity component along the $x-$direction. The inadequacy of the coarsest horizontal grid resolution ($\Delta x = 64$ m, runs of group A) is here less evident that in spectra of the $u-$component (see first panel in Figure 6.8). In fact a hint of inertial subrange is present even in simulations $A2$ and $A3$, with only run $A1$ missing it. In addition the low wavenumber peak of energy production is present even in this latter. But in general the peak is significantly more pronounced in all the spectra in respect to those of the $u-$velocity component, and this is related to the shorter integral length scale of the $w-$velocity turbulent structures. Increasing the spatial resolution of the computational grid causes the shift of the peak towards higher wavenumbers, indicating again a sort of energy redistribution to smaller-scales, and at the same time slightly extend the inertial subrange. Even in these spectra the strongest effect of grid refinement is closer to the surface, and the impact of reducing Δx is greater than diminishing Δz, adding a significant amount of resolved kinetic energy at almost all the scales of turbulence (see fourth panel in Figure 6.9).

6.2.4 Flow visualization

In order to further understand the abilities and deficiencies of RAMS-LES and especially the role of grid spacings, instantaneous $u-$velocity fields in horizontal planes are shown at the same dimensionless heights at which velocity spectra are computed. Figures 6.10 and 6.11 show the nine instantaneous $u-$velocity fields corresponding to the nine examined computational grids, at the dimensionless height $z/H = 0.04$ and $z/H = 0.12$ respectively. The figures are organized with the velocity fields from run $A1$, $A2$ and $A3$ on the upper row; $B1$, $B2$ and $B3$ on the second row; and $C1$, $C2$ and $C3$ on the third row. Therefore vertical grid resolution increases from left to right and the horizontal one from top to bottom.

Both Figures show the typical streaky structures that characterize the pure shear ABL flow in proximity of the surface. These streaks are known to be present in all the three velocity component fields and also in that of the vertical momentum flux $< u'w' >$, but they are stronger

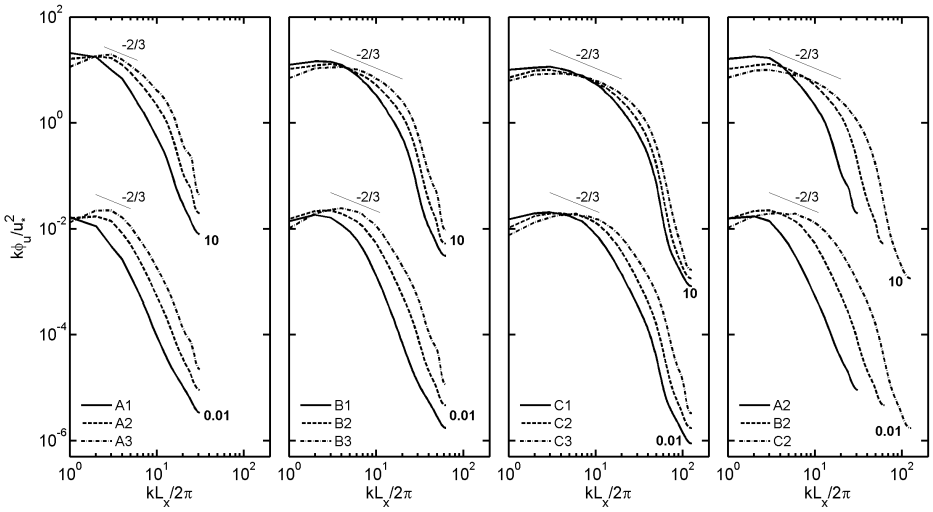

Figure 6.8: Time- and plane-averaged velocity spectra for $u-$component along the $x-$direction. The group of spectra in the top and bottom of each plot are referred to dimensionless height $z/H = 0.12, 0.04$ respectively. Spectral amplitudes in each group are multiplied by the numerical factor on the right-hand side of the plot.

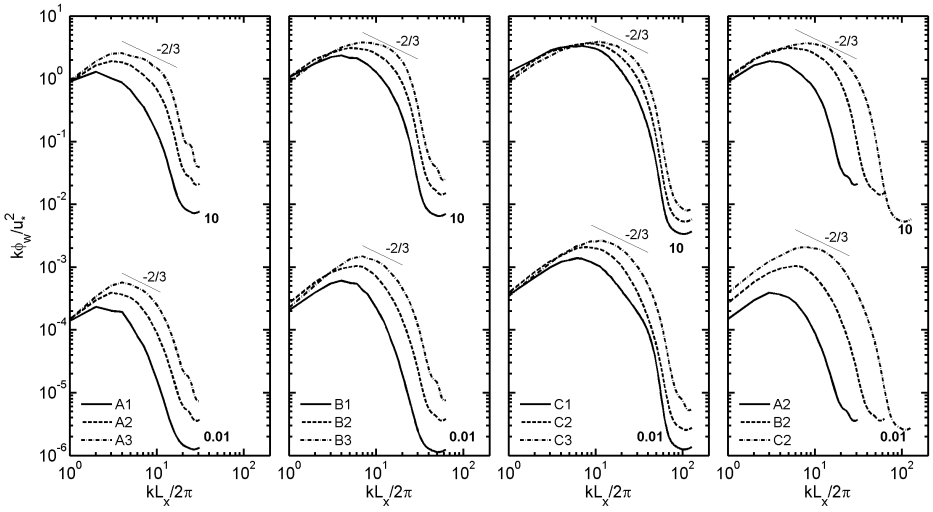

Figure 6.9: Time- and plane-averaged velocity spectra for $w-$component along the $x-$direction. The group of spectra in the top and bottom of each plot are referred to dimensionless height $z/H = 0.12, 0.04$ respectively. Spectral amplitudes in each group are multiplied by the numerical factor on the right-hand side of the plot.

in the field of $u-$velocity component (Moeng and Sullivan, 1994), with a sharp alternation of high-low velocity. Here we show only fields of $u-$velocity for this reason. The turbulent structures are roughly aligned with the mean flow direction, that near the surface is rotated in respect to the direction of the geostrophic wind, that is imposed along the $x-$direction (see Section 6.1), because of the friction with the earth surface. The shear-induced rotation diminishes as increasing z, and the streaky structures are gradually replaced by less coherent eddies and usually are no more present at $z/H = 0.5$ (Moeng and Sullivan, 1994). Even confronting the streaks alignment in Figure 6.10 and 6.11 it can be seen a slight decrease of the rotation, although they are both close to the surface, at $z/H = 0.04$ and $z/H = 0.12$ respectively. The coarser computational grids produce very long highly correlated structures with well defined boundaries, while smaller-scale eddies are almost absent (see for instance runs $A1$, $A2$, $B1$). These elongated streaks are the reason for the absence of a production peak in the $u-$component spectra that has been observed in the previous section. This fact is due to the well known over-dissipative nature of the SGS model here employed (1.5-order-of-closure TKE scheme by Deardorff (1980)), that drains too much energy from the smaller-scale structures, allowing the unrealistic formation of very long streaks (Kirkil et al., 2012). In fact, at heights near to the surface as those here examined, the SGS model has a great influence on the nature of the reproduced turbulence and, when an over-dissipative scheme is employed, as the standard Smagorinsky (1963) or the just mentioned model byDeardorff (1980), too long and too highly correlated streaks are commonly observed in LES results (e.g. Ludwig et al., 2009; Mirocha et al., 2010). A refinement in the grid spacing, horizontal and/or vertical, causes a reduction in the streaks size and coherence and the appearance of more convoluted and intricate interfaces (see for instance runs $B3$, $C2$, $C3$), making the simulated flow field more similar to observations (Hutchins and Marusic, 2007), Direct Numerical Simulations and LESs where more complex and less dissipative SGS schemes are used (Mirocha et al., 2010; Kirkil et al., 2012). Therefore, as previously observed in Section 6.2.2 for velocity variance profiles, it is possible to mitigate the over-dissipative nature of the Deardorff SGS scheme, and to generate results comparable with those obtained with more complex SGS models, by sufficiently refining the computational grid. The high sensitivity of turbulence reconstruction to the computational grid is clearly visible in the instantaneous flow fields here shown, but it has been already

revealed by the velocity spectra of Section 6.2.3. Now it is possible to associate the previously discussed extension of the inertial subrange and energy redistribution from larger- to smaller-scale eddies with the radical transformation of the simulated turbulent structures. Moreover the fundamental importance of adopting a suitable mesh in LES of the neutral ABL can be fully appreciated.

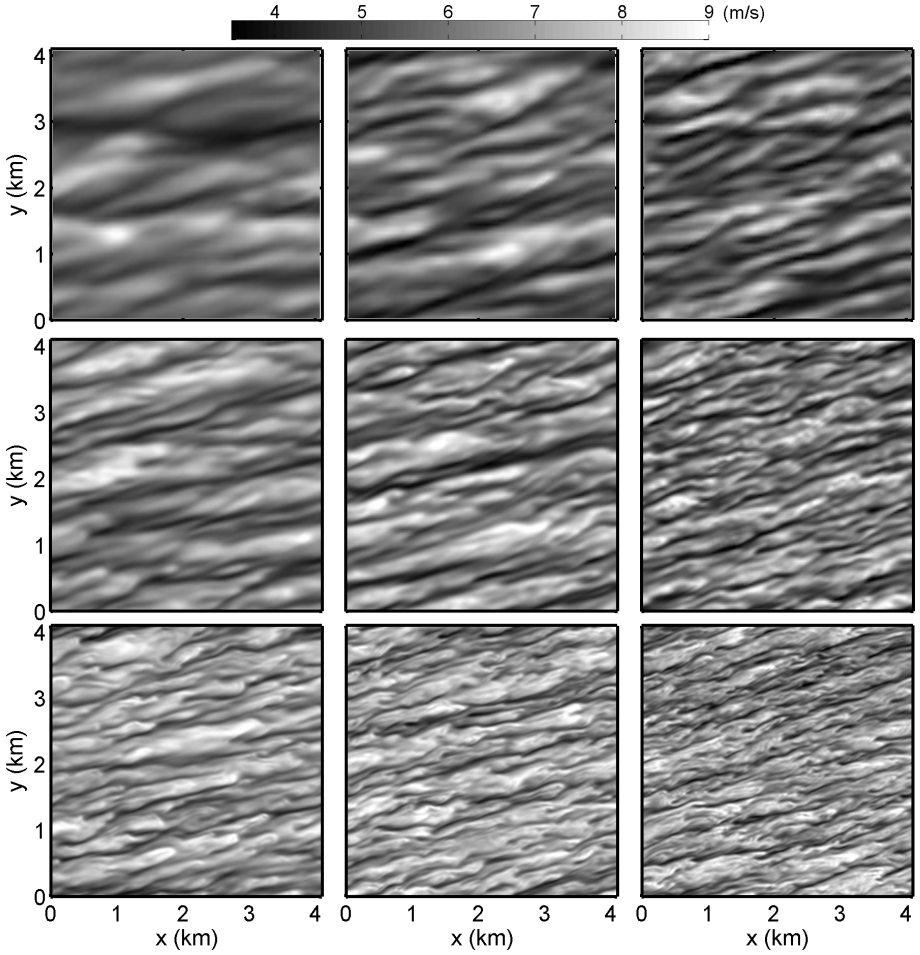

Figure 6.10: Visualization of the instantaneous velocity field for $u-$component in the $xy-$plane at dimensionless height $z/H = 0.04$. Starting from the top left plot and going toward right along rows, velocity fields belong to runs $A1$, $A2$, $A3$, $B1$, $B2$, $B3$, $C1$, $C2$, $C3$.

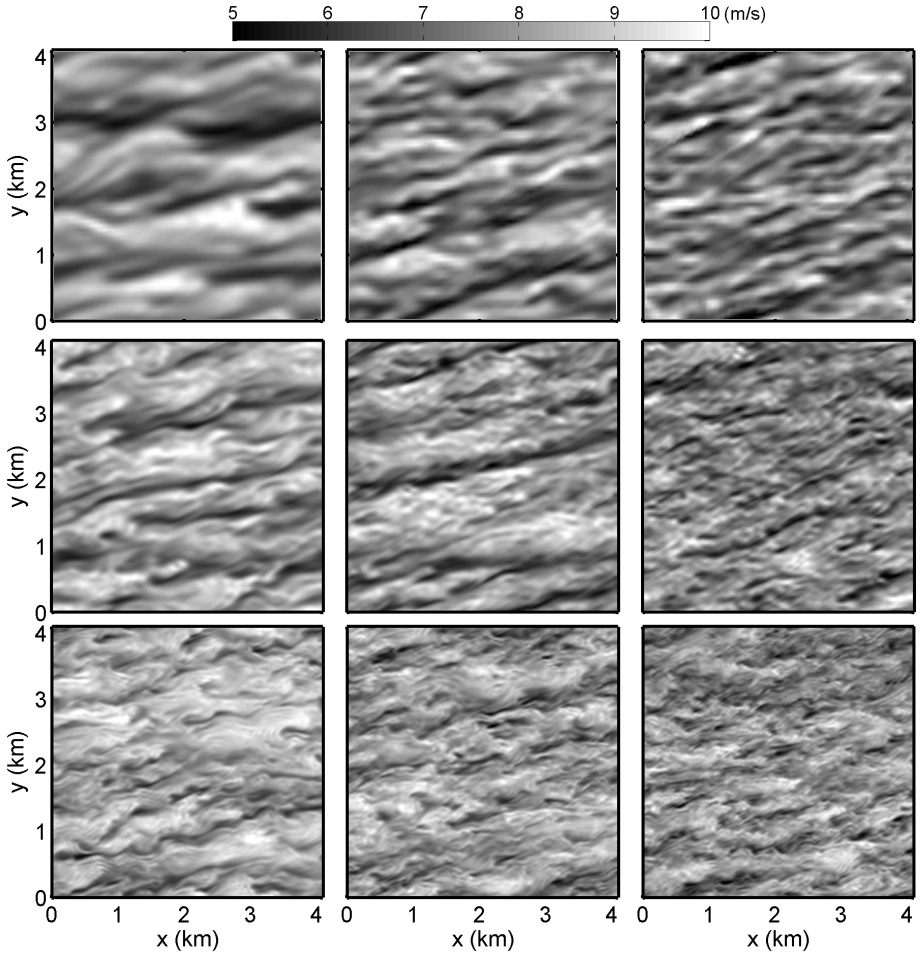

Figure 6.11: Visualization of the instantaneous velocity field for $u-$component in the $xy-$plane at dimensionless height $z/H = 0.12$. Starting from the top left plot and going toward right along rows, velocity fields belong to runs $A1$, $A2$, $A3$, $B1$, $B2$, $B3$, $C1$, $C2$, $C3$.

6.3 Conclusions

The capability of RAMS-LES to simulate the dry neutral atmospheric boundary layer and the impact that grid spacing has on the quality of the results have been here evaluated. Nine simulations have been performed on a fixed computational domain with an identical setup, but with different computational grids. The nine examined meshes have been obtained by the combination of three different horizontal, $\Delta x = 64, 32, 16$ m, and vertical resolutions, $\Delta z = 16, 8, 4$ m. An idealized neutral regime (a steady state ABL over an infinite, flat and homogeneous surface forced by a constant geostrophic wind and without surface heating) has been simulated, and the results have been compared with theoretical expectations and previous LESs. In particular the following turbulent statistics and flow analysis have been computed and discussed: mean profiles of horizontal velocity, of momentum flux and of velocity variances, velocity spectra and flow visualization.

In terms of vertical-streamwise stress all the nine examined computational grid generate profiles with most of the stress resolved, suggesting a possible adequacy of even the coarsest grid spacings. The resolved contribution correctly increases, and the SGS one correctly decreases, as the grid spacing is refined. A more accurate reproduction of the near surface turbulence is pointed out by the height at which the resolved component starts to decrease approaching the surface. This effect can be achieved by refining both the vertical and horizontal resolution. But a deviation from the expected linear profile for the total stress is observed close to the surface, suggesting that the SGS model overestimates the stress in proximity of the wall, in particular for higher resolution simulations (group C).

Vertical profiles of time- and plane-averaged horizontal velocity module and of the dimensionless shear Φ_m reveal that RAMS-LES suffers the longstanding problem of the LOWT mismatch and that grid refinement can mitigate but not eliminate it. In fact, the tendency of underestimating the wind speed immediately above the surface and to recover this deficit aloft remains in all the runs, but its intensity changes in function of the computational grid. A major role for the grid aspect ratio have been identified and the best agreement between the simulated and similarity profile is obtained with an aspect ratio equal to 4 for all the three groups of simulations.

In terms of velocity variance vertical profiles, RAMS-LES reproduces the general shapes shown in previous studies, but tends to un-

derestimate the variance peaks for $v-$ and $w-$velocity variance, while for the $u-$component it gives peaks in the expected range. The general effect of refining the computational grid resolutions is the same for all the three velocity components and consists in an increase of the variance peak and its displacement towards the surface. A similar effect has been obtained in other studies by adopting less dissipative and more complex SGS schemes. This suggests that the shortcomings of the Deardorff scheme here used can be mitigated if a sufficiently fine computational grid is adopted. A greater impact is obtained by diminishing the horizontal grid spacing, with Δz influence decreasing as Δx is refined, revealing that in the examined meshes the limiting factor is the horizontal resolution.

Velocity spectra have confirmed this latter observation, and added more detailed information about grid spacing role and mesh adequacy. In particular the coarsest examined horizontal resolution has resulted to be insufficient, producing spectra that completely miss the inertial subrange. The main effects of grid refinement are the extension of the inertial subrange, the increase of the simulated kinetic energy and also an energy redistribution from larger- to smaller-scale turbulent structures. In fact the Deardorff SGS model here used tends to generate too long and highly correlated streaky structures in proximity of the surface because of its over-dissipative nature, but the grid refinement mitigates this shortcoming as suggested by velocity spectra and clearly shown in velocity fields visualization. Results from higher resolution grids present shorter and less coherent structures, with more convoluted and intricate interfaces while when the mesh is too coarse smaller-scale eddies are almost absent and the boundaries of the large streaks are too well defined.

From the performed analysis it is possible to conclude that RAMS-LES can reach a good level of turbulence reproduction even in neutral ABL if an adequate computational grid is used. In particular it has been found that the horizontal resolution starts to be sufficiently fine at about 30 m and that the best performances in the surface layer are obtained with an aspect ratio of 4. This means that an intermediate level of grid anisotropy is required, coherently with the fact that the typical turbulent structures of this regime are elongated in the mean flow direction in proximity of the surface. But even with the suggested grid aspect ratio some deficiencies have been evidenced near the wall. In fact the over-dissipative nature of the SGS model used by RAMS-LES (i.e. the 1.5-order-of-closure TKE scheme by Deardorff (1980))

negatively conditions the flow when the resolved contribution becomes minor, resulting into the above-discussed issues. But it has been shown that it is possible to mitigate these problems and to generate results comparable with those obtained with more complex SGS schemes by sufficiently refining the computational grid. Therefore the adoption of an adequate mesh is fundamental for RAMS-LES in order to correctly simulate the neutral ABL, with the quality and the characteristics of the reproduced turbulence being strongly influenced by it, in great part because of the used SGS model.

Part III

RAMS-LES coupled with a land-surface model: application to a real case

7

Coupled model comparison with measurements

After the extensive evaluation of RAMS-LES capabilities in reproducing ABL turbulence in idealized regimes provided in Chapter 5 and 6, we now investigate its performances in simulating ABL evolution and land-atmosphere interactions when coupled with a Land Surface Model (LSM) and used in real conditions. In fact, as discussed in Section 3.3, the crucial feedback that exist between the land surface and the ABL (Garratt, 1994; Stull, 1988; Huang and Margulis, 2010) can be simulated by dynamically computing the surface heat fluxes that force the ABL evolution on the basis of the ABL turbulence itself. Therefore lower boundary conditions for sensible and latent heat fluxes are no more imposed *a priori* as in the simulations performed in Chapter 5 and 6, but computed by a LSM at each time step in function of the simulated turbulence. The inclusion of the fundamental feedback mechanism existing between the land surface and the overlaying atmosphere enhances the simulation adherence to the reality. But at the same time additional uncertainty associated with the representation of land and interface processes is introduced in the simulation (Avissar et al., 1998), increasing the complexity of the modelling framework and also of the results interpretation. Therefore the evaluation of the coupled LES-LSM model capability of reproducing a diurnal cycle of ABL evolution and land-atmosphere interactions represents a crucial point in its application for practical purposes such as a support in measurements interpretation (e.g Huang et al., 2008b; Bertoldi et al., 2013) or the assessment of surface heterogeneity impact on ABL (e.g. Courault et al., 2007; Huang and Margulis, 2012).

Here we assess such capability by performing a coupled simulation in real conditions and by comparing model predictions with observations of significant quantities as surface fluxes and micrometeorological states. For this evaluation we refer to the experimental field campaign REFLEX 2012 (Timmermans et al., 2014; Tol et al., 2014), which lasted from July, $18th$ to July, $28th$ in 2012 and took place in the experimental site of Barrax (Albacete, Spain). RAMS-LES is here coupled with its native land surface model, i.e. LEAF3 (Land-Ecosystem-Atmosphere Feedback version 3), that is a dual source, multiple soil and resistance levels scheme. This fact increases the value of the coupled model evaluation, since also LEAF3, as RAMS itself, is designed to work mainly at the mesoscale, and therefore its performances should be carefully assessed when employed at the microscale. At the same time it is important to proceed with the awareness that a complete evaluation of a couped LES-LSM is almost unfeasible, since high resolution spatial and temporal measurements should be available for wind speed, air temperature, scalars in the ABL and also for surface fluxes and large scale atmospheric conditions (Avissar et al., 1998). Therefore specific experimental campaigns should be realized for this aim, but even non-specific campaigns such as REFLEX 2012 can be used to generally assess if the coupled model is able to reproduce spatial and temporal variations of ABL and air-surface interface quantities and phenomena. In fact, quoting Shao et al. (2013), the value of a large-eddy simulation atmospheric-land-surface model does not lie in the quantitative accuracy of the model simulation for specific cases, but in its application to generate understanding of atmospheric-land-surface interactions that are difficult to observe through experiments, and to support the interpretations of the observations. Hence what we should verify is the capability of the coupled model to face non-stationary turbulence, to correctly reproduce the time evolution of typical quantities during a diurnal cycle, to deal with a spatially heterogeneous surface in terms of both reproduction of the lower boundary conditions spatial pattern and impact on the overlaying air.

The chapter is organized as follows. In Section 7.1 preliminary analysis aimed at designing the LES experiment are performed. Details about the coupled simulation setup are provided in Section 7.2, and the comparison between model predictions and experimental observations are discussed in Section 7.3. Finally conclusions are presented in Section 7.4.

7.1 LES design

Before performing the coupled simulation that should reproduce ABL turbulence and surface-atmosphere interactions in real conditions during a full diurnal cycle, it is important to identify a setup for LES that is suitable for the turbulence that we are going to simulate but that at the same time minimizes the computational cost. The main question that should be addressed when setting up a LES of the ABL is: are the domain extent and the grid spacing adequate for the simulated turbulence? Uncoupled homogeneous LES of stationary turbulence are used to face these issues although the LES that we need to design should reproduce a diurnal cycle of the ABL in presence of different surface patches, and hence turbulence is not stationary and surface characteristics are not homogeneous. In fact, as explained in detail in Section 3.3 and 3.4, idealized simulations allow a better quality check on results than realistic simulations, since theoretical expectations about turbulence statistics and other similar LES experiments are available for these regimes. However, the idealized simulations must be representative for the real one that we finally want to setup. To this aim the turbulence forcings and the ABL height to be used in the stationary simulations are recovered from the available measurements. In particular the simulation is started with the potential temperature profile measured at $12:00$ UTC on July, $26th$ in Murcia. It should provide a good approximation of the maximum ABL height in the area of inter-

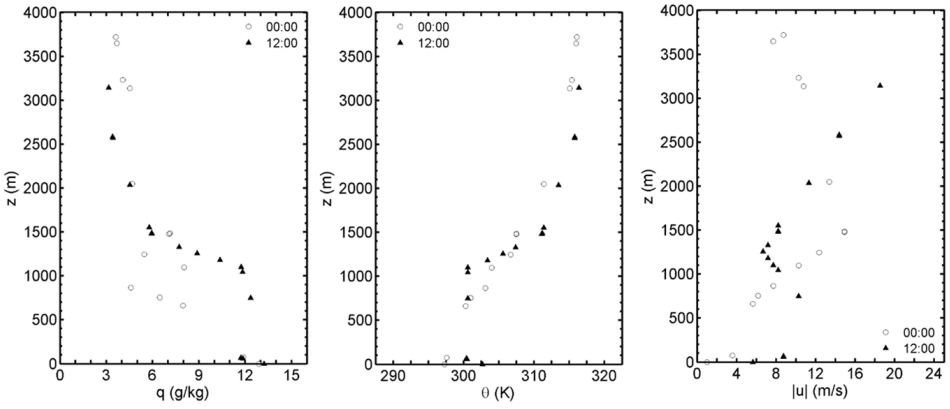

Figure 7.1: Soundings of water vapour mixing ratio, potential temperature and wind speed in Murcia on July, 26th. Open circles are for 00:00 UTC measurements; solid triangles are for 12:00 UTC measurements.

est for the simulated day, i.e. July, 26th. In fact, as described in the appendix of this chapter (Section 7.5), the field campaign we refer to for this experiment (Timmermans et al., 2014) did not include atmospheric soundings and hence the two nearest airport soundings, from Murcia and Madrid, are the reference for atmospheric conditions. Murcia soundings are more representative for the area of interest when the wind is mainly from south-east as in the simulated day (Timmermans et al., 2014). The potential temperature profile is shown in the second panel of Figure 7.1 and it is plotted with solid triangles (open circles are for profiles measured at 00 : 00 UTC of the same day). It presents the shape that is typical for a fully developed convective boundary layer, with almost constant potential temperature in the mixed layer from the surface till a capping inversion of about 12.5 K in 300 m, identifying the CBL height of about 1200 m, and an overlying weaker stable lapse rate in the free atmosphere out of the ABL. The initial profile of air humidity is posed equal to the water vapour mixing ratio sounding shown in the first panel of Figure 7.1. The turbulence forcings in a windy sunny day, as the one to be simulated, are the geostrophic wind and the surface sensible heat flux. The first one is taken equal to the wind measured by Murcia soundings at 12 : 00 UTC and shown in the third panel of Figure 7.1, while the second one is re-

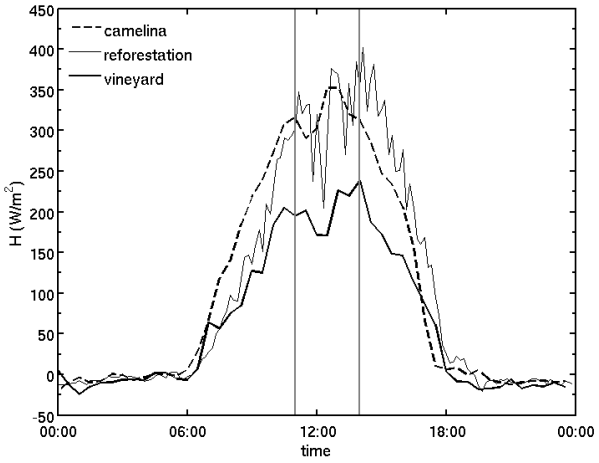

Figure 7.2: Time series of surface sensible heat flux at the three eddy covariance stations available in the area. Vertical gray lines delimit the time interval (11:00-14:00 UTC) from which the time- and space-averaged surface sensible heat flux used in homogeneous and stationary simulations is obtained.

covered by the eddy covariance measurements of surface sensible heat flux (H) available for the area of interest (Tol et al., 2014). The three eddy covariance stations data for the day to be simulated (July, $26th$) are reported in Figure 7.2. In order to perform a homogeneous and stationary LES a time- and space-constant value of H must be used. This value is taken equal to the time- and space-average of the eddy measurements in the time interval from 11 : 00 to 14 : 00 UTC, namely about 280 Wm^{-2}. The simulation setup is completed by the adoption of periodicity at the lateral boundaries and a rigid lid for the domain top, the inclusion of Coriolis effect, a homogeneous surface roughness length $z_0 = 0.007$ m and the 1.5-order-of-closure SGS scheme by Deardorff (1980) (see Section 3.2.1). The duration of the experiment is 90 minutes for turbulence spinup and 60 minutes for data collection in steady conditions. This duration has been seen to be longer enough for turbulence development in strong convective conditions as those here used (see Section 5.3), and at the same time not too long in respect to the imposed capping inversion that should maintain CBL height almost constant during the data collection interval. A vertical domain extent of 2 km is selected on the basis of the mixed layer height of 1.2 km in the potential temperature initial profile, while two possibilities are examined for the horizontal extent. The first one is 3×3.5 km, including only the area directly involved in the field campaign, and the second one is 6×6 km, taking into account recommendations about horizontal domain extension in respect to the CBL height (Schmidt and Schumann, 1989). The computational grid is designed following the guidelines defined in Chapter 5, and therefore 30 m in the horizontal and 10 m in the vertical with an aspect ratio of 3 are used.

In order to address the question whether the domain is large enough in respect to the simulated turbulence, the two simulations results are post-processed in terms of spatial correlation. Instead the grid resolution adequacy is verified through velocity spectra. When periodicity is adopted at the lateral boundaries, the horizontal extent of the domain should be large enough to contain more than one of the longest turbulent structures present in the flow. A typical way to check this requirement is to verify if the spatial correlation of the three velocity components vanishes within one half of the domain (Nakanish, 2001). Figure 7.3 shows the two points spatial autocorrelation for the velocity components along $x-$ and $y-$ directions for the smaller (panel a.) and larger (panel b.) domain simulations in the middle of the ABL.

Black lines refers to correlations along the $x-$direction, while gray lines are for the $y-$direction. Solid lines are for the $u-$velocity component, dashed lines for the $v-$component and lastly dash-dot lines are for the $w-$component. The two points spatial autocorrelation ρ for a generic variable X is computed as

$$\rho(d) = \frac{\sum_{i=1}^{N}(X_i - \mu_x)(X_{i+d} - \mu_x)}{\sum_{i=1}^{N}(X_i - \mu_x)^2} \tag{7.1}$$

where μ_x is the average value of the spatial signal of X in the direction along which ρ is computed, d is the distance at which the autocorrelation refers and hence the distance between the two considered points and N is the number of grid points in the direction of computation. When the autocorrelation refers to the $x-$direction ($y-$direction), (7.1) is used at each y (x) grid point and at every time step. Subsequently the values are averaged over the $y-$direction ($x-$direction) and lastly over time. Figure 7.3.a shows that the smaller domain of 3×3.5 km could not be large enough for the simulation. In fact the autocorrelation for $w-$velocity along the $x-$direction has just settled down to its minimum value at one half of the domain (i.e. 1500 m along x), indicating that only one largest turbulent structure can be

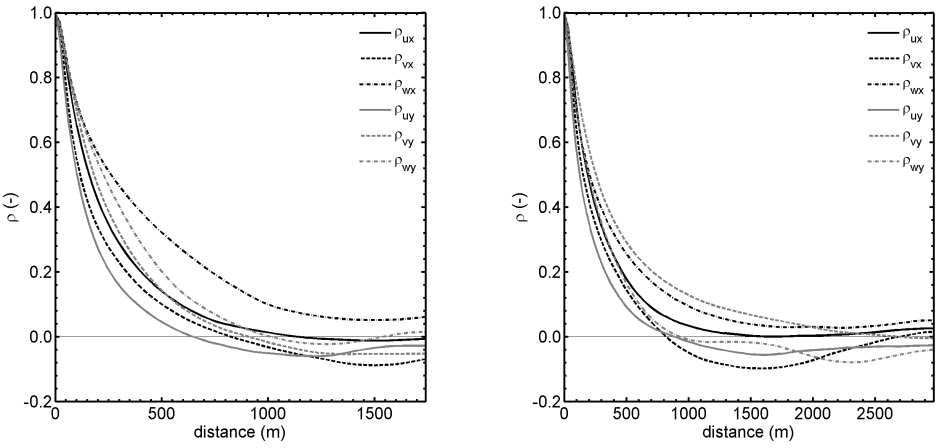

a. Small domain b. Large domain

Figure 7.3: Two points spatial autocorrelation of $u-$, $v-$ and $w-$velocity component along $x-$ and $y-$direction in the middle of the ABL. Panel a. refers to a horizontal domain extent of 3×3.5 km and panel b. refers to a horizontal domain extent of 6×6 km.

contained in one half of the domain. The autocorrelation of the other velocity components goes to zero more rapidly and the domain could be considered large enough for them, especially in the $y-$direction. Figure 7.3.b confirms that, as it can be supposed from the considered ABL height and literature recommendations (Schmidt and Schumann, 1989), the larger domain extent of 6×6 km is sufficient for the simulated turbulence. In fact the autocorrelations vanish significantly before the middle of the domain for all the three velocity components and along both $x-$ and $y-$direction. Figure 7.4 shows compensated spectra (the power spectral density Φ multiplied by the wavenumber k in function of the wavenumber itself) for all the three velocity components along both $x-$ and $y-$direction in a log-log scale. Spectra are presented in dimensionless form, using the convective velocity w_* (see Section 2.4) and the domain length L as scaling quantities. They are averaged over space and time following the procedure described in Section 5.3.3. Plots in the first line of the Figure are for spectra computed along the $x-$direction, while those in the second line refer to the $y-$direction. From left to right spectra are for $u-$, $v-$ and $w-$velocity components respectively. Solid line refer to the smaller domain of 3×3.5 km and dashed line to the larger extent of 6×6 km. They are computed in the middle of the simulated ABL. Being the grid resolution the same in the two simulations, few differences can be identified between the two group of spectra. But some modifications at small wavenumbers (i.e. larger-scale structures) are present in spectra computed along the $x-$direction, suggesting that passing from a x-length of the domain of 3 km to one of 6 km has an impact on the turbulent structures of the flow, especially for $v-$ and $w-$velocity fields. In fact the spectra are more energetic, which could mean that the flow enriches in turbulent eddies when a larger extent is used. In terms of inertial subrange reproduction (signaled by the $-2/3$ slope in compensated spectra) and energy dissipation both the simulations generate acceptable results, with better performances (i.e. longer inertial subrange) along the $y-$direction. This could be explained by the fact that the geostrophic wind acts mostly along $x-$direction, and hence turbulent structures are deformed especially in this direction in respect to the typical convective plumes, and it has been previously shown that RAMS-LES has better performance in free-convection than in pure shear conditions (see Chapter 5 and 6).

In conclusion this preliminary analysis about LES design has evidenced that the smaller tested domain (3×3.5 km) could be insufficient

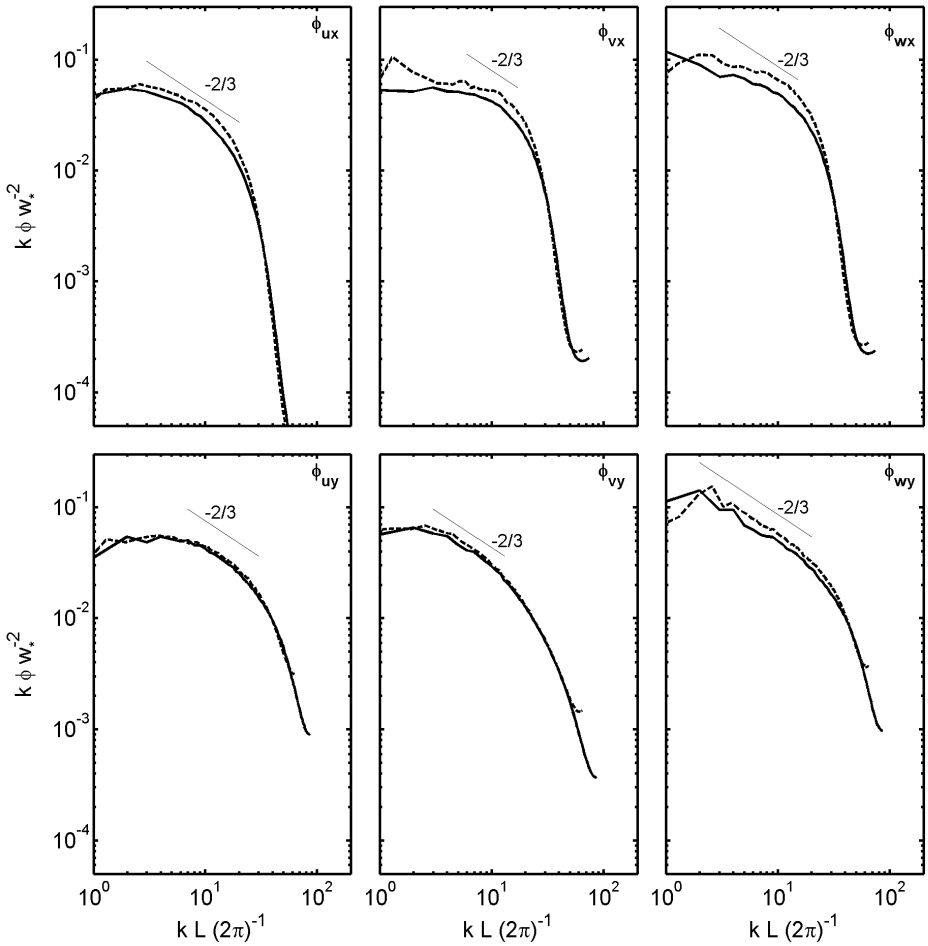

Figure 7.4: Time- and plane-averaged compensated velocity spectra for $u-$, $v-$ and $w-$velocity components computed along $x-$ (first line of the figure) and $y-$direction (second line of the figure) in the middle of the ABL. Solid (dashed) line refers to the simulation with the horizontal domain extent of 3×3.5 km (6×6 km).

for the simulated turbulence and therefore the larger one (6×6 km) will be used hereafter for simulations in real conditions. The too limited extension of the smaller domain has been evidenced by both the spatial autocorrelation of the velocity fields, with ρ_{wx} remaining too correlated at one half of the domain, and the spectral analysis, which has showed a sensitivity to the domain extent along the $x-$direction, suggesting that 3 km could limit a correct turbulence development. In addition, adopting a domain that is larger than the area of interest mitigates the impact that periodic lateral boundary conditions can have on the results in presence of surface heterogeneity, as it will be in the realistic coupled simulation. In fact, we are adding a buffer area surrounding that of interest that should make the flow becoming coherent with the real upwind characteristics of the surface when reaching the central part of the domain, namely the part of interest.

7.2 Experiment setup

In order to verify the capability of the coupled model RAMS-LES - LSM to reproduce ABL turbulence and land-atmosphere interactions in real conditions, a diurnal cycle of the ABL evolution in a specific real site is simulated. Then model results are compared with field measurements of significant quantities. As already mentioned, for this evaluation we refer to the experimental field campaign REFLEX 2012 (Timmermans et al., 2014; Tol et al., 2014), which lasted from July, $18th$ to July, $28th$ in 2012 and took place in the experimental site of Barrax (Albacete, Spain). A detailed description of the site and of the measurements is provided in the appendix of this chapter(Section 7.5). Here we summarize only the characteristics that make the site suitable for a coupled LES-LSM evaluation in real conditions. The area is agricultural with both irrigated and non-irrigated patches, various kinds of cultivations (e.g. maize, poppy, grapevine, sunflower, trees) and bare soil. This fact allows the coupled model evaluation under different conditions (wet and dry soil) and with or without the interaction with the vegetation, making the case study an interesting test. But the two characteristics that are fundamental for a significant evaluation of the coupled model are the flatness of the area and the fact that the water table depth was about $20 - 30$ m during the field campaign. In fact topography effects on ABL turbulence add uncertainty to the LES and the LSM used in the coupling does not include in-

teractions with the groundwater. In addition the REFLEX campaign provides several measurements for the area, namely airborne remote sensing measurements in both visible and infrared bands, eddy covariance, micrometeorological and biophysical ground measurements, that allow both a detailed setting of the LSM and a valuable check of the results.

For the simulation July, $26th$ is selected, since it was a clear sunny day for which airborne measurements are available for both the morning and the previous night. LEAF3, the LSM here used, requires several surface and vegetation parameters as input (see Section 4.3 for a description of the land surface scheme). In particular, it asks for albedo, LAI (Leaf Area Index), vegetation fraction, surface roughness length, emissivity, minimum stomatal resistance, vegetation roots depth and height. The model is designed to receive these inputs in function of a land surface classification already included in the code, but since it is thought to work at the mesoscale the classes and the corresponding values of the parameters are not representative for the case study. Consequently we have modified the code in order to use self-defined classes and parameters. The land use classification for the area of interest has been recovered from airborne remote sensing data and it is shown in Figure 7.5. The classes that have been identified and the corresponding values for the parameters required by LEAF3 are listed in table 7.1. The values of the parameters are from the literature, with the exception of vegetation height h_v, for which some spot measurements from the experimental campaign are used, and the roughness length, that is estimated with the rule of thumb $z_0 = 0.1h_v$ and partially calibrated with a trial and error procedure that required several simulations and therefore considerable computational time. In the map of Figure 7.5 the position of the ground measurements stations is also provided, with eddy towers present in camelina, reforestation and vineyard fields and micrometeorological stations in grass and alfalfa fields. A classification that groups in the same class fields with similar spectral properties have been realized. For instance camelina fields have been inserted into the generic class *stubble*, since the vegetation was dead and partially harvested at the time of the experimental campaign. Similarly no distinction has been made between alfalfa and grass. Instead albedo, LAI and vegetation fraction have been directly obtained from airborne visible remote sensing data, and therefore detailed maps for the area of interest are available (see Figure 7.6). This fact leads to a less uncertain and more detailed description of the area

Class	Description	z_0 (m)	ϵ (-)	$r_{c\ min}$ (sm^{-1})	d_r (m)	h_v (m)
01	vineyard	0.005	0.96	200	0.7	1.8
02	stubble	0.070	0.95	50	0.2	0.3
03	reforestation	0.150	0.95	200	1.0	1.0
04	grass	0.020	0.96	100	0.7	0.3
05	buildings	0.600	0.90	–	–	6.0
06	crop	0.040	0.95	150	1.0	0.4
07	water	0.0001	0.00	–	–	–
08	trees	0.300	0.95	300	1.5	3.0
09	poppy	0.080	0.95	200	0.6	0.8
10	sunflower	0.020	0.95	200	1.7	0.2
11	bare soil	0.005	0.98	–	–	–
12	corn	0.200	0.96	200	0.7	3.0

Table 7.1: Land use classes description and corresponding values of roughness length z_0, emissivity ϵ, minimum canopy resistance r_{cmin}, roots depth d_r and vegetation height h_v.

in terms of these parameters than of those expressed in function of the land use classification. The maps here used are obtained by resampling at 30 m the original ones, which have a resolution of 4 m. To maintain the advantage given by the availability of detailed maps, we have decided to modify the code making it able to receive inputs directly from maps and not only through subdivision into classes. For soil characterization the soil types and the corresponding properties already available in LEAF3 are used (see Section 4.3.1), since no measures focused on soil properties were realized. Soil is considered homogeneous over the whole domain and the *loam* type is selected (Timmermans et al., 2014). Following Liu and Shao (2013) soil layers thickness is imposed such that layers can react to atmospheric forcings oscillations due to turbulent eddies with a consistent time scale. Starting from the surface, the thickness of the 11 soil layers employed in the couple simulation are: 0.01, 0.03, 0.06, 0.09, 0.12, 0.16, 0.20, 0.25, 0.30, 0.40, 0.50 m. Using thicker layers at the surface makes the land surface exerting a quasi-stationary force on the overlying atmosphere instead than interacting with it (Liu and Shao, 2013). The LSM setup is completed by initial conditions for soil temperature and moisture. The horizontal pattern of the soil temperature is derived by the nocturnal airborne infrared image available for July, $26th$ at 00 : 00 UTC. But the coupled simulation is started at 04 : 00 UTC, as it will be explained in more detail in the following, and therefore the nocturnal cooling of the land

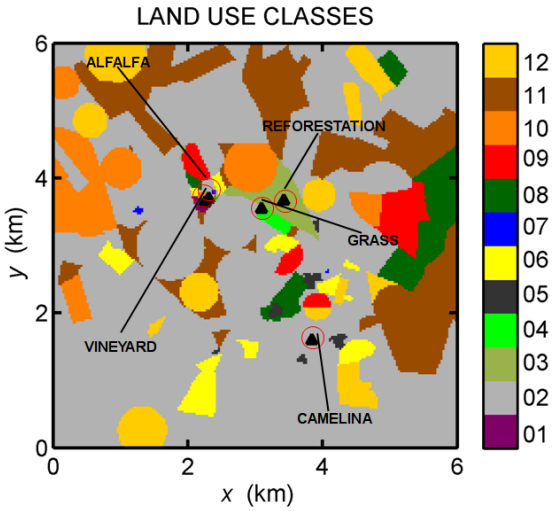

Figure 7.5: Land use classification recovered from remote sensing data and used in the coupled simulation with localization of the ground measurement stations.

surface must be taken into account. To this aim 8 ^{o}C are subtracted to the airborne map. The temperature shift is estimated on the basis of the difference existing between the LST value measured in the camelina field at 04 : 00 UTC and the corresponding value in the map and it is refined in the trial and error procedure that has led to the final setup of the simulation. The initial vertical profile of soil temperature is supposed to be similar in the whole domain and the profile measured in the camelina site at 04 : 00 UTC is used as reference. The map of the initial temperature of the soil surface layer is shown in the first panel of Figure 7.7. The initial soil moisture horizontal distribution is estimated on the basis of ground spot measures of the early morning of July, 26th combined with the soil temperature horizontal pattern. The resulting map for the soil surface layer is shown in the second panel of Figure 7.7. For the vertical profile a typical shape with water content diminishing while approaching the surface is imposed.

The simulation domain is $6\times6\times2$ km and a computational grid with spacings equal to $30 \times 30 \times 10$ m is used, as found out in Section 7.1. The time step is 0.1 s in order to assure a stable and accurate time advancement to LES, that lasts from 04 : 00 till 18 : 00 UTC. The first two hours are dedicated to ABL spinup, and hence results are collected from 06 : 00 UTC. The initial vertical profiles of potential temperature and air humidity are recovered from Murcia soundings of

00 : 00 UTC, as shown in Figure 7.7. Air humidity profile is slightly modified in order to make its shapes more regular, while potential temperature is changed on the basis of the typical evolution of the nocturnal profile combined with air temperature measurements in the Barrax site at 04 : 00 UTC. Being the simulation a coupled LES-LSM in a clear sunny day of the end of July in Spain, the main turbulence forcing is ultimately the solar radiation and a good correspondence between modelled and observed quantities is highly dependent on the similarity between the real solar radiation and those used as input by the model. Therefore the code, that provides incoming shortwave

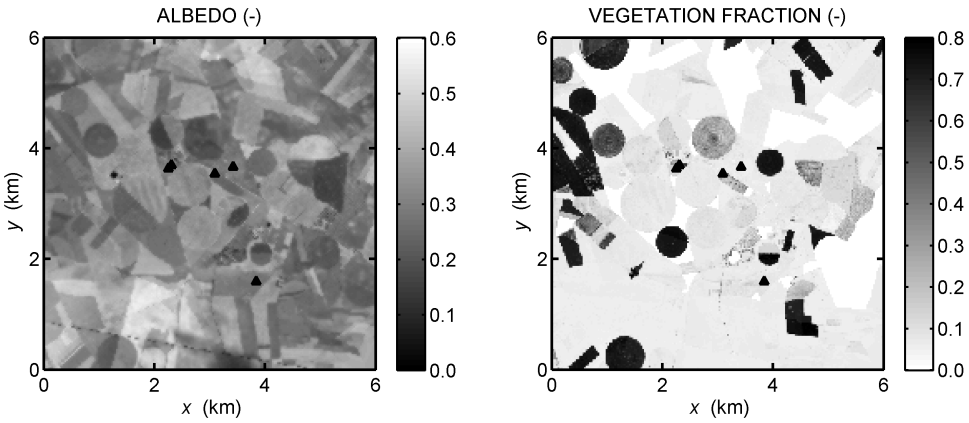

Figure 7.6: Maps of albedo (A) and vegetation fraction (B) recovered by remote sensing data and used in the LSM.

radiation in function of the location of the simulated site and of the day of the year, has been adapted in order to substitute its estimations with measurements of solar radiation. Figure 7.9 shows the time series used in the simulation. The LES setup is completed by periodicity at lateral boundaries, rigid lid with a damping layer of about 70 m at the domain top, lower boundary conditions from the coupling with LEAF3 and a geostrophic wind of about 8 ms^{-1}, as recovered by Murcia soundings.

7.3 Comparison with data

In this section a comparison between observations of significant quantities and the corresponding model predictions is provided in order to evaluate the coupled model ability of reproducing a diurnal cycle

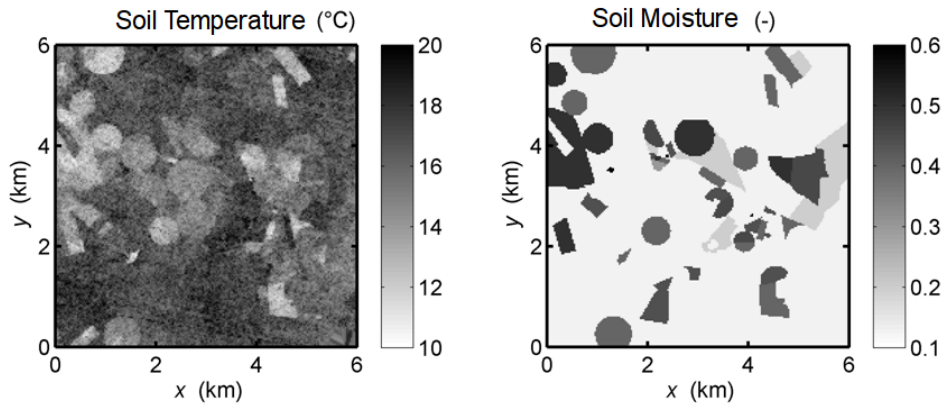

Figure 7.7: Initial temperature and moisture of the soil surface layer used in the LSM.

of ABL evolution and land surface-atmosphere interactions. Surface fluxes and micrometeorological states will be compared at the available stations location for the whole diurnal cycle. In addition surface temperature spatial distribution will be evaluated through comparison with airborne remote sensing images available for the simulated day, and finally atmospheric profiles evolution will be checked in terms of expected results. Three eddy covariance stations are available in the simulated domain, located in camelina, reforestation and vineyard fields, and two micrometeorological stations are present in the grass and alfalfa fields. Their positions are shown in Figure 7.5.

It is important to remember that a complete evaluation of a couped model LES-LSM is a challenging issue, since high resolution spatial and temporal measurements should be available for wind speed, temperature and scalars in the ABL and also for surface fluxes and large scale atmospheric conditions (Avissar et al., 1998). Therefore only a general assessment of RAMS-LES capabilities can be done with data from a standard field campaign at disposal. We verify that the coupled model can reproduce the diurnal cycle of the ABL and of related quantities and that it can deal with surface heterogeneity.

The coupled model provides values of any variable at each time step of the solution, i.e. each 0.1 s, but practical considerations about their storage requires that results are saved at a lower frequency. In our analysis a storage time step of 1 minute has been considered capable of capturing a sufficient number of turbulent oscillations. But in order to filter out the strong turbulent fluctuations, the results showed in this

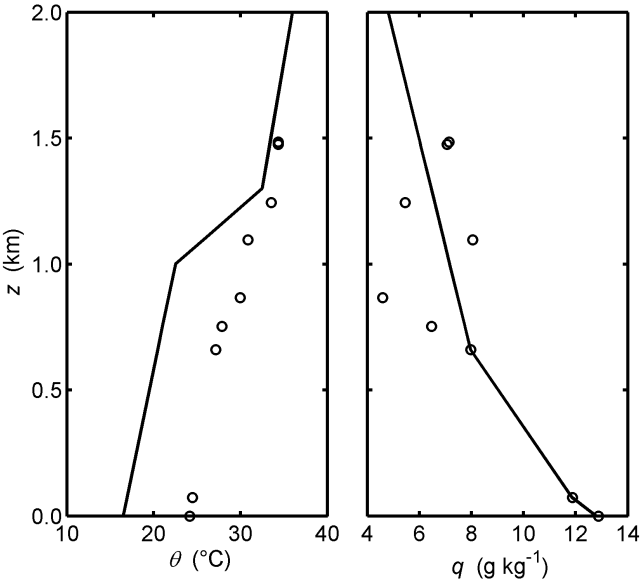

Figure 7.8: Vertical profiles of potential temperature and water vapour mixing ratio. The open circles are measurements from Murcia soundings at 00:00 UTC on July,26th. Solid lines are the profiles used for LES initialization at 04:00 UTC of the same day.

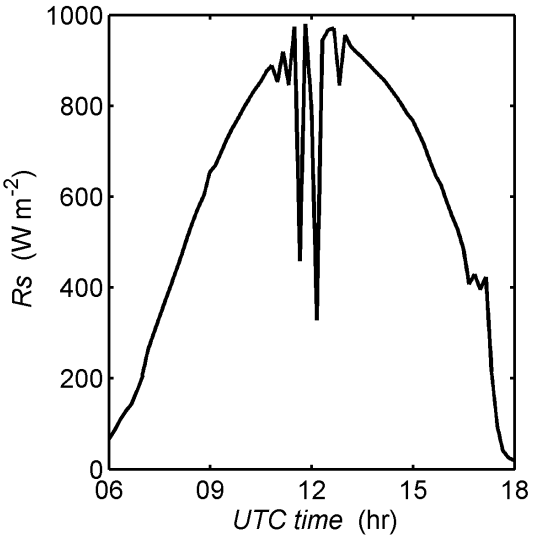

Figure 7.9: Measurements of incoming solar radiation for the simulated day (July,26th).

Section are averaged over a time interval of 10 or 30 minutes according to the necessity.

7.3.1 Surface fluxes

Surface fluxes measured by the eddy covariance towers present in the area of interest are compared to model estimates. Eddy covariance fluxes are representative of an upwind area whose extension and relative contribution to the final measured value are function of both site characteristics (e.g. surface roughness length) and meteorological variables (e.g. wind speed and Monin-Obukhov length) (Vesala et al., 2008). In our case, given the location and the meteorological conditions of the simulated day, the majority of the contribution to the measured fluxes came from the field to which each station belongs to. The only exception is the vineyard station, whose footprint function has resulted to be longer than those of the other stations (i.e. about 500 m versus around 240 m and 340 of camelina and reforestation respectively) and in some moments of the day also longer than the upwind area of the vineyard itself. We have in any case decided to compare all the observed fluxes with the modelled values in the corresponding fields, judging that the error would have been negligible for the aim of our analysis. Estimations of the fluxes source areas have been obtained by applying the analytical footprint model of Hsieh et al. (2000).

As already anticipated, the results here presented are time averages of the model predictions over 10 or 30 minutes according to the specific comparison we are interested in. Figure 7.10 shows the model performances in terms of net radiation Rn. The agreement is good in both the camelina and vineyard site, with the coefficient of determination being respectively 0.87 and 0.96 and a $RMSE$ (Root Mean Squared Error) of 60.6 and 41.6 Wm^{-2}, that can be considered negligible in a day with nearly 600 Wm^{-2} of peak value. Performances are better in the vineyard since a slight tendency of overestimation is present in the camelina site during the central part of the day (i.e. from 09 : 00 to 15 : 00 UTC). Observations are not available for the reforestation field. A good reproduction is obtained also for the surface sensible heat flux H, as shown in Figure 7.11. The best agreement is in the reforestation site with a coefficient of determination equal to 0.93 and $RMSE = 30.7\ \mathrm{Wm}^{-2}$, but also for the other two sites the diurnal evolution is correctly simulated and both the peak and the ascendant and descendant periods are captured. In the Camelina site a time lag of

about 30 minutes between observations and model predictions seems to be present, causing underestimation of H in the morning and overestimation in the afternoon, but still assuring good performances as proved by a coefficient of determination of 0.87 and a $RMSE$ equal to 40.3 Wm^{-2} in a day for which the peak value reaches more than 350 Wm^{-2}. Vineyard observations of H are significantly lower than the others, with a peak value of less than 250 Wm^{-2}, and the model correctly reproduce this difference with only a slight underestimation of morning values and overestimation of afternoon values. This issue could be related to the drip irrigation technique used in the vineyard, that provides a constant amount of water to the vegetation and therefore acts as a regulator for H. However the performances are still good, with a coefficient of determination equal to 0.76 and a $RMSE$ of 35.0 Wm^{-2}. Surface latent heat fluxes LE are dramatically low at all the three sites, with camelina values barely reaching 50 Wm^{-2} and reforestation and vineyard that do not reach 100 Wm^{-2} as shown in Figure 7.12. In addition the observations are highly oscillating, and therefore a worse match in respect to that of H is obtained for LE. But the general trend is correctly predicted, especially in the camelina and reforestation sites, while for vineyard a morning peak around 10 : 00 UTC is predicted but observations does not confirm it. Again the drip irrigation used in this field can be partially responsible for this mismatch. Figure 7.13 shows the comparison between observations and model predictions for the soil heat flux G. Few data are available for the simulated day in the reforestation site, not allowing an evaluation for that field in terms of G. Camelina and vineyard measurements correspond to different depth in the soil, namely about 1 cm and 10 cm respectively, as it can be immediately seen by comparing the two time series. In fact vineyard data have a smoother time evolution, typical of deeper soil layers. In the camelina site model performances are extremely good, with a coefficient of determination of 0.93 and only 20.3 Wm^{-2} of $RMSE$ in comparison with peak values of about 150 Wm^{-2}. In the vineyard site the timing is correctly reproduced, but the model overestimates G. However the global performance can be considered good, especially for the fact that the different evolution in function of the depth is captured by the model. Figure 7.14 shows scatter plots of the just examined quantities, i.e. Rn, H, LE and G, offering a global view of the model performances. Circles, squares and triangles are data at camelina, vineyard and reforestation fields respectively. As already stated, it can be seen that model best agreement with observa-

	Camelina	Reforestation	Vineyard
R^2_H	0.87	0.93	0.76
R^2_{LE}	0.23	0.08	−1.4
R^2_{Rn}	0.87	–	0.96
R^2_G	0.93	–	−0.7
$RMSE_H$	40.3	30.7	35.0
$RMSE_{LE}$	18.5	25.0	46.9
$RMSE_{Rn}$	60.6	–	41.6
$RMSE_G$	20.3	–	35.6
ME_H	−5.4	−5.8	10.9
ME_{LE}	8.9	12.3	34.3
ME_{Rn}	30.3	–	−7.6
ME_G	6.2	–	27.8
MAE_H	35.5	22.8	28.5
MAE_{LE}	13.0	20.4	36.6
MAE_{Rn}	46.5	–	34.9
MAE_G	17.4	–	31.7
$MAEP_H$	17.6	10.9	21.7
$MAEP_{LE}$	51.9	70.4	77.2
$MAEP_{Rn}$	16.3	–	10.9
$MAEP_G$	20.95	–	86.9

Table 7.2: Statistical indexes (coefficient of determination R^2, root mean squared error $RMSE$, mean error ME, mean absolute error MAE and mean absolute percentage error $MAEP$) about agreement between observations and model predictions of surface sensible H and latent LE heat flux, net radiation Rn and soil heat flux G.

tions is obtained for net radiation and surface sensible heat flux, with almost all the points following the $1:1$ line. In the LE scatter plot the general tendency of the model to overestimation for this quantity is evidenced, especially for the vineyard site at higher observed values. Table 7.2 reports coefficient of determination R^2, root mean squared error $RMSE$, mean error ME, mean absolute error MAE and mean absolute percentage error $MAEP$ for Rn, H, LE and G at the three control sites.

7.3.2 Micrometeorological states

Here we present a comparison between model predictions and observations of micrometeorological states, e.g. air temperature, air humidity and land surface temperature, for the whole diurnal cycle. The measurements we are using are from eddy covariance stations and mi-

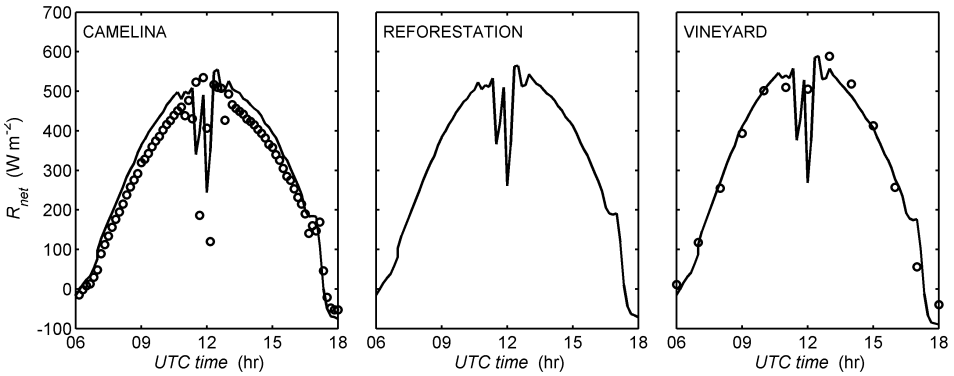

Figure 7.10: Comparison between measurements of net radiation at different locations (open circles) and corresponding coupled model predictions (solid line).

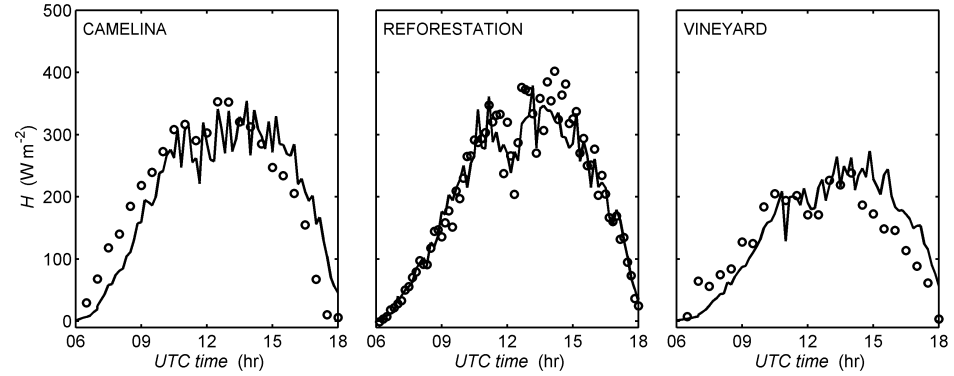

Figure 7.11: Comparison between measurements of surface sensible heat flux at different locations (open circles) and corresponding coupled model predictions (solid line).

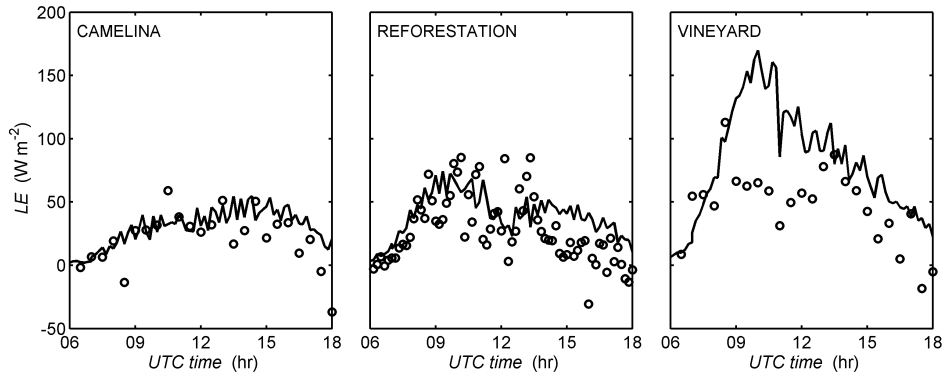

Figure 7.12: Comparison between measurements of surface latent heat flux at different locations (open circles) and corresponding coupled model predictions (solid line).

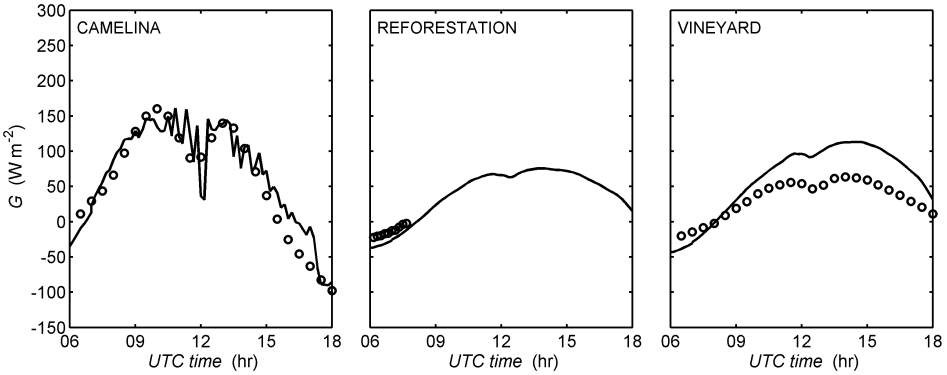

Figure 7.13: Comparison between measurements of soil heat flux at different locations (open circles) and corresponding coupled model predictions (solid line).

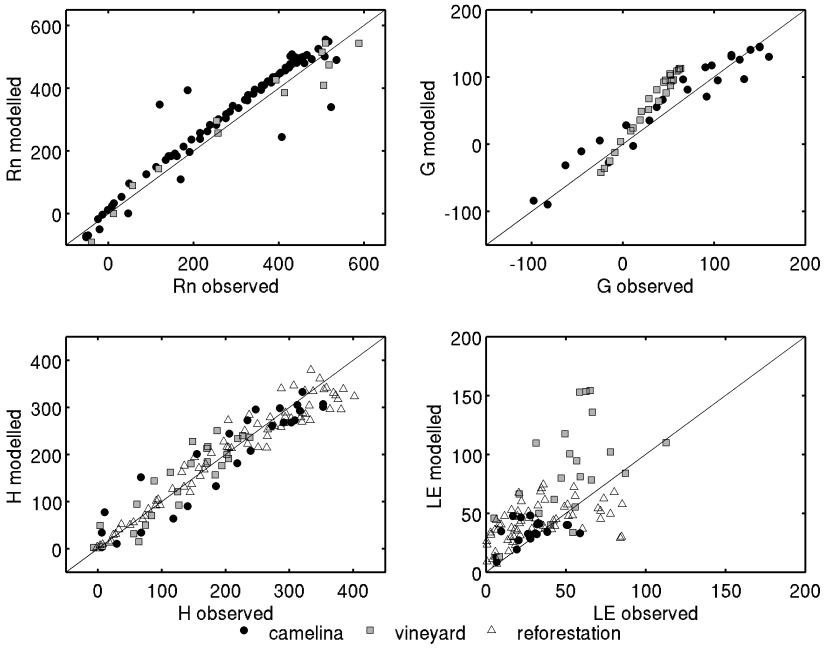

Figure 7.14: Scatter plots of net radiation, soil heat flux, surface sensible heat flux and surface latent heat flux. Circles, squares and triangles are data at camelina, vineyard and reforestation fields respectively.

crometorological stations, therefore five check points are available in the domain (see Figure 7.5 for their localization).

Figure 7.15 shows simulated and observed air temperature time series at the different stations. Observation heights are about 4 m for camelina and reforestation stations, 2 m for grass and alfalfa stations and 5 m for the vineyard one. It is immediately evident that an excellent agreement is obtained in the camelina field, in terms of both temporal evolution and temperatures intensity, and it is confirmed by a coefficient of determination of 0.98 and a $RMSE$ equal to 0.65 ^{o}C in a time series with peak values reaching 34 ^{o}C. In the vineyard site the air temperature is correctly matched in the early morning, while from 10 : 00 UTC it is overestimated up to about $3 - 4$ ^{o}C. At the opposite a tendency to underestimation is deductible in both grass and alfalfa fields, even if these fields observations are available only until 10 : 00. But at all the sites an almost perfect timing reconstruction is

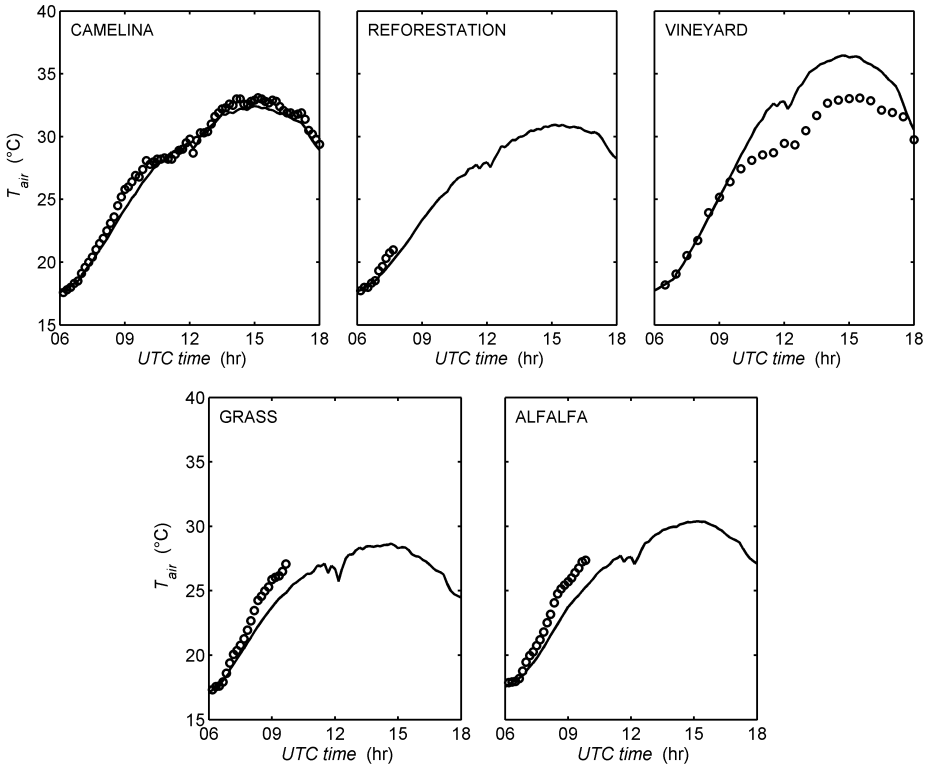

Figure 7.15: Comparison between measurements of air temperature at different locations (open circles) and corresponding coupled model predictions (solid line).

obtained, with ascendant, descendant and peak periods in exact phase with observations time evolution. Few data are available for the reforestation field and hence no considerations can be done for it. Some of the temperatures intensity mismatches could be related to the fact that the modelled air temperature is a conceptual temperature that is representative of the behaviour of the air layer immediately above the surface, but that does not correspond to a specific physical height above the ground. In fact LEAF3 is a Land Surface Model designed to work mainly in mesoscale simulations, where the first atmospheric level is usually placed at several tens of meters (a typical value is 50 m), and hence an air temperature that is strictly linked to the surface is needed to correctly predict land-surface interactions. Therefore it is not straightforward to associate a height to this conceptual temperature and comparisons with measurements made at different heights can be influenced by this fact. For example it is possible that the underestimation observed in grass and alfalfa fields are partially due to the fact that the conceptual temperature is representative of an upper air layer than that at 2 m at which measurements are taken. Figure 7.16 shows simulated and observed time series of land surface temperature at the available measurement stations. The modelled land surface temperature is obtained as a wighted average of surface soil temperature and vegetation temperature, using the vegetation fraction as weight. The coupled model provides significantly lower values than observations at all the sites from 09 : 00 UTC. A complete time series of measurements is available only for camelina and reforestation fields. In this latter the underestimation is higher, up to nearly 10 ^{o}C for the peak values, while for camelina it remains under 7 ^{o}C. The few measurements available for the grass and alfalfa sites suggest a similar behaviour. This common underestimation in all the check points suggests that soil parameters may not be adequate for the kind of soil present in the area. In particular the results suggest that soil heat capacity should be better tuned. In fact in the simulation setup (see Section 7.2) we have selected directly a soil type between those already present in RAMS database. We have not had the possibility of an *a priori* refinement of the values adopted for the various parameters affecting soil behaviour, since we do not have any information about soil properties at disposal. The last micrometeorological variable available for comparison is the air humidity. Figure 7.17 shows time series of predicted and observed relative humidity. It can be seen that a quite good agreement is obtained after 11 : 00 UTC at both the camelina

	Camelina	Reforestation	Vineyard	Grass	Alfalfa
R^2_{Ta}	0.98	–	0.73	0.83	0.79
R^2_{Ts}	0.82	0.63	–	0.56	0.87
$RMSE_{Ta}$	0.65	–	2.59	1.38	1.53
$RMSE_{Ts}$	3.76	5.76	–	2.63	1.92
ME_{Ta}	−0.47	–	2.12	−1.08	−1.27
ME_{Ts}	−3.42	−4.93	–	−2.16	−0.41
MAE_{Ta}	0.53	–	2.12	1.14	1.28
MAE_{Ts}	3.42	5.11	–	2.28	1.41
$MAEP_{Ta}$	1.9	–	7.6	5.2	5.7
$MAEP_{Ts}$	8.8	13.3	–	9.6	5.7

Table 7.3: Statistical indexes (coefficient of determination R^2, root mean squared error $RMSE$, mean error ME, mean absolute error MAE and mean absolute percentage error $MAEP$) about agreement between observations and model predictions of air Ta and soil Ts temperature.

and the vineyard site, while in the morning the model overestimates air humidity. However a general sufficient reconstruction is obtained, especially considering that the initial air humidity profile is imposed on the basis of a sounding that was not conducted in the simulated area (see Section 7.2). Figure 7.18 shows scatter plot of air and land surface temperature, offering a global view of the model performances. Solid circles, squares, triangles, open circles and asterisks correspond to data at camelina, vineyard, reforestation, grass and alfalfa fields respectively. Air temperature is better reproduced than land surface temperature, even if an overestimation of the highest values at vineyard station is present. Land surface temperatures scatter plot shows a common slope for values corresponding to different measurement stations, revealing the general underestimation of surface temperature and confirming the above-said hypothesis of an inadequate (overestimated) value of soil heat capacity for the simulated area. Table 7.3 reports coefficient of determination R^2, root mean squared error $RMSE$, mean error ME, mean absolute error MAE and mean absolute percentage error $MAEP$ for Ta and Ts at the control sites.

7.3.3 Other comparisons

The evaluation of the coupled model ability of reproducing a diurnal cycle of the ABL and land-atmosphere interactions in real conditions is completed by two additional comparisons. Figure 7.19 shows maps

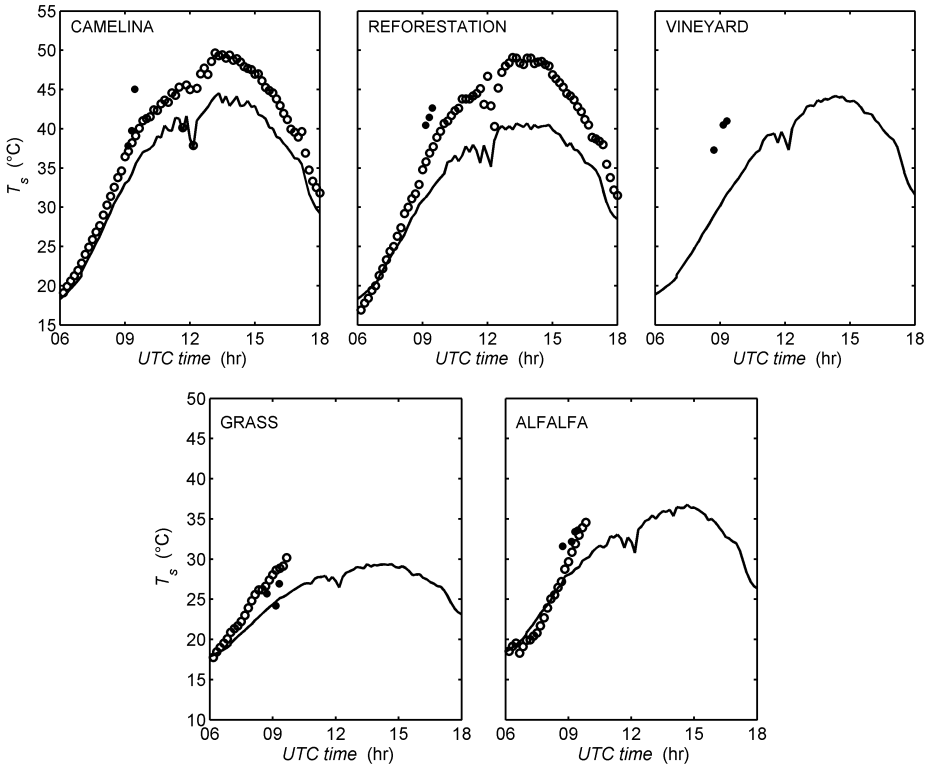

Figure 7.16: Comparison between measurements of land surface temperature at different locations (open circles) and corresponding coupled model predictions (solid line).

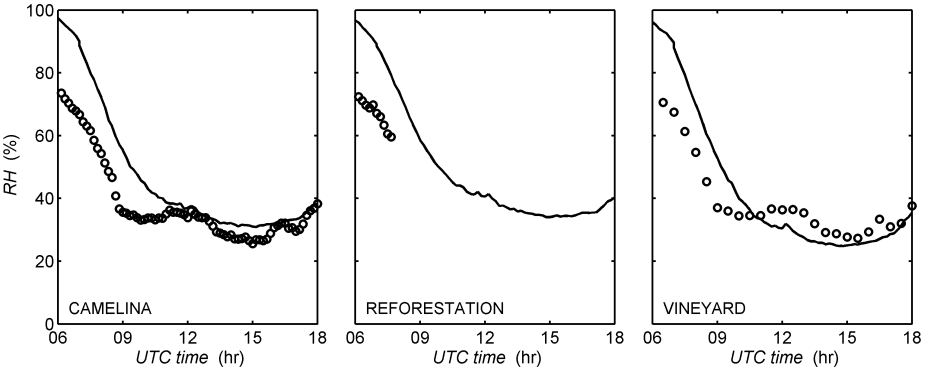

Figure 7.17: Comparison between measurements of relative humidity (open circles) and corresponding coupled model predictions (solid line).

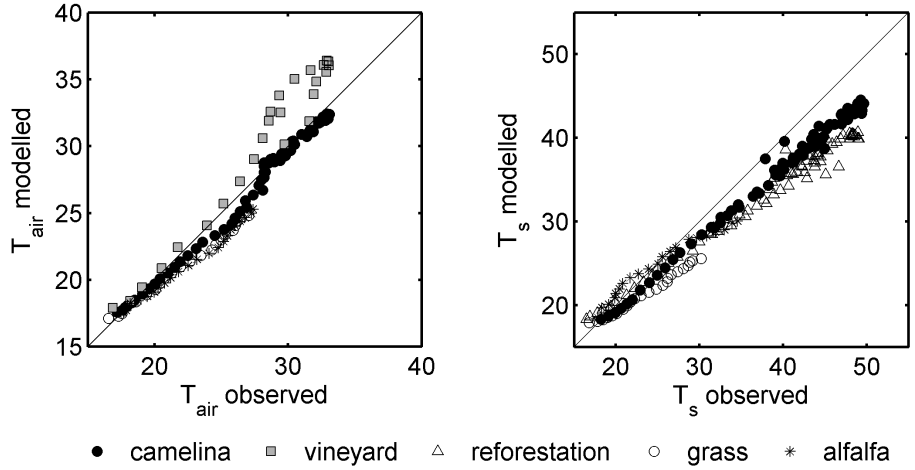

Figure 7.18: Scatter plots of air and land surface temperature. Solid circles, squares, triangles, open circles and asterisks are data at camelina, vineyard, reforestation, grass and alfalfa fields respectively.

of land surface temperature at 09 : 19 UTC from airborne remote sensing (on the left, panel *a*) and from the model (on the right, panel *b*). Other images are available at 08 : 43, 09 : 09, 09 : 27 and 09 : 40 UTC but, since they are very close in time, only one of those having a larger spatial extension is shown here. The model map is globally darker than the airborne one, again revealing that the coupled model underestimates land surface temperature, probably because of the use of an inadequate soil heat capacity. But also a slight overestimation in airborne values has been detected by comparing values with those measured by the ground stations. Airborne temperatures are reported in Figure 7.16 as solid circles and it can be seen that in camelina and reforestation sites they are higher than the corresponding ground measurements. Maps comparison shows that surface heterogeneity is correctly captured by the model, even if not completely, since some simplifications about heterogeneity representations have been done for some model inputs (see Section 7.2 for more details). Figure 7.20 shows domain averaged vertical profiles of potential temperature (on the left) and water vapour mixing ratio (on the right) at 13 : 00 UTC (dashed lines) and their corresponding initial values (solid lines). It is not possible to assess modelled profiles adherence to the reality, because the REFLEX campaign did not include *in situ* atmospheric soundings. Therefore we only observe that the profiles have evolved adequately in

terms of what we qualitatively expect for a sunny day at the end of July in Spain, i.e. a marked mixed layer have developed as proved by the nearly constant values of both potential temperature and water vapour mixing ratio under the entrainment layer. In addition the height of the ABL is correctly increased during the morning because of the strong convective conditions determined by the surface sensible heat fluxes.

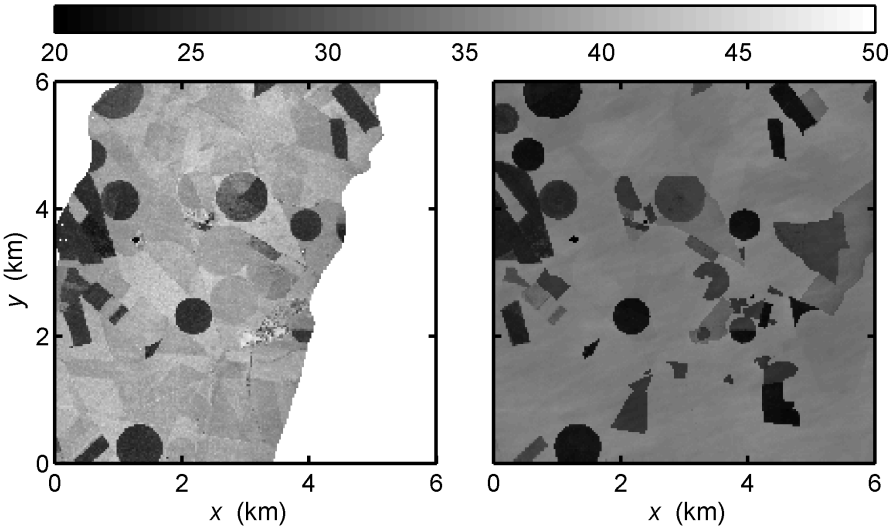

a. Observed LST (°C) b.Modelled LST (°C)

Figure 7.19: Surface temperature from remote sensing measurements and coupled model predictions at 09:19 UTC on July, 26th

7.4 Conclusions

RAMS-LES performances in simulating ABL evolution and land-atmosphere interactions when coupled with a Land Surface Model (LSM) have been investigated in this chapter. To this aim a coupled simulation in real condition has been performed and model predictions compared with observations of significant quantities, as surface fluxes and micrometeorological states. RAMS-LES has been used coupled with its native land surface model, i.e. LEAF3 (Land-Ecosystem-Atmosphere Feedback version 3), that is a dual source, multiple soil and resistance levels scheme. For this evaluation we have referred to the experimental field campaign REFLEX 2012 (Timmermans et al., 2014; Tol et al., 2014), which lasted from July, 18th to July, 28th in 2012 and took place in

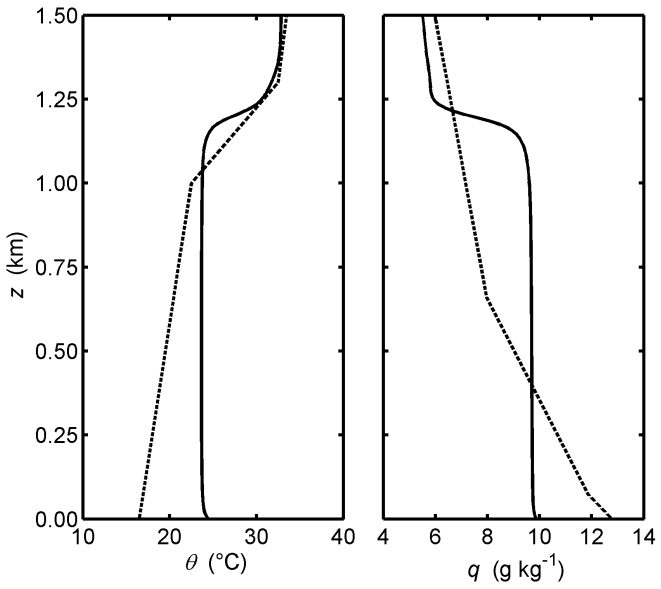

Figure 7.20: Domain averaged vertical profiles of potential temperature and water vapour mixing ratio. The dashed line corresponds to initial profiles; the solid line corresponds to profiles at 13:00 UTC on July, 26th.

the experimental site of Barrax (Albacete, Spain). In particular we have simulated the diurnal cycle of July, $26th$.

Preliminary analysis aimed at defining an appropriate domain extension and grid resolution have been realized. A domain of 3.0×3.5 km, which corresponds to the area involved in the REFLEX 2012 field campaign, has resulted to be insufficient for the simulated turbulence. Therefore a domain with a horizontal extension larger than the area of interest (i.e. 6×6 km) has been adopted, with the added value of mitigating the impact that lateral periodicity could have on the area of interest thanks to a surrounding buffer area. A grid spacing of 30 m in the horizontal and 10 m in the vertical have been verified to be adequate for the simulated turbulence.

The coupled model predictions of surface fluxes are in good agreement with observations at all the three available eddy covariance stations. Excellent results have been obtained for net radiation and also sensible heat flux, especially in the reforestation and camelina fields. Also latent heat flux is globally correctly reproduced, although observations are characterized by very low and oscillating values that are difficult to simulate and therefore a perfect match is not obtained. But

the trend is well captured, with the exception of an overestimation in the vineyard site in the first part of the day. This mismatch could be due to the fact that drip irrigation was used in that field during the experimental campaign, while the model can only deal with an initial soil moisture that is progressively reduced by evapotranspiration and not with a controlled water supply that maintain a sort of constant evapotranspiration rate. Also in terms of soil heat flux we have obtained a good agreement between model predictions and observations, especially at the camelina site. Also micrometeorological states, i.e. air temperature and humidity and land surface temperature, temporal evolution have been reconstructed correctly, but with some mismatch in terms of intensity. Modelled air temperature matches perfectly observations in the camelina site, while it is overestimated in the vineyard field and an underestimation is suggested for grass and alfalfa sites. Some of the temperatures intensity mismatches could be related to the fact that the modelled air temperature is a conceptual temperature that is representative of the behaviour of the air layer immediately above the surface, but that does not correspond to a specific physical height above the ground. In fact LEAF3 is a Land Surface Model designed to work mainly in mesoscale simulations, where the first atmospheric level is usually placed at several tens of meters (a typical value is 50 m) and hence an air temperature that is strictly linked to the surface is needed to correctly predict land-surface interactions. Therefore, it is not straightforward to associate a height to this conceptual temperature and comparisons with measurements made at different heights can be influenced by this fact. A diffuse underestimation of land surface temperature has been revealed from the comparison with both time series of local observations and airborne remote sensed maps, but again the timing is correctly simulated at all the measurements stations. This underestimation is probably due to an inadequate value of soil heat capacity and it could be mitigated if this parameter is better tuned. The time evolution of vertical profiles of air potential temperature and humidity have been verified to be qualitatively in agreement with expectations for a convective ABL. We could not perform a quantitative evaluation since the REFLEX campaign did not include *in situ* atmospheric soundings. In conclusion, the coupled model capability of reproducing a diurnal cycle of ABL turbulence and land-atmosphere interactions in real conditions have been demonstrated, especially considering the insufficiency of available information for the experiment setup and the high uncertainties

that are inherent in this kind of simulations. In fact, to rigorously verify the coupled model performances, high resolution spatial and temporal observations should be at disposal for both atmospheric and surface variables, and also large scale atmospheric conditions should be known (Avissar et al., 1998).

7.5 Appendix: the Barrax site and the REFLEX campaign

The study area is the agricultural area of Barrax in the centre of Spain ($39^o3\prime$ N, $2^o6\prime$ W, 700 m a.s.l) characterized by an alternation of irrigated and dry cultivated area, containing crops such as corn, barley, sunflower, alfalfa and onions (see Figure 7.21). The climate is typically Mediterranean with vernal and autumnal rainfall whose annual average is 400 mm, making it one of the driest areas in Europe. Between 16 to 28 July 2012 the Regional Experiments For Land-atmosphere Exchanges (REFLEX) 2012 campaign has been carried out, where remote sensing and ground measurements used in this study have been collected (Timmermans et al., 2014). Hyper-spectral and thermal airborne images have been acquired during two days while for the entire period three eddy covariance towers and a large aperture scintillometer (LAS) have operated. In selected points some biophysical measurements have been carried out over different land-cover units: among others Fractional Vegetation Cover (FVC), Leaf Area Index (LAI), Photosynthetically Active Radiation (PAR) and soil moisture (SM). During the campaign, a large part of the crops were already harvested with the exception of maize, vineyard, sunflower, orchards and forest nursery (see Figure 7.21).

7.5.1 Ground data

Three micrometeorological towers and LAS measured water and energy fluxes during the field campaign over different crop types. The first station ($EC1$) was located in a camelina field, the second one ($EC2$) in a small vineyard and the third ($EC3$) in a forest nursery. The LAS was installed in a wheat-stubble field (Tol et al., 2014). Latent, sensible and soil heat fluxes were sampled in all fields, whereas net radiation was only recorded in $EC1$ and $EC2$. Station $EC3$ was also equipped with an infrared thermometer for determining outgoing long-

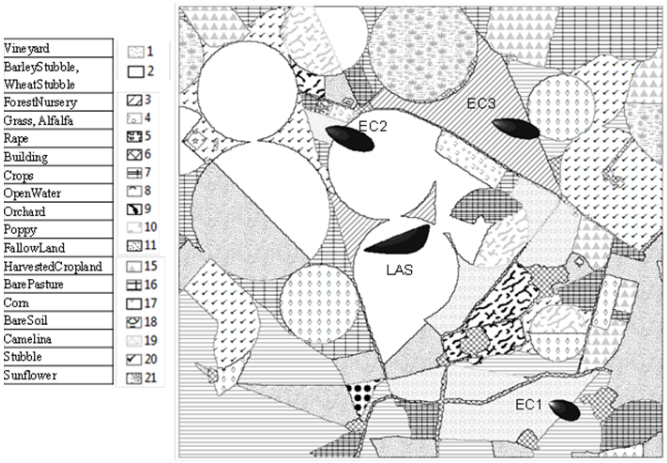

Figure 7.21: Barrax agricultural area, land use and footprint functions for July,25th at 9 : 28 UTC.

wave radiation. All meteorological data typically required by hydrological models (incoming solar radiation, air temperature, air humidity, wind speed) were acquired by the stations. Soil moisture and soil temperature observations were also collected. Raw data from the eddy covariance towers have been corrected following the procedures well assessed in literature (Foken and Nappo, 2008). The $EC1$ and $EC2$ data have been analyzed with the *Alteddy* software (Alterra, WUR, Netherlands, http://www.climatexchange.nl/projects/alteddy/) whereas the $EC3$ data with the *PEC* software (Corbari et al., 2012) due to the availability of only thirty minutes average data. Corbari et al. (2014) compared corrected fluxes from high frequency and from 30 minutes average data in a maize field showing that low errors can be obtained with mean absolute daily difference equal to 6.1 Wm^{-2} for H and 13.2 Wm^{-2} for LE. As well known in literature, there is a general lack of energy balance closure in EC measurements (Twine et al., 2000; Wilson et al., 2002; Foken and Nappo, 2008) and in this context a reasonable small closure gap is obtained for $EC1$ and $EC3$. A poorer behavior is obtained for $EC2$ in the vineyard field. This seems to be linked to the net radiation which, especially during daytime, becomes consistently higher than the sum of the other components of the energy balance equation. This is due to the fact that the field of view of the net radiometer is dominated by canopy, resulting in a lower albedo and thus higher net radiation then when seen from the altitude of the airborne sensors. The soil heat flux measurements at the individual sites

were taken at depths of a few centimeters and needed to be corrected for storage in the soil layer above the sensors. Over the vineyard, one measurement was taken below the vine stand and another one in between the stands, such as to obtain representative observations for this particular site. Soil moisture and soil temperature observations were taken at different depths for the post-processing of the soil heat fluxes.

7.5.2 Airborne data

During the REFLEX campaign, two daytime and one nighttime flights of the *CASA 212-200 N/S 270 "Paternina"* airplane of INTA have been performed with on board the Airborne Hyperspectral Scanner (AHS) and Compact Airborne Imaging Spectrometer ($CASI$) sensors. The AHS sensor covers the thermal infrared part of the electromagnetic spectrum which is fundamental for estimating energy fluxes. A total of 13 daytime and 5 nighttime images are available at a spatial resolution of 4 m. More details on these observations are provided in (Miguel et al., 2014). Land surface temperature values are obtained with the Temperature and Emissivity Separation method (TES) described in Gillespie et al. (1998) and applied to AHS data following Sobrino et al. (2008). Additional remote sensing based quantities such as albedo, NDVI, LAI and vegetation fraction are computed following Timmermans et al. (2011) and Richter et al. (2009).

8

Impact of the spatial resolution of surface parameters on the coupled model results

In this chapter the impact that the spatial resolution of surface parameters has on the results of a coupled LES-LSM is investigated. In fact in such kind of simulations, as already extensively discussed, both horizontal and vertical grid spacings are imposed by LES needs. Hence, understanding which kind of impact one should expect in case only coarser characterization is available for surface heterogeneity can help in increasing modellers confidence with coupled LES-LSM. Moreover, the importance of the spatial resolution issue has been recognized for hydrological modelling (e.g. Wood et al., 1988; Wood, 1994), as well as for remote sensing (e.g. Wood, 1995; Su et al., 1999; Kustas et al., 2004; McCabe and Wood, 2006; Corbari et al., 2013; Ershadi et al., 2013), but it has been faced for coupled LES-LSM only in terms of surface heterogeneity impact on the ABL (e.g. Patton et al., 2005; Courault et al., 2007; Huang and Margulis, 2012). In our analysis five coupled simulations with an identical setup, which is that used in the previous chapter, but with increasingly coarser spatial resolution of surface parameters, are performed. Resolutions equal to 120, 300, 600, 1200 and 6000 m are examined. The role of surface heterogeneity scales is investigated in terms of both ABL characteristics and surface quantities.

Simulations setup is presented in Section 8.1, while results are shown in Section 8.2. Conclusions are discussed in Section 8.3.

8.1 Experiment setup

As extensively discussed in Chapter 5 and 6, grid spacings in both vertical and horizontal directions have a significant impact on LES results. Only an appropriate grid design allows an optimal usage of a certain code for certain specific atmospheric conditions, meaning that in a coupled LES-LSM the horizontal resolution used by the LSM is imposed by LES needs and not by the available information for surface characterization. Consequently, with this analysis we aim at understanding which is the impact of employing surface parameters maps with a coarser spatial resolution than that imposed by the LES needs in a coupled LES-LSM.

In order to assess such impact, we perform five coupled simulations with an identical setup, i.e. that of the previous chapter, but using increasingly coarser spatial resolutions for the surface characterization. In particular each distributed input of the LSM is resampled at 120, 300, 600, 1200 and 6000 m, with the latter case corresponding to horizontal homogeneity. In Figure 8.1 maps of vegetation fraction, albedo and surface roughness length z_0 with increasingly coarser resolutions are showed in comparison with the reference maps at 30 m. We will refer to the various simulations with the abbreviations $R30$, $R120$, $R300$, $R600$, $R1200$ and $R6000$, each one indicating the spatial resolution used for the surface characterization. The same computational grid is employed in all the runs, and it is exactly that of the coupled model capabilities evaluation performed in Chapter 7, i.e. $30 \times 30 \times 10$ m of grid spacings for a domain of $6 \times 6 \times 2$ km.

8.2 Results

In order to assess the role of the spatial resolution of surface parameters on LES-LSM coupled simulations, the results obtained with degraded surface information are compared with those of the reference simulation $R30$. The impact on the simulated atmospheric turbulence is investigated by analyzing typical turbulent statistics of the ABL, such as mean vertical profiles of sensible heat flux, potential temperature and velocity variances, and also velocity spectra. The effect at the surface is evaluated in terms of variations of both spatial distribution and time series of sensible and latent heat fluxes, and surface and air temperatures. In addition spatial correlation of these two latter variables and thermal blending height are computed.

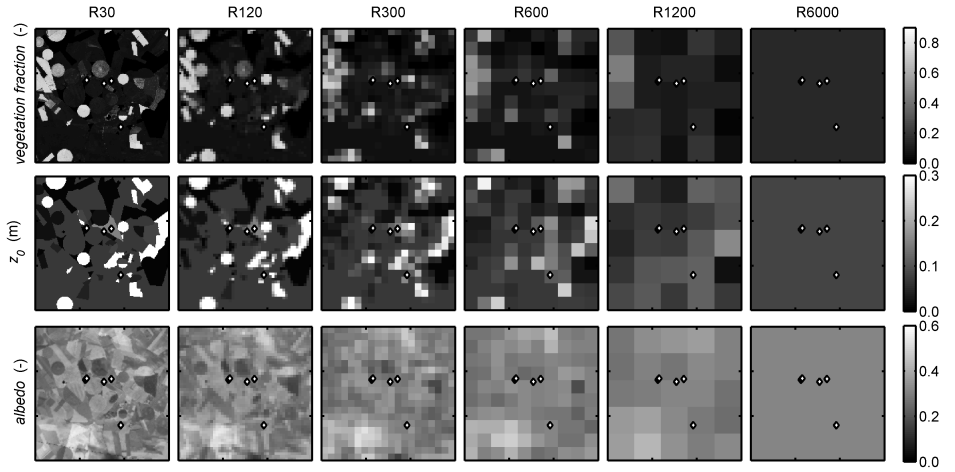

Figure 8.1: Maps of main surface parameters input (vegetation fraction, surface roughness length z_0, albedo) with decreasing spatial resolution going from left to right.

8.2.1 Mean profiles and spectra

The first line of Figure 8.2 shows domain averaged vertical profiles of dimensionless vertical heat flux on the left and of potential temperature on the right, while in the second line the percentage difference between potential temperature profiles and the reference simulation is reported. All the profiles are time-averaged over the interval 12:45 - 13:45 UTC. It can be immediately seen that the surface parameters resolution has a negligible impact on domain-averaged profiles of total (SGS + resolved contribution) vertical heat flux. Even the impact on the entrainment heat flux is negligible, although it is usually more sensitive to model setup than the rest of the profile. The fact that surface heterogeneity has a negligible impact on the total dimensionless vertical heat flux has been already observed in other studies (e.g. Patton et al., 2005; Huang et al., 2009). The heat flux profiles are linear through the ABL, revealing quasi-steady conditions in the considered time interval for all the simulations. Even domain-averaged potential temperature is almost unaffected by the surface heterogeneity representation. All the profiles have the characteristic shape of convective ABL, with a well developed mixed layer characterized by a constant value of potential temperature. Only the homogeneous simulation $R6000$ shows a different profile from the reference $R30$, with a slightly warmer mixed layer. The difference in potential temperature is of about 1 ^{o}C. Per-

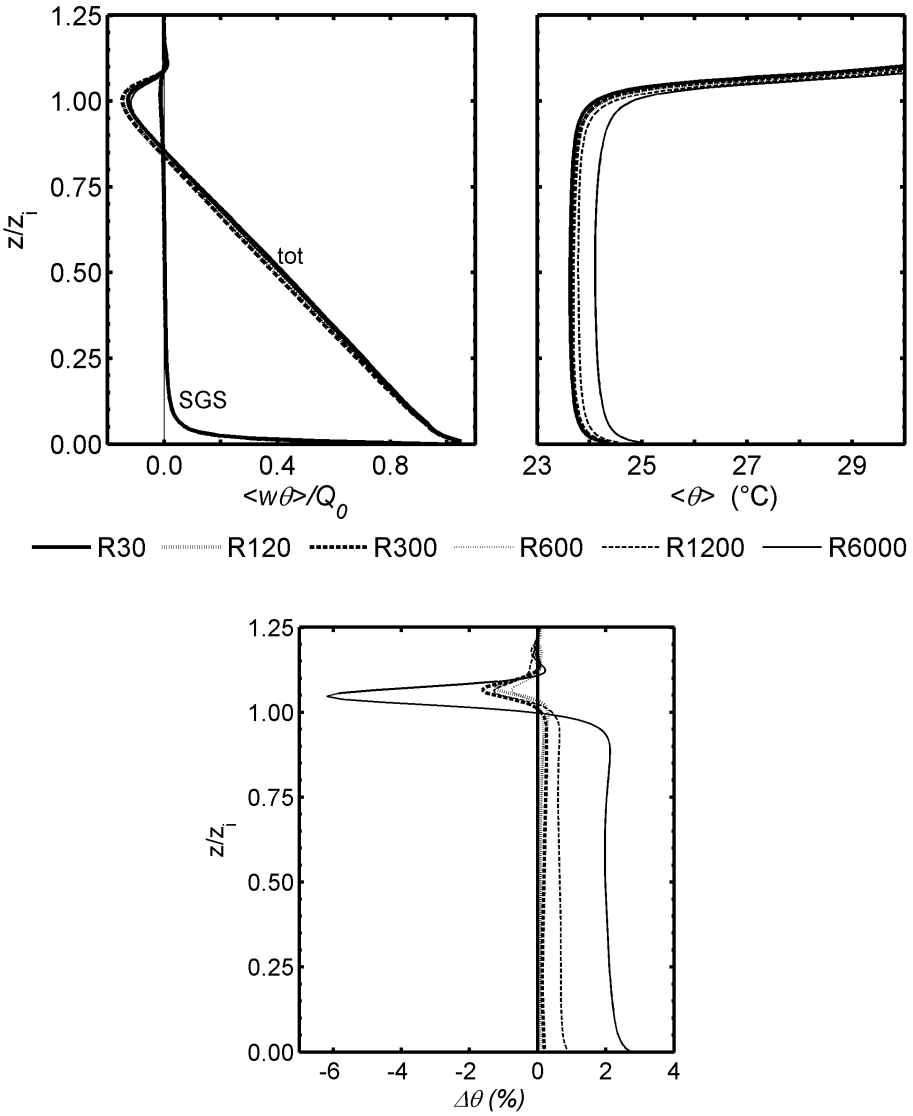

Figure 8.2: Top panel: plane- and time-averaged (from 12:45 to 13:45 UTC) vertical profile of dimensionless vertical heat flux on the left and potential temperature on the right. Bottom panel: vertical profile of percentage difference of potential temperature in respect to the reference simulation R30.

centage differences confirms this limited impact, showing that the only other simulation that differs from the reference in the mixed layer is $R1200$, but of less than 1%. A slightly greater impact is observed in the entrainment layer, with a maximum difference of -6% in $R6000$ and about -2% in all the other runs. Therefore, surface heterogeneity representation has a negligible or very limited impact on bulk thermal properties of the simulated ABL.

Figure 8.3 shows vertical profiles of domain-averaged velocity variances, with horizontal velocity on the left and vertical velocity on the right. Both horizontal and vertical variances present the typical expected shapes for these profiles. They are more influenced by the resolution of the surface parameters in the central and upper part of the ABL. The effect of coarsening the maps resolution is not unique, but varies in function of the scale of representation. The weakest turbulence is obtained in $R600$, with the peak of the dimensionless vertical velocity variance decreasing of about 0.1. Also the variance of the horizontal velocity is lower than the reference $R30$. The homogeneous case $R6000$ has similar profiles, but slightly less weak. This resemblance between $R600$ and $R6000$ could suggest that, for the considered surface heterogeneity, a representation with a resolution of 600 m can not reproduce the effect that the surface characteristics have on the ABL turbulence and, in these terms, it is almost equivalent to a homogeneous surface. This ability is instead almost recovered by $R1200$, whose variance profiles are the most similar to the reference case, together with $R120$ as expected. In fact $R120$ surface representation is practically identical to the reference, as it can be seen in input maps of Figure 8.1. But some differences in the variance profiles are present even in $R120$, especially in those of horizontal velocity, whose value significantly decreases in the central part of the ABL and increases in the upper part. $R300$ significantly differs from the reference despite surface characteristics are still recognizable in the surface maps (see Figure 8.1). In particular, vertical velocity variance decreases in the lower half of the ABL and increases in the upper half, modifying also the peak location from $z/z_i = 0.40$ to $z/z_i = 0.50$. The peak height is instead maintained in all the other simulations. Therefore, $R120$ and $R300$ progressively increase variance in the upper part of the ABL and decrease it in the lower part, with $R300$ significantly differing from the reference. $R600$ profiles are more similar to those of the homogeneous case $R6000$ than to those of the reference, and are the weakest obtained. Instead $R1200$ profiles are the most similar to the reference

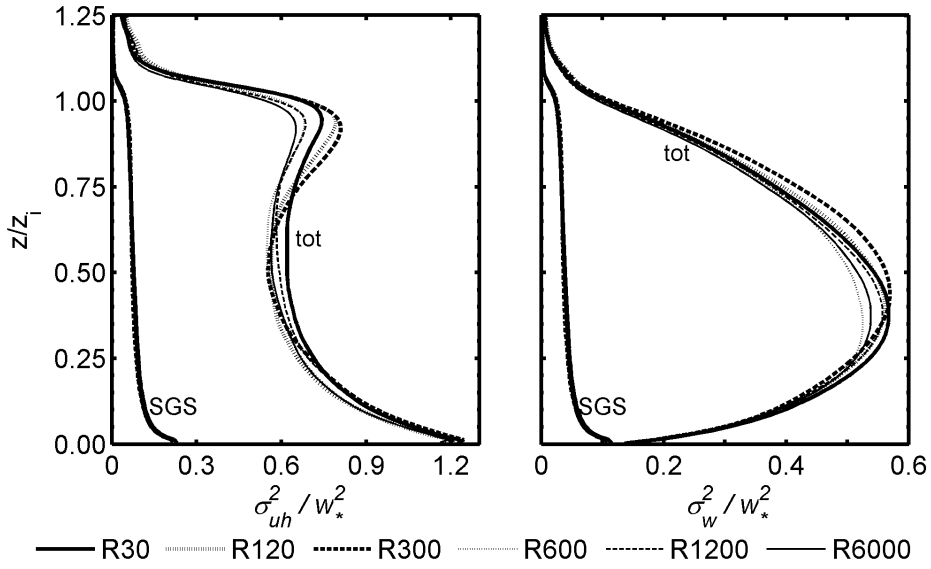

Figure 8.3: Plane- and time-averaged (from 12:45 to 13:45 UTC) vertical profile of horizontal velocity variance on the left and vertical velocity variance on the right.

although surface heterogeneity shapes are no more recognizable in the input maps.

Figure 8.4 shows time- and plane-averaged spectra along the $x-$direction for $w-$velocity component on the left and $u-$component on the right. Spectra are computed at the dimensionless height $z/z_i = 0.5$ in the time interval 12:45 - 13:15 UTC. The energy production peak is at smaller wavenumbers for the horizontal velocity u than for the vertical one in all the simulations. Spectra reveal that the resolution of surface parameters mainly affects larger-scale turbulent structures (length scale ranging about from 600 to 6000 m), while smaller eddies are almost insensitive to surface heterogeneity representation. At the examined height, vertical velocity spectra shows more dependency on surface maps resolution than those of horizontal velocity, in accordance with the variance profiles of Figure 8.3, where more differences are present in $w-$variance profiles than in $u-$profiles at $z/z_i = 0.5$. In particular, in $w-$velocity fields $R6000$ and $R300$ are the least energetic for the whole range of larger-scales (600-6000 m), while in terms of $u-$velocity $R600$ and $R1200$ have more energy associated to the largest eddies in the flow than the other simulations.

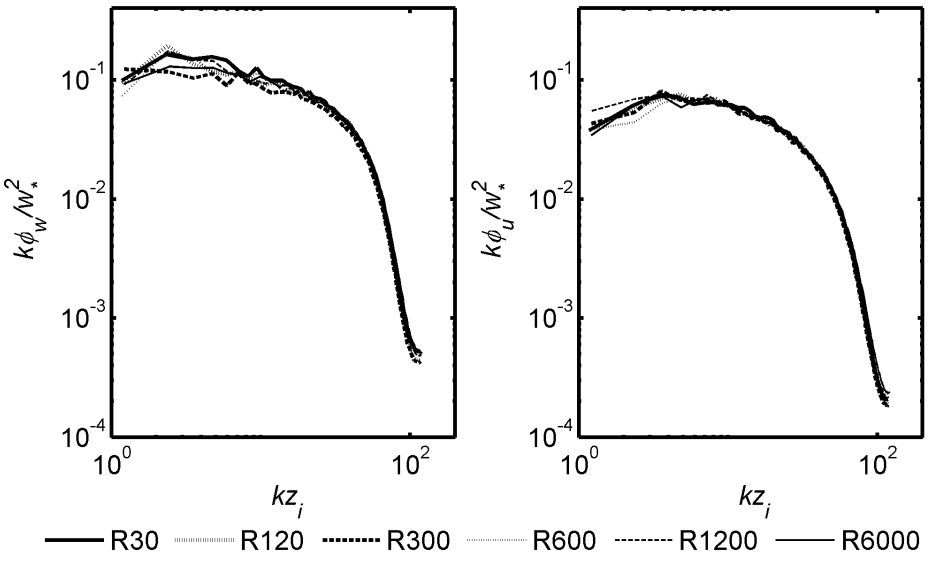

Figure 8.4: Plane- and time-averaged (from 12:45 to 13:45 UTC) velocity spectra along the $x$direction for $w-$velocity component on the left and $u-$velocity component on the right. Spectra refer to the middle of the ABL.

8.2.2 Maps

As expected, surface parameters resolution has a more defined impact on those quantities that are directly linked with them, such as surface fluxes and states. Figure 8.5 shows time-averaged maps of land surface temperature, surface sensible heat flux and surface latent heat flux for all the performed simulations. Time-averaging interval is 12:45 - 13:45 UTC. It is immediately evident that the spatial distribution of all these quantities perfectly reflects the resolution of the surface parameters maps. Visually results of $R120$ are almost equivalent to those of the reference $R30$, and also their spatial mean and standard deviation do not change significantly as shown in Figure 8.6. In $R300$ some general spatial information is lost, but the general pattern and the range of the outputs values are preserved. Also domain-averaged values remain almost constant for all the examined quantities, more for the net radiation and the temperatures than for the turbulent fluxes. Instead the spatial standard deviation decreases for all the quantities. $R600$ can be considered a threshold simulation, where the very general patterns can still be found in the surface outputs maps and the domain averages are still similar to the reference values. In $R1200$

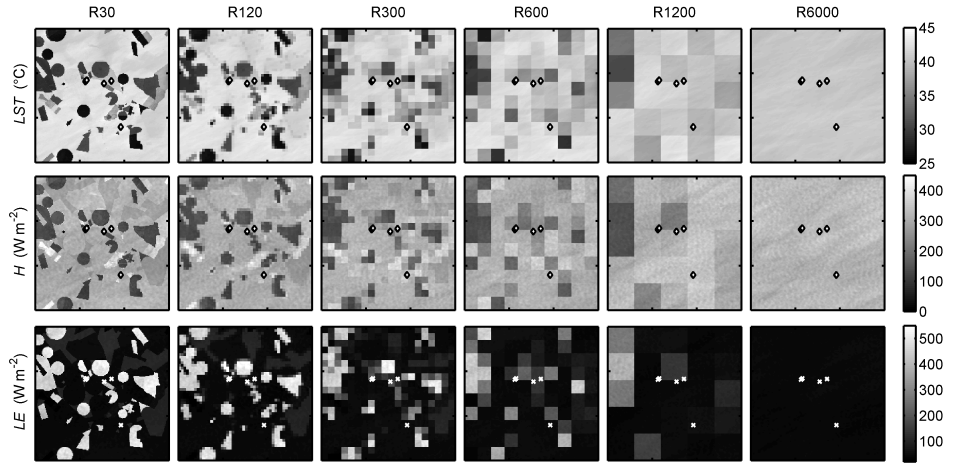

Figure 8.5: Maps of time-averaged land surface temperature LST, surface sensible heat flux H and surface latent heat flux LE obtained in the various performed simulations, with spatial resolution of surface parameters decreasing from left to right. Time-averaging interval is 12:45 - 13:15 UTC.

the spatial organization of surface heterogeneity is completely lost and domain-averaged turbulent fluxes are significantly different from the corresponding references, while mean values of net radiation, air and surface temperatures remain more stable even in the extreme case of spatial homogeneity. This stronger impact of surface properties spatial aggregation on turbulent fluxes than on other quantities such as net radiation and surface temperature is in accordance with Kustas et al. (2004). As it is the fact that surface quantities spatial distribution and intensity change dramatically when the resolution used in surface heterogeneity description is coarser than the spatial scales of the single patches. The field scale has been identified to be a threshold spatial resolution even for information from remote sensing (Anderson et al., 2004).

Figure 8.7, 8.8 and 8.9 show time-averaged differences between the simulations with aggregated surface information and the reference for H, LE and Rn respectively. Each line of the figures corresponds to a different averaging interval: morning, central part of the day and afternoon. The maps are a sort of negative of the results obtained with each resolution. Hence, evident surface shapes in these figures mean that they are not reproduced in the simulations as they should. In turbulent fluxes maps (Figure 8.7 and 8.8) deviations from the ref-

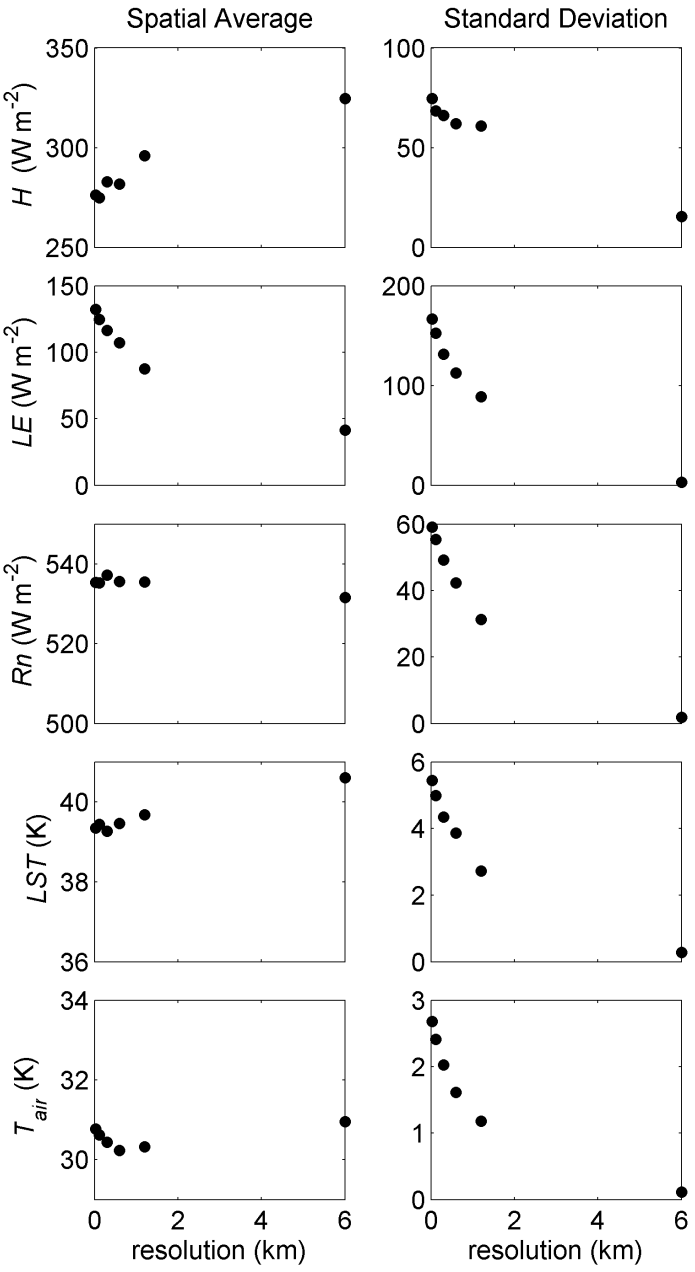

Figure 8.6: Spatial average and standard deviation of time-averaged maps of surface sensible heat flux H, surface latent heat flux LE, net radiation Rn, land surface temperature LST and air temperature T_{air} in function of the spatial resolution of surface parameters. Time-averaging interval is 12:45 - 13:15 UTC.

erence within ± 20 Wm^{-2} are in white, in order to better focus on more relevant values. Following the same rationale the white range in Figure 8.9 is ± 0.5 ^{o}C. Local significant differences in respect to the reference results are present in all the averaging intervals, with greater values in the central part of the day and in the afternoon, i.e. when the reference quantities themselves are greater. It can be seen that for all the three quantities surface heterogeneity patches increasingly disappear as the resolution becomes coarser than the characteristic length scale of the patches themselves. Hence, for this case study, as

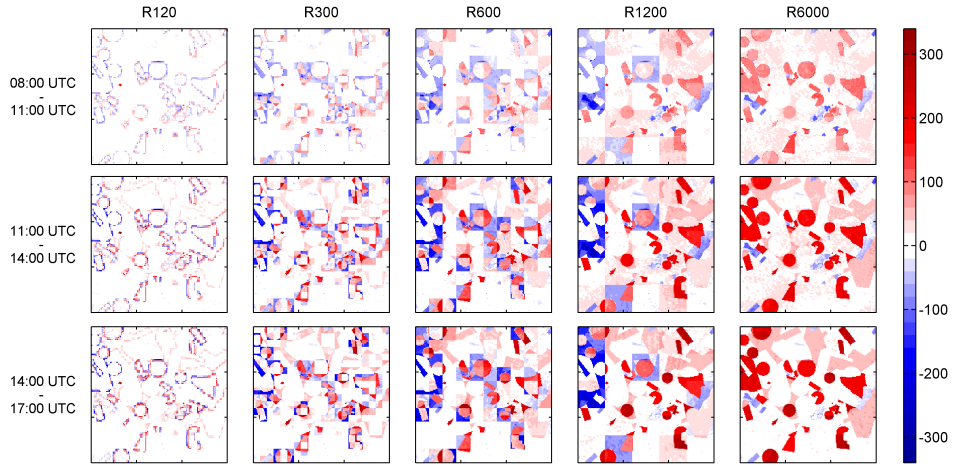

Figure 8.7: Maps of time-averaged difference of surface sensible heat flux H in respect to the reference simulation $R30$. The first line corresponds to the averaging time interval 08:00-11:00 UTC, the second line to 11:00-14:00 UTC and the third line to 14:00-17:00 UTC. Maps are in Wm^{-2}.

already noticed, surface heterogeneity is almost completely lost with a resolution of 600 m. As expected sensible and latent heat fluxes show an opposite tendency, with the first one increasing in areas where the second one decreases. But more intense local differences are present in LE (up to more than 300 Wm^{-2}) than in H (up to about 100 Wm^{-2}). Land surface temperature maps show local deviations up to more than 10 ^{o}C. These high differences are correctly concentrated in those areas where turbulent fluxes have greater mismatches with the reference.

8.2.3 Other results

Figure 8.10 shows time series of domain averaged surface sensible and latent heat fluxes, net radiation and evaporative fraction $EF = \frac{LE}{LE+H}$.

The spatial average of net radiation is not influenced by the resolution used for surface heterogeneity representation and it remains constant between runs during all the diurnal cycle. This fact is in accordance with what observed by Brunsell et al. (2011). The sensible heat flux almost maintains its domain average with the finer grid resolutions, even in $R600$, where surface patches are practically already disappeared. In fact runs that appreciably differ from $R30$ are only $R1200$ and $R6000$, with the latter producing a higher domain-averaged H of about 70 Wm^{-2} and the first one of about 30 Wm^{-2}. Differences appear around 10:00 UTC and remain almost constant until 17:00 UTC. The latent heat flux shows a similar behaviour, with only $R1200$ and $R6000$ producing a domain-averaged LE that significantly underestimates that of $R30$ from around 10:00 until 17:00 UTC. Coherently with these results the evaporative fraction diminishes as the resolution used for surface heterogeneity description coarsens, again with appreciable differences from $R30$ only in $R1200$ and $R6000$. In this extreme case of spatial homogeneity, the underestimation amplifies during the day, passing for instance from 0.25 of the reference to 0.1 at 12:00 UTC. This impact on energy partitioning can be explained by the particular nature of the surface heterogeneity in this case study. In fact the domain is mainly dry, and only small sparse areas with relevant soil moisture are

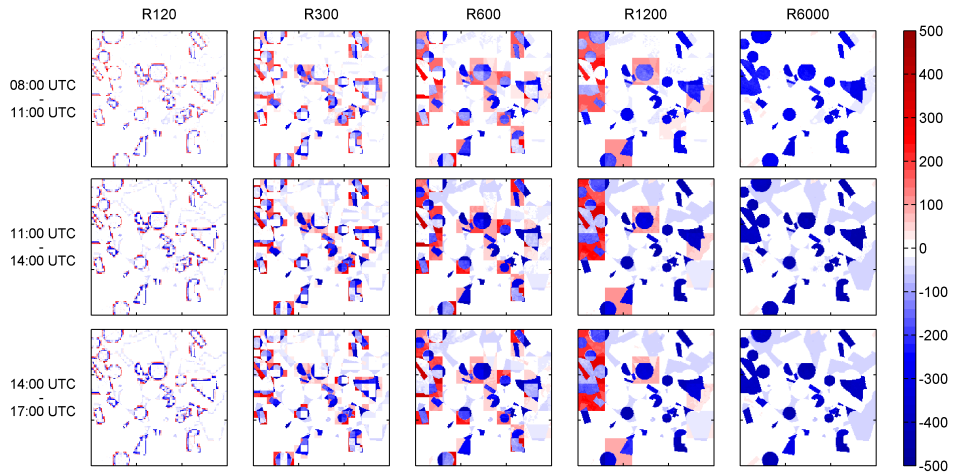

Figure 8.8: Maps of time-averaged difference of surface latent heat flux LE in respect to the reference simulation R30. The first line corresponds to the averaging time interval 08:00-11:00 UTC, the second line to 11:00-14:00 UTC and the third line to 14:00-17:00 UTC. Maps are in Wm^{-2}.

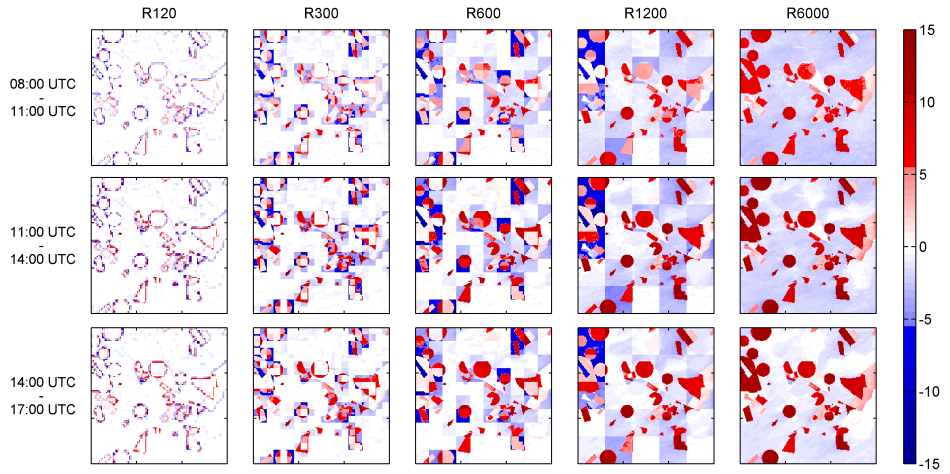

Figure 8.9: Maps of time-averaged difference of land surface temperature in respect to the reference simulation R30. The first line corresponds to the averaging time interval 08:00-11:00 UTC, the second line to 11:00-14:00 UTC and the third line to 14:00-17:00 UTC. Maps are in ^{o}C.

present (see Figure 7.7). These wet fields generate significant latent heat flux during the day until the spatial resolution used for surface characterization is finer enough to correctly represent them. But when these small patches of concentrated soil moisture are averaged over a too large area, the soil remain dry and LE dramatically decreases, as shown also in Figure 8.8.

Figure 8.11 shows two points spatial autocorrelation along $x-$direction of land surface temperature (on the left) and of air temperature close to the surface (on the right). The spatial correlation is computed using equation (7.1). It can be seen that the autocorrelation function is preserved up to $R600$ for both variables, and that only $R1200$ and $R6000$ differ from the reference. Coherently with the fact that surface heterogeneity assumes scales larger than the real ones because of the very coarse resolution, in $R1200$ temperatures remain more correlated than in $R30$, and do more in the extreme case of spatial homogeneity of $R6000$.

Another examined quantity is the thermal blending height, usually defined as the height above the surface at which the influence of surface heterogeneity on potential temperature turbulent structures becomes negligible. Here we estimate thermal blending height following Huang and Margulis (2009), namely through the vertical profile of the coeffi-

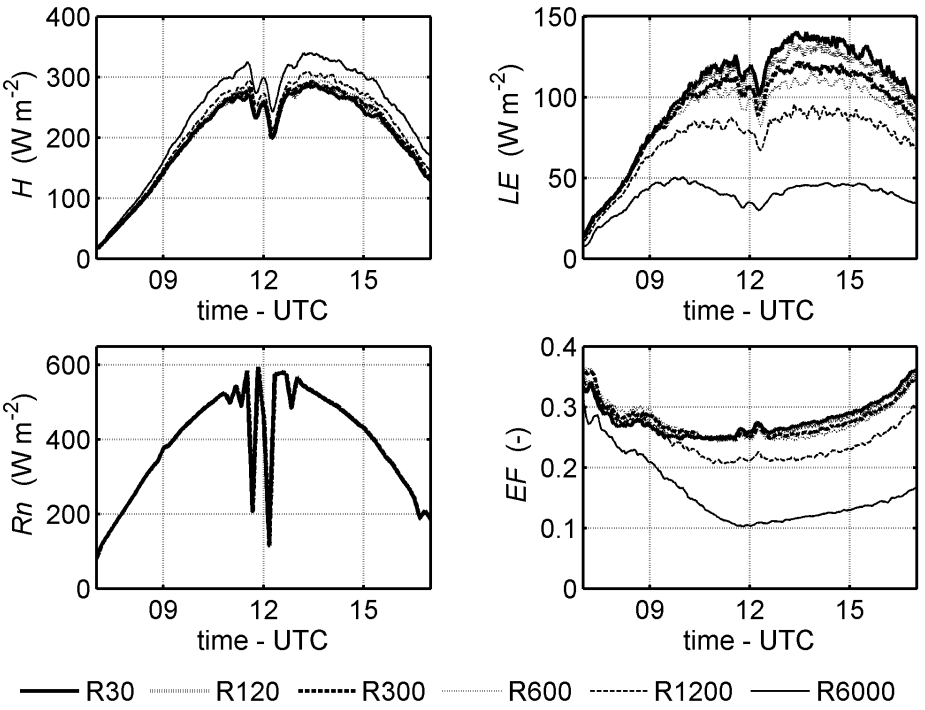

Figure 8.10: Time series of domain-averaged surface sensible heat flux H, surface latent heat flux LE, net radiation Rn and evaporative fraction EF.

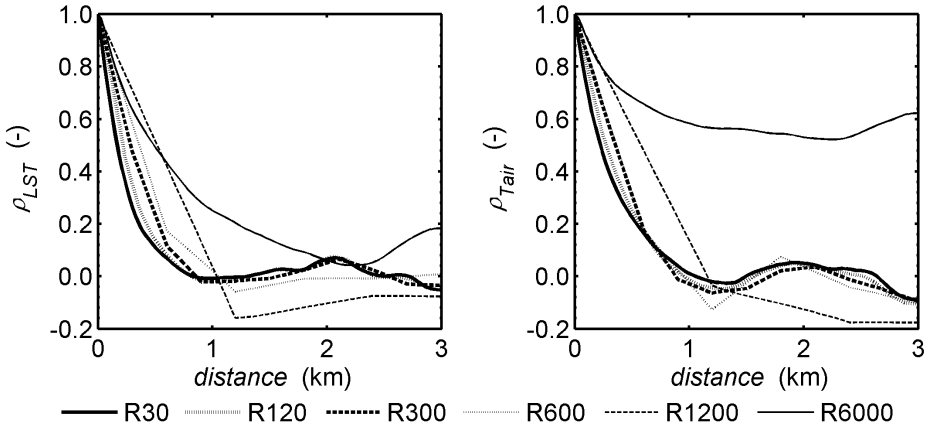

Figure 8.11: Two points spatial autocorrelation of land surface temperature LST and air temperature T_{air} along $x-$direction.

cient of variation of potential temperature CV_θ, computed as

$$CV_\theta(z) = \frac{\sigma_\theta(z)}{\mu_\theta(z)} \tag{8.1}$$

where μ_θ is the plane-averaged potential temperature θ and σ_θ is its spatial standard deviation. By definition a homogeneous surface has a blending height equal to zero. Hence, it is assumed that the close to the surface CV_θ of the homogeneous simulation is representative of a *blended* potential temperature. Consequently, the height at which the CV of heterogeneous simulations assumes the value of the surface CV of the homogeneous case is assumed to be the thermal blending height. Figure 8.12 shows the time-averaged profiles obtained for the interval 12:45 - 13:45 UTC. It can be seen that the reference simulation has a thermal blending height of about 30 m. This value is almost preserved in all the other simulations, with blending heights in the range 30-35 m.

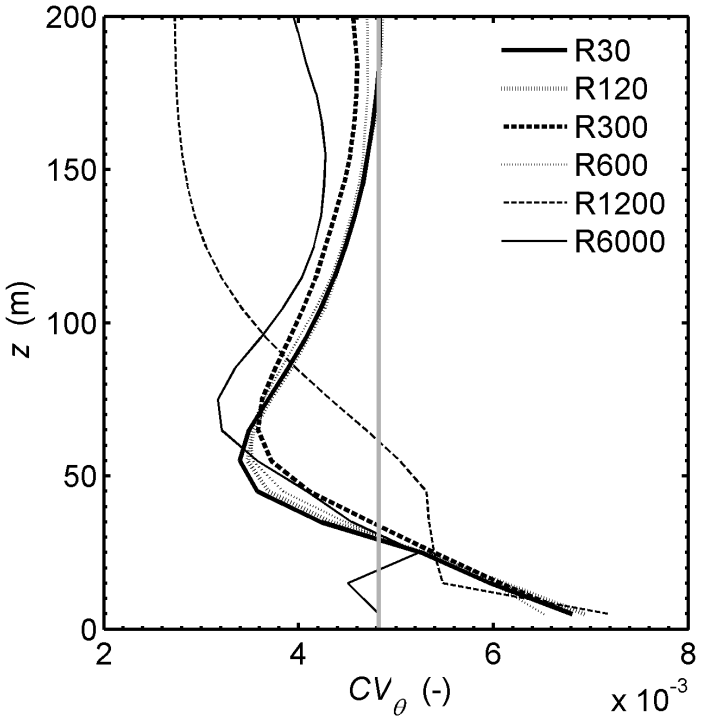

Figure 8.12: Time-averaged (from 12:45 to 13:45 UTC) vertical profile of the coefficient of variation for potential temperature. The vertical coordinate of the intersection with the gray line identifies the thermal blending height.

The only exception is $R1200$, for which a noticeably higher value (about 65 m) is detected. As already found for the spatial correlation, this fact evidences that the artificially enlarged heterogeneity scale induced by the very coarse resolution used for surface representation in $R1200$ influences the ABL turbulence in the surface layer, generating more correlated and persistent structures. LES recovered blending height increasing with surface heterogeneity organization has been detected also in Huang and Margulis (2009).

Finally, Figure 8.13 shows instantaneous vertical sections of $w-$velocity in the $xz-$plane for the performed simulations. No clear visual differences between the runs can be deduced, with the possible exception of $R300$, for which more organized and intense structures seem to be present and might be related to what observed for the vertical velocity variance profile reported in Figure 8.3.

8.3 Conclusions

The role of surface heterogeneity level of description in coupled LES-LSM has been investigated. In such kind of simulations both horizontal and vertical grid spacings are determined by LES needs (see Chapter 5 and 6). Therefore it is possible that the resolution of the available information for surface characterization does not match that imposed by LES. Consequently, we have assessed the impact of using surface parameters maps with a coarser resolution than that required by LES in terms of both ABL bulk characteristics and surface processes. To this aim five coupled simulations with a progressively coarser description of the surface have been realized and compared to the reference run in which surface heterogeneity is represented using the same spatial resolution of that imposed by the LES. The setup is exactly that employed in Chapter 7, with input maps of the LSM resampled at 120, 300, 600, 1200 and 6000 m. It is important to underline that when geostrophic wind is relevant, as it is in our case (about 8 ms^{-1}), the impact of surface heterogeneity on ABL is mitigated (Hadfield et al., 1992, 1991; Avissar and Schmidt, 1998, e.g.). Hence analogous tests should be repeated in absence of significant geostrophic wind to better clarify the situation.

The impact on ABL turbulence has been assessed through velocity spectra and mean vertical profiles of sensible heat flux, potential temperature and velocity variances. A minor impact has been observed

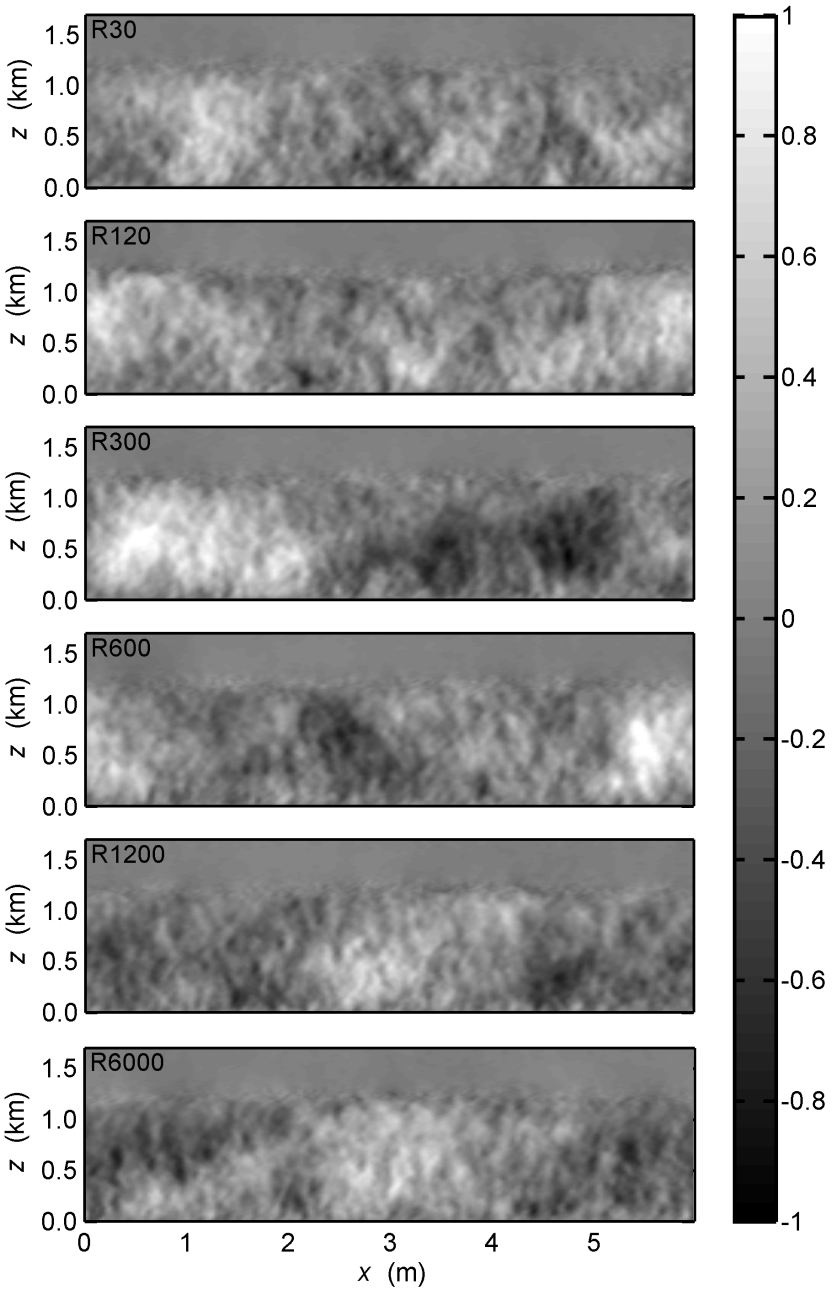

Figure 8.13: Instantaneous vertical sections of $w-$velocity component (ms^{-1}) in the $xz-$plane.

on bulk thermal properties of the simulated ABL. In fact the effect on domain-averaged profiles of vertical sensible heat flux is negligible, and potential temperature profiles are slightly influenced by the level of aggregation of surface heterogeneity. Only the homogeneous simulation $R6000$ shows a mixed layer temperature different from that of the reference $R30$, specifically 1 ^{o}C warmer. Therefore, it can be concluded that thermal properties are mainly dependent from the spatial average of sensible heat flux, whose difference from the reference is significant only in the homogeneous case for our analysis. Profiles of velocity variance has resulted to be more sensitive to the level of aggregation of surface heterogeneity. Variance of both vertical and horizontal profiles changes in function of the resolution of the surface maps and the effect varies for the considered scales of representation. Initially ($R120$ and $R300$) coarsening the resolution causes a progressively increase of the variance in the upper part of the ABL and a decrease in the lower part. $R300$ profiles differ significantly from the reference, even if surface patchiness is still well represented at this resolution. Passing to $R600$, the variances are more similar to those of the homogeneous case $R6000$ than to those of the reference, and they are the weakest obtained. This tendency is reversed in $R1200$, whose profiles are the most similar to the reference. The above-said results seem to suggest that a level of aggregation in surface heterogeneity that still represents correctly the patchiness does not automatically assure the maintenance of turbulence characteristics in the ABL. Furthermore, when the resolution becomes coarser than the surface patches ($R600$), the effect of the heterogeneity seems to be almost lost. But $R1200$ could suggest that a coarse scale, which does not reproduce surface heterogeneity from a visual point of view but which has a resolution comparable with the ABL height, can mimic the effects of a more detailed description of surface patchiness in terms of ABL turbulence. Spectral analysis has shown that the resolution used for surface heterogeneity description mainly affects larger-scale turbulent structures, while smaller eddies can be considered almost insensitive to it. In particular, in the middle of the ABL we have observed a noticeable impact on length scales ranging from about 600 to 6000 m. This impact is more evident in vertical velocity spectrum than that of the horizontal velocity. $R6000$ and $R300$ have the least energetic $w-$velocity fields for the whole range of larger-scales (600-6000 m). Instead, for $u-$velocity, $R600$ and $R1200$ have more energy than the other simulations associated to the largest eddies in the flow. In terms of thermal blending height, it has been

found that only $R1200$ does not match the reference value of about 30 m, suggesting again that its level of organization of surface heterogeneity has exceeded a threshold value over which surface patchiness impacts become of a different nature in respect to those of the reference. The effect of heterogeneity level of representation at the surface is evaluated in terms of variations of both spatial distribution and time series of sensible and latent heat fluxes, and of surface and air temperatures. The general result is that domain-averaged values of turbulent fluxes are more sensitive to surface maps resolution than those of the other quantities. In particular, they almost preserve their average until the resolution is comparable with the characteristic scale of the surface patches (in our case until 600 m), while mean net radiation remains nearly constant for all the performed runs. Both air and land surface temperature averages differ from the reference only in $R1200$ and $R6000$. But local differences in surface quantities can be significant also at higher resolutions, e.g. 100 Wm^{-2} in turbulent fluxes and 5 ^{o}C in land surface temperature in $R300$, indicating that their spatial distribution and intensity change dramatically when the resolution used in surface heterogeneity description is coarser than the spatial scales of the single patches.

In conclusion, it can be asserted that the impact of surface heterogeneity level of description on surface quantities, such as turbulent fluxes and air or land temperature, becomes highly significant as the resolution approaches the characteristic length scale of the surface patches and increases as this limit is exceeded. But in terms of ABL turbulence this monotonic impact is not observed. In fact noticeable differences in turbulence properties are evidenced even at scales for which surface patchiness is still captured (e.g. $R300$), and the resemblance that is progressively lost as the resolution is coarsened could be partially recovered with larger scales of aggregation (e.g. $R1200$). But at the same time a representative length of heterogeneity organization comparable with the ABL height works as a sort of threshold value over which ABL characteristics significantly differ from those obtained with less organized turbulence.

9

Meteorological forcings from RAMS-LES: effect of spatial distribution on an energy and water balance model

In this chapter the role that the meteorological forcings microscale spatial distribution has in a surface energy and water balance is investigated. A distributed energy and water balance model requires spatially distributed inputs in terms of even meteorological forcings and not only of surface parameters. But typically only punctual measurements of incoming shortwave radiation, wind speed, air temperature and air humidity are available, and therefore spatial interpolation is needed to generate maps of these meteorological inputs. The impact of the errors introduced by the interpolation on the energy and water balance could be rigorously assessed only if distributed meteorological data were available at very high spatial resolution in a sufficiently wide area. Here we attempt to realize such assessment using meteorological forcings obtained from the coupled LES-LSM experiment of Chapter 7 as a proxy for real atmospheric fields. In fact, as extensively discussed in Section 3.3, a coupled LES-LSM represents nowadays the most adherent to the reality modelling instrument for ABL, being able to reproduce both atmospheric turbulence and the feedback existing between the surface and the overlaying air (Shao et al., 2013). Therefore, we force an energy and water balance model with physically based distributed inputs of wind speed, air temperature and air humidity in order to generate reference results. Then these reference results are compared with outputs obtained by using interpolated meteorological inputs. For the interpolation the standard Inverse squared-Distance

Weighting (squared-IDW) method (Shepard, 1968) and an alternative procedure proposed and tested in this analysis are used. The punctual registrations at the basis of the interpolations are from virtual measurements stations placed in the simulation domain of the coupled LES-LSM. The impact of the meteorological forcings spatial distribution on the surface energy and water balance is assessed also taking into account the mitigation or amplification of the interpolation error from inputs to outputs.

The chapter is structured with the description of the numerical experiments in Section 9.1 and a focus on the proposed interpolation method in Section 9.1.1. Results of the analysis are presented in Section 9.2 and conclusions are discussed in Section 9.3.

9.1 Experiment setup

In order to assess the impact of meteorological forcings spatial pattern on surface energy and water balance, seven simulations are here performed using the distributed hydrological model FEST-EWB (Corbari et al., 2011). The model imposes the closure of the surface energy balance $Rn - G = H + LE$ in each single cell of the domain, and retrieves from it a representative thermodynamic equilibrium temperature for the land surface, being the latter the unique unknown of the equation. Using the representative thermodynamic equilibrium temperature all the terms of the energy balance are estimated and soil moisture is updated on the basis of the computed LE. A more detailed description of the model can in be found in Appendix 9.4. The simulated domain is the same used in Chapter 7, with an extension of 6×6 km, and the same computational spatial resolution is used for its discretization, i.e. 30×30 m. Simulations are all run for one single diurnal cycle with a time-step of 15 minutes. FEST-EWB requires as input surface parameters and meteorological forcings maps, being a spatially distributed code. The reference run uses air temperature, wind speed and air humidity maps from the coupled LES-LSM simulation of Chapter 7. In fact a coupled LES-LSM can provide physically based meteorological forcings fields, being able to reproduce both atmospheric turbulence and the feedback existing between the surface and the overlaying air (Shao et al., 2013). Therefore, its results are here used in substitution of high spatial resolution meteorological measurements. The maps employed as inputs for FEST-EWB

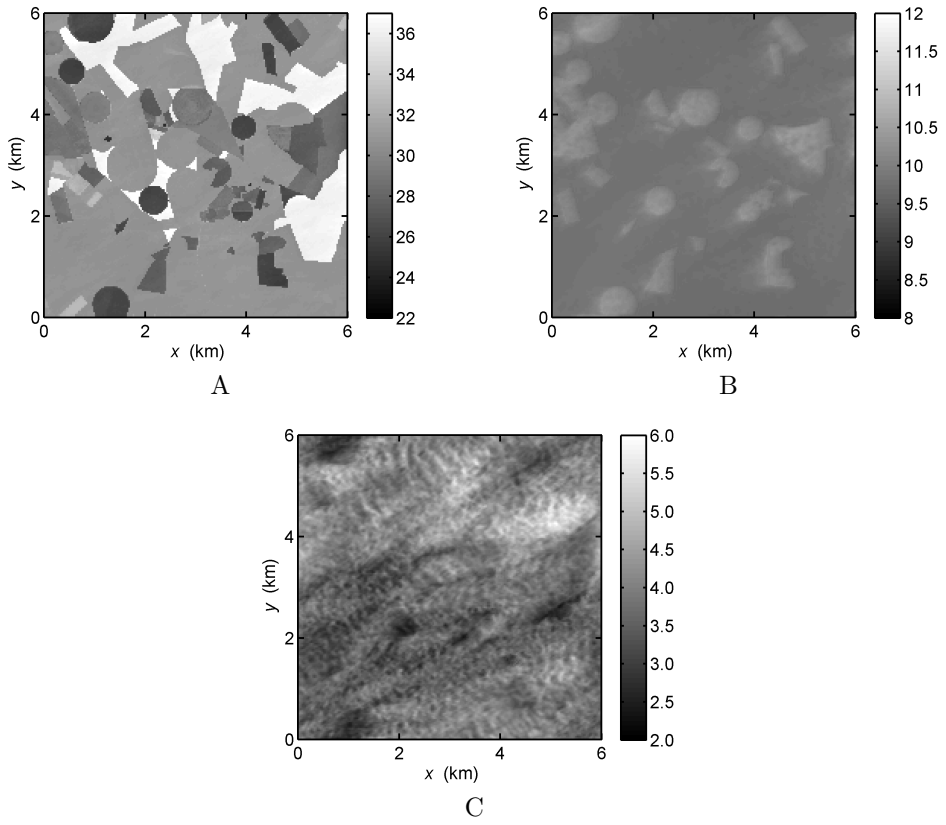

Figure 9.1: Maps of meteorological inputs used in the reference simulation. A is air temperature (^{o}C), B is air humidity in water vapour mixing ratio (gkg^{-1}), C is wind speed (ms^{-1}). Data are time-averages of RAMS results over 15 minutes centered at 13 : 08 UTC.

are time-averages over a period of 15 minutes. The data from RAMS are associated to a height of 5 m. Figure 9.1 shows an example of physically based fields of air temperature (A), air humidity (B) and wind speed (C) used in the reference simulation. It can be seen from both air temperature and humidity that the area can be thought as characterized by a background diffused condition with spot patches of different nature. Incoming shortwave radiation is that shown in Figure 7.9 and it is maintained homogeneous over the domain since its limited extension. The model requires also maps of typical surface parameters as albedo, vegetation fraction, emissivity, roughness length and stomatal resistance. We employ the maps described in Section 7.2, with the exception of roughness length and stomatal resistance, that

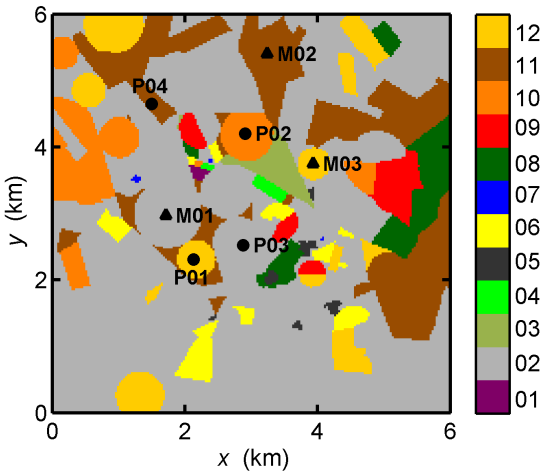

Figure 9.2: Land use map of the simulated domain with localization of virtual meteorological stations $M01$, $M02$, $M03$ and of control points $P01$, $P02$, $P03$, $P04$. Land use classes are indicated in Table 7.1

have been calibrated with a trial and error procedure against measurements presented in Section 7.3. The comparison between the model predictions and the observation is not shown here, since the only aim of the calibration was to obtain reasonable results. In fact the focus is on comparing the reference simulation against those using interpolated inputs, and not against measurements.

The role of spatial distribution of meteorological forcings is assessed by performing six simulations that use the just described setup, but whose maps of air temperature, wind speed and air humidity come from punctual information. We have placed three virtual meteorological stations in the domain of the coupled LES-LSM. Their localization is shown in Figure 9.2. The three stations are tunefully distributed over the simulated area and placed in fields with different characteristics. $M01$ is in a stubble field, that is representative of most of the simulated domain, $M02$ is over bare soil and $M03$ is in a vegetated area. Six different groups of meteorological inputs (air temperature, air humidity and wind speed) are built using data registered at the three virtual stations and used to force six simulations. Maps of simulations $M01$, $M02$ and $M03$ are spatially homogeneous, using data from stations $M01$, $M02$ and $M03$ respectively. Maps of $M04$ are obtained with the squared-IDW method applied to data from stations

$M02$ and $M03$. $M05$ is analogous but uses data from all the three stations. Finally, $M06$ interpolates air temperature and humidity with an alternative procedure that is here proposed and described in Section 9.1.1. Instead, wind speed maps of $M06$ are reconstructed with the standard squared-IDW method. The alternative method interpolates meteorological forcings fields on the basis of surface resemblance between the area corresponding to the available measurement stations and the points where the information is to be estimated, and not on the basis of physical distance between known and unknown points. Figure 9.3 shows air temperature maps obtained for 13 : 08 UTC. It can be seen that only $M06$ reproduces the spatial variability present in the reference physically based field (see Figure 9.1.A), while in the others it is completely absent. In fact, the complexity of meteorological patterns, that at the microscale mainly arises from surface heterogeneity, can not be reconstructed on the basis of physical distance with only three known points, although organically distributed in the area. While taking into account surface characteristics allows to better reproduce meteorological forcings spatial distribution.

Figure 9.4 shows differences between interpolated and reference maps of air temperature (A) and humidity (B) at 13 : 08 UTC. The corresponding distributions are reported in Figure 9.5, whose statistics are summarized in Table 9.1 for air temperature and in Table 9.2 for air humidity. $M02$ and $M03$ respectively overestimates and underestimates air temperature in most of the domain, with a domain-averaged error of $+5.30$ ^{o}C and -4.72 ^{o}C. In fact $M02$ approximates air temperature of the whole domain with values characteristics of bare soil, and hence warmer than those of vegetated or rougher areas. On the opposite $M02$ imposes values from a vegetated and moist field, colder than those of drier or less rough areas. Since both $M02$ and $M03$ uses spatially homogeneous maps of meterological quantities, distributions of the differences in respect to the reference are exactly the same for the two cases, but translated towards positive or negative values. Also $M03$ has the same error distribution, but centered around zero and with a significantly smaller mean value (-0.30 ^{o}C). The reason lies in the fact that the imposed air temperature comes from an area that is representative of most of the domain. Therefore the diffused background temperature observed in Figure 9.1 is captured and consequently it is also the domain-averaged value. But Figure 9.5-A clearly shows that the heterogeneity is completely lost. $M04$ and $M05$ maps of air temperature differences in respect to the reference appear very

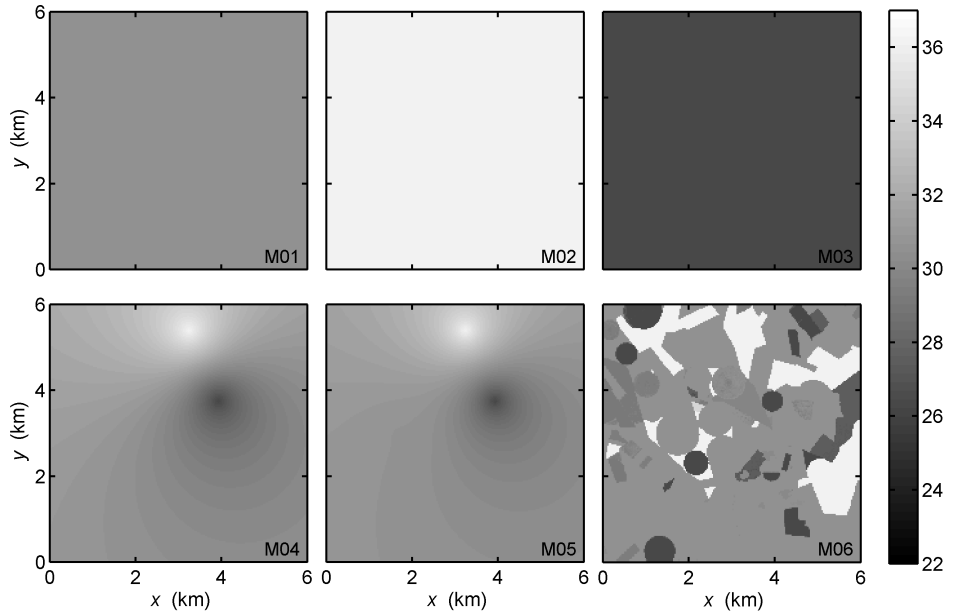

Figure 9.3: Maps of air temperature (^{o}C) obtained on the basis of data registered by the virtual meteorological stations. $M01$, $M02$ and $M03$ use spatial homogeneous data from stations $M01$, $M02$ and $M03$ respectively. $M04$ and $M05$ are squared-IDW interpolations of measures from $M02$ and $M03$ and from $M01$, $M02$ and $M03$ respectively. $M06$ is obtained by applying the alternative interpolation method. All the maps refer to 13 : 08 UTC.

similar between them, and comparable with $M01$ map, meaning that only the spatial mean is reproduced but not the heterogeneity. In fact domain-averaged error is small for both cases and close to that of $M01$ (-0.19 ^{o}C and -0.22 ^{o}C respectively), but the range within which the 80% of the errors lies is still wide (around 7.5 ^{o}C for both cases), although slightly lower than that of the homogeneous maps (8.5 ^{o}C). These observations suggest that a squared-IDW interpolation can not reproduce microscale heterogeneity in case of surface characteristics dissimilarities that are not geometrically organized into large macro-areas, but sparse and fragmented, unless using a unsustainable number of measurements stations. $M06$ seems to overcome these limitations, producing an air temperature field where such heterogeneity is captured, as shown in Figure 9.4-A. Coherently the error distribution has a significant lower standard deviation, i.e. 0.86 ^{o}C against about 2.70 ^{o}C of the other cases, and the 10^{th} and 90^{th} are equal to

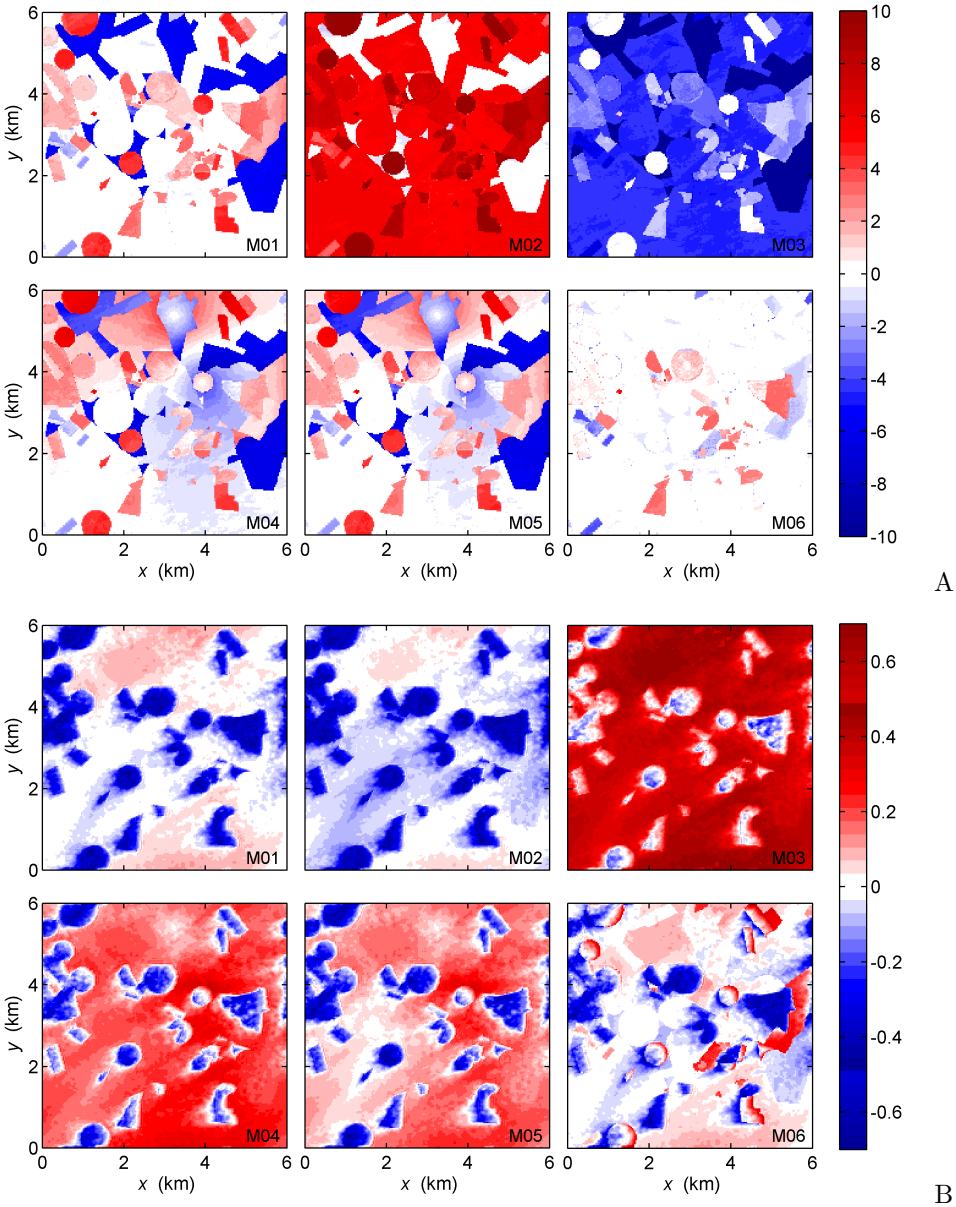

Figure 9.4: Differences between interpolated and reference maps of air temperature (A - (^{o}C)) and water vapour mixing ratio (B - (g kg^{-1})). Interpolation methods are those described in Figure 9.3.

-0.39 ^{o}C and $+0.42$ ^{o}C with the 80% of the errors within a range of 0.81 ^{o}C centered around zero. Also the domain-averaged error is reduced to 0.06 ^{o}C. Therefore, as already observed, taking into account surface characteristics allows to better reproduce microscale variations of air temperature than using a classical IDW interpolation. Analogous considerations can be made about air humidity on the basis of maps of Figure 9.4-B and distributions of Figure 9.5-B with the corresponding statistics reported in Table 9.2. But the physically based air humidity field is less heterogeneous than the temperature one (see Figure 9.5-A and -B), mainly because of the diffused dry condition of the soil throughout the domain, and therefore the above-discussed observations about air temperature are here still valid but less pronounced. In addition, the error distribution shows a fat and long left tail for all the interpolation methods, indicating that part of the heterogeneity remains unresolved. Although this fact, $M06$ remains the best approximation of the physically based field of air humidity, as demonstrated by the statistics of Table 9.2 and the visual inspection of the maps and the corresponding distributions. In particular, it can be noticed that the only error distributions with the mode around zero are $M06$ and $M01$, suggesting that in this case IDW interpolation can even cause a slight worsening of the reconstruction in respect to that obtained by using a homogeneous value from the background area of the domain.

Figure 9.6 shows time series of air temperature for the six interpolations and the reference in the four control points $P01$, $P02$, $P03$ and $P04$, whose locations are reported in Figure 9.2. They are placed over fields with different land covers. In particular, $P01$ and $P02$ are in vegetated areas, $P03$ corresponds to stubble and $P04$ to bare soil. The diurnal evolution of air temperature is matched at each control point by data from the same surface class, e.g. in $P04$ by $M02$ or in $P03$ by $M01$. But only $M06$ adequately reproduces time series in all the four control points, confirming that IDW interpolation has limitations in dealing with microscale heterogeneity of meteorological quantities such as air temperature. In fact local interpolation errors can even exceed 5 ^{o}C for IDW method ($M04$ and $M05$).

9.1.1 Alternative interpolation method

The spatial interpolation procedure used for $M06$ maps is based on the idea that at the microscale, where large scale atmospheric condi-

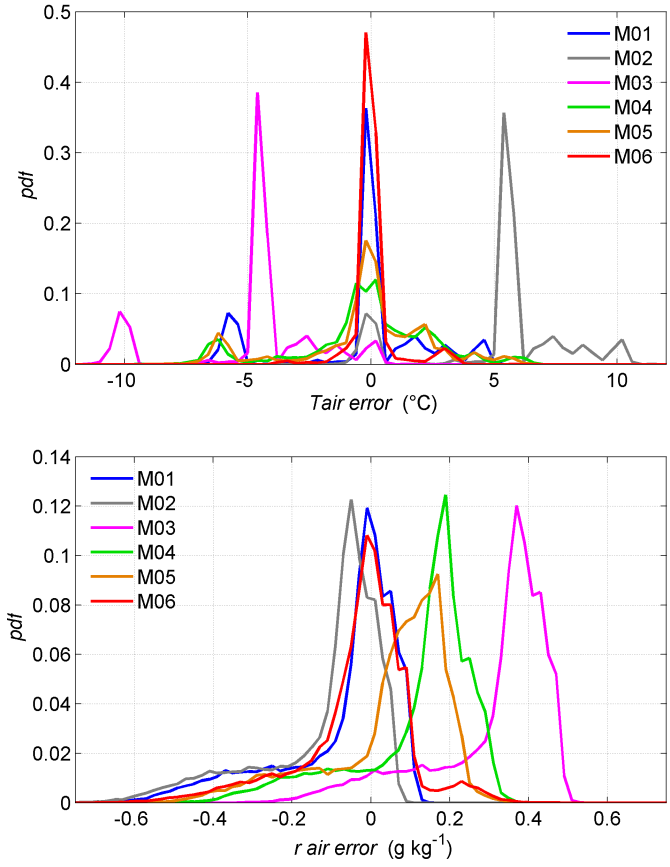

Figure 9.5: Distributions of differences between interpolated and reference maps of air temperature (A) and water vapour mixing ratio (B). Interpolation methods are those described in Figure 9.3. Distributions refer to 13 : 08 UTC.

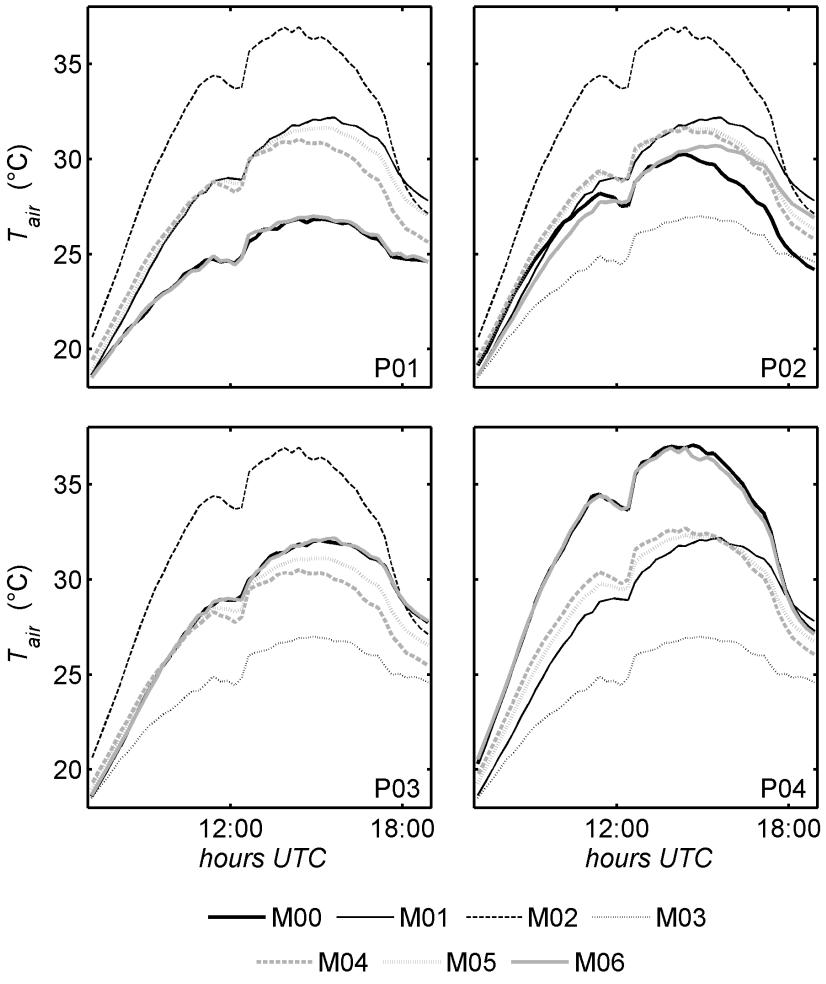

Figure 9.6: Time series of air temperature (^{o}C) in the control points from the reference $M00$ and the interpolated inputs. Interpolation methods are those described in Figure 9.3.

	Mean	STD	Skewness	10^{th} pr	90^{th} pr	$(90^{th} - 10^{th})$	MAE
$M01$	−0.30	2.69	−0.77	−5.59	2.94	8.52	1.65
$M02$	5.30	2.69	−0.77	0.02	8.54	8.52	5.36
$M03$	−4.72	2.69	−0.77	−10.00	−1.48	8.52	4.73
$M04$	−0.19	2.76	−0.59	−4.57	2.82	7.39	1.95
$M05$	−0.22	2.68	−0.67	−5.08	2.57	7.64	1.82
$M06$	0.06	0.86	1.30	−0.39	0.42	0.81	0.42

Table 9.1: Mean, standard deviation STD, skewness, 10^{th} and 90^{th} percentile, the distance between them and the mean of the absolute value (namely the mean absolute error in respect to the reference, MAE) of the distribution shown in Figure 9.5-A, i.e. air temperature (^{o}C) difference in respect to the reference.

	Mean	STD	Skewness	10^{th} pr	90^{th} pr	$(90^{th} - 10^{th})$	MAE
$M01$	−0.07	0.15	−1.42	−0.33	0.07	0.39	0.11
$M02$	−0.11	0.15	−1.42	−0.37	0.02	0.39	0.13
$M03$	0.31	0.15	−1.42	0.05	0.45	0.39	0.32
$M04$	0.12	0.15	−1.39	−0.13	0.26	0.39	0.18
$M05$	0.05	0.16	−1.31	−0.20	0.19	0.40	0.14
$M06$	0.03	0.14	0.95	−0.22	0.09	0.32	0.09

Table 9.2: Mean, standard deviation STD, skewness, 10^{th} and 90^{th} percentile, the distance between them and the mean of the absolute value (namely the mean absolute error in respect to the reference, MAE) of the distribution shown in Figure 9.5-B, i.e. air humidity (gkg^{-1}) difference in respect to the reference.

tions are the same, the most important factors determining the spatial variability of quantities such as air temperature and humidity are surface characteristics. An analogous rationale was followed by Joly et al. (2003), where air temperature fields were interpolated at the very fine scale of 2×2m taking into account land cover properties of the area. Spatial interpolation of meteorological quantities have always been a relevant issue (e.g. Barnes, 1964), but literature is focused mainly on evaluation and improvements of methods at the regional scale (e.g. Nuss and Titley, 1994; Robeson, 1994; Courault and Monestiez, 1999; Hijmans et al., 2005). But when the final aim is to use maps of such variables at the microscale, for instance for agrometeorological or hydrological simulations at the field scale, some limitations could appear in procedures mainly designed to work at larger scales (Pape et al., 2009).

Therefore the method here proposed is based on surface resemblance between the points with known data and those where the variable has

to be estimated, and not on the physical distance between them. The two surface characteristics here employed to quantify surface resemblance are the roughness length z_0 and the vegetation fraction f_v. The value of a generic variable X in a point i is computed as the weighted average between the estimates based on roughness length resemblance $X_{i_{z0}}$ and vegetation fraction resemblance $X_{i_{fv}}$. The optimal weights for the present application have been evaluated to be $\beta_{z0} = 0.7$ and $\beta_{fv} = 0.3$.

$$X_i = \beta_{z0} X_{i_{z0}} + \beta_{fv} X_{i_{fv}} \tag{9.1}$$

The estimates $X_{i_{z0}}$ and $X_{i_{fv}}$ are computed as weighted averages of the known values $\hat{X}_j$ with weights proportional to the inverse of the squared distance in terms of roughness length and vegetation fraction respectively.

$$X_{i_{z0}} = \sum_j \alpha_{ij_{z0}} \hat{X}_j \tag{9.2}$$

$$X_{i_{fv}} = \sum_j \alpha_{ij_{fv}} \hat{X}_j \tag{9.3}$$

$$\alpha_{ij_{z0}} = \frac{1}{(z_{0i} - z_{0j})^2} \Big/ \sum_j \frac{1}{(z_{0i} - z_{0j})^2} \tag{9.4}$$

$$\alpha_{ij_{fv}} = \frac{1}{(f_{vi} - f_{vj})^2} \Big/ \sum_j \frac{1}{(f_{vi} - f_{vj})^2} \tag{9.5}$$

9.2 Results

Figure 9.7 shows maps of FEST-EWB results at 13 : 08 UTC for the reference simulation, namely that forced by physically based fields of meteorological quantities from the coupled LES-LSM of Chapter 7. Panel A is the net radiation, B, C and D are respectively the soil, sensible and latent heat fluxes and panel E is the land surface temperature. It can be seen that the latent heat flux is very small almost everywhere (around 50 Wm^{-2}) with the exception of few fields, that are the unique non-dry areas of the domain. In those fields the model correctly estimates lower surface temperatures. Figure 9.8 shows maps of differences between simulations with interpolated meteorological forcings and the reference run for selected outputs of the model, i.e. the sensible heat flux (panel A) and the land surface temperature (panel

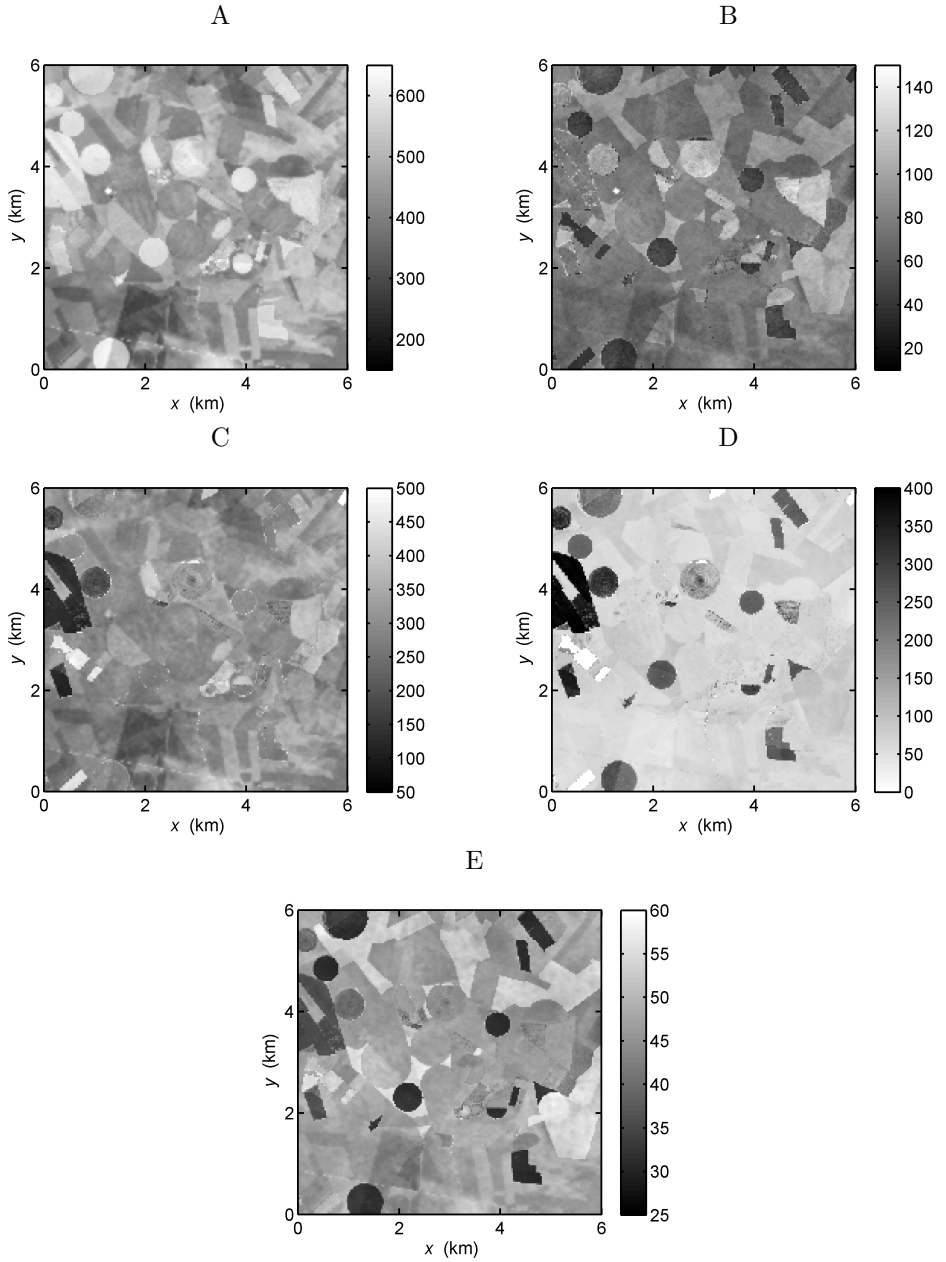

Figure 9.7: Maps of FEST-EWB outputs for the reference simulation at 13 : 08 UTC. A is net radiation (Wm^{-2}), B is soil heat flux (Wm^{-2}), C is sensible heat flux (Wm^{-2}), D is latent heat flux (Wm^{-2}) and E is the representative land surface temperature (^{o}C).

B). The sensible heat flux seems to be less sensitive than the surface temperature to the quality of forcings reconstruction. In fact in most of the domain the error remain lower than about 50 Wm^{-2} in all the simulations, although air temperature and humidity maps are systematically affected by a diffused underestimation (or overestimation). Moreover $M05$ reveals a better agreement with the reference than $M04$, indicating that the introduction of an additional source of information in the IDW interpolation benefits the simulation results as desired. But significant local errors (exceeding also 100 Wm^{-2}) are present in all the simulations with the exception of $M03$ and $M06$. These significant local errors are in those fields where the latent heat flux is not negligible, that in turn means non-dry conditions for the soil. Therefore ,it seems that the limited sensitivity of H to the meteorological forcings reconstruction is only apparent, i.e. strictly related to the particular conditions of most of the simulated domain, namely the diffused dryness of the soil. Soil moisture acts like adding degrees of freedom to the system, increasing the sensitivity of H to the disturbances in the forcings. On the opposite dryness stabilizes the solution in terms of sensible heat flux, namely it results to be highly constrained in presence of dry soil. $M03$ and $M06$ are excluded from this phenomena because they are the only cases in which meteorological conditions are correctly reconstructed over the wet fields. In $M03$ this happens because it uses spatially homogeneous forcings whose values come from a virtual station placed in a similar field. Instead $M06$ is the only interpolation that reproduces microscale heterogeneity in the meteorological forcings as showed in the previous section. The impact of the meteorological forcings spatial distribution reconstruction on H can be further analyzed by using the error distributions showed in Figure 9.9-A and the corresponding statistics of Table 9.3. $M02$, $M05$ and $M06$ are the only cases with the most frequent error being around zero. But $M02$ is characterized by a large dispersion, with a standard deviation of about 46 Wm^{-2} and the 10^{th} and 90^{th} percentile being equal to 58.9 Wm^{-2} and 24.7 Wm^{-2} respectively. Instead, $M01$ shows a tendency to underestimation and both $M03$ and $M04$ to overestimation. However the mode of $M01$ and $M03$ is respectively around ± 25 Wm^{-2} and therefore quite small, and that of $M04$ is even smaller (about 12 Wm^{-2}). This slight tendency to a diffused overestimation of $M04$ is overcome by $M05$, namely by the inclusion of a third source of information in the IDW interpolation. But the better adherence of $M06$ than of $M05$ to the reference results is firstly pointed out by

the smaller dispersion of the error distribution, with a standard deviation of 14 Wm^{-2} against 21 Wm^{-2} of $M05$ and the 80% of the values spread over a range of 34 Wm^{-2} against the 45 Wm^{-2} of $M05$. Secondly $M06$ error distribution is more symmetrical than that of $M05$ with a skewness of -0.09 against -1.45 of $M05$.

As already noticed, the land surface temperature seems to be more influenced by the spatial distribution of the meteorological forcings than sensible heat flux. In particular the control effect that soil moisture exerts on the intensity of the impact on H seems to be not valid for land surface temperature. In fact in the maps of Figure 9.8-B an evident distinction between dry and wet areas in terms of differences with the reference temperature is not present. On the contrary the maps suggest that the pattern of the errors introduced by spatial interpolation in the forcings is mostly maintained for the land surface temperature. For instance in the homogeneous cases not negligible distortions of the surface temperature are present in the whole domain, except that in those areas for which the value of the forcings imposed as homogeneous is representative. Moreover the maps of Figure 9.8-B seems to indicate that the sign of the error is mostly preserved passing from the air to the surface temperature. For instance in $M02$ the general tendency to overestimation observed for air temperature is present also in surface temperature, and at the opposite the diffused air temperature underestimation of $M03$ is maintained in the corresponding surface temperature map. For $M04$, $M05$ and $M06$ cases the situation is more complex since they use spatially heterogeneous maps of the forcings. However, it can be observed that $M05$ shows a better agreement with the reference than $M04$, pointing out again that adding a third source of information in the IDW interpolation improves the the results as desired. Visually $M06$ produces the best match with the reference. It removes almost all the intense and localized residual differences still present in $M05$, and it succeeds in this thanks to the fact that they have been removed from the input maps of air temperature. But a diffused and slight background difference, already found in $M05$, is almost perfectly duplicated in $M06$. This fact suggests that wind speed is the responsible for it, since the two cases uses the same IDW interpolation for it (see Section 9.1). Furthermore, the spatial pattern of this background difference nearly replicates that of wind speed fields (see Figure 9.11 in the Appendix 9.5). The error distributions shown in Figure 9.9-B and the corresponding statistics of Table 9.4 confirm that in our experiments the land surface temperature is more sensitive

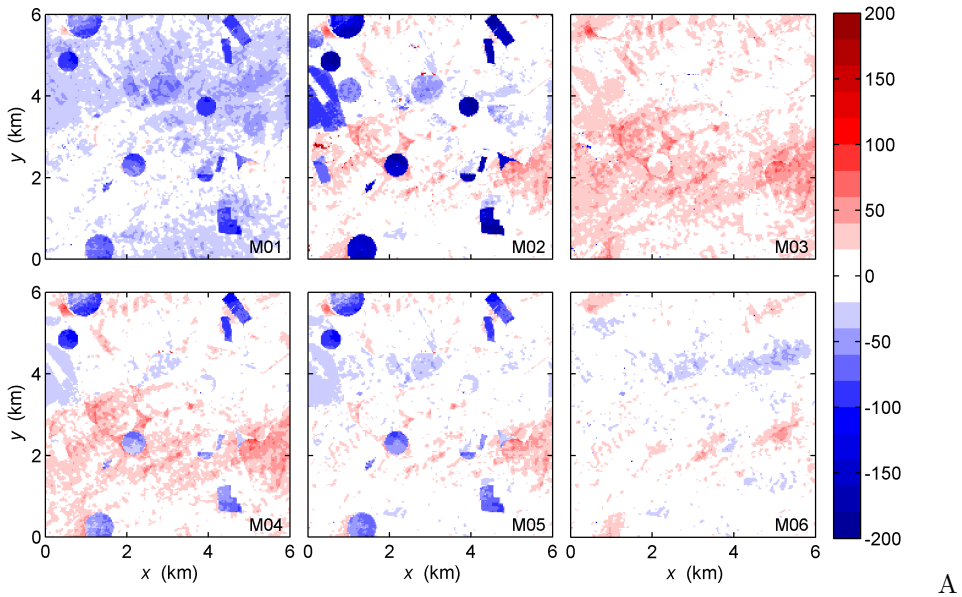

A

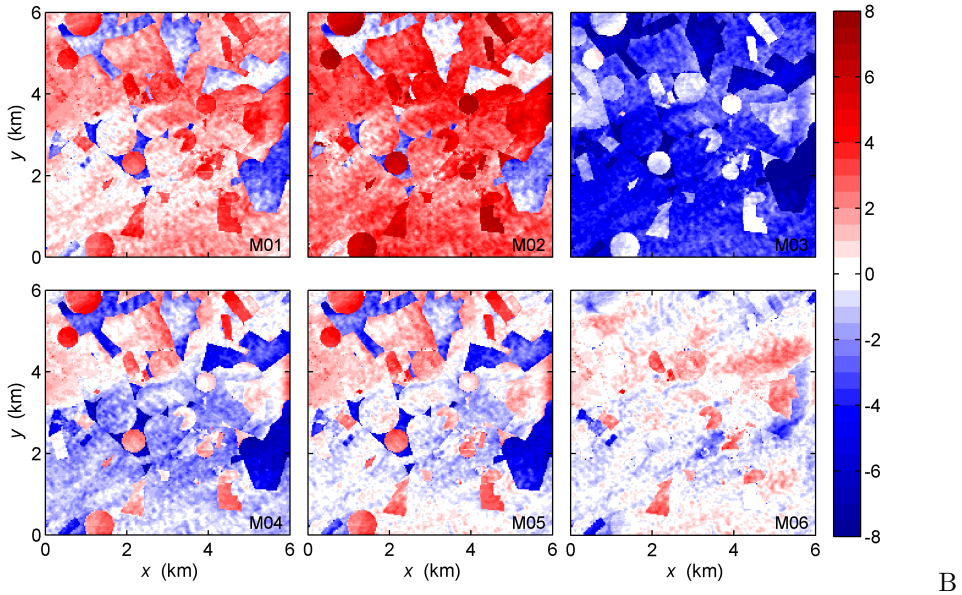

B

Figure 9.8: Maps of differences between simulations with interpolated meteorological inputs and the reference one for sensible heat flux (A - (Wm^{-2})) and representative land surface temperature (B - (^{o}C)). Interpolation methods are those described in Figure 9.3.

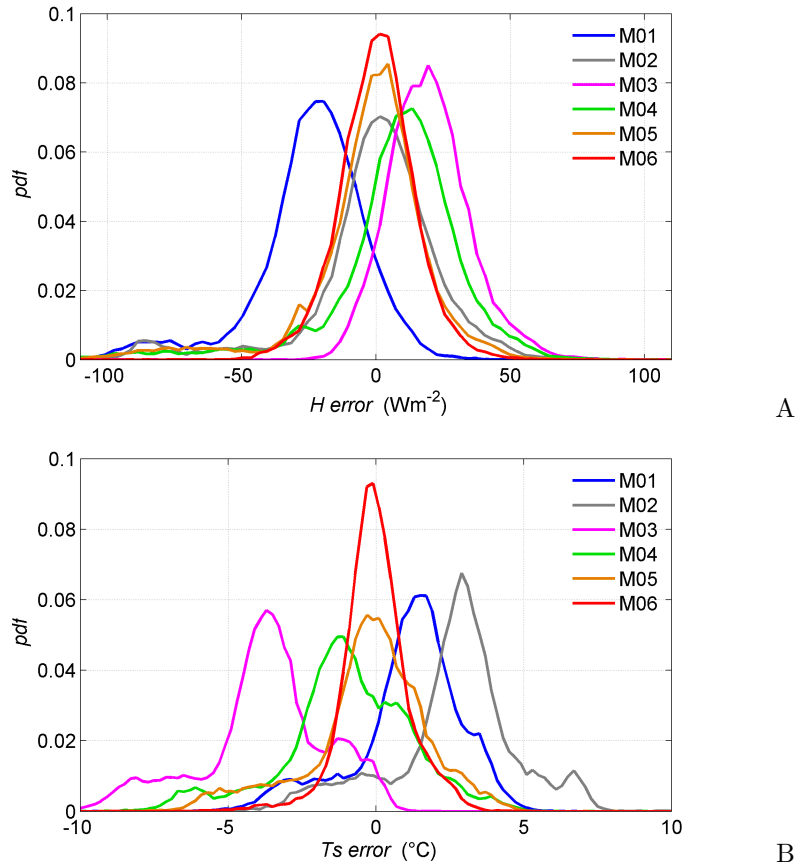

Figure 9.9: Distributions of differences between sensible heat flux (A - (Wm^{-2})) and representative land surface temperature (B - (^{o}C)) maps from simulations with interpolated meteorological inputs and the reference one. Interpolation methods are those described in Figure 9.3. Distributions refer to 13 : 08 UTC.

to the spatial distribution of meteorological forcings than the sensible heat flux. Only $M05$ and $M06$ have the most frequent value around zero and all the distributions show a relevant dispersion with fat tails. The only exception is $M06$. The standard deviation is about 1 ^{o}C for $M06$ and 2 ^{o}C for all the others, and the 80% of the errors lies in an interval of 2.5 ^{o}C in $M06$ and of 6 and 5 ^{o}C for $M03$ and $M04$ or $M05$ respectively. As already noticed from the maps of Figure 9.8-B, $M02$ and $M03$ duplicate the tendency they have for air temperature in terms of land surface temperature, i.e. $M02$ overestimates both while $M03$ underestimates them. But the mean error of +5.3 ^{o}C of

	Mean	STD	Skewness	10^{th} pr	90^{th} pr	$(90^{th} - 10^{th})$	MAE
$M01$	−23.7	20.9	−1.02	−47.1	−0.8	46.3	25.2
$M02$	−9.5	46.1	−2.23	−58.9	24.7	83.6	25.8
$M03$	19.4	15.5	−0.06	1.1	38.6	37.4	20.7
$M04$	7.7	25.4	−1.49	−18.9	32.9	51.8	19.8
$M05$	−2.5	22.9	−1.48	−25.6	19.6	45.2	15.3
$M06$	0.4	14.1	−0.09	−17.0	17.3	34.3	10.8

Table 9.3: Mean, standard deviation STD, skewness, 10^{th} and 90^{th} percentile, the distance between them and the mean of the absolute value (namely the mean absolute error in respect to the reference, MAE) of the distribution shown in Figure 9.9-A, i.e. sensible heat flux (Wm^{-2}) difference in respect to the reference.

	Mean	STD	Skewness	10^{th} pr	90^{th} pr	$(90^{th} - 10^{th})$	MAE
$M01$	1.07	1.84	−0.85	−1.70	3.20	4.90	1.81
$M02$	2.63	2.16	−0.47	−0.57	5.16	5.73	3.02
$M03$	−3.76	2.16	−0.57	−6.97	−0.96	6.01	3.78
$M04$	−0.96	2.20	−0.43	−3.70	1.65	5.35	1.83
$M05$	−0.28	2.03	−0.69	−3.17	2.03	5.19	1.50
$M06$	−0.03	1.14	−0.42	−1.23	1.34	2.57	0.83

Table 9.4: Mean, standard deviation STD, skewness, 10^{th} and 90^{th} percentile, the distance between them and the mean of the absolute value (namely the mean absolute error in respect to the reference, MAE) of the distribution shown in Figure 9.9-B, i.e. land surface temperature (^{o}C) difference in respect to the reference.

$M02$ in air temperature is decreased to +2.6 ^{o}C when passing to land surface temperature, and for $M03$ we have −4.7 ^{o}C transformed into −3.7 ^{o}C. Therefore the water and energy balance model seems to attenuate temperature errors from input to output. The interaction between air temperature errors and those of the other meteorological forcings is more evident when the first one does not have a marked tendency to underestimation or overestimation. For instance in $M01$ the most frequent value in air temperature error distribution is around zero, but that of land surface temperature is about 1.5 ^{o}C. This could be due to the diffused underestimation of wind speed (see Figure 9.12), that causes a decrease of H and through it an increase of surface temperature. In $M02$ an opposite effect is observable. $M06$ shows the best adherence with the reference even in case of land surface temperature, with a mean error of −0.03 ^{o}C, a MAE of 0.83 ^{o}C and a reduction of the tails in respect to the other cases.

Figure 9.10 shows time series of sensible heat flux (panel A) and of

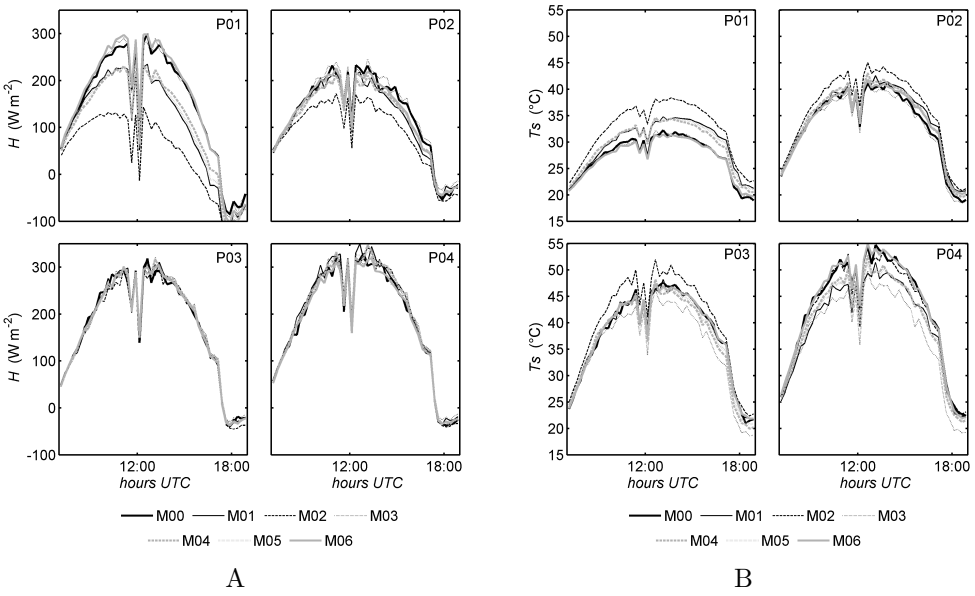

Figure 9.10: Time series of sensible heat flux (A - (Wm^{-2})) and representative land surface temperature (B - (^{o}C)) in the control points from the reference simulation $M00$ and those using interpolated meteorological inputs. Interpolation methods are those described in Figure 9.3.

land surface temperature (panel B) in the four control points, whose positions are reported in Figure 9.2. It can be seen that in dry areas ($P03$ and $P04$) the diurnal evolution of the sensible heat flux remains almost the same in all the simulations, confirming that soil moisture scarcity strongly constraints the solution in terms of heat fluxes. But in presence of soil water availability, as in points $P01$ and $P02$, the sensible heat flux can change significantly in consequence of errors in meteorological forcings. For instance, in $P01$ the difference with the reference exceeds 150 Wm^{-2} for $M02$. Instead land surface temperature is affected by errors in meteorological inputs in both dry and wet soil conditions during all the diurnal cycle, but with a greater impact in the middle of the day as expected. Maximum differences are in the range of $4-6$ ^{o}C. Also in terms of time series the best agreement with the reference outputs is obtained in $M06$, i.e. with meteorological forcings interpolated on the basis of surface characteristics as described in Section 9.1.1.

9.3 Conclusions

The impact of the meteorological forcings microscale spatial distribution on a surface energy and water balance has been investigated using the distributed hydrological model FEST-EWB (Corbari et al., 2011) and the physically based fields of air temperature, air humidity and wind speed provided by the coupled LES-LSM realized in Chapter 7. A reference simulation has been realized by employing the above-said full meteorological fields, and then compared with six simulations with an identical setup but forced with approximated spatial distributions of the meteorological quantities. The six groups of approximated forcings are built on the basis of data registered by three virtual measurement stations placed over different kinds of land cover, representative of the heterogeneity of the simulated area. Three groups ($M01$, $M02$, $M03$) have spatially homogeneous maps, each one using data from the corresponding virtual station. Maps of other two groups ($M04$, $M05$) are obtained with the squared-IDW method of interpolation, using data from two of the three stations and from all the three stations respectively. Finally in the sixth group ($M06$) air temperature and humidity are interpolated using an alternative procedure that is based on surface resemblance and not on physical distance between known and unknown points (see Section 9.1.1). Maps of wind speed are instead obtained using the squared-IDW method.

This alternative method has been proved to better perform than the standard IDW method at the microscale. In fact IDW interpolation has failed in reproducing heterogeneity of both air temperature and humidity reference fields, while the alternative procedure succeeded in it. The complexity of meteorological patterns at the microscale mainly arises from surface heterogeneous characteristics, since large scale atmospheric conditions are the same. Therefore the alternative method, that is based on them, provides better interpolations than the IDW scheme. In particular, when surface heterogeneity is sparse and fragmented and not organized into homogeneous macro-areas, as it is in this case study, the IDW method would require a high number of measurement stations to obtain the same level of reproduction. In conclusion, it has been proved that at the microscale it is more convenient and important to take into account surface resemblance than physical distance for meteorological forcings fields interpolation.

The impact of surface distribution of meteorological forcings has resulted to be different between turbulent fluxes and land surface tem-

perature. The intensity of the effect on sensible heat flux (and even more on latent heat flux) has been found to be regulated by soil water content. Under dry conditions the results of the water and energy balance model are highly constrained in terms of heat fluxes, and the impact of errors in meterological fields reconstruction is limited. But in presence of a sufficient soil moisture the impact can become highly significant, up to more than 150 Wm^{-2} in our tests. Therefore, soil water availability acts like adding degrees of freedom to the system, increasing H (and LE) sensitivity to spatial distribution of meteorological forcings. Instead, the effect on land surface temperature has resulted to be almost unrelated to soil moisture and therefore a more diffused impact has been observed in our study case, with spatial pattern of the error mainly maintained between the inputs and the outputs. When air temperature maps have a diffused tendency to overestimation or underestimation, the same tendency is preserved also in land surface temperature and the intensity remain comparable, even if generally reduced. Instead, when the average error in air temperature is around zero, air humidity and wind speed distortions are determinant. Furthermore, the analyzed results suggest that the water and energy balance model attenuates input errors when passing to outputs and does not amplify them. However, the best agreement between reference results and those obtained with approximate meteorological forcings fields has been obtained with the alternative interpolation method ($M06$), the one that have provided the best reproduction of the reference inputs fields. Therefore it can be asserted that, although smoothed out, the errors of the forcings are transmitted to the outputs, and consequently particular care should be taken in interpolating meteorological data when the objective is to perform an accurate hydrological simulation, especially in non-dry areas.

9.4 Appendix A: FEST-EWB model

FEST-EWB (Flash–flood Event–based Spatially–distributed rainfall–runoff Transformation–Energy Water Balance) is a distributed hydrological energy water balance model (Corbari et al., 2011, 2013) developed from the FEST-WB model (Mancini, 1990; Rabuffetti et al., 2008). FEST-EWB simulates the main processes of the hydrological cycle: evapotranspiration, infiltration, surface runoff, flow routing, subsurface flow (Ravazzani et al., 2011) and snow dynamics (Corbari

et al., 2009). The computational domain is discretized into a mesh of regular square cells in which every parameter is defined or calculated. As inputs the model requires:

- Distributed meteorological forcings (solar radiation, air temperature, air humidity, wind speed, atmospheric pressure)
- Distributed soil and vegetation parameters
- Digital elevation model
- Landuse/landcover map

Core of the model is the system of the water and energy balance equations (equations (9.6) and (9.7)) which are linked through the evapotranspiration term. Basically the energy balance is solved by looking for a Representative Equilibrium Temperature (RET) that is the land surface temperature that closes the energy balance equation. This equilibrium surface temperature, which is an internal model variable, is comparable to the land surface temperature as retrieved from remote sensing data. The soil moisture evolution for a given cell at position (i,j) is described by the energy and water balance equations:

$$Rn_{i,j} - G_{i,j} - H_{i,j} - LE_{i,j} = 0 \tag{9.6}$$

$$\frac{\partial SM_{i,j}}{\partial t} = \frac{1}{dz_{i,j}}(P_{i,j} - R_{i,j} - PE_{i,j} - ET_{i,j}) \tag{9.7}$$

where SM is the soil moisture (mm m^{-1}), P is the precipitation rate (mm h^{-1}), R the runoff flux (mm h^{-1}), PE the drainage flux (mm h^{-1}), ET the evapotranspiration rate (mm h^{-1}), z the soil depth (m), Rn (W m^{-2}) the net radiation, G (W m^{-2}) the soil heat flux and H (W m^{-2}) and LE (W m^{-2}) are respectively the sensible and latent heat fluxes. All these terms of the system are functions of the input soil and vegetation parameters. In particular ET is linked to the latent heat flux through the latent heat of vaporization (λ) and the water density (ρ_w):

$$LE = \rho_w \lambda ET \tag{9.8}$$

The latent heat flux, as reported in Corbari et al. (2011), is computed as:

$$LE = \frac{\rho_a c_p}{\gamma}(e^* - e_a)\left[\frac{f_v}{r_a + r_c} + \frac{1 - f_v}{r_{a_{BS}} + r_{soil}}\right] \tag{9.9}$$

where ρ_a is the air density (kg m^{-3}), γ is the psychometric constant (Pa ^{o}C^{-1}), f_v is the vegetation fraction (-) and c_p is the specific heat

of humid air (MJ kg^{-1} K^{-1}). The saturation vapour pressure e^* is computed as function of RET (Brutsaert, 2005) and the vapour pressure e_a is a function of air temperature. The canopy resistance r_c is expressed following Jarvis (1976), while the soil resistance r_{soil} accordingly to Sun (1982). The aerodynamic resistance (r_a for vegetation and $r_{a_{BS}}$ for bare soil) is computed using the model from Thom (1975). The sensible heat flux is computed as:

$$H = \rho_a c_p \left(RET - T_a\right) \left[\frac{f_v}{r_a} + \frac{1 - f_v}{r_{a_{BS}}}\right] \tag{9.10}$$

where T_a is the air temperature (K). The net radiation is computed as the algebraic sum of the incoming and outgoing short wave and long wave radiation:

$$Rn = R_s(1 - \alpha) + \epsilon_a \sigma T_a^4 - \epsilon_s \sigma RET^4 \tag{9.11}$$

where R_s is the incoming shortwave radiation (W m^{-2}), α is albedo (-), ϵ_a is the atmosphere emissivity (-), ϵ_s is surface emissivity (-) and σ is the Stefan-Boltzmann constant (W m^{-2} K^{-4}). The soil heat flux is the heat exchanged by conduction with the sub-surface soil and it is evaluated as:

$$G = \frac{\lambda_{soil}}{dz}(RET - T_{soil}) \tag{9.12}$$

where λ_{soil} is soil thermal conductivity (W m^{-1} K^{-1}) and T_{soil} is soil temperature (K) at 10 cm depth (McCumber and Pielke, 1981). All the terms of the energy balance depend on RET, so the energy balance equation can be solved by looking for the thermodynamic equilibrium temperature that satisfies it. A Newton–Raphson scheme is used to solve the equation iteratively. FEST-EWB has been validated against energy and mass exchange measurements acquired by an eddy covariance station (Corbari et al., 2011) and also against ground and remote sensing information at agricultural district scale (Corbari et al., 2013) as well as at basin scale (Corbari and Mancini, 2014).

FEST-EWB model falls into a category of models which couple energy and water balance schemes that predict soil moisture dynamics and usually river runoff as well as the surface energy fluxes on a continuous basis. Therefore they are usually more complex and over parameterized than residual energy balance models that use LST as input variable, since for them LST is a modelled variable. These types of models can overcome the limitations related to cloud coverage typical of thermal infrared satellite images and moreover provide continuous

estimates of evapotranspiration and also of soil moisture. Of course some limitations are present in these models linked to the modelling of irrigation, lateral flows and groundwater which are difficult to parameterize. Another limitation is the need of many hydraulic soil input parameters that are often not easily available at large scales, nor at high spatial resolution, even though they have an important role in the computation of the principal mass and energy fluxes.

9.5 Appendix B: additional results

In this appendix we show additional results that complete the analysis performed in this chapter and can support in results interpretation.

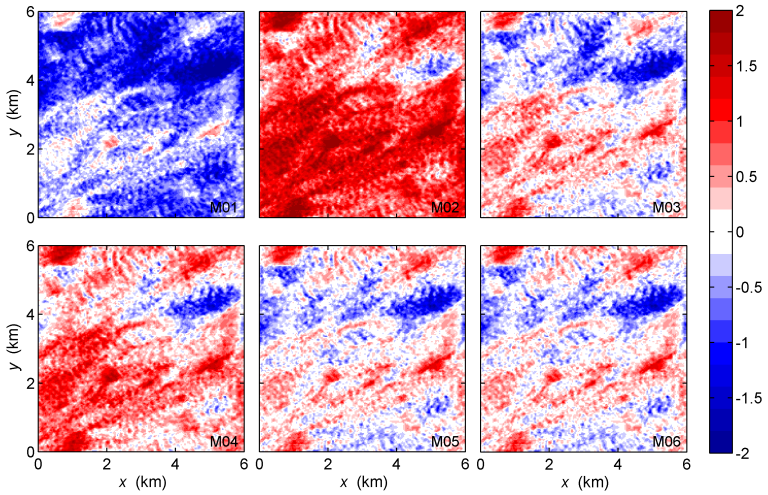

Figure 9.11: Differences between interpolated and reference maps of wind speed (ms^{-1}). Interpolation methods are those described in Figure 9.3.

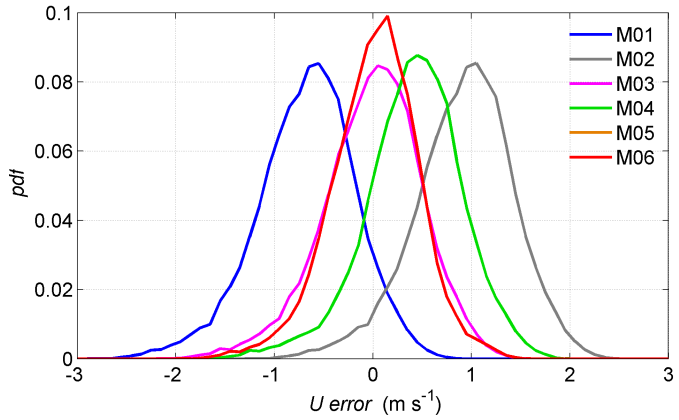

Figure 9.12: Distributions of differences between interpolated and reference maps of wind speed (ms^{-1}). Interpolation methods are those described in Figure 9.3. Distributions refer to 13 : 08 UTC.

	Mean	STD	Skewness	10^{th} pr	90^{th} pr	$(90^{th} - 10^{th})$	MAE
$M01$	−0.68	0.50	−0.39	−1.32	−0.07	1.25	0.71
$M02$	0.92	0.50	−0.39	0.28	1.53	1.25	0.95
$M03$	−0.01	0.50	−0.39	−0.65	0.60	1.25	0.39
$M04$	0.41	0.49	−0.43	−0.20	1.01	1.21	0.54
$M05$	0.02	0.44	−0.29	−0.54	0.55	1.08	0.35
$M06$	0.02	0.44	−0.29	−0.54	0.55	1.08	0.35

Table 9.5: Mean, standard deviation STD, skewness, 10^{th} and 90^{th} percentile, the distance between them and the mean of the absolute value (namely the mean absolute error in respect to the reference, MAE) of the distribution shown in Figure 9.5-C, i.e. wind speed (ms^{-1}) difference in respect to the reference.

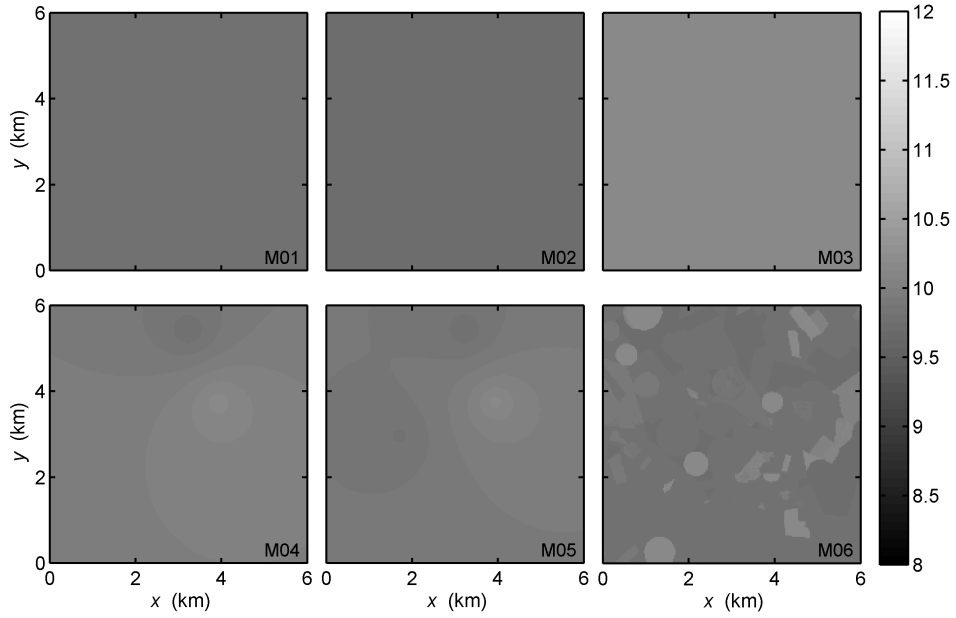

Figure 9.13: Maps of water vapour mixing ratio (g kg^{-1}) obtained on the basis of data registered by the virtual meteorological stations. Interpolation methods are those described in Figure 9.3. All the maps refer to 13 : 08 UTC.

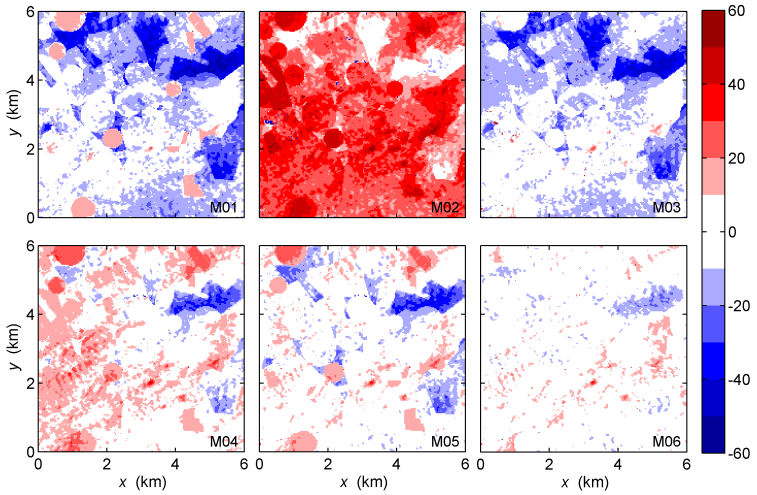

Figure 9.14: Maps of differences between simulations with interpolated meteorological inputs and the reference one for net radiation (Wm^{-2}). Interpolation methods are those described in Figure 9.3.

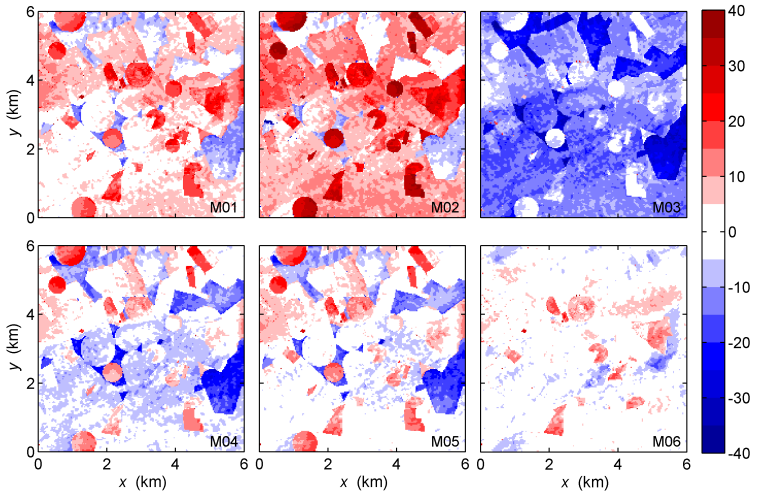

Figure 9.15: Maps of differences between simulations with interpolated meteorological inputs and the reference one for soil heat flux (Wm^{-2}). Interpolation methods are those described in Figure 9.3.

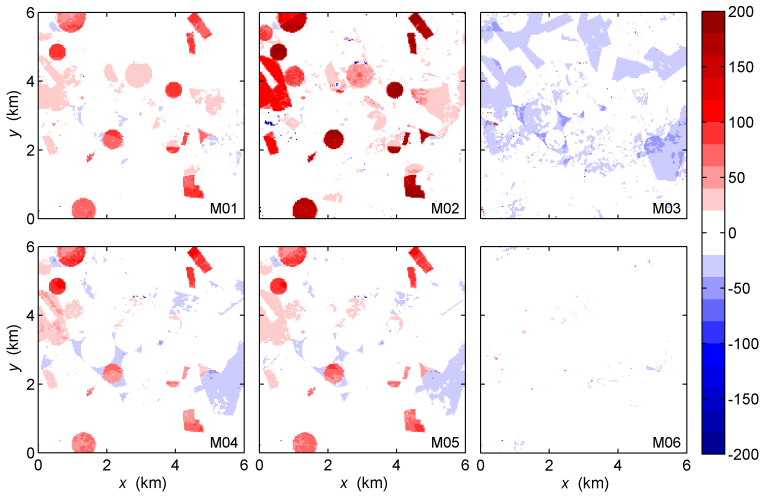

Figure 9.16: Maps of differences between simulations with interpolated meteorological inputs and the reference one for latent heat flux (Wm^{-2}). Interpolation methods are those described in Figure 9.3.

10

Aerodynamic resistance comparison between RAMS-LES estimates, eddy covariance measurements and literature formulas

In this chapter some considerations about the importance of aerodynamic resistance in the estimation of surface heat fluxes, and a comparison between literature formulas and measurements are presented. The aim of this brief analysis is to recall the well known relevance of a correct estimation of aerodynamic resistance in order to obtain valuable results in terms of surface turbulent fluxes, and more specifically in terms of sensible and latent heat fluxes in an hydrological context. A correct quantification of such fluxes is required in several fields of application of hydrological and agrometeorological models. For instance, sustainable water management at the regional scale and irrigation planning at the field scale. Moreover, as extensively discussed in almost all the previous chapters, these fluxes represent the feedback existing between the land surface and the atmospheric boundary layer, being at the same time the product and the source of atmospheric turbulence. Therefore, a their accurate estimation is fundamental in order to correctly simulates ABL turbulence and evolution. The key role of the aerodynamic resistance may be considered a significant weakness of the complex coupled LES-LSM modelling system. In this context, evaluating literature formulas performances represents a starting point for improving the coupled system analyzed in the present thesis.

10.1 Relevance of aerodynamic resistance

Aerodynamic resistance r_a is a fundamental parameter when estimating surface turbulent fluxes by assuming first order closure for turbulence, namely when computing the vertical flux of a certain quantity as proportional to the vertical gradient of the mean value of the quantity itself. According to Monin–Obukhov Similarity (MOS) theory (Monin and Obukhov, 1954), that implies the assumptions of stationary turbulence and surface homogeneity, the aerodynamic resistance for scalars r_{ah} under neutral atmospheric conditions is

$$r_{ah} = \frac{ln\left(\frac{z-d}{z_{oh}}\right) ln\left(\frac{z-d}{z_{om}}\right)}{k^2 U(z)} \tag{10.1}$$

where z is the reference height, d is the displacement height, z_{oh} and z_{om} are the aerodynamic roughness length for scalars and momentum respectively, $U(z)$ is the wind speed at the reference height and k is the Von Karman constant, typically taken equal to 0.4. Under the same assumptions, the kinematic sensible heat flux H_{kin} is computed as

$$H_{kin} = \frac{(T_{surf} - T_{air})}{r_{ah}} \tag{10.2}$$

where T_{surf} and T_{air} are surface and air temperature respectively. MOS theory corrects equation (10.1) for atmospheric stability with integral stability functions that depend on Monin-Obukhov length $L = \frac{u_*^3 T_{air}}{kgH_{kin}}$, where u_* is the surface friction velocity and g is the gravitational acceleration. As equation (10.2) clearly communicates, the mixing and transfer capabilities of turbulence are completely represented by r_{ah}, meaning that very different estimations of the sensible heat can be obtained in function of the value of r_{ah}, although in presence of the same bulk temperature difference. The role of the aerodynamic resistance is therefore quite complex, since it must summarize turbulent eddies effect in only one value, and at the same time it can deeply impact fluxes estimations. Figure 10.1 has the aim to offer an immediate visualization of this concept, even though the simple inverse proportionality of equation (10.2) is already sufficiently clear. In panel A sensible heat flux H is plotted against aerodynamic resistance for 5 different values of temperature difference, ranging from 0.1 K to 10 K. The corresponding normalized curve is plotted in panel B. Since doubling the aerodynamic resistance reduces the sensible heat flux to one

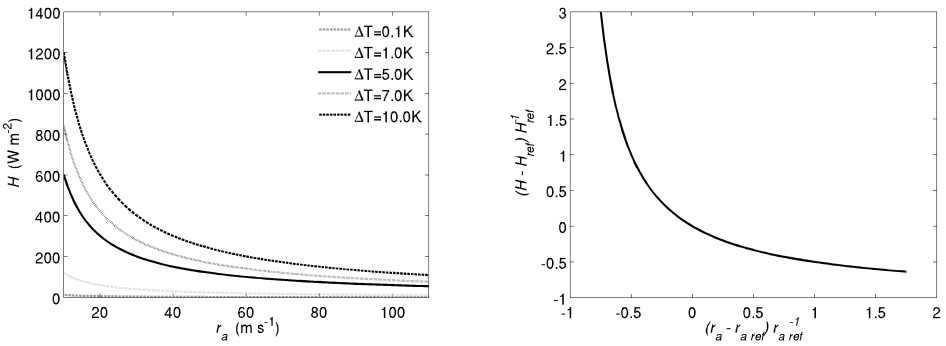

Figure 10.1: Sensible heat flux H against aerodynamic resistance r_{ah} for 5 values of temperature differences governing the exchange (A) and the corresponding normalized curve (B).

half and vice versa, in presence of significant temperature differences between the surface and the overlaying air, i.e. more than 1 K, even a slight overestimation or underestimation of r_{ah} traduces into an error of tens of Wm^{-2} in terms of H. Hence, in order to produce accurate estimations of surface heat fluxes, it is required to take into account corrections for atmospheric stability. The above-mentioned stability function provided by MOS (see Stull (1988) or Garratt (1994) for a detailed description) have a highly non-linear character under unstable conditions, and an iterative procedure must be used to compute aerodynamic resistance (Thom, 1975). In order to simplify r_{ah} computation many parameterizations for unstable atmospheric conditions have been developed. Some studies have evaluated these various parameterizations (e.g Kalma, 1989). One of the most recent and comprehensive analysis is Liu et al. (2007). The most relevant conclusion of Liu et al. (2007) is that better estimations of scalar aerodynamic resistance can be obtained if the difference existing between roughness length for momentum and scalars is considered.

10.2 Comparison between different estimates

In this section we compare measurements of aerodynamic resistance with values obtained by literature formulas and also with estimations deducible by the coupled LES-LSM results presented in Chapter 7. With measurements of aerodynamic resistance we refer to values ob-

tained by the inversion of equation (10.2) using observations of sensible heat fluxes, air and surface temperatures. We employ data from the REFLEX 2012 campaign (see Section 7.5), already used for the assessment of the coupled LES-LSM in Chapter 7. For the camelina field observations from the diurnal cycle simulated in Chapter 7, i.e. July, $26th$, are used, while for the reforestation field we refer to July, $25th$ since no measurements of air temperature are available for July, $26th$. The vineyard field is excluded from the analysis, since it lacks surface temperature measurements. Coherently aerodynamic resistance for momentum is computed as

$$r_{am} = \frac{U}{u_*^2} \tag{10.3}$$

The same procedure is used to derive the corresponding estimations from the coupled LES-LSM results. The parameterizations mainly used in hydrological models are based on the bulk Richardson number Ri_B (Stull, 1988),

$$Ri_B = \frac{g}{T_{air}} \frac{(T_{air} - T_{surf})(z - d)}{U^2} \tag{10.4}$$

on the basis of which a multiplicative coefficient for the neutral aerodynamic resistance is estimated. In order to assure data quality, observations have been selected following similar criteria to those used by Liu et al. (2007), namely:

- measurements done between 06 : 00 UTC and 18 : 00 UTC
- wind speed $U > 1$ ms^{-1}
- sensible heat flux $H > 20$ Wm^{-1}
- $T_{surf} - T_{air} > 0.1$ K
- $H\,(T_{surf} - T_{air}) > 0$ K

Here we evaluate four parameterizations already tested in Liu et al. (2007), and for which it is suggested to discriminate between roughness length for scalars z_{0h} and for momentum z_{0m}, even in cases where it was not originally done. Therefore, in all the four following formulas r_{ahN} is the aerodynamic resistance for scalars in neutral conditions computed using equation (10.1).

- Xie (1988) - $r_{ah} = r_{ahN}\left[1 + \frac{\left[1-16Ri_B ln\left(\frac{z-d}{z_{0m}}\right)\right]^{-0.5}}{ln\left(\frac{z-d}{z_{0m}}\right)}\right]$
- Choudhury et al. (1986) - $r_{ah} = r_{ahN}\left(1 - 5Ri_B\right)^{-3/4}$
- Hatfield et al. (1983) - $r_{ah} = r_{ahN}\left(1 + 5Ri_B\right)$
- Verma et al. (1976) - $r_{ah} = r_{ahN}\left(1 - 16Ri_B\right)^{-1/4}$

The only formulation that originally distinguishes between momentum and scalars roughness length is that by Choudhury et al. (1986). In our analysis we simply apply the rule of thumb $z_{0h} = 0.1z_{0m}$. Figure 10.2-A (upper panel) shows time series of aerodynamic resistance in the camelina field for July, $26th$ obtained from RAMS, literature parameterizations and measurements. In the lower panel the corresponding values of Ri_B are plotted. Figure 10.2-B shows time series of sensible heat flux that are obtained with the various aerodynamic resistance estimations, namely the measured difference of temperature between land surface and air is divided by the them. The first important observation is that measured momentum aerodynamic resistance is significantly lower than that measured for scalars, namely about 20 sm^{-1} for the first one against about 60 sm^{-1} for the latter. This fact support the already cited recommendation by Liu et al. (2007) to distinguish between momentum and scalars. Figure 10.2-B clearly shows the huge impact that neglecting the distinction can have on heat fluxes, with H exceeding 1000 Wm^{-2} in case aerodynamic resistance for momentum is used, while the corresponding measured value is about 300 Wm^{-2}. Estimations of aerodynamic resistance from RAMS preserve the distinction between values for scalars and momentum. Furthermore, RAMS values for momentum are in good agreement with measurements, especially after 12 : 00 UTC. But those for scalars are instead increasingly underestimated during the day, although starting from a situation of overestimation in the early morning. For instance at 15 : 00 UTC RAMS aerodynamic resistance for scalars is about 40 sm^{-1}, against about 60 sm^{-1} of observations, traducing into a sensible heat flux equal to about 400 Wm^{-2} following RAMS, that significantly overestimates the about 250 Wm^{-2} from measurements. Literature parameterizations provide values in the same range of those from RAMS, and therefore underestimate observations. Their descending trend during the day is less pronounced than that of RAMS. The reason lies in the fact that literature formulas use measured wind speed

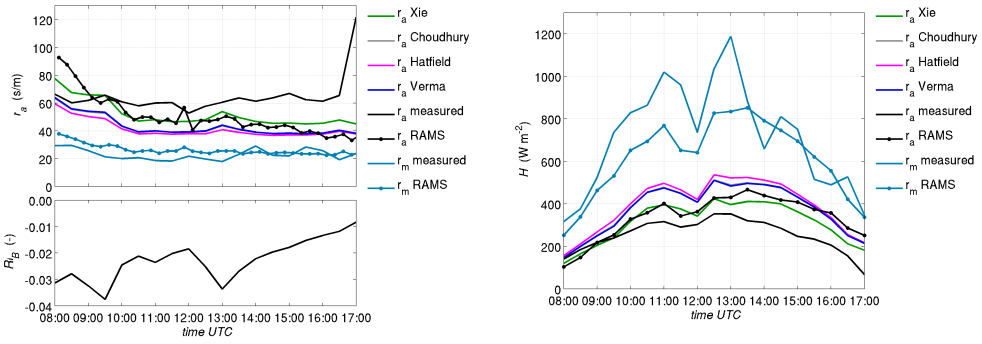

Figure 10.2: Time series of aerodynamic resistance in the camelina field for July, 26*th* obtained from RAMS, literature parameterizations and measurements in the upper panel and corresponding Ri_B values in the lower panel (A). Time series of sensible heat flux obtained with the various aerodynamic resistance estimations (B).

values, while RAMS estimations come from the simulated ABL, whose mean wind does not follow exactly the real one. *Hatfield*, *Verma* and *Choudhury* values are almost identical and they are the lowest ones. Instead *Xie* estimations are the highest ones, with a difference of about 10 sm^{-1} in respect to *Verma*'s, *Hatfield*'s and *Choudhury*'s. From 09 : 00 to 15 : 00 UTC *Xie* values are in agreement with RAMS, and represent the best estimation of measured aerodynamic resistance between those tested. In terms of H it means an overestimation of $50 - 70$ Wm^{-2}. Figure 10.3 shows scatter plots of measured aerodynamic resistance for scalars against all the considered estimations, i.e. from literature formulas, from RAMS results and observations of resistance for momentum. Values are from both camelina and reforestation fields. As already noticed, momentum resistances, both observed and from RAMS, sensibly underestimate measured resistances for scalars, being unsuitable approximations of them. Also RAMS estimations for scalars have a generally tendency to underestimation, but less pronounced and without outliers as high as those from literature formulas. These latter provide better results in case of lower measured aerodynamic resistances (< 100 sm^{-1}). In particular, *Xie* is the best in this range, but significantly overestimates higher values. On the contrary *Verma* performs better for higher values and underestimates the lower ones. *Choudhury* shows a similar behaviour. Finally, *Hatfield* has a diffuse tendency to underestimation.

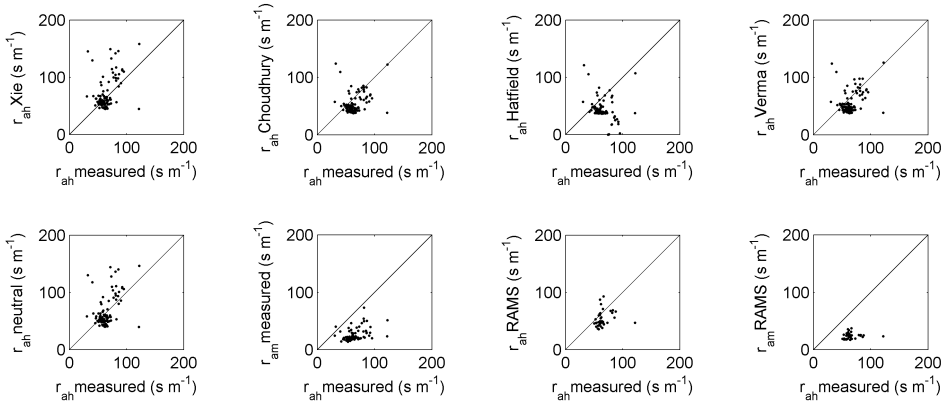

Figure 10.3: scatter plots of measured aerodynamic resistance for scalars against the considered estimations.

10.3 Conclusions

This brief analysis has the aim to recall the relevance of a correct estimation of aerodynamic resistance. In fact small variations in it correspond to significant changes in terms of heat fluxes, and their correct quantification is fundamental for practical applications of hydrological models such as water management or irrigation planning. An accurate computation of surface heat fluxes is of great importance also in coupled LES-LSM simulations, since the turbulent fluxes represent the feedback between the land surface and the overlaying air.

Observation from the REFLEX 2012 campaign have been used to retrieve measured values of resistances during a diurnal cycle. It has been showed that momentum resistances are unsuitable approximations of those for scalars, confirming that with literature formulas better results are obtained if different roughness lengths are used for momentum and scalars. Measurements have been compared against literature formulas and RAMS estimations. RAMS shows a good agreement with observations in terms of momentum resistances, but underestimates scalar resistances. Also literature formulas underestimate the observed values, especially *Hatfield* and *Choudhury*. The best estimates are obtained with *Xie* in the range r_{ah} <100 sm^{-1} and with *Verma* for higher values. However, the level of accordance remains comparable with that provided by RAMS, indicating that only a slightly enhancement of its performances in coupled LES-LSM could be obtained by substituting its parameterization with one of the examined literature formulas.

Part IV

Conclusions

11

Conclusions

In the first part of the thesis the capabilities of the mesoscale model RAMS (Regional Atmospheric Modeling System) to perform LES of the ABL have been deeply investigated. In fact RAMS appears to be an appealing instrument for hydrologically-oriented applications of LES of the ABL, since its equations of motions are natively coupled with a LSM. Furthermore, it provides also the possibility of nesting, that could be used to relate the microscale flow with the mesoscale one. But RAMS is a model designed to work mainly at the mesoscale, and hence it requires an accurate assessment of its capability in simulating microscale flows (Paiva et al., 2009; Gibbs and Fedorovich, 2014a).

The performed analysis has proved that RAMS is actually a suitable instrument to perform LES of the ABL in both convective and neutral regimes. Moreover, an adequate turbulence reconstruction has been obtained with an affordable computational load. The analysis has focused on the impact that the computational grid has on the results, since in this code grid spacing implicitly determines the filtering of the LES . Guidelines have been obtained for grid design in LES of the ABL under both convective and neutral regimes. A key role has been identified for cell aspect ratio (horizontal over vertical resolution) in terms of quality of turbulence reconstruction. Namely the best results do not correspond simply to the finest affordable horizontal and vertical resolutions, but an optimal ratio between them must be maintained. Different values of the minimum horizontal resolution and of the optimal cell aspect ratio have been found for convective and neutral regimes.

In convective conditions a horizontal resolution of 30 is suggested if a good turbulence reconstruction is desired also in proximity of the ground. In fact, a value of 60 m has resulted to be acceptable, but still providing some flows, especially in the near-wall region. Coarser horizontal resolutions do not produce correct turbulent statistics and spectra. Velocity spectra corresponding to the tested grid spacing of 120 m do not show nor turbulence production neither dissipation range. The results suggest that an aspect ratio of 3 provides the best velocity and temperature fields, while higher values cause the appearance of spurious smaller-scale structures in the flow. Hence, the quality of the results can worsen because of an indiscriminate refinement of the vertical grid spacing.

The analysis in free convection conditions has been carried out also for WRF (Weather Research and Forecasting) model. Significantly different results in terms of grid design recommendations have been obtained. In WRF the vertical resolution has a negligible impact on results, at least until the horizontal one is the limiting factor in the computational grid. Therefore high cell aspect ratios are admissible, namely they do not cause the appearance of smaller-scale spurious structures in the flow as they does in RAMS, but refining the vertical resolution does not improve turbulence reconstruction significantly. The different response to changes in aspect ratio between RAMS and WRF is due to the different numerics employed in the two codes, as discussed in Chapter 5. Because of the same reason, better results are obtained with WRF in respect to RAMS when the same horizontal resolution is adopted.

Under neutral conditions finer grid spacings are required, coherently with the smaller size of the typical turbulent structures in this regime. In particular, a horizontal resolution of 64 m provides poor results, while they start to be acceptable with a value of 32 m. A more anisotropic grid than in free convection is suggested, with the best results corresponding to a cell aspect ratio of 4. This is probably due to the elongated shape of the eddies in the near-wall region under neutral conditions. But the over-dissipative nature of the Deardorff (1980) SGS model used in RAMS generates some discrepancies between the expected and the obtained results in proximity of the ground, i.e. where the resolved contribution become minor in respect to the modelled one. However, a refinement of the computational grid associated with the suggested aspect ratio provides results comparable with those obtained with more complex SGS schemes.

RAMS-LES has been also tested in reproducing a real diurnal cycle of the ABL over a heterogeneous surface, in this case coupled with its land-surface model LEAF-3. The coupled model predictions have shown a good agreement with observations. In particular, excellent results have been obtained for net radiation and sensible heat flux, and a general good match for the other surface quantities (latent and soil heat flux, air temperature and humidity) has been found. A diffused underestimation of surface temperature has been observed over the whole domain, but it could probably be reduced if soil heat capacity is tuned. A qualitatively correct time evolution of mean vertical profiles has been assessed. Therefore, we have demonstrated that the coupled model can properly simulate a diurnal cycle of the ABL and of land-atmosphere interactions in real conditions.

The analysis concerning RAMS-LES capabilities and the factors affecting them has continued with the evaluation of the impact that surface heterogeneity level of description has on the coupled model results. It has been found that the predictions of surface quantities (e.g. surface turbulent fluxes, land temperature etc) significantly differs from the reference as the level of aggregation of the heterogeneity approaches the patches size. The differences increase as the surface parameters resolution coarsens. Instead, ABL turbulence has shown non-negligible differences even at scales that still reproduce almost correctly the surface heterogeneity (e.g. 300 m). At the same time larger scales of aggregation (e.g. 1200 m) produce results that are more similar to the reference than those corresponding to a more detailed description of the heterogeneity. But, at the same time, when the scale exceeds the ABL height, the impact of a more organized turbulence appears.

After the extensive assessment of RAMS-LES capabilities, the results of a coupled LES-LSM in real conditions have been used to evaluate the role of the meteorological forcings microscale spatial distribution in a water and energy balance model. Different responses have been detected for turbulent fluxes and for land surface temperature. It has been found that soil moisture regulates the impact on sensible and latent heat fluxes. In presence of dry soil the heat fluxes predicted by the water and energy balance model remain almost fixed even in presence of errors in meteorological forcings spatial distribution reconstruction. Instead, in presence of a sufficient soil water content, the impact becomes significant (in our tests differences in respect to the reference exceed 150 Wm^{-2}). Hence soil moisture increases the sensi-

tivity of latent and sensible heat fluxes to the spatial distribution of meteorological forcings. Conversely, the impact on land surface temperature is almost unrelated to soil water availability and mainly influenced by air temperature distortions. The analysis seems to suggest that the water and energy balance model attenuates the errors when passing from forcings to results, but the spatial pattern of the input distortions is generally still recognizable in the outputs. Therefore, the spatial interpolation of punctual measurements of the meteorological data is important if an accurate simulation is desired. In this context we have proposed and tested an alternative method to interpolates observations at the microscale. It is based on surface properties and not on physical distances as the standard IDW scheme, since at the microscale the complexity of meteorological fields is mainly related to surface heterogeneity, since large atmospheric conditions are the same. The analysis has shown that it actually performs better than the IDW method in presence of a fragmented surface heterogeneity, i.e. with differences not organized into homogeneous macro-areas.

References

Albertson, J. D., Kustas, W. P., and Scanlon, T. M. (2001). Large-eddy simulation over heterogeneous terrain with remotely sensed land surface conditions. *Water Resources Research*, 37(7):1939–1953.

Albertson, J. D. and Parlange, M. B. (1999a). Natural integration of scalar fluxes from complex terrain. *Advances in Water Resources*, 23(3):239–252.

Albertson, J. D. and Parlange, M. B. (1999b). Surface length scales and shear stress: Implications for land-atmosphere interaction over complex terrain. *Water Resources Research*, 35(7):2121–2132.

Anderson, M. C., Norman, J., Mecikalski, J. R., Torn, R. D., Kustas, W. P., and Basara, J. B. (2004). A multiscale remote sensing model for disaggregating regional fluxes to micrometeorological scales. *Journal of Hydrometeorology*, 5(2):343–363.

Andren, A., Brown, A., Mason, P., Graf, J., Schumann, U., Moeng, C.-H., and Nieuwstadt, F. (1994). Large-eddy simulation of a neutrally stratified boundary layer: A comparison of four computer codes. *Quarterly Journal of the Royal Meteorological Society*, 120(520):1457–1484.

Arya, P. S. (2001). *Introduction to micrometeorology*, volume 79. Academic press.

Asselin, R. (1972). Frequency filter for time integrations. *Monthly Weather Review*, 100(6):487–490.

Avissar, R., Eloranta, E. W., Gürer, K., and Tripoli, G. J. (1998). An evaluation of the large-eddy simulation option of the regional atmospheric modeling system in simulating a convective boundary layer: a fife case study. *Journal of the Atmospheric Sciences*, 55(7):1109–1130.

Avissar, R. and Schmidt, T. (1998). An evaluation of the scale at which ground-surface heat flux patchiness affects the convective boundary layer using large-eddy simulations. *Journal of the Atmospheric Sciences*, 55(16):2666–2689.

Barnes, S. L. (1964). A technique for maximizing details in numerical weather map analysis. *Journal of Applied Meteorology*, 3(4):396–409.

Bertoldi, G., Kustas, W. P., and Albertson, J. D. (2013). Evaluating source area contributions from aircraft flux measurements over heterogeneous land using large-eddy simulation. *Boundary-layer meteorology*, 147(2):261–279.

Beyrich, F., Richter, S., Weisensee, U., Kohsiek, W., Lohse, H., De Bruin, H., Foken, T., Göckede, M., Berger, F., Vogt, R., et al. (2002). Experimental determination of turbulent fluxes over the heterogeneous litfass area: Selected results from the litfass-98 experiment. *Theoretical and Applied Climatology*, 73(1-2):19–34.

Bou-Zeid, E., Parlange, M. B., and Meneveau, C. (2007). On the parameterization of surface roughness at regional scales. *Journal of the Atmospheric Sciences*, 64(1):216–227.

Brasseur, J. G. and Wei, T. (2010). Designing large-eddy simulation of the turbulent boundary layer to capture law-of-the-wall scaling. *Physics of Fluids*, 22(2):021303–021303.

Brunsell, N. A., Mechem, D., and Anderson, M. (2011). Surface heterogeneity impacts on boundary layer dynamics via energy balance partitioning. *Atmospheric Chemistry and Physics*, 11(7):3403–3416.

Brutsaert, W. (2005). *Hydrology: an introduction*. Cambridge University Press.

Cai, X., Chen, J., and Desjardins, R. L. (2010). Flux footprints in the convective boundary layer: large-eddy simulation and lagrangian stochastic modelling. *Boundary-layer meteorology*, 137(1):31–47.

Cai, X., Steyn, D., and Gartshore, I. (1995). Resolved-scale turbulence in the atmospheric surface layer from a large eddy simulation. *Boundary-Layer Meteorology*, 75(3):301–314.

Cai, X.-M. (1999). Large-eddy simulation of the convective boundary layer over an idealized patchy urban surface. *Quarterly Journal of the Royal Meteorological Society*, 125(556):1427–1444.

Cai, X.-M. (2012). Effects of wall heating on flow characteristics in a street canyon. *Boundary-Layer Meteorology*, 142(3):443–467.

Cai, X.-M. and Steyn, D. (1996). The von kármán constant determined by large eddy simulation. *Boundary-Layer Meteorology*, 78(1-2):143–164.

Campo, L. (2006). *Land-atmosphere interactions in a non-hydrostatic atmospheric model with improved satellite and surface data-assimilation*. PhD thesis, Universitá degli Studi di Firenze.

Choudhury, B., Reginato, R., and Idso, S. (1986). An analysis of infrared temperature observations over wheat and calculation of latent heat flux. *Agricultural and Forest Meteorology*, 37(1):75–88.

Chow, F. K., Street, R. L., Xue, M., and Ferziger, J. H. (2005). Explicit filtering and reconstruction turbulence modeling for large-eddy simulation of neutral boundary layer flow. *Journal of the Atmospheric Sciences*, 62(7):2058–2077.

Clark, T. L. (1977). A small-scale dynamic model using a terrain-following coordinate transformation. *Journal of Computational Physics*, 24(2):186–215.

Clark, T. L. and Farley, R. (1984). Severe downslope windstorm calculations in two and three spatial dimensions using anelastic interactive grid nesting: A possible mechanism for gustiness. *Journal of the Atmospheric Sciences*, 41(3):329–350.

Clark, T. L. and Hall, W. D. (1991). Multi-domain simulations of the time dependent navier-stokes equations: Benchmark error analysis of some nesting procedures. *Journal of computational physics*, 92(2):456–481.

Corbari, C. and Mancini, M. (2014). Calibration and validation of a distributed energy–water balance model using satellite data of land

surface temperature and ground discharge measurements. *Journal of Hydrometeorology*, 15(1):376–392.

Corbari, C., Masseroni, D., Ceppi, A., Facchi, A., Gandolfi, C., and Mancini, M. (2014). Comparison between high frequency and thirty minutes averaged data from eddy covariance measurements for operative water management. *Journal of Irrigation and Drainage Engineering*, Under Review.

Corbari, C., Masseroni, D., and Mancini, M. (2012). Effetto delle correzioni dei dati misurati da stazioni eddy covariance sulla stima dei flussi evapotraspirativi. *Rivista italiana di agrometeorologia= Italian journal of agrometeorology*.

Corbari, C., Ravazzani, G., and Mancini, M. (2011). A distributed thermodynamic model for energy and mass balance computation: Fest–ewb. *Hydrological Processes*, 25(9):1443–1452.

Corbari, C., Ravazzani, G., Martinelli, J., and Mancini, M. (2009). Elevation based correction of snow coverage retrieved from satellite images to improve model calibration. *Hydrology and Earth System Sciences*, 13(5):639–649.

Corbari, C., Sobrino, J. A., Mancini, M., and Hidalgo, V. (2013). Mass and energy flux estimates at different spatial resolutions in a heterogeneous area through a distributed energy–water balance model and remote-sensing data. *International Journal of Remote Sensing*, 34(9-10):3208–3230.

Cotton, W. R., Pielke Sr, R., Walko, R., Liston, G., Tremback, C., Jiang, H., McAnelly, R., Harrington, J., Nicholls, M., Carrio, G., et al. (2003). Rams 2001: Current status and future directions. *Meteorology and Atmospheric Physics*, 82(1-4):5–29.

Courault, D., Drobinski, P., Brunet, Y., Lacarrere, P., and Talbot, C. (2007). Impact of surface heterogeneity on a buoyancy-driven convective boundary layer in light winds. *Boundary-Layer Meteorology*, 124(3):383–403.

Courault, D. and Monestiez, P. (1999). Spatial interpolation of air temperature according to atmospheric circulation patterns in southeast france. *International Journal of Climatology*, 19(4):365–378.

Cui, Z., Cai, X., and J Baker, C. (2004). Large-eddy simulation of turbulent flow in a street canyon. *Quarterly Journal of the Royal Meteorological Society*, 130(599):1373–1394.

Davies, H. (1976). A lateral boundary formulation for multi-level prediction models. *Quarterly Journal of the Royal Meteorological Society*, 102(432):405–418.

Deardorff, J. W. (1970). Preliminary results from numerical integrations of the unstable planetary boundary layer. *Journal of the Atmospheric Sciences*, 27(8):1209–1211.

Deardorff, J. W. (1972). Numerical investigation of neutral and unstable planetary boundary layers. *Journal of the Atmospheric Sciences*, 29(1):91–115.

Deardorff, J. W. (1974). Three-dimensional numerical study of turbulence in an entraining mixed layer. *Boundary-Layer Meteorology*, 7(2):199–226.

Deardorff, J. W. (1980). Stratocumulus-capped mixed layers derived from a three-dimensional model. *Boundary-Layer Meteorology*, 18(4):495–527.

Driedonks, A. (1982). Models and observations of the growth of the atmospheric boundary layer. *Boundary-Layer Meteorology*, 23(3):283–306.

Durran, D. R. and Klemp, J. B. (1982). The effects of moisture on trapped mountain lee waves. *Journal of the Atmospheric Sciences*, 39(11):2490–2506.

Ershadi, A., McCabe, M., Evans, J., and Walker, J. (2013). Effects of spatial aggregation on the multi-scale estimation of evapotranspiration. *Remote Sensing of Environment*, 131:51–62.

Fedorovich, E. E., Rotunno, R., and Stevens, B. (2010). *Atmospheric turbulence and mesoscale meteorology*. Cambridge University Press.

Foken, T. and Nappo, C. J. (2008). *Micrometeorology*. Springer.

Gadd, A. (1978). A split explicit integration scheme for numerical weather prediction. *Quarterly Journal of the Royal Meteorological Society*, 104(441):569–582.

Gal-Chen, T. and Somerville, R. C. (1975). On the use of a coordinate transformation for the solution of the navier-stokes equations. *Journal of Computational Physics*, 17(2):209–228.

Garratt, J. R. (1994). *The atmospheric boundary layer*. Cambridge university press.

Germano, M., Piomelli, U., Moin, P., and Cabot, W. H. (1991). A dynamic subgrid-scale eddy viscosity model. *Physics of Fluids A: Fluid Dynamics (1989-1993)*, 3(7):1760–1765.

Gibbs, J. A. and Fedorovich, E. (2014a). Comparison of convective boundary layer velocity spectra retrieved from large-eddy-simulation and weather research and forecasting model data. *Journal of Applied Meteorology and Climatology*, 53(2):377–394.

Gibbs, J. A. and Fedorovich, E. (2014b). Effects of temporal discretization on turbulence statistics and spectra in numerically simulated convective boundary layers. *Boundary-Layer Meteorology*, 153(1):19–41.

Gillespie, A., Rokugawa, S., Matsunaga, T., Cothern, J. S., Hook, S., and Kahle, A. B. (1998). A temperature and emissivity separation algorithm for advanced spaceborne thermal emission and reflection radiometer (aster) images. *Geoscience and Remote Sensing, IEEE Transactions on*, 36(4):1113–1126.

Grant, A. (1992). The structure of turbulence in the near-neutral atmospheric boundary layer. *Journal of the atmospheric sciences*, 49(3):226–239.

Hadfield, M., Cotton, W., and Pielke, R. (1991). Large-eddy simulations of thermally forced circulations in the convective boundary layer. part i: A small-scale circulation with zero wind. *Boundary-Layer Meteorology*, 57(1-2):79–114.

Hadfield, M., Cotton, W., and Pielke, R. (1992). Large-eddy simulations of thermally forced circulations in the convective boundary layer. part ii: The effect of changes in wavelength and wind speed. *Boundary-Layer Meteorology*, 58(4):307–327.

Hatfield, J., Perrier, A., and Jackson, R. (1983). Estimation of evapotranspiration at one time-of-day using remotely sensed surface temperatures. *Agricultural Water Management*, 7(1):341–350.

Hechtel, L. M., Stul, R. B., and Moeng, C.-H. (1990). The effects of nonhomogeneous surface fluxes on the convective boundary layer: A case study using large-eddy simulation. *Journal of the Atmospheric Sciences*, 47(14):1721–1741.

Hijmans, R. J., Cameron, S. E., Parra, J. L., Jones, P. G., and Jarvis, A. (2005). Very high resolution interpolated climate surfaces for global land areas. *International journal of climatology*, 25(15):1965–1978.

Hill, G. E. (1974). Factors controlling the size and spacing of cumulus clouds as revealed by numerical experiments. *Journal of the Atmospheric Sciences*, 31(3):646–673.

Hsieh, C.-I., Katul, G., and Chi, T.-w. (2000). An approximate analytical model for footprint estimation of scalar fluxes in thermally stratified atmospheric flows. *Advances in Water Resources*, 23(7):765–772.

Huang, H.-Y. and Margulis, S. A. (2009). On the impact of surface heterogeneity on a realistic convective boundary layer. *Water Resources Research*, 45(4).

Huang, H.-Y. and Margulis, S. A. (2010). Evaluation of a fully coupled large-eddy simulation–land surface model and its diagnosis of land-atmosphere feedbacks. *Water Resources Research*, 46(6).

Huang, H.-Y. and Margulis, S. A. (2012). Impact of soil moisture heterogeneity length scale and gradients on daytime coupled land-cloudy boundary layer interactions. *Hydrological Processes*.

Huang, H.-Y., Stevens, B., and Margulis, S. A. (2008a). Application of dynamic subgrid-scale models for large-eddy simulation of the daytime convective boundary layer over heterogeneous surfaces. *Boundary-Layer Meteorology*, 126(3):327–348.

Huang, J., Lee, X., and Patton, E. G. (2008b). A modelling study of flux imbalance and the influence of entrainment in the convective boundary layer. *Boundary-layer meteorology*, 127(2):273–292.

Huang, J., Lee, X., and Patton, E. G. (2009). Dissimilarity of scalar transport in the convective boundary layer in inhomogeneous landscapes. *Boundary-layer meteorology*, 130(3):327–345.

Hutchins, N. and Marusic, I. (2007). Evidence of very long meandering features in the logarithmic region of turbulent boundary layers. *Journal of Fluid Mechanics*, 579:1–28.

Inagaki, A., Letzel, M. O., Raasch, S., and Kanda, M. (2006). Impact of surface heterogeneity on energy imbalance: a study using les. *Journal of the Meteorological Society of Japan*, 84(1):187–198.

Jarvis, P. (1976). The interpretation of the variations in leaf water potential and stomatal conductance found in canopies in the field. *Philosophical Transactions of the Royal Society of London. B, Biological Sciences*, 273(927):593–610.

Joly, D., Nilsen, L., Fury, R., Elvebakk, A., and Brossard, T. (2003). Temperature interpolation at a large scale: test on a small area in svalbard. *International Journal of Climatology*, 23(13):1637–1654.

Jonker, H. J., Duynkerke, P. G., and Cuijpers, J. W. (1999). Mesoscale fluctuations in scalars generated by boundary layer convection. *Journal of the Atmospheric Sciences*, 56(5):801–808.

Kaimal, J. C. and Finnigan, J. J. (1994). *Atmospheric boundary layer flows: their structure and measurement*. Oxford University Press.

Kalma, J. D. (1989). *A comparison of expressions for the aerodynamic resistance to sensible heat transfer*. CSIRO Institute of Natural Resources and Environment, Division of Water Resources.

Kanda, M., Inagaki, A., Letzel, M. O., Raasch, S., and Watanabe, T. (2004). Les study of the energy imbalance problem with eddy covariance fluxes. *Boundary-Layer Meteorology*, 110(3):381–404.

Khanna, S. and Brasseur, J. G. (1997). Analysis of monin–obukhov similarity from large-eddy simulation. *Journal of Fluid Mechanics*, 345:251–286.

Kim, H.-J., Noh, Y., and Raasch, S. (2004). Interaction between wind and temperature fields in the planetary boundary layer for a spatially heterogeneous surface heat flux. *Boundary-layer meteorology*, 111(2):225–246.

Kirkil, G., Mirocha, J., Bou-Zeid, E., Chow, F. K., and Kosovic, B. (2012). Implementation and evaluation of dynamic subfilter-scale stress models for large-eddy simulation using WRF. *Monthly Weather Review*, 140(1):266–284.

Klemp, J. and Lilly, D. (1978). Numerical simulation of hydrostatic mountain waves. *Journal of the atmospheric sciences*, 35(1):78–107.

Klemp, J. B. and Durran, D. R. (1983). An upper boundary condition permitting internal gravity wave radiation in numerical mesoscale models. *Monthly Weather Review*, 111(3):430–444.

Klemp, J. B., Skamarock, W. C., and Dudhia, J. (2007). Conservative split-explicit time integration methods for the compressible nonhydrostatic equations. *Monthly Weather Review*, 135(8):2897–2913.

Klemp, J. B. and Wilhelmson, R. B. (1978a). The simulation of three-dimensional convective storm dynamics. *Journal of the Atmospheric Sciences*, 35(6):1070–1096.

Klemp, J. B. and Wilhelmson, R. B. (1978b). Simulations of right-and left-moving storms produced through storm splitting. *Journal of the Atmospheric Sciences*, 35(6):1097–1110.

Kosovic, B. (1997). Subgrid-scale modelling for the large-eddy simulation of high-reynolds-number boundary layers. *Journal of Fluid Mechanics*, 336:151–182.

Kundu, P. and Cohen, I. (2000). *Fluid Mechanics, 730 pp.* Elsevier, New York.

Kustas, W., Li, F., Jackson, T., Prueger, J., MacPherson, J., and Wolde, M. (2004). Effects of remote sensing pixel resolution on modeled energy flux variability of croplands in iowa. *Remote sensing of Environment*, 92(4):535–547.

Kustas, W. P. and Albertson, J. D. (2003). Effects of surface temperature contrast on land-atmosphere exchange: A case study from monsoon 90. *Water Resources Research*, 39(6).

Laprise, R. (1992). The euler equations of motion with hydrostatic pressure as an independent variable. *Monthly Weather Review*, 120(1):197–207.

Leclerc, M. Y., Shen, S., and Lamb, B. (1997). Observations and large-eddy simulation modeling of footprints in the lower convective boundary layer. *Journal of Geophysical Research: Atmospheres (1984–2012)*, 102(D8):9323–9334.

Lee, X. and Black, T. A. (1993). Atmospheric turbulence within and above a douglas-fir stand. part ii: Eddy fluxes of sensible heat and water vapour. *Boundary-Layer Meteorology*, 64(4):369–389.

Lenschow, D., Wyngaard, J. C., and Pennell, W. T. (1980). Mean-field and second-moment budgets in a baroclinic, convective boundary layer. *Journal of the Atmospheric Sciences*, 37(6):1313–1326.

Lenschow, D. H., Lothon, M., Mayor, S. D., Sullivan, P. P., and Canut, G. (2012). A comparison of higher-order vertical velocity moments in the convective boundary layer from lidar with in situ measurements and large-eddy simulation. *Boundary-Layer Meteorology*, 143(1):107–123.

Lilly, D. K. (1962). On the numerical simulation of buoyant convection. *Tellus*, 14(2):148–172.

Lilly, D. K. (1967). The representation of small scale turbulence in numerical simulation experiments.

Lilly, D. K. (1992). A proposed modification of the germano subgrid-scale closure method. *Physics of Fluids A: Fluid Dynamics (1989-1993)*, 4(3):633–635.

Lin, C.-L., Moeng, C.-H., Sullivan, P. P., and McWilliams, J. C. (1997). The effect of surface roughness on flow structures in a neutrally stratified planetary boundary layer flow. *Physics of Fluids (1994-present)*, 9(11):3235–3249.

Liu, S., Lu, L., Mao, D., Jia, L., et al. (2007). Evaluating parameterizations of aerodynamic resistance to heat transfer using field measurements. *Hydrology and Earth System Sciences Discussions*, 11(2):769–783.

Liu, S. and Shao, Y. (2013). Soil-layer configuration requirement for large-eddy atmosphere and land surface coupled modeling. *Atmospheric Science Letters*, 14(2):112–117.

Liu, Y., Miao, S., Zhang, C., Cui, G., and Zhang, Z. (2012). Study on micro-atmospheric environment by coupling large eddy simulation with mesoscale model. *Journal of Wind Engineering and Industrial Aerodynamics*, 107:106–117.

Liu, Y., Warner, T., Liu, Y., Vincent, C., Wu, W., Mahoney, B., Swerdlin, S., Parks, K., and Boehnert, J. (2011). Simultaneous

nested modeling from the synoptic scale to the les scale for wind energy applications. *Journal of Wind Engineering and Industrial Aerodynamics*, 99(4):308–319.

Lothon, M., Lenschow, D. H., and Mayor, S. D. (2009). Doppler lidar measurements of vertical velocity spectra in the convective planetary boundary layer. *Boundary-Layer Meteorology*, 132(2):205–226.

Louis, J.-F. (1979). A parametric model of vertical eddy fluxes in the atmosphere. *Boundary-Layer Meteorology*, 17(2):187–202.

Ludwig, F. L., Chow, F. K., and Street, R. L. (2009). Effect of turbulence models and spatial resolution on resolved velocity structure and momentum fluxes in large-eddy simulations of neutral boundary layer flow. *Journal of Applied Meteorology and Climatology*, 48(6):1161–1180.

Mahrt, L. (1998). Flux sampling errors for aircraft and towers. *Journal of Atmospheric and Oceanic technology*, 15(2):416–429.

Mancini, M. (1990). *La modellazione distribuita della risposta idrologica: effetti della variabilit spaziale e della scala di rappresentazione del fenomeno dellassorbimento*. PhD thesis, Politecnico di Milano.

Mao, S., Leclerc, M. Y., and Michaelides, E. E. (2008). Passive scalar flux footprint analysis over horizontally inhomogeneous plant canopy using large-eddy simulation. *Atmospheric Environment*, 42(21):5446–5458.

Markkanen, T., Steinfeld, G., Kljun, N., Raasch, S., and Foken, T. (2009). Comparison of conventional lagrangian stochastic footprint models against les driven footprint estimates. *Atmospheric Chemistry and Physics*, 9(15):5575–5586.

Mason, P. J. and Thomson, D. (1992). Stochastic backscatter in large-eddy simulations of boundary layers. *Journal of Fluid Mechanics*, 242:51–78.

McCabe, M. F. and Wood, E. F. (2006). Scale influences on the remote estimation of evapotranspiration using multiple satellite sensors. *Remote Sensing of Environment*, 105(4):271–285.

McCumber, M. C. and Pielke, R. A. (1981). Simulation of the effects of surface fluxes of heat and moisture in a mesoscale numerical model:

1. soil layer. *Journal of Geophysical Research: Oceans (1978–2012)*, 86(C10):9929–9938.

Mesinger, F. and Arakawa, A. (1976). Numerical methods used in atmospheric models, volume 1. In *Global Atmospheric Research Program World Meteorological Organization, Geneva (Switzerland).*, volume 1.

Michioka, T. and Chow, F. K. (2008). High-resolution large-eddy simulations of scalar transport in atmospheric boundary layer flow over complex terrain. *Journal of Applied Meteorology and Climatology*, 47(12):3150–3169.

Miguel, E. D., Jimenez, M., Perez, I., Camara, O. G. d. l., Munoz, F., and Gomez-Sanchez, J. A. (2014). Image processing methods and results for the reflex airborne remote sensing campaign. *Acta Geophysica*, Under review.

Mirocha, J., Lundquist, J., and Kosovic, B. (2010). Implementation of a nonlinear subfilter turbulence stress model for large-eddy simulation in the advanced research WRF model. *Monthly Weather Review*, 138(11):4212–4228.

Moeng, C., Dudhia, J., Klemp, J., and Sullivan, P. (2007). Examining two-way grid nesting for large eddy simulation of the PBL using the WRF model. *Monthly Weather Review*, 135(6):2295–2311.

Moeng, C.-H. (1984). A large-eddy-simulation model for the study of planetary boundary-layer turbulence. *Journal of the Atmospheric Sciences*, 41(13):2052–2062.

Moeng, C.-H. and Sullivan, P. P. (1994). A comparison of shear-and buoyancy-driven planetary boundary layer flows. *Journal of the Atmospheric Sciences*, 51(7):999–1022.

Moeng, C.-H. and Wyngaard, J. C. (1988). Spectral analysis of large-eddy simulations of the convective boundary layer. *Journal of the Atmospheric Sciences*, 45(23):3573–3587.

Monin, A. and Obukhov, A. (1954). Basic laws of turbulent mixing in the surface layer of the atmosphere. *Contrib. Geophys. Inst. Acad. Sci. USSR*, 151:163–187.

Nakanish, M. (2001). Improvement of the mellor–yamada turbulence closure model based on large-eddy simulation data. *Boundary-layer meteorology*, 99(3):349–378.

Nieuwstadt, F. and Brost, R. (1986). The decay of convective turbulence. *Journal of the atmospheric sciences*, 43(6):532–546.

Nieuwstadt, F., Mason, P. J., Moeng, C., and Schumann, U. (1993). Large-eddy simulation of the convective boundary layer: A comparison of four computer codes. In *Turbulent Shear Flows 8*, pages 343–367. Springer.

Nuss, W. A. and Titley, D. W. (1994). Use of multiquadric interpolation for meteorological objective analysis. *Monthly Weather Review*, 122(7):1611–1631.

Orlanski, I. (1976). A simple boundary condition for unbounded hyperbolic flows. *Journal of computational physics*, 21(3):251–269.

Paiva, L., Bodstein, G. C., and Menezes, W. F. (2009). Numerical simulation of atmospheric boundary layer flow over isolated and vegetated hills using RAMS. *Journal of Wind Engineering and Industrial Aerodynamics*, 97(9):439–454.

Panin, G., Tetzlaff, G., and Raabe, A. (1998). Inhomogeneity of the land surface and problems in the parameterization of surface fluxes in natural conditions. *Theoretical and Applied Climatology*, 60(1-4):163–178.

Pape, R., Wundram, D., Löffler, J., et al. (2009). Modelling near-surface temperature conditions in high mountain environments: an appraisal. *Climate Research*, 39(2):99–109.

Patton, E. G., Sullivan, P. P., and Moeng, C.-H. (2005). The influence of idealized heterogeneity on wet and dry planetary boundary layers coupled to the land surface. *Journal of the atmospheric sciences*, 62(7):2078–2097.

Pedersen, J. G., Kelly, M., Gryning, S.-E., Floors, R., Batchvarova, E., and Peña, A. (2012). Comparison of large eddy simulations of a convective boundary layer with wind LIDAR measurements. *Advances in Science and Research*, 8(1):83–86.

Pielke, R., Cotton, W., Walko, R. e. a., Tremback, C. J., Lyons, W. A., Grasso, L., Nicholls, M., Moran, M., Wesley, D., Lee, T., et al.

(1992). A comprehensive meteorological modeling systemRAMS. *Meteorology and Atmospheric Physics*, 49(1-4):69–91.

Piomelli, U., Cabot, W. H., Moin, P., and Lee, S. (1991). Subgrid-scale backscatter in turbulent and transitional flows. *Physics of Fluids. A: Fluid Dynamics*, 3:1766.

Pope, S. B. (2000). *Turbulent flows*. Cambridge university press.

Porté-Agel, F., Meneveau, C., and Parlange, M. B. (2000). A scale-dependent dynamic model for large-eddy simulation: application to a neutral atmospheric boundary layer. *Journal of Fluid Mechanics*, 415:261–284.

Prabha, T., Leclerc, M., and Baldocchi, D. (2008). Comparison of in-canopy flux footprints between large-eddy simulation and the lagrangian simulation. *Journal of Applied Meteorology and Climatology*, 47(8):2115–2128.

Press, W. H., Teukolsky, S. A., Vetterling, W. T., and Flannery, B. P. (1996). *Numerical recipes in C*, volume 2. Citeseer.

Raasch, S. and Harbusch, G. (2001). An analysis of secondary circulations and their effects caused by small-scale surface inhomogeneities using large-eddy simulation. *Boundary-layer meteorology*, 101(1):31–59.

Rabuffetti, D., Ravazzani, G., Corbari, C., and Mancini, M. (2008). Verification of operational quantitative discharge forecast (qdf) for a regional warning system–the amphore case studies in the upper po river. *Natural Hazards and Earth System Science*, 8(1):161–173.

Ravazzani, G., Rametta, D., and Mancini, M. (2011). Macroscopic cellular automata for groundwater modelling: A first approach. *Environmental Modelling & Software*, 26(5):634–643.

Richter, K., Timmermans, W., et al. (2009). Physically based retrieval of crop characteristics for improved water use estimates. *Hydrology and Earth System Sciences*, 13(5):663–674.

Robert, A. J. (1966). The integration of a low order spectral form of the primitive meteorological equations(spherical harmonics integration of low order spectral form of primitive meteorological equations). *Journal of the Meteorological Society of Japan*, 44:237–245.

Robeson, S. M. (1994). Influence of spatial sampling and interpolation on estimates of air temperature change. *Climate Res*, 4:1191126.

Sagaut, P. (2002). *Large eddy simulation for incompressible flows*. Springer.

Schmidt, H. and Schumann, U. (1989). Coherent structure of the convective boundary layer derived from large-eddy simulations. *Journal of Fluid Mechanics*, 200:511–562.

Schröter, M., Bange, J., and Raasch, S. (2000). Simulated airborne flux measurements in a les generated convective boundary layer. *Boundary-layer meteorology*, 95(3):437–456.

Shao, Y., Liu, S., Schween, J. H., and Crewell, S. (2013). Large-eddy atmosphere-land-surface modelling over heterogeneous surfaces: Model development and comparison with measurements. *Boundary-Layer Meteorology*, pages 1–24.

Shen, S. and Leclerc, M. Y. (1995). How large must surface inhomogeneities be before they influence the convective boundary layer structure? a case study. *Quarterly Journal of the Royal Meteorological Society*, 121(526):1209–1228.

Shepard, D. (1968). A two-dimensional interpolation function for irregularly-spaced data. In *Proceedings of the 1968 23rd ACM national conference*, pages 517–524. ACM.

Skamarock, W., Klemp, J., Dudhia, J., Gill, D., and Barker, D. (2008). A description of the advanced research wrf version 3. NCAR tech. Technical report, Note NCAR/TN-4751STR.

Skamarock, W. C. and Klemp, J. B. (1992). The stability of time-split numerical methods for the hydrostatic and the nonhydrostatic elastic equations. *Monthly Weather Review*, 120(9):2109–2127.

Smagorinsky, J. (1963). General circulation experiments with the primitive equations: I. the basic equations. *Monthly Weather Review*, 91(3):99–164.

Sobrino, J., Jiménez-Muñoz, J., Sòria, G., Gómez, M., Ortiz, A. B., Romaguera, M., Zaragoza, M., Julien, Y., Cuenca, J., Atitar, M., et al. (2008). Thermal remote sensing in the framework of the sen2flex project: field measurements, airborne data and applications. *International Journal of Remote Sensing*, 29(17-18):4961–4991.

Steinfeld, G., Letzel, M. O., Raasch, S., Kanda, M., and Inagaki, A. (2007). Spatial representativeness of single tower measurements and the imbalance problem with eddy-covariance fluxes: results of a large-eddy simulation study. *Boundary-Layer Meteorology*, 123(1):77–98.

Stull, R. B. (1988). *An introduction to boundary layer meteorology*. Kluwer academic publishers.

Su, Z., Pelgrum, H., and Menenti, M. (1999). Aggregation effects of surface heterogeneity in land surface processes. *Hydrology and Earth System Sciences*, 3:549–563.

Sühring, M., Maronga, B., Herbort, F., and Raasch, S. (2014). On the effect of surface heat-flux heterogeneities on the mixed-layer-top entrainment. *Boundary-Layer Meteorology*, 151(3):531–556.

Sühring, M. and Raasch, S. (2013). Heterogeneity-induced heat-flux patterns in the convective boundary layer: Can they be detected from observations and is there a blending height?a large-eddy simulation study for the litfass-2003 experiment. *Boundary-Layer Meteorology*, pages 1–23.

Sullivan, P. P., McWilliams, J. C., and Moeng, C.-H. (1994). A subgrid-scale model for large-eddy simulation of planetary boundary-layer flows. *Boundary-Layer Meteorology*, 71(3):247–276.

Sullivan, P. P. and Patton, E. G. (2011). The effect of mesh resolution on convective boundary layer statistics and structures generated by large-eddy simulation. *Journal of the Atmospheric Sciences*, 68(10):2395–2415.

Sun, S. F. (1982). Moisture and heat transport in a soil layer forced by atmospheric conditions. Master's thesis, University of Connecticut, Storrs.

Talbot, C., Bou-Zeid, E., and Smith, J. (2012). Nested mesoscale large-eddy simulations with wrf: performance in real test cases. *Journal of Hydrometeorology*, 13(5):1421–1441.

Tennekes, H. and Lumley, J. L. (1972). *A first course in turbulence*. MIT press.

Thom, A. (1975). Momentum, mass and heat exchange of plant communities. *Vegetation and the Atmosphere*, 1:57–109.

Timmermans, W., Bertoldi, G., Albertson, J., Olioso, A., Su, Z., and Gieske, A. (2008). Accounting for atmospheric boundary layer variability on flux estimation from rs observations. *International Journal of Remote Sensing*, 29(17-18):5275–5290.

Timmermans, W. J., Jimenez-Munoz, J.-C., Hidalgo, V., Richter, K., Sobrino, J. A., d'Urso, G., Satalino, G., Mattia, F., De Lathauwer, E., and Pauwels, V. R. (2011). Estimation of the spatially distributed surface energy budget for agrisar 2006, part i: Remote sensing model intercomparison. *Selected Topics in Applied Earth Observations and Remote Sensing, IEEE Journal of*, 4(2):465–481.

Timmermans, W. J., Tol, C. v. d., Timmermans, J., Ucer, M., Chen, X., Alonso, L., Moreno, J., Carrara, A., Lopez, R., Tercero, F. d. l. C., Corcoles, H. L., Miguel, E. d., Sanchez, J. A. G., Perez, I., Franch, B., Munoz, J.-C. J., Skokovic, D., Sobrino, J., Soria, G., MacArthur, A., Vescovo, L., Reusen, I., Andreu, A., Burkart, A., Cilia, C., Contreras, S., Corbari, C., Calleja, J. F., Guzinski, R., Hellmann, C., Herrmann, I., Kerr, G., Lazar, A.-L., Leutner, B., Mendiguren, G., Nasilowska, S., Nieto, H., Pachego-Labrador, J., Pulanekar, S., Raj, R., Schikling, A., Siegmann, B., Bueren, S. v., , and Su, Z. (2014). An overview of the regional experiments for land-atmosphere exchanges (REFLEX) 2012 campaign. *Acta Geophysica*, Accepted.

Tol, C. v. d., Timmermans, W. J., Corbari, C., Carrara, A., Timmermans, J., and Su, Z. (2014). Eddy covariance and large aperture scintillometer data collection during the REFLEX campaign. *Acta Geophysica*, Under review.

Tremback, C., Tripoli, G., Arritt, R., Cotton, W., and Pielke, R. (1986). The regional atmospheric modeling system. In *Proceedings of an International Conference on Development Applications of Computer Techniques Environmental Studies*, pages 601–607. Computational Mechanics Publication, Rewood Burn Ltd.

Tremback, C. and Walko, R. (2006). Rams regional atmospheric modeling system version 6.0, users guide–introduction. *ATMET, LLC, Boulder, Colorado*.

Tremback, C. J. (1985). A surface temperature and moisture parameterization for use in mesoscale numerical models. In *Preprints, 7th Conference on Numerical Weather Prediction*. AMS.

Tripoli, G. and Cotton, W. (1982). The colorado state university three-dimensional cloud/mesoscale model-1982. part i: General theoretical framework and sensitivity experiments. *Journal de Recherches Atmospheriques*, 16:185–220.

Twine, T. E., Kustas, W., Norman, J., Cook, D., Houser, P., Meyers, T., Prueger, J., Starks, P., and Wesely, M. (2000). Correcting eddy-covariance flux underestimates over a grassland. *Agricultural and Forest Meteorology*, 103(3):279–300.

Verma, S., Rosenberg, N., Blad, B., and Baradas, M. (1976). Resistance-energy balance method for predicting evapotranspiration: Determination of boundary layer resistance and evaluation of error effects. *Agronomy Journal*, 68(5):776–782.

Vesala, T., Kljun, N., Rannik, Ü., Rinne, J., Sogachev, A., Markkanen, T., Sabelfeld, K., Foken, T., and Leclerc, M. (2008). Flux and concentration footprint modelling: State of the art. *Environmental Pollution*, 152(3):653–666.

Walko, R. and Tremback, C. (2001). Rams technical description.

Walko, R. L., Cotton, W. R., and Pielke, R. A. (1992). Large-eddy simulations of the effects of hilly terrain on the convective boundary layer. *Boundary-Layer Meteorology*, 58(1-2):133–150.

Walko, R. L., Tremback, C. J., Pielke, R. A., and Cotton, W. R. (1995). An interactive nesting algorithm for stretched grids and variable nesting ratios. *Journal of Applied Meteorology*, 34(4):994–999.

Wicker, L. J. and Skamarock, W. C. (2002). Time-splitting methods for elastic models using forward time schemes. *Monthly Weather Review*, 130(8):2088–2097.

Wilson, K., Goldstein, A., Falge, E., Aubinet, M., Baldocchi, D., Berbigier, P., Bernhofer, C., Ceulemans, R., Dolman, H., Field, C., et al. (2002). Energy balance closure at fluxnet sites. *Agricultural and Forest Meteorology*, 113(1):223–243.

Wood, E. F. (1994). Scaling, soil moisture and evapotranspiration in runoff models. *Advances in water resources*, 17(1):25–34.

Wood, E. F. (1995). Scaling behaviour of hydrological fluxes and variables: empirical studies using a hydrological model and remote sensing data. *Hydrological Processes*, 9(3-4):331–346.

Wood, E. F., Sivapalan, M., Beven, K., and Band, L. (1988). Effects of spatial variability and scale with implications to hydrologic modeling. *Journal of Hydrology*, 102(1):29–47.

Wyngaard, J. C. (2010). *Turbulence in the Atmosphere*, volume 774. Cambridge University Press Cambridge.

Xie, X. (1988). An improved energy balance-aerodynamic resistance model used estimation of evapotranspiration on the wheat field. *Acta Meteorology Sinica (in Chinese)*, 46(1):102–106.

Zhou, Y., Brasseur, J. G., and Juneja, A. (2001). A resolvable subfilter-scale model specific to large-eddy simulation of under-resolved turbulence. *Physics of Fluids (1994-present)*, 13(9):2602–2610.